Precision Measurement of Neutron Spin Asymmetry A_1^n at Large x_{Bj} Using CEBAF at 5.7 GeV

by

Xiaochao Zheng

Submitted to the Department of Physics
in partial fulfillment of the requirements for the degree of

Doctor of Philosophy

at the

MASSACHUSETTS INSTITUTE OF TECHNOLOGY

December 2002

©Massachusetts Institute of Technology 2002

Author .....
Department of Physics
December 13, 2002

Certified by .....
William Bertozzi
Professor of Physics
Thesis Supervisor

Accepted by .....
Thomas J. Greytak
Associate Department Head for Education

Precision Measurement of Neutron Spin Asymmetry A_1^n at Large x_{Bj} Using CEBAF at 5.7 GeV

by

Xiaochao Zheng

Submitted to the Department of Physics
on December 13, 2002, in partial fulfillment of the
requirements for the degree of
Doctor of Philosophy

Abstract

Nucleon spin structure has remained one of the key issues of hadronic physics since the 1980's. Among the unsolved questions, the neutron spin structure in the valence quark region (the large Bjorken variable x_{Bj} region) is of particular interest. The few data that existed in the large x_{Bj} region are very imprecise. Also, theoretical predictions based on Quantum Chromo-Dynamics (QCD) are difficult to carry out accurately in this non-perturbative region and having good experimental data is very important to test the models.

Taking advantage of the polarized continuous-wave (CW) electron beam at Jefferson Laboratory (JLAB) and a high-density polarized ^{3}He target in Hall A, we have measured the neutron spin asymmetry A_1^n and spin structure function g_1^n to a good precision at three kinematics $x = 0.33$, 0.47 and 0.60, with $Q^2 = 2.7$, 3.5 and 4.8 (GeV/c)^2, respectively. The data at the two higher x_{Bj} points have improved the statistical accuracy of the world data by one order of magnitude. They show a zero crossing point around $x_{Bj} = 0.47$ and the datum at $x_{Bj} = 0.60$ is significantly positive. To determine A_1^n and g_1^n, cross sections and asymmetries of inclusive $^3\vec{\mathrm{H}}\mathrm{e}(\vec{e}, e')$ scattering have been measured in the deep-inelastic region. The transverse spin asymmetry A_2^n and structure function g_2^n were also extracted from data, though with less statistical precision. The asymmetries of pion photoproduction A^{π^-} were obtained as a byproduct. Combined with world fit of proton g_1^p/F_1^p data and the quark distribution ratio d/u, the polarized quark distributions $(\Delta u+\Delta\bar{u})/(u+\bar{u})$ and $(\Delta d+\Delta\bar{d})/(d+\bar{d})$ have been obtained from g_1^n/F_1^n data. Results of $(\Delta d+\Delta\bar{d})/(d+\bar{d})$ at all three x_{Bj} points are negative, in disagreement with the predictions from pQCD based hadron helicity conservation.

This dissertation will first give an introduction to the theories and formalism of polarized deep inelastic scattering and a review of the theories of A_1^n. Next the experiment E99-117 at JLAB Hall A will be described, followed by the data analysis which yields results for $A_1^{^3He}$, A_1^n, $g_1^{^3He}$, g_1^n, $A_2^{^3He}$, A_2^n, $g_2^{^3He}$, g_2^n, A_π, $(\Delta u + \Delta\bar{u})/(u + \bar{u})$ and $(\Delta d + \Delta\bar{d})/(d + \bar{d})$. The data presented greatly improve the current world fit of neutron polarized structure functions and provide valuable insight in the understanding

of the neutron spin structure.

Thesis Supervisor: William Bertozzi
Title: Professor of Physics

Acknowledgments

I have been looking forward to this moment for years. Because I thought this would be the time to show my sincere appreciation to a lot of people who helped me during my graduate school study and the research at Jefferson Lab.

My deepest appreciation goes to Bill Bertozzi, for his help in guiding my graduate study, especially in helping me preparing for the doctoral qualification oral exam. He can ask questions to the end and that's why I always tell other people: If you can answer all his questions, it means you really know the physics. I also appreciate very much for his help in correcting my draft thesis. I would like to thank June Matthews and William Donnelly for being on my thesis committee, reviewing my thesis and for all their encouragement. For my graduate school course work, I would like to mention the lecturers of two courses that I went to during the first year at MIT – Barton Zwiebach for his Electromagnetism and John Negele for his Relativistic Quantum Field Theory – their lectures not only helped me to understand the physics, but also set up a standard of what good lectures mean. If there is anything not ideal in my graduate school study, it would be that I only spent 10 months on campus and did not have enough time to experience all the good courses held there, and that I did not have much chance to chat with Bill and ask him what his understanding of being a good physicist is.

I appreciate the help from all other members of MIT Nuclear Interaction Group. I thank Shalev Gilad and David Rowntree for their help in my research in the spring of 2000. I am grateful for Doug Higinbotham and Simon Sirca for their help during my experiment. I thank Zheng-Wei Chai, Bin Zhang and Marat Rvachev for their friendship and for showing me around and helping me adjust to the new environment during the early time at Jefferson Lab. Thanks to Lingyan Zhu who came to MIT with me in the same year. Later we went to JLab together and those who have experienced such big changes would understand how important such a company is.

Then of course, I would like to thank the polarized ^{3}He collaboration at JLab. I thank Jian-Ping Chen, Zein-Eddine Meziani and Paul Souder for giving me the chance to work with them. I thank Jian-Ping for his friendship, for being my research advisor at JLab and for his thorough understanding of the subject of my thesis experiment; also for his toughness at work without which I would have been contented with some sloppy results and stop improving my analysis.

I thank Wolfgang Korsch for his support and understanding during the busiest time of experimental running and I hope I will pay it off to other people. There are several other people whose images will not vanish – Among all my colleagues I would like to mention Kevin Kramer, who ran his thesis experiment right after mine. I remember the time when he worked 40 hours continuously to change the target cell and the moment that he ran into counting house at 11 pm and said "Good Morning". That was true since I believe we both did not see sunshine during that four months, a long summer. I remember that Piotr Zolnierczuk always came to the counting house

at 8 am and say "Zao Shang Hao" with his Polish accent. I remember my strange friendship with Xiaofeng Zhu. I said it was strange because I always laughed at his work in a not so nice way (I think) but he was always tolerant and never complained. Now I truly hope that he will get his visa and come back here soon.

I also thank Todd Averett, Gordon Cates, Seonho Choi, Alexandre Deur, Nilanga Liyanage, Karl Slifer, Jaideep Singh, Patricia Solvignon and Vincent Sulkosky for their help during the experiment and the data analysis afterwards. I thank Sebastian Binet, Etienne Burtin and David Lhuillier and their colleagues for their help on the Compton polarimeter.

During my thesis writing, I would like to thank Antonin Vacheret for his explanation of parity DAQ and Doug Higinbotham for his broad knowledge on Hall A instrumentation. I appreciate the help and encouragement from Alexandre Deur in the last two months. He read and corrected my draft thesis at least two times and I should say my thesis defense went smoothly mostly because of his support.

Doing experiments without theoretical support is like walking in a forest without a map. I thank Mark Strikman for his intuitive suggestion of extracting $\Delta q/q$ from g_1/F_1 data. I thank Wally Melnitchouk, theorist at JLab for his help in data analysis, for his explanation of many other things and for giving comments on the theory chapters of the very first draft of my thesis. I also appreciate the help from other theorists who did calculations for A_1^n – Nathan Isgur, Elliot Leader, Dimitar Stamenov, Claude Bourrely, Jacques Soffer, Leonard Gamburg, Herbert Weigel, Anthony Thomas and their colleagues.

And in the end, I would like to thank several people for being my friends and for supporting me during the time at MIT and at JLab – Ghislain Granger, Yukun Gao, Alexandre Deur, Lei Guo, Peter Monaghan, Mina Nozar, Bodo Reitz, Min Qu and Lingyan Zhu.

Certainly this is not a complete list for all the people who have helped me in the past. It is like the pavement of a road, I can only see the most recently made ones and the people who made them. Life is a balance of loss and earning, help and being helped; I truly hope that I will contribute equally to other people's long journey towards their goals and success and keep the balance of life, since I believe this is the basis of true happiness and inner peace for everyone.

Contents

1 Introduction **19**

1.1 Spin Structure of the Nucleon 19
1.2 Probing Structure of the Nucleon - Experimental Methods 20
1.3 Electron Scattering 21
1.4 Deep Inelastic Scattering 24
1.5 Unpolarized Structure Functions 25
1.6 Polarized Structure Functions 27
1.7 Bjorken Scaling 28
1.8 Structure Functions in the Quark-Parton Model 29
1.9 Scaling Violation 30
1.10 From Bjorken limit to finite Q^2 - Operator Product Expansion 31
1.11 The Virtual Photon-Nucleon Asymmetries 32
1.12 Electron Asymmetries 34
1.13 Extracting Polarized Structure Functions from Asymmetries 35

2 Neutron Asymmetry A_1^n at Large x_{Bj} **37**

2.1 The $x \to 1$ Limit 37
2.2 Basic SU(6) Model 38
2.3 SU(6) Breaking and Hyperfine Perturbed Constituent Quark Model . 41
2.4 Perturbative QCD 43
2.5 Angular Momentum and Quark Helicity Conservation 44
2.6 Statistical Approach for Polarized Structure Functions 45
2.7 Local Duality 47
2.8 Chiral Soliton Model 48
2.9 Instanton and Polarized Structure functions 50
2.10 Lattice QCD and Polarized Structure Functions 50
2.11 Existing Measurements of A_1^n at large x 51

3 Experimental Setup **53**

3.1 Overview 53
3.2 The Accelerator and the Polarized Electron Source 56
3.3 Hall-A Overview 58

3.4 Beamline . . . 59
3.5 Beam Energy Measurement . . . 59
3.5.1 Arc Measurement . . . 59
3.5.2 eP Measurement . . . 61
3.5.3 Beam Energy During the A_1^n Experiment . . . 62
3.6 Beam Polarization Measurement . . . 63
3.6.1 Møller Polarimetry . . . 63
3.6.2 Compton Polarimetry . . . 64
3.6.3 Beam Polarization Measurements during A_1^n Experiment . . . 66
3.6.4 Beam Helicity . . . 67
3.7 Beam Charge Measurement . . . 69
3.8 Beam Charge Asymmetry Feedback . . . 70
3.8.1 Beam Charge Asymmetry . . . 71
3.8.2 PITA Effect . . . 71
3.8.3 Parity DAQ and Charge Asymmetry Feedback . . . 72
3.8.4 Beam Half-wave Plate and Beam Helicity . . . 75
3.9 Raster and Beam Position Monitor . . . 75
3.10 Hall A Spectrometers . . . 77
3.10.1 High Resolution Spectrometers . . . 77
3.10.2 Detector Package . . . 77
3.10.3 Scintillators and Trigger Electronics . . . 80
3.10.4 VDCs . . . 82
3.10.5 Gas Čerenkov Detector . . . 84
3.10.6 Lead Glass Counters . . . 85
3.11 Data Acquisition System . . . 87
3.11.1 Data Acquisition System . . . 87
3.11.2 Electronic Deadtime Measurement . . . 88

4 The Polarized ^{3}He Target 89
4.1 Principles . . . 89
4.1.1 Optical Pumping . . . 89
4.1.2 Spin Exchange . . . 92
4.1.3 Polarization Evolution . . . 92
4.2 Target Cell . . . 96
4.2.1 ^{3}He Cell at JLAB . . . 96
4.2.2 Target Cell Characteristics . . . 96
4.3 Target Setup . . . 97
4.4 Laser System . . . 100
4.5 NMR Polarimetry . . . 102
4.5.1 Principle . . . 102
4.5.2 Calibration . . . 105
4.5.3 Water Calibration . . . 106

4.5.4 NMR with Field Gradient . . . 108
4.6 EPR Polarimetry . . . 108
4.6.1 Principle . . . 108
4.6.2 Setup . . . 109
4.6.3 EPR Frequency Modulation Sweep . . . 110
4.6.4 EPR AFP Sweep . . . 111
4.6.5 EPR Analysis . . . 113
4.6.6 Polarization Gradient . . . 118
4.7 Target Polarization . . . 122
4.7.1 Target Polarization During the A_1^n Experiment . . . 122
4.7.2 Masing Effect . . . 122

5 Data Analysis 127
5.1 Analysis Procedure . . . 127
5.2 Detector Analysis . . . 129
5.2.1 VDC Efficiency . . . 129
5.2.2 Particle Identification Efficiency . . . 131
5.2.3 HRS Acceptance . . . 135
5.3 Monte-Carlo Simulation - SAMC . . . 137
5.4 Elastic Analysis . . . 139
5.4.1 Physics Formulae for $\vec{e} - {}^3\vec{\mathrm{He}}$ Elastic Scattering . . . 140
5.4.2 Elastic Simulation . . . 143
5.4.3 Kinematics, Parameters and Simulation Quality . . . 144
5.4.4 N_2 Dilution for Elastic Data . . . 147
5.4.5 ^{3}He Pressure Curve . . . 150
5.4.6 Systematic Error Estimate for Elastic Analysis . . . 151
5.4.7 Elastic Cross Section Results . . . 153
5.4.8 Elastic Asymmetry Results . . . 154
5.5 $\Delta(1232)$ Transverse Asymmetry . . . 155
5.6 DIS Analysis . . . 157
5.6.1 Charge Asymmetry and Beam Trips . . . 157
5.6.2 Sign Convention for Asymmetries . . . 157
5.6.3 False Asymmetries . . . 159
5.6.4 Positron Background . . . 160
5.6.5 N_2 Dilution for DIS Data . . . 160
5.6.6 Radiative Corrections . . . 161
5.6.7 Systematic Error Estimate for DIS Analysis . . . 163
5.6.8 DIS Cross Section Analysis . . . 165
5.7 From ^{3}He to Neutron . . . 167
5.7.1 ^{3}He Model - Convolution Approach . . . 168
5.7.2 ^{3}He Model - Complete Analysis . . . 169
5.7.3 Extracting g_1^n and A_1^n from E99-117 ^{3}He Data . . . 170

5.7.4 Inputs for Nuclear Corrections . . . 171
5.7.5 Comparison of Two Models . . . 173
5.8 Systematic Uncertainty of Neutron Asymmetries and Structure Function Ratios . . . 174

6 Results and Conclusions **177**
6.1 ^{3}He Results . . . 178
6.1.1 ^{3}He Electron Asymmetries $A_{\|}^{^3\mathrm{He}}$ and $A_{\perp}^{^3\mathrm{He}}$ . . . 178
6.1.2 ^{3}He Structure Function Ratios $g_1^{^3\mathrm{He}}/F_1^{^3\mathrm{He}}$ and $g_2^{^3\mathrm{He}}/F_1^{^3\mathrm{He}}$ . . . 178
6.1.3 ^{3}He Asymmetries $A_1^{^3\mathrm{He}}$ and $A_2^{^3\mathrm{He}}$ . . . 179
6.1.4 ^{3}He Polarized Structure Functions $g_1^{^3\mathrm{He}}$ and $g_2^{^3\mathrm{He}}$ . . . 180
6.2 Neutron Results . . . 181
6.2.1 Neutron Asymmetries A_1^n and A_2^n . . . 181
6.2.2 Neutron Structure Function Ratios g_1^n/F_1^n and g_2^n/F_1^n . . . 183
6.2.3 Neutron Polarized Structure Functions g_1^n and g_2^n . . . 185
6.3 Flavor Decomposition of Polarized Quark Distribution Functions . . . 187
6.4 Pion Asymmetries . . . 192
6.5 Discussion . . . 193
6.5.1 A_1^n and Models . . . 193
6.5.2 A_1^n and Parton Distribution Parameterizations . . . 196
6.5.3 Future of A_1^n Measurements . . . 198
6.6 Conclusions . . . 198

A ^{3}He Unpolarized Structure Functions from World Fits **201**

B Radiation Length of Materials for Hall A Polarized ^{3}He Target **203**

C Cell Wall Thickness Data **207**

D Structure Functions for Radiative Corrections **211**
D.1 Internal Radiative Correction . . . 211
D.2 External Radiative Correction . . . 213

E Polarized Structure Functions from the E155 Fit **215**

F Fit for Proton and Neutron g_1/F_1 **217**

List of Figures

1-1 Electron scattering through one-photon exchange. 21
1-2 Cross section (in arbitrary units) for inclusive electron scattering off a light nuclear target. M_T is the target mass, M is the nucleon mass, and W is the invariant mass. The excitation peak positions (N, Δ, ...) change when Q^2 and ν vary but stay at constant W. For a nucleon target, there is no quasi-elastic peak. 22
1-3 Kinematics of polarized electron scattering. 28
1-4 Higher orders processes of electron scattering which cannot be separated from one-photon exchange. 30
1-5 Q^2 dependence of $F_2^p(x, Q^2)$ data [13] and fit from global analysis [14]. 31
1-6 Definition of virtual photon asymmetry A_1. 33

2-1 A global fit [21] of parton distribution functions (pdf's) for the proton at $Q^2 = 5$ (GeV/c)^2; $u(d)$: valence $u_V(d_V)$ quark, $\bar{u}(\bar{d})$: sea $u(d)$ quark; $s(=\bar{s})$: strange sea quarks; g: gluons; Valence quark distributions are measured up to $x = 0.8$. 38
2-2 SU(6) wavefunction for the neutron. 38
2-3 A_1^p and A_1^n as predicted from SU(6) symmetry, shown as a black line at 5/9 for the proton and 0 for the neutron. 39
2-4 SLAC data [31] on the F_2^n/F_2^p ratio. The horizontal line at 2/3 shows the SU(6) prediction. 41
2-5 A_1^p and A_1^n as predicted from the CQM [36] and the comparison to world data. 42
2-6 A_1^n as predicted from pQCD HHC based BBS (curve (1)) and LSS(BBS) parameterization (curve (2)). 44
2-7 g_1^p/F_1^p and g_1^n/F_1^n from LSS parameterization. Curves (bottom, middle and top) correspond to calculations of g_1^p/F_1^p and g_1^n/F_1^n at Q^2=3, 5, and 100 (GeV/c)^2, respectively. 45
2-8 Predictions of A_1^p and A_1^n from statistical model. Curves (bottom, middle and top for A_1^p, and bottom, middle and top at $x > 0.6$ for A_1^n) correspond to calculation at Q^2=4, 10, and 10 (GeV/c)^2, respectively. 46
2-9 Predictions of A_1^p and A_1^n from the local duality method (green curves) compared with world data. 47

2-10 g_1^n/F_1^n as predicted from chiral soliton model at Q^2=0.4 (GeV/c)^2. . . 49
2-11 Existing data on A_1^n in comparison to various theoretical predictions including: A_1^n from CQM (yellow band (1)); g_1/F_1 at $Q^2 = 5$ (GeV/c)^2 from LSS parameterization (red curve (2)); A_1^n from pQCD based BBS parameterization (blue curve (3)); A_1^n from pQCD based LSS(BBS) parameterization (cyan curve (4)); A_1^n from statistical model at $Q^2 =$ 4 (GeV/c)^2 (blue curve (5)); A_1^n from local duality (green curve (6)); A_1^n from chiral soliton model at $Q^2 = 0.4$ (GeV/c)^2 (purple curve (7)); and A_1^n from E155 g_1/F_1 experimental fit at $Q^2 = 4$ (GeV/c)^2 (black curve (8)). 52

3-1 The ^{3}He wavefunction. 54
3-2 Kinematic coverage of the A_1^n experiment - Q^2, W^2 and x_{Bj}. 55
3-3 The Jefferson LAB accelerator. 56
3-4 Structure of strained GaAs cathode and the level diagram of the conduction and valence bands. 57
3-5 Hall-A floor plan during the A_1^n experiment. 58
3-6 Hall coordinate system (left): Z is the beam direction, Y is vertically pointing up; and the spectrometer coordinate system (right): Z is the HRS central ray direction, X is vertically pointing down and is called the dispersive direction, Y is called the transverse direction, ϕ (θ) is the in-plane (out-of-plane) scattering angle with respective to the HRS central ray direction. 59
3-7 The arc section of the beamline. 60
3-8 Layout of eP device 61
3-9 Layout of the Møller polarimeter 64
3-10 Layout of the Compton polarimetry. 65
3-11 Beam polarization during the A_1^n experiment. 67
3-12 Helicity signals in toggle (left) and pseudorandom (right) modes. The four signals are: H+ from MCC, H+ and H− generated by the HRS helicity circuitry, and the DAQ helicity state. 68
3-13 Schematic of beam current monitors. 69
3-14 The PITA effect. 73
3-15 Beam charge asymmetry feedback system. 73
3-16 Beam position distribution for a circular raster. 76
3-17 Schematic layout of HRS spectrometer and the detector hut. Dimensions are in meters. 78
3-18 Configuration of left and right HRS detectors, side view. 79
3-19 Configuration of scintillators. 80
3-20 Schematic diagram (left) and sideview (right) of wire chamber configuration. 83
3-21 Configuration of wire chambers. 83

3-22 Configuration of the pion rejectors on the left HRS. 86
3-23 Configuration of the total shower detector on the right HRS. 87

4-1 Energy level of ^{85}Rb, the Zeeman splitting is given by ν_Z. 90
4-2 Optical pumping of Rb by circularly polarized light. 91
4-3 Spin exchange between Rb atom and ^{3}He nuclei. 92
4-4 Spin up curve measured in the polarized ^{3}He target lab at JLAB [113]. 95
4-5 A regular JLAB target cell, dimensions are given in mm for a cell used during the A_1^n experiment. The name of the cell is "Tilghman". . . . 96
4-6 Target setup overview (schematic). 98
4-7 Helmholtz coil orientation and the field coordinate system (topview). 99
4-8 Target setup in Hall A, the laser hut and the target. 99
4-9 Target setup in Hall A, the laser hut and the right spectrometer (topview) 100
4-10 Laser optics setup (schematic). 101
4-11 Principle of ^{3}He spin reversal using Adiabatic Fast Passage (AFP). . 104
4-12 A typical NMR signal for ^{3}He. The resonance frequency is not exact 28.06 Gauss because of the field drifting. 105
4-13 NMR signal on a water sample. 107
4-14 EPR Optics setup in hall, during summer 2001. 109
4-15 EPR frequency modulation sweep setup. 110
4-16 A typical frequency modulation sweep spectrum. 111
4-17 EPR AFP sweep setup. 112
4-18 A typical spectrum of EPR AFP sweep measurement. 113
4-19 EPR frequency shift spectrum 115
4-20 Location of temperature sensors on a 25 cm cell. 116
4-21 Holding field magnitude during E99-117. 118
4-22 Target performance during the A_1^n experiments. Data of EPR measurements are obtained from equilibrium solutions. 123
4-23 Masing during an EPR measurement. 125

5-1 Procedure for asymmetry analysis. 127
5-2 Procedure for cross section analysis. 129
5-3 Right HRS VDC track number distribution. 130
5-4 Summed ADC signal of left HRS gas Čerenkov detector, without cut (black), after lead glass counters' electron cut (red) and pion cut (blue). The vertical line shows a cut $\sum \mathrm{ADC}_i > 400$ for selecting electrons. . 132
5-5 Two-dimensional distribution of energy deposits in the two layers of lead glass counter in the left HRS, after the gas Čerenkov electron cut (red) and the pion cut (blue). Black straight lines show the boundary of the 2D cut for selecting electrons. 133

5-6 Two-dimensional distribution of energy deposits in the two layers of lead glass counter in the right HRS, after the gas Čerenkov ADC electron cut (red) and the pion cut (blue). Black straight lines show the boundary of the 2D cut to select electrons. 133
5-7 PID efficiencies of the left and the right HRS detectors in the range of $0.8 < p_0 < 2.0$ (GeV/c). 134
5-8 Boundary of acceptance. Top left: $\phi_{\rm tg}$ vs. $y_{\rm tg}$; top right: $\theta_{\rm tg}$ vs. $\delta_{\rm tg}$; bottom left: $\phi_{\rm tg}$ vs. $\theta_{\rm tg}$; bottom right: $\delta_{\rm tg}$ vs. $\phi_{\rm tg}$. 136
5-9 Flow chart for the single arm Monte-Carlo simulation program SAMC 139
5-10 Polar and azimuthal angles of the target spin. 142
5-11 Reconstructed target variables $\theta_{\rm tg}$, $\phi_{\rm tg}$, $\delta_{\rm tg}$ and $y_{\rm tg}$, for the left and right HRS, with an acceptance cut $R > 0$ applied. 145
5-12 R-function distribution. An acceptance cut1 $R > 0$ is used for the asymmetry analysis and cut2 $R > 0.005$ is used for cross section analysis.146
5-13 Cell window contamination. Cut $|y_{\rm tg}| < 0.02$ m is used in the elastic analysis to exclude events scattered from cell windows. 146
5-14 $W_{^3{\rm He}}$ spectrum of ^{3}He elastic peak. 147
5-15 $(W_{\rm N_2} - M_{\rm N_2})$ spectrum of the N_2 elastic peak from the left and right HRS data, with cuts $(W_{^3{\rm He}} - M_{^3{\rm He}}) < 0$ & $-0.02 < (W_{\rm N_2} - M_{\rm N_2}) < 0.05$ GeV/c^2 applied. 148
5-16 N_2 pressure curves from the left and right HRS data. Each curve is zoomed in on the right side. 149
5-17 Elastic ^{3}He pressure curve. 150
5-18 Elastic cross section results. A systematic error of 6.7% has been added to each data point. 153
5-19 Elastic longitudinal asymmetry results. A 4.5% systematic uncertainty has been included in the total error. The combined asymmetry and its total error from ~ 20 elastic runs are shown by the horizontal solid and dashed lines, respectively. 154
5-20 Measured $\Delta(1232)$ transverse raw asymmetry $A^{\Delta}_{\perp,raw}/(P_b P_t)$ without sign correction. No correction for radiative effect and N_2 dilution has been applied. A cut $|W_{^3{\rm He}} - M_{\Delta}| < 0.02$ GeV/c^2 has been used to select events from $\Delta(1232)$ resonance. The beam half-wave plate was inserted and target spin direction was 270°. The expected value $A^{\Delta}_{\perp,raw}/(P_b P_t)$=1.45% is shown as a blue line. 156
5-21 Beam trip removal at 5.7 GeV running. 158
5-22 False asymmetry results for four different combinations of beam half-wave plate status and beam helicity signal mode. Data were taken on an unpolarized ^{12}C foil target; The kinematics was $E_b = 5.73$ GeV, $E' = 1.32$ GeV and $\theta = 35°$. 159

5-23 DIS cross sections. The simulation is performed using world fits of unpolarized structure functions [142][143] for the DIS evaluation, the peaking approximation for the evaluation of the elastic and quasi-elastic elastic tails. A 6% error bar has been plotted for each data point for the cross sections and the ratio of $\sigma^{data}/\sigma^{MC}$. 166

5-24 Difference in A_1^n between using the complete analysis and the convolution approach. 174

5-25 Sources of error in A_1^n. The total errors are dominated by the statistical uncertainty. The three main sources of the systematic error are those due to the uncertainties in the effective nucleon polarization P_n and P_p, the radiative corrections and the proton asymmetry A_1^p. 176

6-1 ^{3}He results – $A_1^{^3\mathrm{He}}$. 179

6-2 ^{3}He results - $g_1^{^3\mathrm{He}}$. 180

6-3 Neutron A_1^n results. Curve: E155 fit at $Q^2 = 4$ (GeV/c)^2. 182

6-4 A_2^n results; Curve: $A_2^{n,WW}$ using E155 fit at $Q^2 = 4$ (GeV/c)^2. 183

6-5 Neutron $(g_1/F_1)^n$ results. Curve: E155 fit at $Q^2 = 4$ (GeV/c)^2. 184

6-6 g_1^n results. Curve: g_1^n from E155 fit at $Q^2 = 4$ (GeV/c)^2. 186

6-7 Results for xg_2^n. Curve: $xg_2^{n,WW}$ from E155 fit at $Q^2 = 4$ (GeV/c)^2. . 186

6-8 d/u ratio extracted from proton and deuteron data from SLAC, using the off-shell deuteron calculation (solid circles) and using the on-shell calculation (open circles) [173]. Also shown is the ratio extracted from neutrino measurements by the CDHS collaboration [175]. The three curves show the d/u central values (black curve), the minimal (lower red curve), and the maximal values (higher red curve) used in the analysis presented in this section. 188

6-9 Results for $(\Delta u + \Delta\bar{u})/(u + \bar{u})$ and $(\Delta d + \Delta\bar{d})/(d + \bar{d})$, The error bars on the HERMES preliminary data are statistical uncertainties [172]. The error band in the middle shows the uncertainty due to neglecting s and $\bar{s}$ contributions. 190

6-10 Pion asymmetry A^{π^-} results. 192

6-11 A_1^n results compared with model predictions. Curves: predictions of A_1^n from pQCD based BBS parameterization [38], constituent quark model (yellow, or light shaded band) [36] and the SU(6) symmetry [22]. 194

6-12 A_1^n results compared with A_1^n predictions from the pQCD based LSS(BBS) parameterization and from the statistical model at Q$^2 = 4$ (GeV/c)^2. 196

6-13 g_1^n/F_1^n results compared with g_1^n/F_1^n predictions from the LSS parameterization at Q$^2 = 5$ (GeV/c)^2. 197

B-1 Radiation length of materials for Hall A Polarized ^{3}He Target 204

C-1 "Gore" wall thickness data from UVa (cyan labels) and JLAB (purple labels); The arrows show the upstream and downstream extremes of the acceptance for $x = 0.61$ (blue) and elastic (green) kinematics. . . 209
C-2 "Tilghman" wall thickness data from UVa (cyan labels) and JLAB (purple labels); The arrows show the upstream and downstream extremes of the acceptance for $x = 0.33$ and 0.48 kinematics. 209
C-3 25 cm reference cell wall thickness data from UVa (cyan labels) and JLAB (purple labels); The arrows show the upstream and downstream extremes of the acceptance for $x = 0.33$ and 0.48 (cyan), $x = 0.61$ (blue), and elastic (green) kinematics. 210

D-1 Kinematic range needed by POLRAD 2.0 for internal radiative corrections. 212
D-2 Kinematic range for external radiative corrections 214

F-1 Results of the fit $g_1^p/F_1^p = x^\alpha(a+bx)(1+\beta/Q^2)$. The three curves show the new fit from this analysis (red), the error in the new fit (green), and the E155 fit [20] (black). 220
F-2 Results of the fit $g_1^n/F_1^n = (a+bx+cx^2)(1+\beta/Q^2)$. The three curves show the new fit from this analysis (red), the error in the new fit (green), and the E155 fit [20] (black). 221

List of Tables

2.1 Measurements of A_1^n before 2001. 51

3.1 Development of $^3\vec{\mathrm{He}}$ target technology. 54
3.2 Kinematics of the A_1^n experiment. 55
3.3 Beam energy measurement for the A_1^n experiment, all energies are given in MeV. 62
3.4 Møller beam polarization measurements during the A_1^n experiment. . 66
3.5 Mott beam polarization measurements during the A_1^n experiment. . . 66
3.6 Calibration for BCM's, January 12th, 2001. 70
3.7 Hall A HRS general characteristics. 79

4.1 Main characteristics of the two cells used during the A_1^n experiment. . 97
4.2 The average polarization for each cell from equilibrium solution of EPR measurements. Polarizations and errors are given as absolute values in %. 122
4.3 The average polarization for each cell, dynamic solution. Polarizations and errors are given as absolute values in %. 122

5.1 Fraction of zero-, one- and multiple-track events from elastic scattering data, $E_b = 1.196$ GeV, $E' = 1.191$ GeV, $\theta = 19.985°$. 130
5.2 N_2 dilution factor for DIS analysis. 160
5.3 Internal radiative corrections to $A_{\|}^{^3\mathrm{He}}$ and $A_{\perp}^{^3\mathrm{He}}$, given as absolute values (not percentage). 162
5.4 External radiative corrections to $A_{\|}^{^3\mathrm{He}}$ and $A_{\perp}^{^3\mathrm{He}}$, given as absolute values (not percentage). Errors are from the uncertainties in the structure functions and the cell wall thickness. 162
5.5 More calculations of the effective nucleon polarizations P_n and P_p. . . 173
5.6 Total errors for A_1^n, all numbers are absolute values given in %. . . . 175

6.1 ^{3}He results – $A_{\|}^{^3\mathrm{He}}$ and $A_{\perp}^{^3\mathrm{He}}$. 178
6.2 ^{3}He results – $g_1^{^3\mathrm{He}}/F_1^{^3\mathrm{He}}$ and $g_2^{^3\mathrm{He}}/F_1^{^3\mathrm{He}}$. 178
6.3 ^{3}He results – $A_1^{^3\mathrm{He}}$ and $A_2^{^3\mathrm{He}}$. 179
6.4 ^{3}He results – $g_1^{^3\mathrm{He}}$ and $g_2^{^3\mathrm{He}}$. 180

6.5 Neutron results – A_1^n and A_2^n. 181
6.6 Neutron results – g_1^n/F_1^n and g_2^n/F_1^n. 184
6.7 Neutron results – g_1^n and g_2^n. 185
6.8 Polarized quark distribution results for $(\Delta u + \Delta\bar{u})/(u + \bar{u})$ and $(\Delta d + \Delta\bar{d})/(d + \bar{d})$. The three error bars are the statistical error (stat.), systematic error (sys.) and the model uncertainty (mod.) due to the uncertainties in the fits for g_1^p/F_1^p data and the d/u ratio. 189

B.1 Radiation length X_0 and density for material traversed by the electrons during the A_1^n experiment. 205

C.1 Cell window thickness data. For each cell, the two windows are labeled either by numbers or by letters. 207
C.2 Data taking kinematics and the three cells used for the A_1^n experiment. 208
C.3 "Gore" wall thickness data from UVa and JLAB. 208
C.4 "Tilghman" wall thickness data from UVa and JLAB. 208
C.5 25 cm reference cell wall thickness data from UVa and JLAB. 209

F.1 Reduced chi-square of five fitting function for g_1^p/F_1^p and g_1^n/F_1^n . . . 219
F.2 Result of the fit $g_1^p/F_1^p = x^\alpha(a + bx)(1 + \beta/Q^2)$. 219
F.3 Result of the fit $g_1^n/F_1^n = (a + bx + cx^2)(1 + \beta/Q^2)$. 219

Chapter 1

Introduction

Protons and neutrons are the constituents of all observable matter in the universe. The positively charged proton is the nucleus of the hydrogen atom. Protons and neutrons, the protons' uncharged analogs, are bound together to form all other atomic nuclei and hence are called "nucleons". A deeper layer to nuclear matter has also been uncovered: Nucleons are composed of light weight, point-like quarks and gluons. These constituents possess another type of charge, known as "color", which is the source of the strong interaction that clusters the quarks and gluons to make protons and neutrons, and in turn grips these nucleons to one another, forming atomic nuclei. The fundamental theory underpinning all of these phenomena is known as quantum chromodynamics (QCD). A central goal of nuclear physics is to understand the structure and properties of protons and neutrons, and ultimately atomic nuclei, in terms of the quarks and gluons of QCD. Important questions being studied include:

- How exactly are the nucleons made from the different types of quarks?
- How do various constituents of the nucleon contribute to its overall spin?

1.1 Spin Structure of the Nucleon

Interest in the spin structure of nucleons became prominent in the 1980's when the first spin structure function experiments at SLAC [1] and CERN [2] on the integral of proton polarized structure function g_1^p showed that the total spin carried by quarks was very small, $\sim 12 \pm 17\%$ [2], in contrast to the simple relativistic quark model prediction [3] in which the spin of the valence quarks carry 75% of the proton spin and the remaining 25% comes from the orbital angular momentum. Because the quark model is very successful in describing static properties of the hadrons, the fact that quark spin carries only a small part of the nucleon spin was a big surprise and generated very productive experimental and theoretical activities on this topic in the following twenty years. Present understanding [4][5] of the nucleon spin is that the

total spin is distributed among valence quarks, $q-\bar{q}$ sea quarks, their orbital angular momenta, and gluons. Only about 30% of the nucleon spin is carried by the quarks. The nucleon spin can be written as

$$S_z^N = S_z^q + L_z^q + J_z^g = \frac{1}{2} , \tag{1.1}$$

where S_z^q and L_z^q represent the intrinsic and the orbital angular momentum of quarks, respectively. J_z^g is the total angular momentum of gluons. Each of these three terms can be calculated as the integral of a spin-dependent distribution function, with a parameter of, for example, the fraction of nucleon's momentum carried by the quark or gluon. These distribution functions can provide more detailed information than their integrals about how each constituent contributes to the nucleon spin and the dynamic mechanism behind it. However, although extensive experimental and theoretical efforts have been made to measure and to understand the spin structure, many questions remain and little has been understood about Eq. (1.1) and the spin-dependent distribution functions. Namely, exactly how is the nucleon spin distributed among all its constituents? Is it possible to separate the orbital angular momentum of the gluons from their spin [5]? What is the spin structure in the valence quark region; can the constituent quark model (CQM) explain it? How does the QCD vacuum contribute to the nucleon spin?

1.2 Probing Structure of the Nucleon - Experimental Methods

The fundamental quark and gluon structure of strongly interacting matter is studied primarily through experiments that emphasize hard scattering from the quarks and gluons at sufficiently high energies. Two important ways of probing the distribution of quarks and antiquarks inside nucleons are lepton scattering and the Drell-Yan process.

In the case of lepton scattering, a lepton (an electron or a muon) scatters from a single quark (antiquark) inside the target nucleon (proton or neutron) and transfers a large fraction of its energy and momentum via an exchanged photon. Such deep inelastic scattering measurements carried out with high energy beams have been the primary source of experimental information on the quark and gluon structure of matter. The lepton exquisitely probes the quark substructure of the nucleon with a known spatial resolution. Moreover, if a scattering occurs between a polarized lepton beam and a polarized target, the spin structure of the nucleon becomes accessible.

In the case of the Drell-Yan process, the antiquarks present in the target nucleon are probed directly when a quark inside an incident hadron (a proton) has enough energy to annihilate with one of the antiquarks. The energy released by the annihilation produces a "virtual" photon, which then materializes as an electron-positron or

muon-antimuon pair at very high relative energy. Such processes involve the strong interaction and thus have much higher yield than pure electromagnetic (EM) reactions. Consequently other reaction channels of proton-proton scattering at high energy have the potential to provide new vistas on the quark and gluon structure of the proton, with very good sensitivities. The Drell-Yan process has been widely used to study the sea quark distribution inside the nucleon. However, it is not of interest here and will not be discussed in the rest of this dissertation.

In the following we will first give a general picture of electron scattering focusing on its excitation spectrum. Then the theories and the formalism of deep inelastic scattering will be reviewed.

1.3 Electron Scattering

The simplest picture of electron scattering is the one photon exchange, as shown in Figure 1-1 [6]. In this picture a virtual photon with four momentum $q = (\nu, \vec{q})$ strikes the target nucleus (or nucleon). For the case of inclusive measurement, only the scattered electron is detected. We denote by m the electron mass, $k = (E, \vec{k})$ and

Figure 1-1: Electron scattering through one-photon exchange.

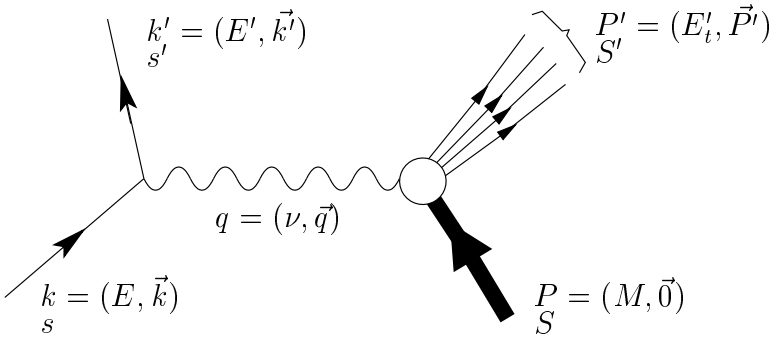

$k' = (E', \vec{k'})$ the initial and final electron four-momenta; s and s' are the initial and final lepton covariant spin four-vectors such that $s \cdot k = 0$ ($s' \cdot k' = 0$) and $s \cdot s = -1$ ($s' \cdot s' = -1$); the target has a mass M_T and its initial, final four-momenta and spin four-vectors are, respectively, $P = (E_t, \vec{P})$, $P' = (E'_t, \vec{P'})$ and S, S'. In the case of a scattering with fixed target, one has $P = (M_T, \vec{0})$ in the laboratory frame. The relativistic invariants characterizing the scattering are:

- The virtuality of the exchanged photon $Q^2 \equiv -q^2$, where $q = k - k' = (\nu, \vec{q})$ is the four momentum of the exchanged photon, ν is its energy and is also called the 'energy loss' of the electron. The virtual photon can be viewed as a probe to the structure of the target nucleus (or nucleon) and Q^2 describes the spatial resolution of the probe;

- The invariant mass defined by

$$W \equiv \sqrt{\mathrm{M}^2 + 2\mathrm{M}\nu - Q^2}\ , \tag{1.2}$$

  where M is usually the mass of the nucleus (or nucleon) target in the case of elastic scattering, and is the nucleon mass in other cases, as will be described later.

The cross section for electron scattering is a function of Q^2 and ν. Figure 1-2 shows a cross section spectrum for a typical inclusive scattering off a light nuclear target. As Q^2 and ν change, the target undergoes different excitation states. The spectrum comprises elastic scattering, quasi-elastic scattering, the resonance region and the deep inelastic region.

Figure 1-2: Cross section (in arbitrary units) for inclusive electron scattering off a light nuclear target. M_T is the target mass, M is the nucleon mass, and W is the invariant mass. The excitation peak positions (N, Δ, ...) change when Q^2 and ν vary but stay at constant W. For a nucleon target, there is no quasi-elastic peak.

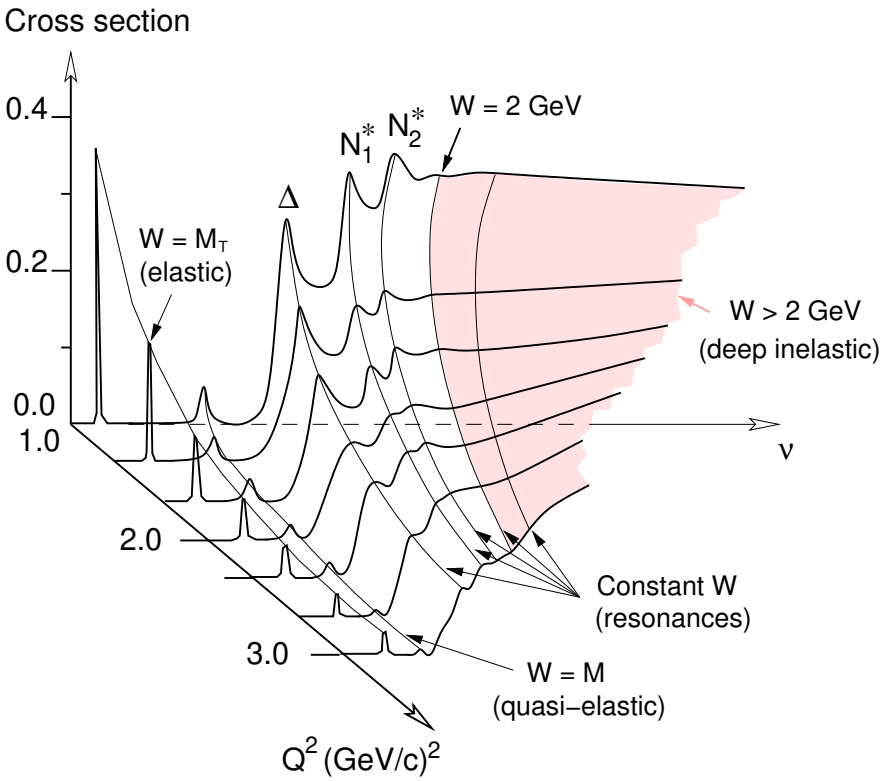

- Elastic scattering
  At low Q^2 and ν the spatial resolution of the process is not high enough to see

the target's composition. The target nucleus stays intact and reacts coherently during the scattering. The momentum transfer is shared among all the nucleons. The invariant mass of elastic scattering satisfies $W^2 \equiv M_T^2 + 2M_T\nu - Q^2 = M_T^2$, with M_T the mass of the nuclear (or nucleon) target. The theory and formalism of $\vec{e} - {}^3\vec{\mathrm{He}}$ elastic scattering will be presented in Section 5.4.1;

- Quasi-elastic scattering
  When ν is larger than the nuclear binding energy, the target nucleus no longer stays intact. The nucleus can be viewed as a set of quasi-free nucleons bound in a mean potential (the Fermi gas model [7]). The electron scatters elastically from a nucleon which is ejected from the nucleus. This is called quasi-elastic scattering. Its threshold, with respect to the elastic peak, is equal to the nuclear binding energy (5.49 MeV for ^{3}He two body breakup and 7.72 MeV for three body breakup). Now the scattering centers are the nucleons inside the nuclear target. Unlike the elastic case, they are not at rest in the laboratory frame. The nucleons have a typical momenta of $55 \sim 250$ MeV/c due to their "Fermi motion" [7]. The motion of the nucleons causes a broadening of the quasi-elastic peak around $\nu = Q^2/(2M)$ with M the nucleon mass, which is the energy loss of elastic scattering off a free nucleon. The invariant mass satisfies $W^2 \equiv M^2 + 2M\nu - Q^2 = M^2$ in the case of quasi-elastic scattering;

- Resonances
  As Q^2 and ν increase, electron scattering enters the resonance region, which usually refers to the region $1.2 < W < 2.0$ GeV/c^2. In this region the substructure of the nucleon is explored. The nucleons are formed by quarks, which absorb the virtual photons and form excitation states called "nucleon resonances". The invariant mass satisfies $W^2 \equiv M^2 + 2M\nu - Q^2 = M_{N^*}^2$, with M_{N^*} the mass of the resonance N^*.
  The first resonance is the $\Delta(1232)$ with $M_\Delta = 1.232$ GeV/c^2. Usually only the $\Delta(1232)$ is unambiguously visible in inclusive experiments. Beyond $W > 1.4$ GeV/c^2 the higher resonances and their tails overlap;

- Deep inelastic scattering
  The last domain of Figure 1-2 is the deep inelastic scattering (DIS) region. It is traditionally defined as $W > 2$ GeV/c^2 and $Q^2 > 1.0$ (GeV/c)^2. In the DIS region the Q^2 and ν of the virtual photon are large enough so the constituents of the nucleon – the partons – are resolved. We define a relativistically invariant variable, the Bjorken scaling variable x_{Bj} as

$$\begin{aligned} x &= x_{Bj} \equiv \frac{Q^2}{2P \cdot q} \\ &= \frac{Q^2}{2M\nu} \quad \text{for fixed target .} \end{aligned} \tag{1.3}$$

When Q^2 is large enough DIS can be interpreted as scattering off an asymptotically free quark or antiquark inside the nucleon. In this case, it turns out that the parton model can be formulated the simplest in the frame where the nucleon is moving with momentum approaching ∞ along the direction of $\vec{q}$. This frame is an example of the many possible choices of an "infinite momentum frame". The Bjorken variable x_{Bj} is just the fraction of the nucleon's momentum carried by the struck quark in the infinite momentum frame. The DIS region is where the nucleon's partonic structure is explored.

Our experiment was carried out in the DIS domain so in the rest of this dissertation, we will focus on deep inelastic scattering.

1.4 Deep Inelastic Scattering

In the following sections the formalism of deep inelastic scattering will be reviewed according to the convention given in [8].

In the deep inelastic regime, the virtual photon strikes a quark or an antiquark inside the nucleon, which at large four momentum transfer can be considered free. The differential cross-section for detecting the final polarized lepton in the solid angle $\mathrm{d}\Omega$ and in the final energy range (E', $E'+\mathrm{d}E'$) in the laboratory frame can be written as

$$\frac{\mathrm{d}^2\sigma}{\mathrm{d}\Omega \mathrm{d}E'} = \frac{\alpha^2}{2Mq^4}\frac{E'}{E}L_{\mu\nu}W^{\mu\nu} , \tag{1.4}$$

where α is the fine structure constant. $L_{\mu\nu}$ and $W_{\mu\nu}$ are the leptonic and hadronic tensors, respectively.

The leptonic tensor $L_{\mu\nu}$ is given by

$$L_{\mu\nu}(k,s;k',s') = \Big[\bar{u}(k',s')\gamma_\mu u(k,s)\Big]^* \Big[\bar{u}(k',s')\gamma_\nu u(k,s)\Big] , \tag{1.5}$$

and can be split into symmetric (S) and antisymmetric (A) parts under μ, ν interchange:

$$\begin{aligned} L_{\mu\nu}(k,s;k',s') &= L^{(S)}_{\mu\nu}(k;k') + iL^{(A)}_{\mu\nu}(k,s;k') \\ &\quad + L'^{(S)}_{\mu\nu}(k,s;k',s') + iL'^{(A)}_{\mu\nu}(k;k',s') . \end{aligned} \tag{1.6}$$

The unknown hadronic tensor $W_{\mu\nu}$ is similarly defined as

$$W_{\mu\nu}(q;P,S) = W^{(S)}_{\mu\nu}(q;P) + iW^{(A)}_{\mu\nu}(q;P,S) \tag{1.7}$$

with

$$\begin{aligned}\frac{1}{2M}W^{(S)}_{\mu\nu}(q;P) &= \Big(-g_{\mu\nu}+\frac{q_\mu q_\nu}{q^2}\Big)W_1(P\cdot q,q^2)\\ &\quad+\Big[\Big(P_\mu-\frac{P\cdot q}{q^2}q_\mu\Big)\Big(P_\nu-\frac{P\cdot q}{q^2}q_\nu\Big)\Big]\frac{W_2(P\cdot q,q^2)}{M^2} \qquad (1.8)\\ \frac{1}{2M}W^{(A)}_{\mu\nu}(q;P,S) &= \epsilon_{\mu\nu\alpha\beta}q^\alpha\Big\{MS^\beta G_1(P\cdot q,q^2)\\ &\quad+\Big[(P\cdot q)S^\beta-(S\cdot q)P^\beta\Big]\frac{G_2(P\cdot q,q^2)}{M}\Big\}\,, \qquad (1.9)\end{aligned}$$

where W_1, W_2 and G_1, G_2 are the unpolarized and the polarized structure functions, respectively. Then one obtains

$$\begin{aligned}\frac{\mathrm{d}^2\sigma}{\mathrm{d}\Omega\mathrm{d}E'} &= \frac{\alpha^2}{2Mq^4}\frac{E'}{E}\Big[L^{(S)}_{\mu\nu}W^{\mu\nu(S)}+L'^{(S)}_{\mu\nu}W^{\mu\nu(S)}\\ &\quad-L^{(A)}_{\mu\nu}W^{\mu\nu(A)}-L'^{(A)}_{\mu\nu}W^{\mu\nu(A)}\Big]\,. \qquad (1.10)\end{aligned}$$

The cross section with particular initial and final polarizations can in principle always be expressed as a combination of W_1, W_2 and G_1, G_2. The usual unpolarized cross-section is proportional to $L^{(S)}_{\mu\nu}W^{\mu\nu(S)}$:

$$\frac{\mathrm{d}^2\sigma^{\mathrm{u}}}{\mathrm{d}\Omega\mathrm{d}E'}(k,P;k') = \frac{\alpha^2}{2Mq^4}\frac{E'}{E}2L^{(S)}_{\mu\nu}W^{\mu\nu(S)}\,. \qquad (1.11)$$

In the polarized case, the differences of cross sections with opposite target spins are

$$\begin{aligned}\sum_{s'}\Big[\frac{\mathrm{d}^2\sigma}{\mathrm{d}\Omega\mathrm{d}E'}(k,s,P,-S;k',s') &- \frac{\mathrm{d}^2\sigma}{\mathrm{d}\Omega\mathrm{d}E'}(k,s,P,S;k',s')\Big]\\ &= \frac{\alpha^2}{2Mq^4}\frac{E'}{E}4L^{(A)}_{\mu\nu}W^{\mu\nu(A)}\,. \qquad (1.12)\end{aligned}$$

1.5 Unpolarized Structure Functions

From Eq. (1.11) the cross section for scattering unpolarized electrons from an unpolarized target is

$$\frac{\mathrm{d}^2\sigma}{\mathrm{d}\Omega\mathrm{d}E'} = \Big(\frac{\mathrm{d}^2\sigma}{\mathrm{d}\Omega}\Big)_{Mott}\Big[W_2(P\cdot q,Q^2)+2W_1(P\cdot q,Q^2)\tan^2\frac{\theta}{2}\Big]\,, \qquad (1.13)$$

with θ the scattering angle of the electron in the laboratory frame. The four momentum transfer Q^2 can be calculated as

$$Q^2 = 2EE'(1-\cos\theta) \ . \tag{1.14}$$

The Mott cross section is given by

$$\left(\frac{\mathrm{d}^2\sigma}{\mathrm{d}\Omega}\right)_{Mott} = \frac{\alpha^2\cos^2\frac{\theta}{2}}{4E^2\sin^4\frac{\theta}{2}} \ , \tag{1.15}$$

which is the cross section for scattering relativistic electrons from a point-like infinitely heavy target. Consequently, the unpolarized structure functions $W_1(P\cdot q, Q^2)$ and $W_2(P\cdot q, Q^2)$ describe the structure of the target. For a fixed target, $P\cdot q = M\nu$, they can be written as $W_1(\nu, Q^2)$ and $W_2(\nu, Q^2)$.

The structure functions W_1 and W_2 are commonly expressed in terms of functions F_1 and F_2, which are functions of Q^2 and the Bjorken variable x:

$$MW_1(\nu, Q^2) = F_1(x, Q^2) \ ; \tag{1.16}$$

$$\nu W_2(\nu, Q^2) = F_2(x, Q^2) \ . \tag{1.17}$$

They satisfy

$$F_1(x, Q^2) = \frac{F_2(x, Q^2)(1+\gamma^2)}{2x\Big(1+R(x, Q^2)\Big)} \ , \tag{1.18}$$

$$\text{with} \quad \gamma^2 = \frac{Q^2}{\nu^2} = \frac{(2Mx)^2}{Q^2} \ . \tag{1.19}$$

R is the ratio of longitudinal to transverse virtual photon cross sections:

$$R \equiv \frac{\sigma_L}{\sigma_T} \ . \tag{1.20}$$

The unpolarized cross section can then be expressed as

$$\frac{\mathrm{d}^2\sigma}{\mathrm{d}\Omega\mathrm{d}E'} = \left(\frac{\mathrm{d}^2\sigma}{\mathrm{d}\Omega}\right)_{Mott}\left[\frac{1}{\nu}F_2(x, Q^2) + \frac{2}{M}F_1(x, Q^2)\tan^2\frac{\theta}{2}\right] \ . \tag{1.21}$$

Note that for a nuclear target with mass number A, there are two commonly used definitions for the unpolarized structure function F_1 and F_2. These two definitions differ by a factor of A. We write them as $F_1^{(1)} = AF_1^{(2)}$ and $F_2^{(1)} = AF_2^{(2)}$, with (1) and (2) in the superscripts a label to distinguish between the two definitions. To clarify, we call the $F_1^{(1)}$ and $F_2^{(1)}$ the unpolarized structure functions *not per nucleon*, and the $F_1^{(2)}$ and $F_2^{(2)}$ the unpolarized structure functions *per nucleon*. In this dissertation only the first definition will be used, unless otherwise notified.

1.6 Polarized Structure Functions

In the polarized case, the difference between cross sections for scattering a polarized lepton with spin s from a polarized target with spin S and that with spin $-S$ is

$$\begin{aligned}\frac{\mathrm{d}^2\sigma_{s,S}}{\mathrm{d}\Omega\ \mathrm{d}E'} &- \frac{\mathrm{d}^2\sigma_{s,-S}}{\mathrm{d}\Omega\ \mathrm{d}E'} \\ &= \sum_{s'}\left[\frac{\mathrm{d}^2\sigma}{\mathrm{d}\Omega\ \mathrm{d}E'}(k,s,P,S;k',s') - \frac{\mathrm{d}^2\sigma}{\mathrm{d}\Omega\ \mathrm{d}E'}(k,s,P-S;k',s')\right] \\ &= \frac{8m\alpha^2E'}{q^4E}\Big\{\left[(q\cdot S)(q\cdot s)+Q^2(s\cdot S)\right]MG_1(P\cdot q,Q^2) \\ &\quad + Q^2\Big[(s\cdot S)(P\cdot q)-(q\cdot S)(P\cdot s)\Big]\frac{G_2(P\cdot q,Q^2)}{M}\Big\}\ , \qquad (1.22)\end{aligned}$$

where $G_1(P\cdot q,Q^2)$ and $G_2(P\cdot q,Q^2)$ are the polarized structure functions. They can be rewritten as functions of x and Q^2 as

$$\frac{\nu}{(P\cdot q)}G_1(P\cdot q,Q^2) = g_1(x,Q^2)\ ; \qquad (1.23)$$

$$\frac{\nu^2}{(P\cdot q)^2}G_2(P\cdot q,Q^2) = g_2(x,Q^2)\ . \qquad (1.24)$$

In the case where the lepton spin is longitudinally polarized, i.e., polarized along or opposite to the direction of motion, while the target nucleons are at rest and are polarized with spin S or $-S$, one obtains

$$\begin{aligned}\frac{\mathrm{d}^2\sigma_{\uparrow,S}}{\mathrm{d}\Omega\ \mathrm{d}E'} &- \frac{\mathrm{d}^2\sigma_{\uparrow,-S}}{\mathrm{d}\Omega\ \mathrm{d}E'} = -\frac{4\alpha^2}{Q^2}\ \frac{E'}{E} \qquad (1.25)\\ &\times \left\{\Big[E\cos\beta + E'\cos\Theta\Big]MG_1 + 2EE'\Big[\cos\Theta-\cos\beta\Big]\ G_2\right\}\ ,\end{aligned}$$

with β the angle between the incident electron momentum $\vec{k}$ and the target spin direction $\vec{S}$. Θ is the angle between the outgoing electron momentum $\vec{k}'$ and $\vec{S}$, given by

$$\cos\Theta = \sin\theta\sin\beta\cos\phi + \cos\theta\cos\beta\ . \qquad (1.26)$$

where θ is the scattering angle formed by $\vec{k}$ and $\vec{k}'$, ϕ is the angle between the scattering plane $(\vec{k},\vec{k}')$ and the polarization plane $(\vec{k},\vec{S})$. The angles β, ϕ, θ and Φ are illustrated in Figure 1-3.

For particular values of β one finds familiar results. If the target nucleons are

Figure 1-3: Kinematics of polarized electron scattering.

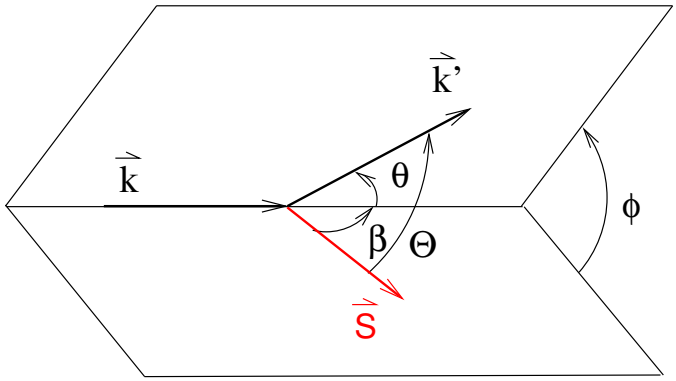

longitudinally polarized, then one has $\beta = 0$ and $\Theta = \theta$ and

$$\frac{\mathrm{d}^2\sigma_{\uparrow\Uparrow}}{\mathrm{d}\Omega \mathrm{d}E'} - \frac{\mathrm{d}^2\sigma_{\uparrow\Downarrow}}{\mathrm{d}\Omega \mathrm{d}E'} = \frac{4\alpha^2 E'}{\nu E Q^2}\Big[(E + E'\cos\theta)g_1(x,Q^2) - 2Mxg_2(x,Q^2)\Big] \ . \tag{1.27}$$

If the target nucleons are transversely polarized, then $\beta = \pi/2$, $\Theta = \arccos(\sin\theta\cos\phi)$ and

$$\frac{\mathrm{d}^2\sigma_{\uparrow\Rightarrow}}{\mathrm{d}\Omega \mathrm{d}E'} - \frac{\mathrm{d}^2\sigma_{\uparrow\Leftarrow}}{\mathrm{d}\Omega \mathrm{d}E'} = \frac{4\alpha^2 E'^2}{\nu E Q^2}\sin\theta\Big[g_1(x,Q^2) + \frac{2ME}{\nu}g_2(x,Q^2)\Big] \ . \tag{1.28}$$

1.7 Bjorken Scaling

A very interesting feature of structure functions is their scaling behavior in the Bjorken limit. The Bjorken limit [9] is defined as

$$Q^2 \to \infty, \text{ and } \nu \to \infty, \quad \text{with } x = \frac{Q^2}{2M\nu} \quad \text{fixed} \ . \tag{1.29}$$

In the Bjorken limit, x is just the fraction of the nucleon momentum carried by the struck quark in the infinite momentum frame. It turns out that in the Bjorken limit these structure functions are independent of Q^2 and can be written as $F_1(x)$, $F_2(x)$, $g_1(x)$ and $g_2(x)$. Moreover, since σ_L vanishes [6] and $R(x,Q^2) = 0$ in the Bjorken limit, Eq. (1.18) reduces to

$$F_2(x) \ = \ 2xF_1(x) \ , \tag{1.30}$$

known as the Callan-Gross relation.

1.8 Structure Functions in the Quark-Parton Model

While the phenomenon of scaling had been anticipated by Bjorken [9] and was put to the test by the original SLAC data [10], the quark-parton model [11] gives the clearest physical idea of what scaling means. Any object with a finite size must have a form factor and hence introduce some Q^2 dependence. Thus the scaling behavior of structure functions implies that the proton must contain point-like objects, the 'partons', which absorb the virtual photon. In the quark-parton model the nucleon is viewed as a collection of non-interacting, point-like constituents, one of which has fraction x of the nucleon's longitudinal momentum and absorbs the virtual photon.

Within the quark-parton model, the nucleon cross section is just the sum of the cross sections for scattering from individual partons, weighted by their number densities. Since partons interact with virtual photons through the electromagnetic interaction, each term should also be weighted by its electric charge squared. Therefore $F_1(x)$ and $g_1(x)$ can be related to the spin-averaged and spin-dependent quark distributions as [6]

$$F_1(x) = \frac{1}{2}\sum_i e_i^2 q_i(x) = \frac{1}{2}\sum_i e_i^2 \left[q_i^{\uparrow}(x) + q_i^{\downarrow}(x)\right] ; \tag{1.31}$$

$$g_1(x) = \frac{1}{2}\sum_i e_i^2 \Delta q_i(x) = \frac{1}{2}\sum_i e_i^2 \left[q_i^{\uparrow}(x) - q_i^{\downarrow}(x)\right] , \tag{1.32}$$

where $q_i(x) = q_i^{\uparrow}(x) + q_i^{\downarrow}(x)$ is the unpolarized parton distribution function of the i^{th} parton, defined as the probability that the i^{th} quark inside nucleon carries the fraction x of the nucleon's momentum. $\Delta q_i(x) = q_i^{\uparrow}(x) - q_i^{\downarrow}(x)$ is the polarized parton distribution function, where $q_i^{\uparrow}(x)$ ($q_i^{\downarrow}(x)$) is the number density, or the probability that the spin of the i^{th} quark is aligned parallel (anti-parallel) to the nucleon spin, when it carries the fraction x of the nucleon's momentum.

By measuring unpolarized and polarized cross sections on different target nucleons, one is able to extract partly how different quarks form a nucleon and how the quarks' spins are aligned along the nucleon spin direction. In addition to the method of electron scattering, neutral particles (e.g., neutrinos) interact with partons through the weak interaction, hence the structure functions measured in neutral particle scattering do not involve the electric charge of the partons [12]. Moreover information of antiquark distributions can be provided by the Drell-Yan process. Therefore by combining results from electron scattering, neutrino scattering and the Drell-Yan process, one can separate quark and antiquark distributions of each quark flavor in the nucleon. Eventually one will be able to pin down the nucleon structure to each constituent and find the answer to the two main questions listed at the beginning of this chapter.

The transverse polarized structure function $g_2(x)$ does not have a simple interpretation within the quark parton model [6]. However, it carries information about the

quark-gluon interaction inside the nucleon, which will be introduced in Section 1.10.

1.9 Scaling Violation

As been stated in Section 1.7, the scaling behavior of structure functions and Callan-Gross relation are exact only in the Bjorken limit; at finite Q^2 they are only approximations. This is because although Figure 1-1 describes the major process of electron scattering, there are higher order hard processes that occur which cannot be separated from the one-photon exchange process. These processes are due to the fact that both the initial and scattered quarks can emit soft gluons. Figure 1-4 shows the leading order gluon radiative effects. These soft gluon radiations give rise to an

Figure 1-4: Higher orders processes of electron scattering which cannot be separated from one-photon exchange.

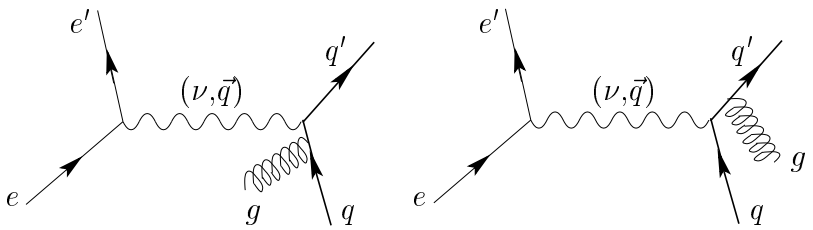

infinite cross section which can only be treated consistently when all other processes (Feynman graphs) at the same order are included. Consequently when we calculate a cross section for charged particle scattering there are gluon radiative corrections to be made, which gives to the cross section a logarithmic dependence on Q^2. Figure 1-5 shows data on the proton structure function $F_2^p(x, Q^2)$ from the New Muon Collaboration (NMC) [13] which clearly shows a Q^2 dependence. This relatively weak, logarithmic variation is why Bjorken scaling is only "a good approximation". The Q^2 dependence of structure functions can be well calculated in QCD using evolution equations first developed by Dokshitzer, Gribov, Lipatov, Altarelli, and Parisi (DGLAP equations) [15].

By incorporating the Q^2 dependence into the definition of the parton distributions one can generalize

$$F_1(x, Q^2) = \frac{1}{2} \sum_i e_i^2 \left[q_i^{\uparrow}(x, Q^2) + q_i^{\downarrow}(x, Q^2) \right] ; \tag{1.33}$$

$$g_1(x, Q^2) = \frac{1}{2} \sum_i e_i^2 \left[q_i^{\uparrow}(x, Q^2) - q_i^{\downarrow}(x, Q^2) \right] . \tag{1.34}$$

Now $q_i^{\uparrow(\downarrow)}(x, Q^2)$ should be interpreted as the probability of finding the i^{th} quark with

Figure 1-5: Q^2 dependence of $F_2^p(x, Q^2)$ data [13] and fit from global analysis [14].

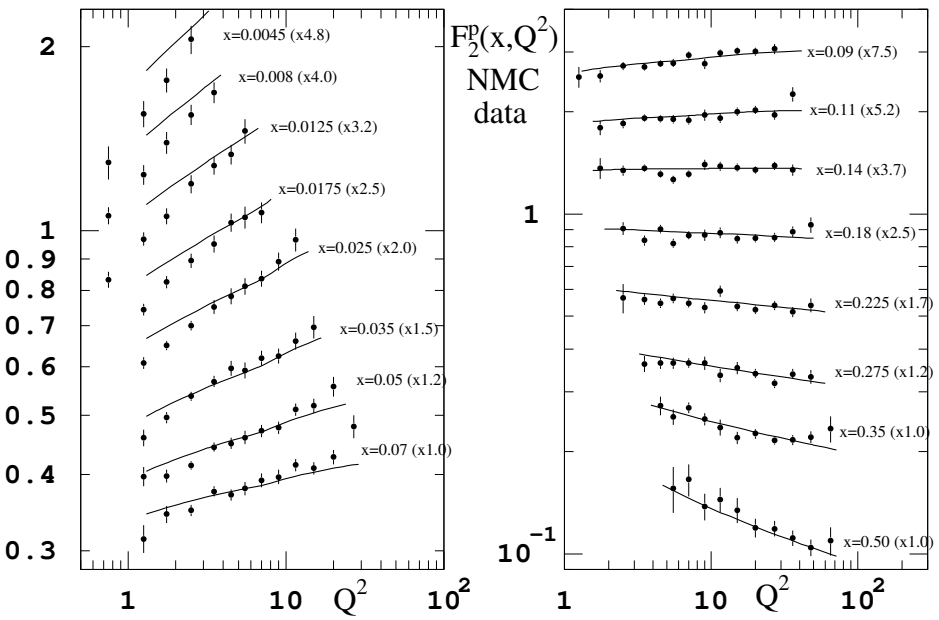

momentum fraction x and spin parallel (anti-parallel) to the nucleon spin *when viewed with a spatial resolution determined by* Q^2.

The physical picture associated with this interpretation is very simple. If one looks at the proton with low Q^2 and hence with a large wavelength ($\lambda \sim 1/\sqrt{Q^2}$) and poor spatial resolution, one cannot resolve much of its internal structure. Thus one expects the proton structure functions at low Q^2 to be dominated by the three current quarks "dressed" by the sea quarks and gluons. However, as Q^2 increases so does the resolving power and one expects to see more and more of the "bare" current quarks, $q\bar{q}$ pairs and gluons which make up the proton in QCD.

1.10 From Bjorken limit to finite Q^2 - Operator Product Expansion

In order to calculate the cross section at finite Q^2, a method called the Operator Product Expansion is applied to deep inelastic scattering (DIS) which can separate the non-perturbative part of cross section from its perturbative part.

The Operator Product Expansion (OPE) [16] was introduced in 1969 by Wilson in an attempt to introduce a substitute to Quantum Field Theory (QFT), in order to

carry out the QFT non-perturbative calculations. The OPE separates the perturbative part of a product of local operators from the non-perturbative part. In the limit of small distance $d \to 0$ the product of two operators can be written as

$$\sigma_a(d)\sigma_b(0) \;=\; \sum_k C_{abk(d)}\sigma_k(0)\ , \tag{1.35}$$

where C_{abk} are the Wilson coefficients which contain the perturbative part and are perturbatively calculable. Operators σ_k contain the non-perturbative information and are not perturbatively calculable. In DIS this formalism is used to develop a product of currents on a local operator basis. It has been shown that any operator σ_k contributes to the cross section as a factor $x^{-n}(M/Q)^{D-2-n}$, with n the spin and D the dimension of the operator [16], M the nucleon mass and $Q = \sqrt{Q^2}$. One defines the "twist" $t \equiv D - n$. At large Q^2 the leading twist $t = 2$ dominates. While at small Q^2 higher twist operators need to be taken into account.

The structure function $g_2(x, Q^2)$ has a special meaning because it can be separated cleanly into twist-2 and higher twist terms, and that the twist-2 term is determined by the structure function $g_1(x, Q^2)$. Ignoring quark mass effects, $g_2(x, Q^2)$ can be written as [17]:

$$g_2(x, Q^2) \;=\; g_2^{WW}(x, Q^2) + \bar{g}_2(x, Q^2)\ , \tag{1.36}$$

where $g_2^{WW}(x, Q^2)$ is a purely twist-2 contribution and is entirely determined by $g_1(x, Q^2)$ as

$$g_2^{WW}(x, Q^2) \;=\; -g_1(x, Q^2) + \int_x^1 \frac{g_1(y, Q^2)}{y}\mathrm{d}y\ . \tag{1.37}$$

Hence $g_2(x, Q^2)$ contains information about the higher twist effects which can be related to the quark-gluon interaction.

1.11 The Virtual Photon-Nucleon Asymmetries

Virtual photon asymmetries are defined in terms of a helicity decomposition of the virtual photon-nucleon scattering cross sections [18]. Figure 1-6 shows scattering of a circularly polarized virtual photon (with helicity ± 1) off a longitudinally polarized nucleon. There are two helicity cross sections $\sigma_{1/2}$ and $\sigma_{3/2}$. The subscript 1/2(3/2) is the projection of the total spin along the direction of virtual photon momentum $\vec{q}$, corresponding to the scattering with virtual photon spin anti-parallel (parallel) to the nucleon spin.

Figure 1-6: Definition of virtual photon asymmetry A_1.

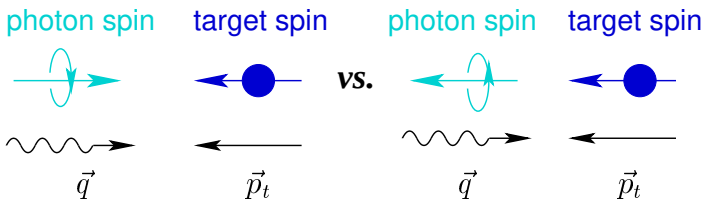

The longitudinal asymmetry A_1 is given by

$$A_1(x,Q^2) \equiv \frac{\sigma_{1/2}-\sigma_{3/2}}{\sigma_{1/2}+\sigma_{3/2}} . \tag{1.38}$$

A_2 is a virtual photon asymmetry that results from an interference between transverse and longitudinal virtual photon-nucleon amplitudes

$$A_2(x,Q^2) \equiv \frac{2\sigma_{LT}}{\sigma_{1/2}+\sigma_{3/2}} . \tag{1.39}$$

σ_{LT} results from the decomposition of the total virtual photo-absorption cross sections [18]. Unlike $\sigma_{1/2}$ and $\sigma_{3/2}$, σ_{LT} cannot be interpreted as the cross section for a real physics process.

There exists a Soffer's bound on the value of A_2 [19]:

$$A_2(x,Q^2) \leqslant \sqrt{\frac{R}{2}\Big[1+A_1(x,Q^2)\Big]} , \tag{1.40}$$

where $R = \sigma_L/\sigma_T$.

These two virtual photon asymmetries, in general functions of x and Q^2, are related to the nucleon spin structure functions $g_1(x,Q^2)$, $g_2(x,Q^2)$ and $F_1(x,Q^2)$ via

$$A_1(x,Q^2) = \frac{g_1(x,Q^2)-\gamma^2 g_2(x,Q^2)}{F_1(x,Q^2)} ; \tag{1.41}$$

$$A_2(x,Q^2) = \frac{\gamma\Big[g_1(x,Q^2)+g_2(x,Q^2)\Big]}{F_1(x,Q^2)} . \tag{1.42}$$

with γ given by Eq. (1.19). A_1, A_2 and $g_1(x,Q^2)/F_1(x,Q^2)$ can be related as

$$A_1(x,Q^2)+\gamma A_2(x,Q^2) = (1+\gamma^2)\frac{g_1(x,Q^2)}{F_1(x,Q^2)} . \tag{1.43}$$

At high Q^2, one has $\gamma^2 \ll 1$ and from Eq. (1.41)

$$A_1(x,Q^2) \approx \frac{g_1(x,Q^2)}{F_1(x,Q^2)} . \tag{1.44}$$

As a ratio of the structure functions, theoretically the asymmetry A_1 has less Q^2 dependence than the structure functions since the leading order (LO) Q^2 evolutions of $g_1(x,Q^2)$ and $F_1(x,Q^2)$ follow the same QCD evolution described by DGLAP equations and tend to cancel. Experimental data on the proton and neutron asymmetries A_1^p and A_1^n showed little Q^2 dependence [20]. Also from an experimental point of view, it is usually easier to measure an asymmetry since it doesn't require an absolute cross section measurement. If one can predict the value of A_1 from theories, then in addition to structure functions, A_1 can be another important tool to study the nucleon spin structure, and is somewhat more convenient than structure functions because of the features described above.

1.12 Electron Asymmetries

In an experiment it is usually difficult to align the virtual photon spin direction along the target spin direction, while keeping some flexibility in other kinematic variables. Alternatively the incident electron spin is aligned parallel (anti-parallel) or perpendicular (anti-perpendicular) to the target spin. The virtual photon asymmetries can be related to the measured lepton asymmetries through polarization and kinematic factors. For a target polarized parallel to the beam direction, the experimental longitudinal electron asymmetry is given by [12]

$$A_{\parallel} \equiv \frac{\sigma_{\downarrow\Uparrow} - \sigma_{\uparrow\Uparrow}}{\sigma_{\downarrow\Uparrow} + \sigma_{\uparrow\Uparrow}} = \frac{1-\epsilon}{(1-\epsilon R)W_1}\Big[M(E+E'\cos\theta)G_1 - Q^2 G_2\Big] , \tag{1.45}$$

where $\sigma_{\downarrow\Uparrow}(\sigma_{\uparrow\Uparrow})$ is the cross section for scattering off a longitudinally polarized target, with incident electron spin anti-parallel (parallel) to the target spin. Similarly the transverse electron asymmetry is defined for a target polarized perpendicular to the beam direction as [12]

$$A_{\perp} \equiv \frac{\sigma_{\downarrow\Rightarrow} - \sigma_{\uparrow\Rightarrow}}{\sigma_{\downarrow\Rightarrow} + \sigma_{\uparrow\Rightarrow}} = \frac{(1-\epsilon)E'}{(1-\epsilon R)W_1}\Big[MG_1 + 2EG_2\Big]\cos\theta , \tag{1.46}$$

where $\sigma_{\downarrow\Rightarrow}(\sigma_{\uparrow\Rightarrow})$ is the cross section for scattering off a transversely polarized target, with incident electron spin anti-parallel (parallel) to the beam direction, and the scattered electrons being detected on the same side of the beam as that to which the target spin is pointing. The electron asymmetries can be given in terms of A_1 and

A_2 as

$$A_{\parallel} = D(A_1 + \eta A_2) \; ; \tag{1.47}$$
$$A_{\perp} = d(A_2 - \xi A_1) \; . \tag{1.48}$$

The virtual photon polarization factor D is given by

$$D = \frac{1-(1-y)\epsilon}{1+\epsilon R} \approx y \; , \tag{1.49}$$

where $y \equiv \nu/E$ is the fraction of energy loss of the scattered electron, ϵ is the magnitude of the virtual photon's transverse polarization:

$$\epsilon = 1/\Big[1 + 2(1+1/\gamma^2)\tan^2(\theta/2)\Big] \; . \tag{1.50}$$

Other kinematic factors are

$$\eta = (\epsilon\sqrt{Q^2})/(E - E'\epsilon) \; , \tag{1.51}$$
$$\xi = \eta(1+\epsilon)/(2\epsilon) \;\; \text{and} \tag{1.52}$$
$$d = D\sqrt{2\epsilon/(1+\epsilon)} \; . \tag{1.53}$$

1.13 Extracting Polarized Structure Functions from Asymmetries

From Eq. (1.47) and (1.48) the virtual photon asymmetries A_1 and A_2 can be extracted from measured electron asymmetries $A_{\parallel}$ and $A_{\perp}$ as

$$A_1 = \frac{1}{D(1+\eta\xi)}A_{\parallel} - \frac{\eta}{d(1+\eta\xi)}A_{\perp} \;\; \text{and} \tag{1.54}$$
$$A_2 = \frac{\xi}{D(1+\eta\xi)}A_{\parallel} + \frac{1}{d(1+\eta\xi)}A_{\perp} \; . \tag{1.55}$$

If the unpolarized structure function $F_1(x,Q^2)$ is known, then the polarized structure functions can be extracted from measured electron asymmetries $A_{\parallel}$ and $A_{\perp}$ as [8]

$$g_1(x,Q^2) = \frac{F_1(x,Q^2)}{D'}\Big[A_{\parallel} + \tan(\theta/2)\cdot A_{\perp}\Big] \;\; \text{and} \tag{1.56}$$
$$g_2(x,Q^2) = \frac{F_1(x,Q^2)}{D'}\frac{y}{2\sin\theta}\Big[\frac{E+E'\cos\theta}{E'}A_{\perp} - \sin\theta\cdot A_{\parallel}\Big] \; , \tag{1.57}$$

where the kinematic factor D' is given by

$$D' = \frac{(1-\epsilon)(2-y)}{y[1+\epsilon R(x,Q^2)]} \, . \tag{1.58}$$

Chapter 2

Neutron Asymmetry A_1^n at Large x_{Bj}

As described in Chapter 1, the virtual photon asymmetry A_1 is an important physical quantity which can provide information about the spin structure of the nucleon. The value of A_1^n at large x is of particular interest because of the following reasons:

- Valence quarks dominate at large x, as shown in Figure 2-1. Hence there is less contribution from q-$\bar{q}$ sea quarks and gluons to the physical quantity, A_1^n, that is being measured. So it is a relatively simple region to study the spin structure of the nucleon;
- Several theoretical calculations are available, which give different predictions. These calculations will be described in Sections 2.2 to 2.9;
- The world data for A_1^n available before 2001 did not have the precision to distinguish among different predictions. This is mainly due to two technical difficulties in carrying out the experiment: (1) There exists no free neutron target; (2) High polarized luminosity is required in the large x region.

In this chapter we first clarify the meaning of the $x \to 1$ limit discussed in this dissertation. Results from several models and calculations for A_1^n are presented in Sections 2.2 to 2.9. An overview of existing A_1^n data is presented in Section 2.11.

2.1 The $x \to 1$ Limit

In Section 1.3 we have listed different kinematic regions of the excitation spectrum for electron scattering. Only in the deep inelastic region can the nucleon's substructure be resolved and its constituents – the partons – be seen. Therefore, to study the partonic structure of the nucleons, only the deep inelastic domain is of interest. The measurement of A_1^n described by this dissertation was carried out in the deep inelastic

Figure 2-1: A global fit [21] of parton distribution functions (pdf's) for the proton at $Q^2 = 5$ (GeV/c)^2; $u(d)$: valence $u_V(d_V)$ quark, $\bar{u}(\bar{d})$: sea $u(d)$ quark; $s(=\bar{s})$: strange sea quarks; g: gluons; Valence quark distributions are measured up to $x = 0.8$.

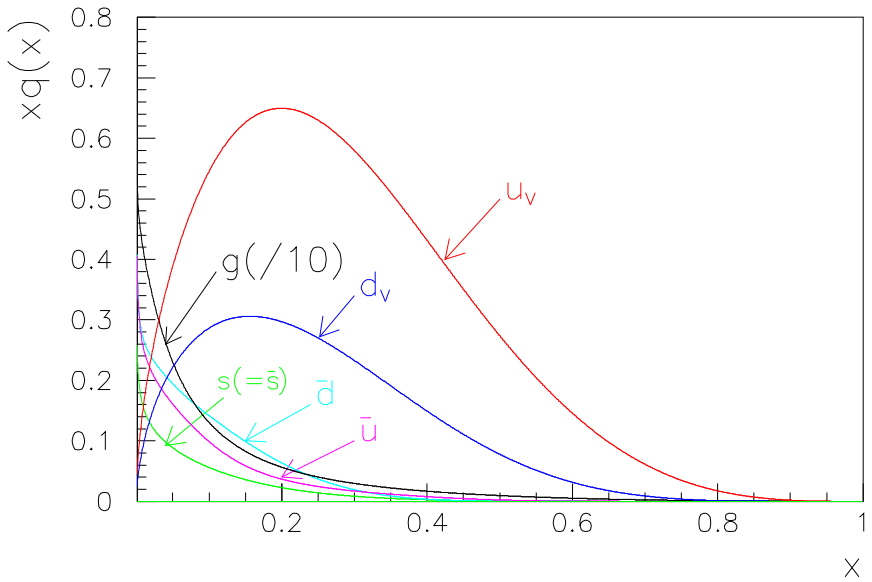

region and the theoretical predictions presented are made for the behavior of A_1^n in the deep inelastic region. In the rest of this dissertation, the "$x \to 1$ limit" is always referring to that of the deep inelastic domain.

2.2 Basic SU(6) Model

In the non-relativistic constituent quark model [34], the nucleon is described in terms of a symmetric SU(6) wavefunction, as shown in Figure 2-2. The only assumptions are that isospin and spin are 1/2 and that the non-color part of the wavefunction is

Figure 2-2: SU(6) wavefunction for the neutron.

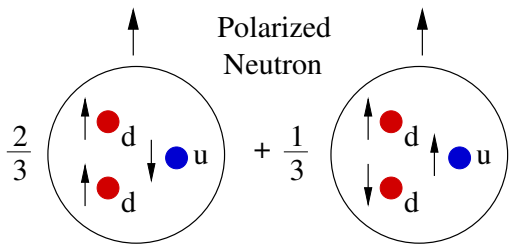

perfectly symmetric. More explicitly the wavefunction of a neutron polarized in the

$+Z$ direction ($S = 1/2, S_Z = +1/2$) has the form [22]:

$$\begin{aligned} |n\uparrow\rangle_{S=1/2,S_Z=+1/2} \;=\; & \frac{1}{\sqrt{2}}\,|d\uparrow(ud)_{S=0,S_Z=0}\rangle + \frac{1}{\sqrt{18}}\,|d\uparrow(ud)_{S=1,S_Z=0}\rangle \\ & -\frac{1}{3}\,|d\downarrow(ud)_{S=1,S_Z=1}\rangle - \frac{1}{3}\,|u\uparrow(dd)_{S=1,S_Z=0}\rangle \\ & -\frac{\sqrt{2}}{3}\,|u\downarrow(dd)_{S=1,S_Z=1}\rangle \;\;, \end{aligned} \tag{2.1}$$

where S in the subscript denotes the total spin of the 'diquark' state and S_Z is its projection along the $+Z$ direction. For the case of the proton one needs to merely exchange the u and d quarks in Eq. (2.1). In this limit where SU(6) is an exact symmetry, both diquark spin states with $S = 1$ and $S = 0$ contribute equally to the observables of interest, leading to the predictions:

$$A_1^p = \frac{5}{9}; \quad \text{and } A_1^n = 0 \;. \tag{2.2}$$

Data for A_1^p, A_1^n, g_1^p/F_1^p and g_1^n/F_1^n are shown in Figure 2-3. In this chapter

Figure 2-3: A_1^p and A_1^n as predicted from SU(6) symmetry, shown as a black line at 5/9 for the proton and 0 for the neutron.

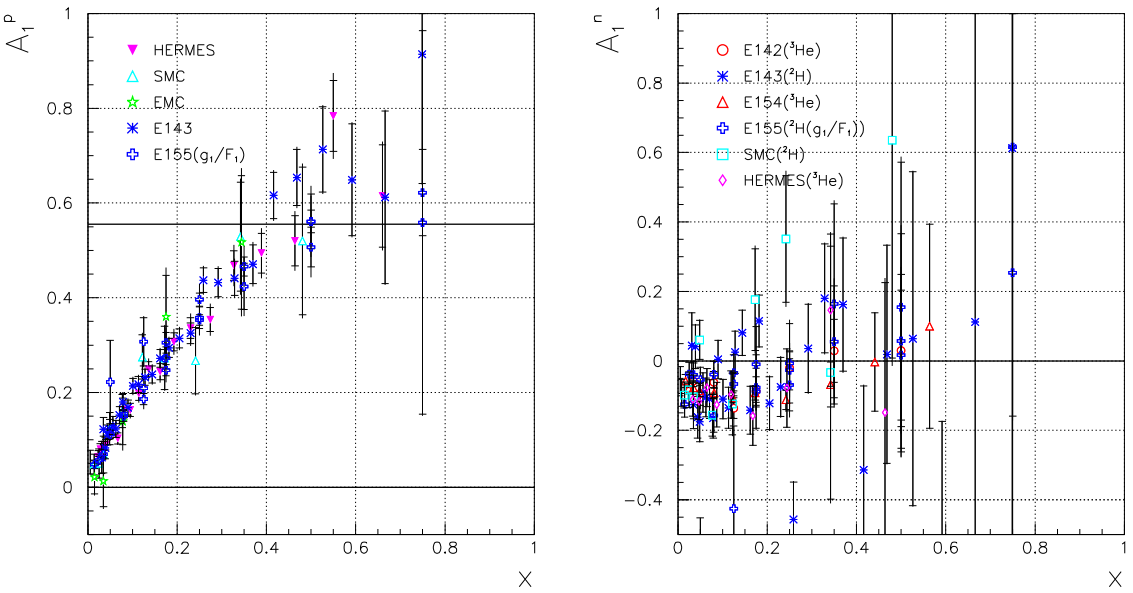

we plot data for g_1^p/F_1^p and g_1^n/F_1^n along with A_1^p and A_1^n since within the kinematics of most of the available measurements $A_1 \approx g_1/F_1$. Proton A_1^p data are from E143 [23] and E155 [20] experiments at Stanford Linear Accelerator (SLAC), the European Muon Collaboration (EMC) experiment [24] and the Spin Muon Collaboration (SMC) experiment [25] at CERN ; Neutron A_1^n data are from E142 [26]

and E154 [27] experiments at SLAC using a ^{3}He target, the SMC experiment [28] at CERN using a deuteron (^{2}He) target, and the HERMES experiment [29] at Deutsches Elektronen-Synchrotron (DESY) using a ^{3}He target; Proton g_1^p/F_1^p data include those from E143 [23] and E155 [20] experiments at SLAC and the HERMES experiment [30] at DESY; Neutron g_1^n/F_1^n data are from E143 [23] and E155 [20] experiments at SLAC using a ^{2}H target.

In the region of $x > 0.4$, the $A_1^p(x)$ data have large errors and are consistent with the SU(6) prediction 5/9. The statistical accuracy of $A_1^n(x)$ data is even worse than that of the proton. The $A_1^n(x)$ data at $x > 0.4$ are consistent with being zero everywhere.

We denote $u(x) \equiv u^p(x)$, $d(x) \equiv d^p(x)$ and $s(x) \equiv s^p(x)$ the parton distribution functions (PDF) for the proton. For a neutron one has $u^n(x) = d^p(x) = d(x)$, $d^n(x) = u^p(x) = u(x)$ based on isospin symmetry. The strange quark distribution for the neutron is assumed to be the same as that of the proton, $s^n(x) = s^p(x) = s(x)$. In the following all PDF's are for the proton, unless specified by a superscript 'neutron'.

In deep inelastic scattering, exact SU(6) symmetry implies equivalent shapes for the valence quark distributions, related simply by $u(x) = 2d(x)$ for all x. Using Eq. (1.18) and (1.31), one can write the ratio of neutron and proton F_2 structure functions as

$$R^{np} \equiv \frac{F_2^n}{F_2^p} = \frac{u(x) + 4d(x)}{4u(x) + d(x)} \ . \tag{2.3}$$

Applying $u(x) = 2d(x)$ gives

$$R^{np} = \frac{2}{3} \ . \tag{2.4}$$

Data for R^{np} [31] are shown in Figure 2-4. In this case, they agree poorly with the SU(6) prediction. $R^{np}(x)$ is a straight line starting with $R^{np}(0) = 1$ but constantly dropping to approximately $R^{np}(1) = 1/4$ at large x. In addition, $A_1^p(x)$ is small at low x, as shown in Figure 2-3. The fact that $R^{np}(0) = 1$ may be explained by the presence of a large amount of sea quarks in the low x region and the fact that $A_1^{n,p}(0) \sim 0$ is because these sea quarks are not highly polarized. At large x, however, there are few sea quarks and data indicate there must be problems with the SU(6) wavefunction. In fact, SU(6) symmetry is well known to be broken [32] and the details of possible SU(6)-breaking mechanism is a basic question in hadronic physics.

Figure 2-4: SLAC data [31] on the F_2^n/F_2^p ratio. The horizontal line at 2/3 shows the SU(6) prediction.

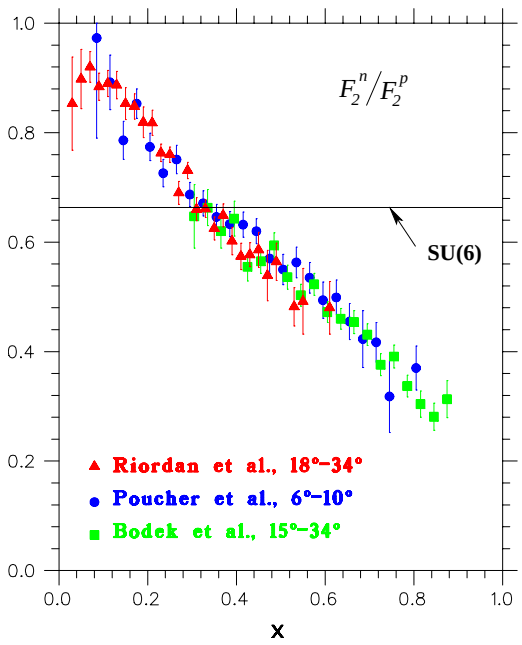

2.3 SU(6) Breaking and Hyperfine Perturbed Constituent Quark Model

A natural explanation of SU(6) symmetry breaking based on phenomenological arguments [32] is the so called hyperfine interaction, or chromomagnetic interaction among the quarks, described as $\vec{S}_i \cdot \vec{S}_j \; \delta^3(\vec{r}_{ij})$, where $\vec{S}_i$ is the spin of i^{th} quark. It is this interaction that explains the 300 MeV difference between the nucleon and the $\Delta(1232)$ masses. The effect of this perturbation on the wavefunction is to lower the energy of the $S = 0$ diquark state, allowing the first term of Eq. (2.1), $|d \uparrow (ud)_{S=0,S_Z=0}\rangle^{\rm neutron}$, to be more stable and hence dominate the high energy tail of the quark momentum distribution that is probed as $x \to 1$. Since the struck $d^{\rm neutron}$ quark in this term has its spin parallel to that of the neutron, the dominance of this term at $x \to 1$ implies $(\Delta d/d)^{\rm neutron} \to 1$, $(\Delta u/u)^{\rm neutron} \to -1/3$, or

$$\Delta u/u \to 1; \Delta d/d \to -1/3 \;\; \text{as } x \to 1 \; , \tag{2.5}$$

where $\Delta u(\Delta d)$ and $u(d)$ are the polarized and the unpolarized quark distribution functions for the proton. They are functions of x; however in the following the argument x will not be explicitly written if only the limiting behavior at $x \to 1$ is

discussed. One also obtains

$$R^{np} = \frac{F_2^n}{F_2^p} \to \frac{1}{4} \text{ as } x \to 1 \ , \tag{2.6}$$

which could explain the deviation of $R^{np}(x)$ data from the SU(6) prediction. Based on the same mechanism, we can give predictions for $A_1^p(x)$ and $A_1^n(x)$:

$$A_1^p \to 1, A_1^n \to 1 \text{ as } x \to 1 \ . \tag{2.7}$$

The constituent quark model (CQM) [34] is the best model so far to describe the phenomenology of low energy hadronic physics. Constituent quarks share with the fundamental QCD quarks their conserved charges and quantum numbers; they have angular momentum 1/2 and are fermions. On the other hand, constituent quarks are supposed to have effective masses exceeding the current quark masses of perturbative QCD. Qualitatively, a constituent quark may be viewed as an object in which a "bare" (current) valence quark is dressed by clouds of quark-antiquark pairs and gluons. Although it is not clear from QCD - the theory of strong interaction - how current quarks are dressed through the strong interactions and form constituent quarks, the CQM has been accepted for a long time because of its success in describing many aspects of low energy hadronic physics, especially in constructing hadron spectroscopy and structure. On the other hand, QCD has been successful in explaining some detailed behaviors of structure functions, for example, their Q^2 evolution. However so far QCD has been unsuccessful in constructing structure functions.

Figure 2-5: A_1^p and A_1^n as predicted from the CQM [36] and the comparison to world data.

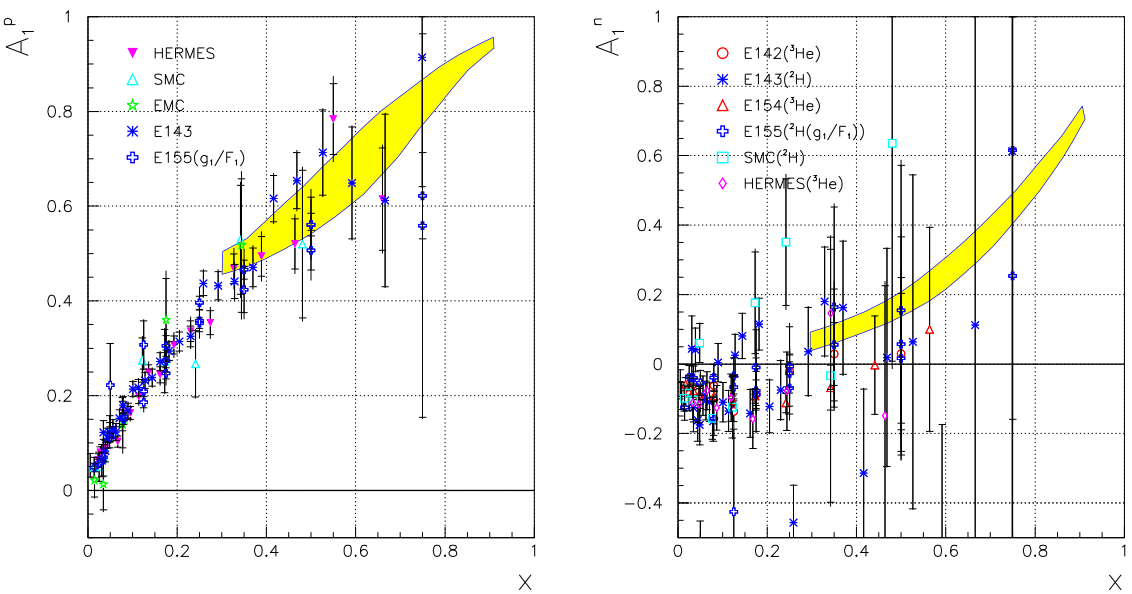

A CQM incorporating the hyperfine interaction has been developed by Isgur and Karl [35] which can adequately describe the baryon spectrum. The same idea can be used to construct structure functions in the large x region. This can be justified by valence quark dominance in this region. That is, in the large x region almost all quantum numbers, momentum and spin of the nucleon are carried by the three valence quarks, which can therefore be identified as constituent quarks. Results for the asymmetries A_1^p and A_1^n from hyperfine perturbed CQM [36] are shown in Figure 2-5, the relativistic effect has been included. There are two additional assumptions in this calculation. The first one is $d(x)/u(x) \approx \kappa(1-x)$ as $x \to 1$ with $\kappa \approx 0.5 \sim 0.6$, which satisfies the fact that the $d(x)$ vanishes at $x = 1$ because of the hyperfine interaction. The second assumption is $c_A(x) = nx(1-x)^n, n = 2 \sim 4$ and $c_A(x)$ describes the probability that the spin of a quark is flipped because of relativistic effects.

2.4 Perturbative QCD

Another approach focuses directly on relativistic quarks instead of the non-relativistic quarks of the above discussion. Farrar and Jackson [37] in the early 1970's, in one of the first applications of perturbative QCD (pQCD), noted that at $x \to 1$, the scattering is from a high energy quark, and the process can be treated perturbatively. Assuming the orbital angular momentum of quarks is zero and based on angular momentum conservation, Farrar and Jackson proceeded to show that a quark carrying nearly all the momentum of the nucleon (i.e. $x \to 1$) must have the same helicity as the nucleon. This mechanism is usually referred to as Hadron Helicity Conservation (HHC). In this picture, quark-gluon interactions cause only the $S = 1$, $S_z = 1$ diquark spin projection component, rather than the full $S = 1$ diquark system to be suppressed as $x \to 1$. It gives

$$d^{\downarrow}/d^{\uparrow} \to 0,\ u^{\downarrow}/u^{\uparrow} \to 0; \qquad \Delta u/u \to 1,\ \Delta d/d \to 1 \ \text{ as } x \to 1\ ; \tag{2.8}$$

$$\frac{d}{u} = \frac{d^{\uparrow}}{u^{\uparrow}} \to \frac{1}{5} \qquad \text{as } x \to 1\ ; \tag{2.9}$$

$$A_1^p \to 1, A_1^n \to 1; \qquad R^{np} \to \frac{3}{7} \ \text{ as } x \to 1\ . \tag{2.10}$$

This is one of the few places where QCD can make an absolute prediction for the x dependence of the structure functions (here a ratio of structure functions). It is uncertain how low in x and Q^2 this picture is reliable. This pQCD prediction has been imposed in the fits to polarized DIS data by Brodsky, Burkhardt and Schmidt [38], known as the BBS parameterization. In this calculation, the first moment of the proton g_1^p data from polarized DIS experiments was used in the fitted data set and the neutron data were not included. However their treatment was rough and the Q^2 evolution was not included. This was improved by E. Leader, Sidorov and Stamenov, known as LSS(BBS) parameterization [39]. They fit to proton and neutron A_1 data

Figure 2-6: A_1^n as predicted from pQCD HHC based BBS (curve (1)) and LSS(BBS) parameterization (curve (2)).

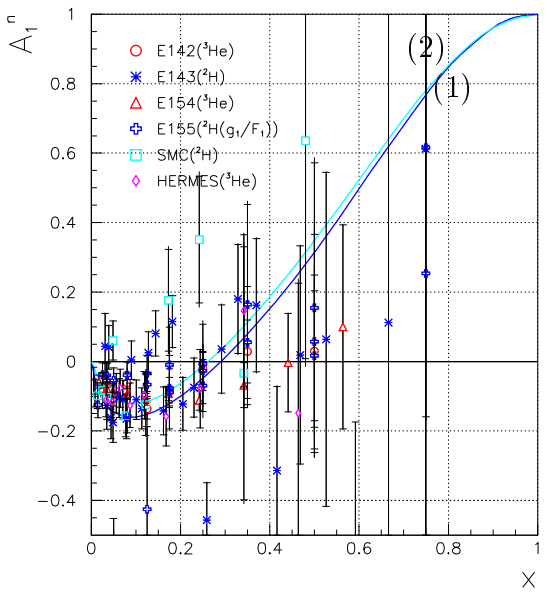

directly and the Q^2 evolution was carefully treated. Results for A_1^n using BBS and LSS(BBS) parameterizations are shown in Figure 2-6.

2.5 Angular Momentum and Quark Helicity Conservation

However, hadron helicity conservation was deduced from angular momentum conservation based on the assumption that the orbital angular momentum of the quarks is zero. As recently pointed out [40], quarks do not necessarily have a vanishing orbital angular momentum. Consequently the struck quark can flip its helicity by transferring a unit of orbital angular momentum. Hence it becomes questionable to apply the pQCD based HHC to the struck quark in deep inelastic scattering. This mechanism has been used to interpret the observation that the ratio of proton Pauli and Dirac form factors data $F_2^{p,el}(Q^2)/F_1^{p,el}(Q^2)$ is proportional to $1/Q$ above $Q^2 = 2$ (GeV/c)^2 [41][42], in contrast to the pQCD HHC based prediction that $F_2^{p,el}(Q^2)/F_1^{p,el}(Q^2) \sim 1/Q^2$ [43]. Calculations of g_1^p/F_1^p and g_1^n/F_1^n *without* pQCD based HHC constraint were performed using a world fit of polarized and unpolarized parton distribution functions, the LSS parameterizations [44]. Results for g_1^p/F_1^p and g_1^n/F_1^n for Q^2=3, 5, 100 (GeV/c)^2 [45] are shown in Figure 2-7.

In addition to SU(6), hyperfine-perturbed constituent quark models and pQCD

Figure 2-7: g_1^p/F_1^p and g_1^n/F_1^n from LSS parameterization. Curves (bottom, middle and top) correspond to calculations of g_1^p/F_1^p and g_1^n/F_1^n at Q^2=3, 5, and 100 (GeV/c)^2, respectively.

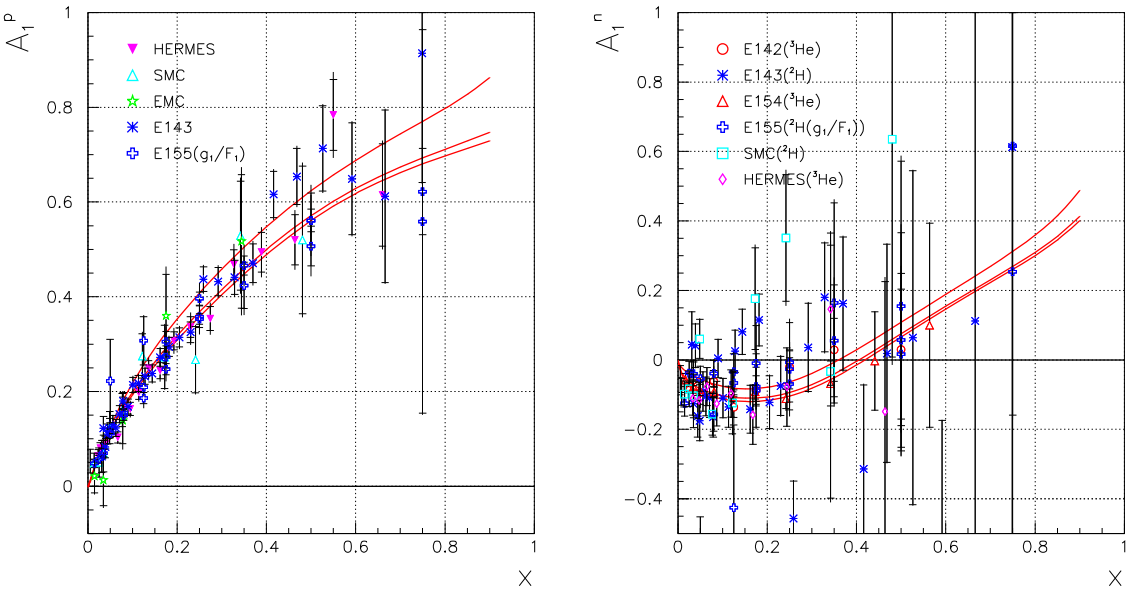

based models, there are a few other models which can give a prediction for A_1^n at large x, as will be described in the following sections.

2.6 Statistical Approach for Polarized Structure Functions

In the statistical approach the nucleon is viewed as a gas of massless partons (quarks, antiquarks, gluons) in equilibrium at a given temperature in a finite volume [46]. The parton distribution $p(x)$, at an input energy scale Q_0^2, is proportional to

$$\{e^{\frac{x-X_{0p}}{\bar{x}}} \pm 1\}^{-1}. \tag{2.11}$$

The *plus* sign is for quarks and antiquarks and corresponds to a Fermi-Dirac distribution. The *minus* sign is for gluons and corresponds to a Bose-Einstein distribution. X_{0p} is a constant which plays the role of the thermo-dynamical potential of the parton p. $\bar{x}$ is the *universal temperature* and is the same for all partons. Based on this statistical picture of the nucleon, a global Next-to-Leading Order (NLO) QCD analysis of unpolarized and polarized DIS data is performed, and a good description has been obtained in a broad range of x and Q^2, of all measured structure functions F_2^p, F_2^D, g_1^p, g_1^D, and g_1^n [46].

Figure 2-8: Predictions of A_1^p and A_1^n from statistical model. Curves (bottom, middle and top for A_1^p, and bottom, middle and top at $x > 0.6$ for A_1^n) correspond to calculation at Q^2=4, 10, and 10 (GeV/c)^2, respectively.

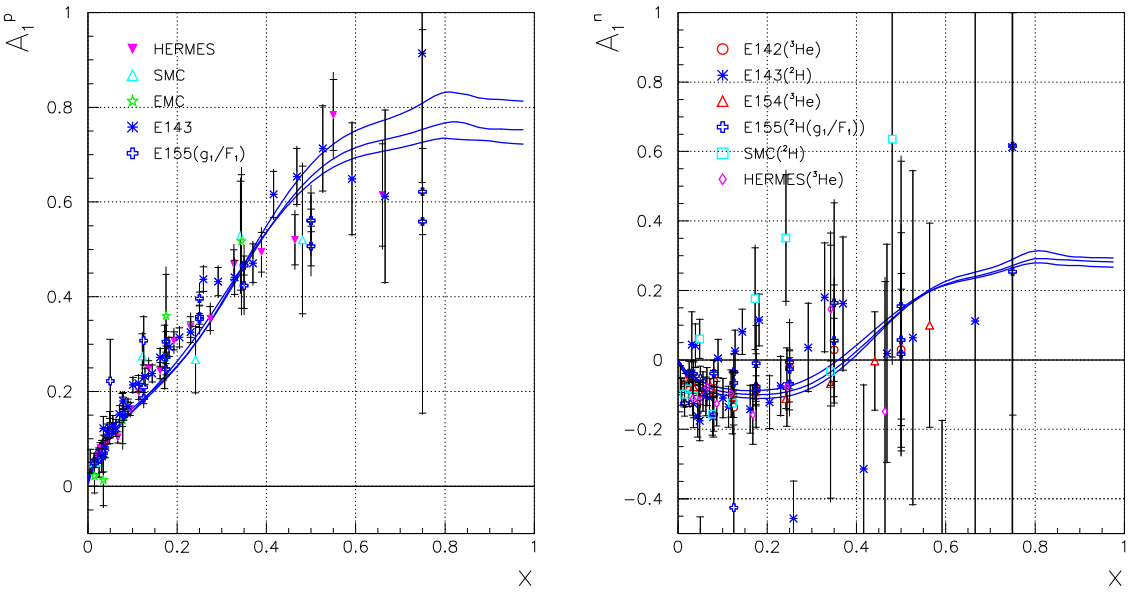

For the asymmetry A_1, first consider the ratio g_1/F_1. Assuming that the u quark dominates at large x, from Eq. (1.18), (1.31) and (1.32) one obtains

$$\frac{g_1(x,Q^2)}{F_1(x,Q^2)} \sim \frac{g_1(x,Q^2)}{F_2(x,Q^2)} \frac{[1+R(x,Q^2)]}{[1+\gamma^2(x,Q^2)}\ . \tag{2.12}$$

Next, assuming higher twist effects are small, the structure function $g_2(x,Q^2)$ can be estimated by its twist-2 term $g_2^{WW}(x,Q^2)$ in Eq. (1.37). Once both $g_1(x,Q^2)$ and $g_2(x,Q^2)$ are known, A_1 can be calculated using Eq. (1.41).

In the statistical approach $\Delta u/u \to 0.77$, $\Delta d/d \to -0.46$ and $A_1^{p,n} < 1$ at $x \to 1$. Results of A_1^p and A_1^n at Q^2=4, 10, 100 (GeV/c)^2 [47] are shown in Figure 2-8.

Because the statistical model is more focused on the global behavior of partons inside the nucleon, in this sense it is a good approximation at low x region where the $q-\bar{q}$ sea and gluons dominate and form a 'parton zoo' with valence quarks. In the large x region valence quarks dominate so one should see more individual aspects of partons, rather than global ones. Hence in the large x region (a conservative estimation is $x > 0.6$), the calculations based on the statistical approach become questionable.

2.7 Local Duality

Quark-hadron duality was first established by Bloom and Gilman [48]. In early 1970s it has been observed that the unpolarized F_2 structure function at low W generally follows a global scaling curve which describes high W data, to which the resonance structure function averages. Furthermore, the equivalence of the averaged resonance and scaling structure functions appears to hold for each resonance, over restricted regions in W, so that the resonance-scaling duality also exists locally.

For elastic scattering, the connection between the elastic form factors at large Q^2 and the $x \to 1$ behavior of structure functions was established by Drell and Yan [49], and West [50]. Recently more interest has arisen in connection with the asymmetry A_1 and the F_2^n/F_2^p ratio, whose $x \to 1$ limits reflect mechanisms for the breaking of spin-flavor SU(6) symmetry in the nucleon. Based on local duality, one can use measured structure functions in the resonance region at large ξ to directly extract elastic form factors [51]. Here ξ is a counterpart of x in DIS, with a correction factor taking into account the finite target mass effect.

Conversely, empirical elastic electromagnetic form factors at large Q^2 can be used to predict the $x \to 1$ behavior of deep-inelastic structure functions [52]. It has been shown that asymptotically in the $Q^2 \to \infty$ limit each of the structure functions F_1, F_2 and g_1 are determined by the slope of the square of the elastic magnetic form factor G_M, while g_2 (which in deep-inelastic scattering is associated with higher twists) is

Figure 2-9: Predictions of A_1^p and A_1^n from the local duality method (green curves) compared with world data.

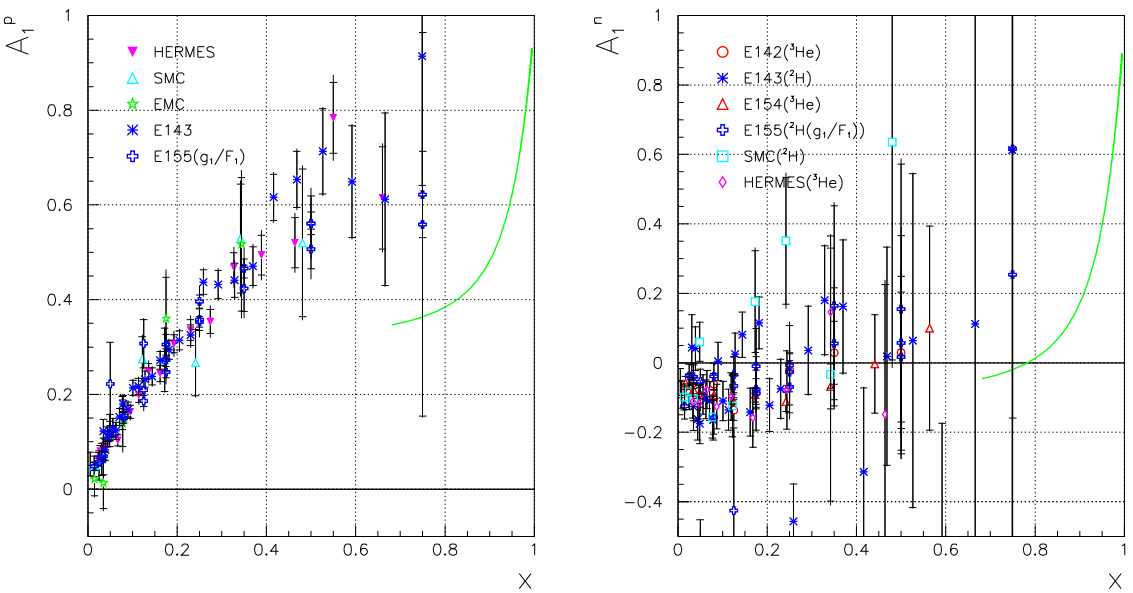

determined by a combination of G_E and G_M. As a ratio of structure functions, the

$x \to 1$ behavior of the asymmetry A_1 has been predicted from a parameterization of global form factor data [53]. Results of A_1^p and A_1^n [54] are shown in Figure 2-9.

There is one precaution that needs to be made for a local duality calculation. For the prediction shown in Figure 2-9, although the curves are plotted for $x > 0.7$, one should note that the region below the pion threshold $x = x_{\rm th} \approx 0.8$ corresponds to $Q^2 \approx 1$ GeV^2, where duality is not expected to be a good approximation, so the reliability of the local duality predictions there would be questionable. Moreover, duality itself is more motivated by phenomenology and has not been well understood on a theoretical basis. A robust prediction of local duality, however, is that $A_1 \to 1$ as $x \to 1$.

2.8 Chiral Soliton Model

Whereas perturbative QCD works well in the high energy hadronic physics, theories suitable for hadronic phenomena in the low energy, non-perturbative regime are much more difficult to construct. Promising models in this regime are chiral effective theories and the lattice QCD method. There exist predictions for the structure functions and the moments of structure functions from these non-perturbative theories. Experimental data can help to improve these theories by providing more constraints.

In this section, the theories of chiral dynamics [55] and the concepts of baryons as chiral solitons [61] will be briefly reviewed first, then chiral soliton calculations for A_1 will be presented.

The QCD Lagrangian with N_f massless flavors is known to possess a large global symmetry, namely a symmetry under unitary flavor transformations of the corresponding left- and right-handed quark fields, or under $U_L(N_f) \times U_R(N_f)$ rotations. This symmetry is called *chiral* [56]. If this symmetry were exact, one would observe parity degeneracy of all states with all other quantum numbers being the same. In reality the splittings between states with the same quantum numbers but opposite parities are huge. For example, the splitting between the vector ρ and the axial meson a_1 is (1260-770) $\approx$ 500 MeV. The splittings are too large to be explained by the existence of small current quark masses ($m_u \approx 4$ MeV, $m_d \approx 7$ MeV and $m_s \approx 150$ MeV), which break the chiral symmetry explicitly. These facts in hadron phenomenology lead to the conclusion that the chiral symmetry of the QCD Lagrangian is broken *spontaneously* [55]. The role of chiral symmetry, its spontaneous breaking and its consequences in hadron physics, have served as a basis for modeling the strong interactions.

Additional guidance can be obtained if one generalizes QCD from the gauge group SU(3) to SU(N_C) with an arbitrary large number of colors N_C [58] [59]. For large N_C, $1/N_C$ might be considered as an implicit expansion parameter and QCD can be treated perturbatively in the low-energy regime. In this case QCD reduces to an effective theory of infinitely many weakly interacting mesons and glueballs. Although

one might wonder at this point whether this provides a sound basis for a perturbative analysis since $N_C = 3$ in the real world, models can be constructed based on this idea and it turns out to be fruitful. In this effective meson theory baryons can be built from N_C quarks, and moreover can be identified as solitonic solutions of the field equations [57].

In 1961 Nambu and Jona-Lasinio (NJL) [60] constructed a local four fermion interaction with a global $U(1) \times SU(2)_L \times SU(2)_R$ chiral symmetry. Later all chirally invariant models with local four-fermion (u_L, d_L, u_R and d_R) interactions (or even six-fermion interactions) were called NJL models. Using a special technique called the functional integral, the NJL model can be converted to an effective meson theory and therefore it has a QCD basis in the large N_C limit. This model can directly construct the quark flavor dynamics and baryons emerge as *chiral solitons* of the pseudo-scalar fields [61]. Although the NJL model has some difficulties in explaining hyperon static properties (using six-fermion version, i.e., three flavors), it is successful in the case of nucleons. A collective wave-function for the nucleon with good flavor and spin quantum numbers has been achieved [62].

Based on the chiral soliton picture of the nucleons, a calculation has been done for g_1^n/F_1^n using the four-fermions NJL model at $Q^2 = 0.4$ (GeV/c)^2 [63], as shown in Figure 2-10. Note that this is a pure model calculation and does not require any fit to world data. The result can be evolved to higher Q^2 using the DGLAP equations. Calculations for A_1^n and g_2^n/F_1^n are in progress and reliable results will be available in 2003.

Figure 2-10: g_1^n/F_1^n as predicted from chiral soliton model at Q^2=0.4 (GeV/c)^2.

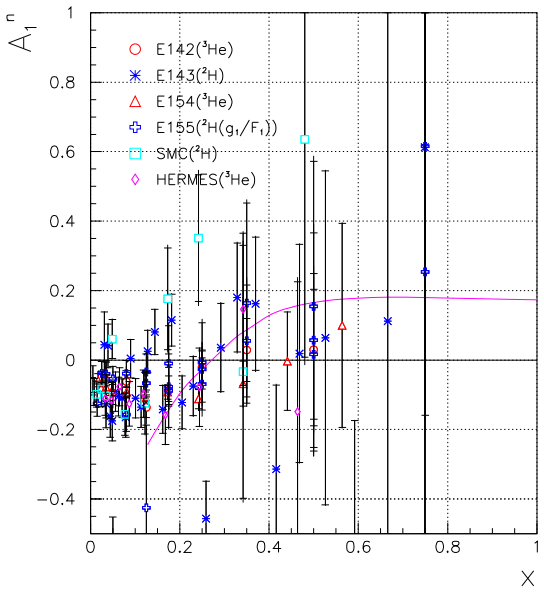

One open issue is that there is no quark confinement in the NJL models. However,

soliton models are very attractive because of their connection to QCD in the limit of large N_C mentioned above, and the possibility to generalize them to three flavors. Also they provide a very comprehensive picture of baryons ranging from static properties of nucleons and meson-nucleon scattering involving systems with a heavy quark, to applications in the context of nuclear matter. These models use only a very limited number of parameters. Present studies of chiral soliton models apparently serve to further complete this comprehensive picture.

2.9 Instanton and Polarized Structure functions

The non-perturbative vacuum fluctuations of the gluon fields, so-called instantons, are widely used in the description of the non-perturbative effects in strong interactions. The instantons describe the sub-barrier transitions between different classical QCD vacuum states, that have different values of quark helicities. Therefore they can remove helicity from valence quarks and transfer it to gluons and quark-antiquark pairs, introducing quark depolarization inside the nucleon. Based on this motivation, the instanton model was introduced to explain the observed violation of the Ellis-Jaffe sum rule, or the so-called 'spin-crisis' of the proton [64].

The contribution of the quark-quark and quark-gluon interactions induced by instantons to the valence quarks and to the proton spin-dependent structure functions $g_1^p(x, Q^2)$ have been estimated within the instanton liquid model for the QCD vacuum [64]. The result shows that contributions to the nucleon spin from instanton induced q-q and q-g interactions are both negative, and are x-dependent. They give a reasonable Ellis-Jaffe sum rule violation for the proton, and can explain the decrease of the $g_1^p(x)$ structure function at large x. On the other hand, the prediction of the instanton model for the neutron g_1^n structure function is very sensitive to the details of the violation of the SU(6) symmetry for the valence quark distribution function and was not discussed in [64]. However, if negative contributions are formed by q-q and q-g interactions for the neutron, as they do for the proton, then it is possible that A_1^n is near zero or even negative in the large x region [65].

2.10 Lattice QCD and Polarized Structure Functions

It has been mentioned that lattice QCD provides the only known QCD simulation for non-perturbative calculation of hadron structure in the low-energy regime. A lattice QCD calculation has been done for the moments of the nucleon polarized structure functions g_1^p and g_1^n [66]. However there is no calculation available for A_1 yet.

2.11 Existing Measurements of A_1^n at large x

The world data for A_1^n available before 2001 have poor statistical accuracy at $x > 0.4$ and cannot distinguish among different models, see Figure 2-11. Table 2.1 gives a summary of all measurements. Clearly, there is a great need for data at $x > 0.4$.

Table 2.1: Measurements of A_1^n before 2001.

Experiment	Beam	Target	x	Q^2 in $(\mathrm{GeV/c})^2$)
E142 [26]	19.42, 22.66, 25.51 GeV e^-	^{3}He	0.03∼0.6	2
E154 [27]	48.3 GeV e^-	^{3}He	0.014∼0.7	1∼17
HERMES [29]	27.5 GeV e^+	^{3}He	0.023∼0.6	1∼15
E143 [23]	9.7, 16.2, 29.1 GeV e^-	Ammonia	0.024∼0.75	0.5∼10
E155 [20]	48.35 GeV e^-	Ammonia	0.014∼0.9	1∼40
SMC [28]	190 GeV μ^-	deuterated butanol	0.003∼0.7	1∼60

Figure 2-11: Existing data on A_1^n in comparison to various theoretical predictions including: A_1^n from CQM (yellow band (1)); g_1/F_1 at $Q^2 = 5$ (GeV/c)^2 from LSS parameterization (red curve (2)); A_1^n from pQCD based BBS parameterization (blue curve (3)); A_1^n from pQCD based LSS(BBS) parameterization (cyan curve (4)); A_1^n from statistical model at $Q^2 = 4$ (GeV/c)^2 (blue curve (5)); A_1^n from local duality (green curve (6)); A_1^n from chiral soliton model at $Q^2 = 0.4$ (GeV/c)^2 (purple curve (7)); and A_1^n from E155 g_1/F_1 experimental fit at $Q^2 = 4$ (GeV/c)^2 (black curve (8)).

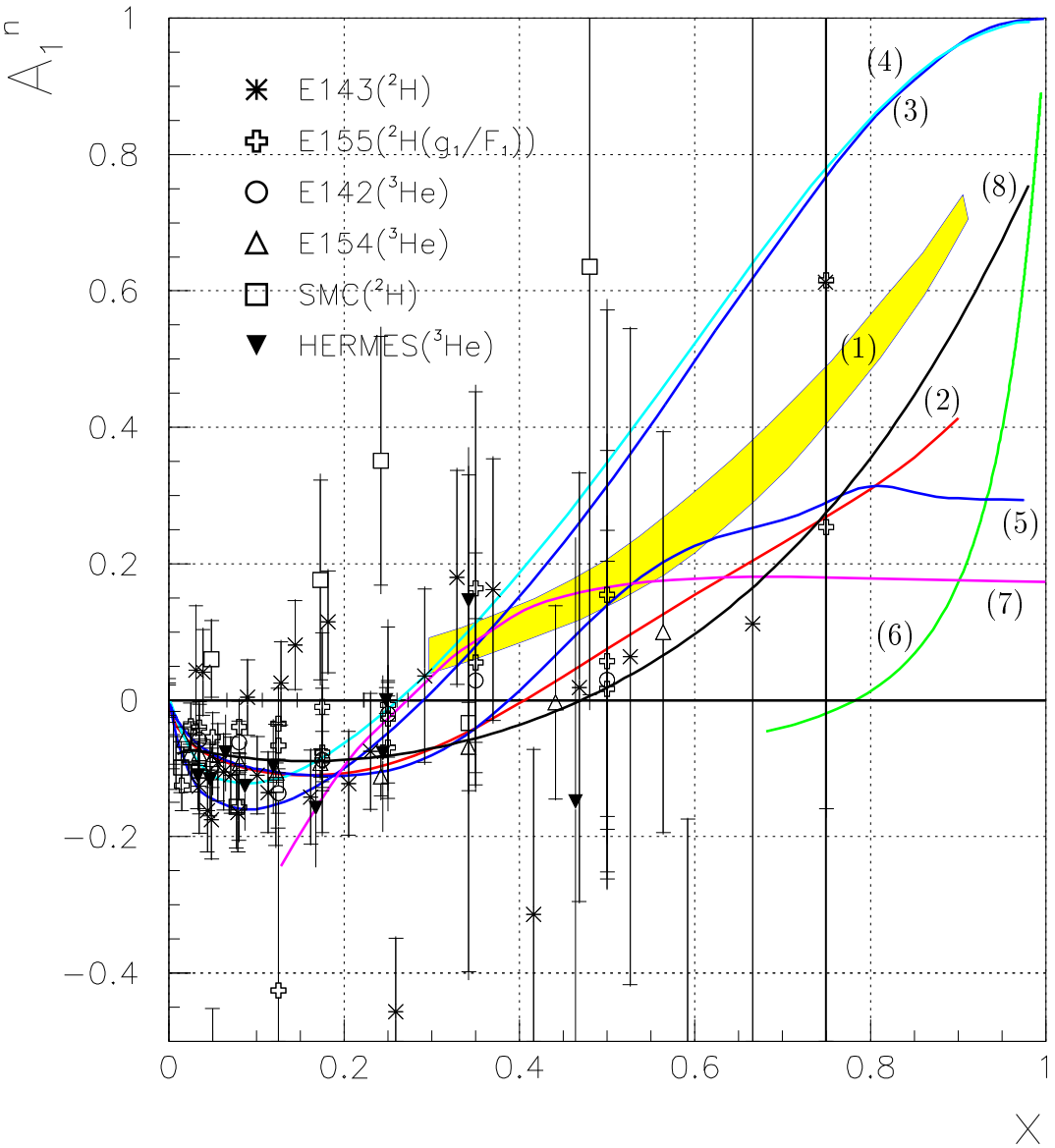

Chapter 3

Experimental Setup

During the summer of 2001 in Hall A of the Thomas Jefferson National Accelerator Facility (Jefferson Lab, or JLAB; formerly known as Continuous Electron Beam Accelerator Facility, or CEBAF), the neutron asymmetry A_1^n was measured at three kinematics $x = 0.33$, 0.47 and 0.60, with $Q^2 = 2.71$, 3.52 and 4.83 $(\mathrm{GeV/c})^2$, respectively. To determine A_1^n, both electron asymmetries $A_{\parallel}$ and $A_{\perp}$ of inclusive $^3\vec{\mathrm{He}}(\vec{e}, e')$ scattering have been measured in the deep inelastic region. This chapter describes the experimental setup and most of the instrumentation. The polarized ^{3}He target will be described in Chapter 4. Data analysis associated with part of the instrumentation will be presented in the beginning of Chapter 5.

3.1 Overview

As mentioned in Chapter 2, the experimental difficulties to measure A_1^n in the large x region are the following

- There exists no free neutron target which is dense enough to carry out a scattering experiment. This is mainly because of neutron's short lifetime ($\sim$ 886 sec);
- High polarized luminosity is required for precision measurements in the large x region.

Because there exists no dense free neutron target, polarized nuclear targets such as ^{2}H or ^{3}He are commonly used as effective polarized neutron targets. Consequently, nuclear corrections need to be made to extract neutron information from nuclei target. For a polarized deuteron, approximately half of the deuteron spin comes from the proton and the other half comes from the neutron. Therefore the neutron results extracted from the deuteron have a large uncertainty coming from the uncertainty of proton data.

Compared to a polarized deuteron, the spin of a polarized ^{3}He comes mainly from the neutron ($\sim$ 86%). Figure 3-1 shows the ^{3}He ground state wavefunction which

consists of S, S' and D states. The two protons' spins cancel in the dominant S state ($\sim$ 88.2%). Therefore there is less model dependence in the ^{3}He nuclear correction for the spin-dependent observables.

At large x, the advantage of using a polarized ^{3}He target is more clear in the case of the neutron spin asymmetry A_1^n. The neutron asymmetry in this region is much smaller than that of the proton, therefore the procedure of extracting A_1^n is more sensitive to the nuclear model being used.

Figure 3-1: The ^{3}He wavefunction.

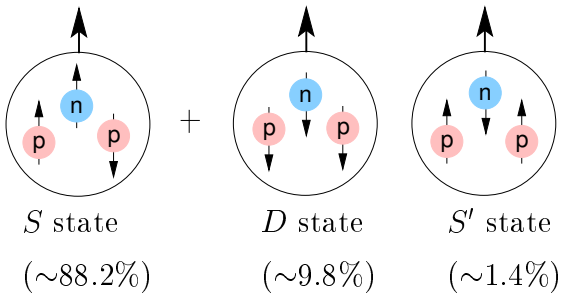

Table 3.1: Development of $^3\vec{\text{He}}$ target technology.

Lab/Exp	year	beam	I[μA]	ρ[cm^{-2}]	$\mathcal{L}$[s^{-1}cm^{-2}]	P_{targ}
MIT/Bates(I)	90	e^-	6	7.5×10^{20}	2.8×10^{34}	0.19
MIT/Bates(IIa)	90	e^-	11	1.1×10^{19}	7.6×10^{32}	0.30
TRIUMF	91	p	3.5×10^{-3}	20×10^{21}	4.4×10^{31}	0.60
SLAC(E142)	92	e^-	1.5	7×10^{21}	6.6×10^{34}	0.35
MIT/Bates(IIb)	93	e^-	25	3.3×10^{18}	5.1×10^{32}	0.38
IUCF	93	p	70	1.5×10^{14}	6.6×10^{28}	0.46
HERMES	95	e^+	20×10^3	3.3×10^{14}	4.1×10^{31}	0.46
NIKHEF	95	e^-	80×10^3	7×10^{14}	3.5×10^{32}	0.50
SLAC(E154)	95	e^-	1.5	8×10^{21}	7.5×10^{34}	0.38
MAMI	97	e^-	7	5×10^{20}	2.2×10^{32}	0.50
JLAB	98$\sim$	e^-	12$\sim$15	(8$\sim$10)$\times10^{21}$	6.7×10^{35}	0.35$\sim$0.45

In the large x region, the cross section is low because of the high Q^2. To achieve a good statistical precision, high luminosity is required. Table 3.1 shows a comparison in luminosity of all laboratories which have used a polarized ^{3}He target and are able

to perform a measurement of neutron asymmetry A_1^n. The polarized electron beam at JLAB, combined with the polarized ^{3}He target in Hall A, provides the highest polarized luminosity in the world. Hence it is the best place to measure the neutron spin structure in the large x region.

The experiment E99-117 [67] was carried out in Hall A at JLAB in the summer of 2001 to measure A_1^n at three kinematics at x =0.33, 0.47 and 0.60. In the following sections it will be referred to as "the A_1^n experiment". The kinematic coverage of this experiment is shown in Figure 3-2. The average values of x, Q^2 and W^2 of each kinematics are listed in Table 3.2. To measure A_1^n, the asymmetries $A_{||}$ and

Figure 3-2: Kinematic coverage of the A_1^n experiment - Q^2, W^2 and x_{Bj}.

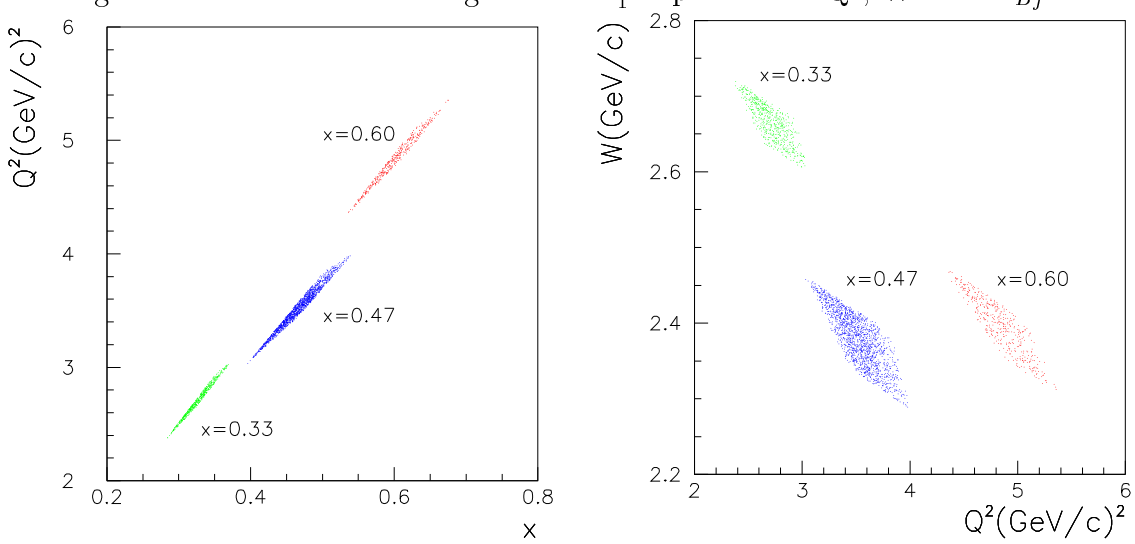

Table 3.2: Kinematics of the A_1^n experiment.

x_{Bj}	Q^2 (GeV/c)^2	W^2 (GeV)^2
0.327	2.709	6.462
0.466	3.516	4.908
0.601	4.833	4.090

$A_\perp$ of polarized e^- scattering off a polarized ^{3}He target have been measured. The polarized electron beam at JLAB was used at the highest available energy 5.7 GeV and the Hall A polarized ^{3}He target was used as an effective neutron target. The two standard Hall A High Resolution Spectrometers (HRS) were used to detect the scattered electrons.

3.2 The Accelerator and the Polarized Electron Source

JLAB operates a radio frequency (RF) electron accelerator that re-circulates the beam five times through two super-conducting linear accelerators (linac). This beam is sent to three experimental halls, named Hall A, B, and C. The primary mission of JLAB is to probe the nucleus of the atom to study the quark structure of matter. It was commissioned during the early 1990s and produced the first experimental beam in October of 1994.

The accelerator uses a state-of-the-art photocathode gun system that is capable of delivering continuous-wave (CW) beams of high polarization and high current to Hall A and Hall C while maintaining high polarization low current beam delivery to Hall B. The source of the injector is a strained GaAs cathode providing polarized beam of above 70% polarization and maximum current of ~200 μA. Polarized electrons from the source are first accelerated to 45 MeV, then are injected into the north linac. The north and south linacs are joined by two 180° arcs with a radius of 80 m, forming a

Figure 3-3: The Jefferson LAB accelerator.

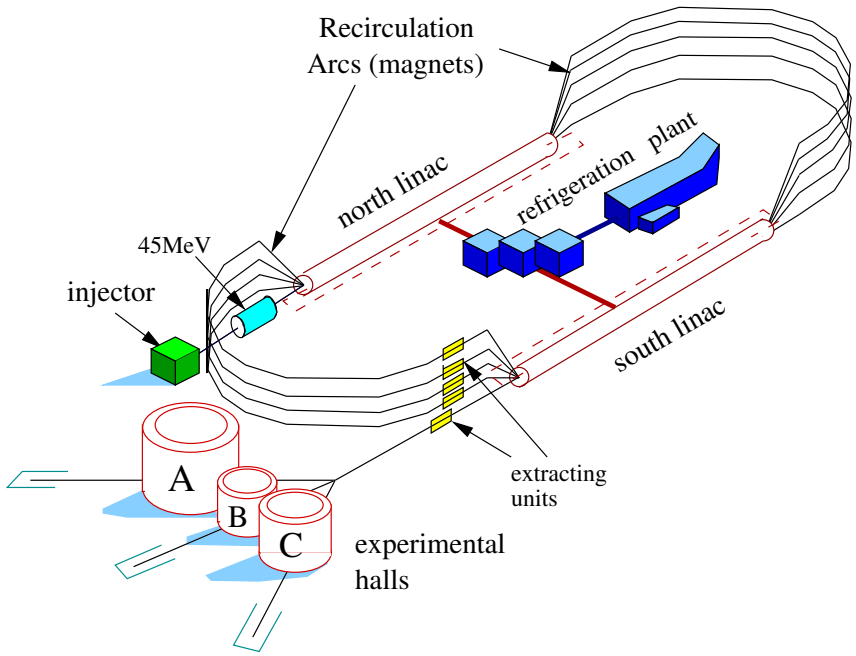

unique recirculating beamline that looks like a "racetrack", as shown in Figure 3-3. Twenty RF cryomodules, each containing eight super-conducting niobium cavities, comprise the two linacs. Liquid helium, produced at the Central Helium Liquefier (CHL), keeps the accelerating cavities super-conducting at a temperature of 2 K.

The linac energies are each set identically and the RF cavities are phased to provide maximum acceleration. Quadrupole and dipole magnets in each arc provide the field which focuses and steers the beam as it passes through each arc. More than 2,200 magnets are necessary to keep the beam on a precise path and tightly focused. The nominal gain of each linac was designed to be 400 MeV. However, this gain can be tuned up to about 500 MeV, if required by the experimental halls. This brings the maximum beam energy to about 5.7 GeV.

After passing through the south linac, the beam can either circle around the west recirculation arc for another pass around the accelerator, or be directed into a hall's transport channel using magnetic or RF extraction. For the first four passes the accelerator can provide beam at a particular energy to one hall only. The fifth pass can be sent to all three halls simultaneously. The beam received by each hall is made of bunches at a frequency of 499 MHz, with the bunch length being 1.7 ps.

The polarized electron source is a strained GaAs cathode evolved from the source used at the Stanford Linear Accelerator Center (SLAC) [68]. The cathode is created by growing layers of various GaAs combinations, as shown in Figure 3-4. The top layer is pure GaAs, then the layer below is made of $GaAs_{0.72}P_{0.28}$. The shorter lattice spacing of $GaAs_{0.72}P_{0.28}$ (5.5968 $\AA$) causes the natural spacing of the GaAs (5.6533 $\AA$) to shrink slightly, hence creates strain [69]. The strain induces a gap in the different sublevels of the $P_{3/2}$ electrons in the valence band of the GaAs. By tuning a left-handed circularly polarized laser (helicity -1, denoted as σ^-) to the proper frequency, electrons from the $P_{3/2}$ $m = 3/2$ state can be excited to the $S_{1/2}$ $m = 1/2$ level of the conduction band. From there the polarized electrons diffuse to the surface and escape into the surrounding vacuum. Because the strain creates a sufficiently wide

Figure 3-4: Structure of strained GaAs cathode and the level diagram of the conduction and valence bands.

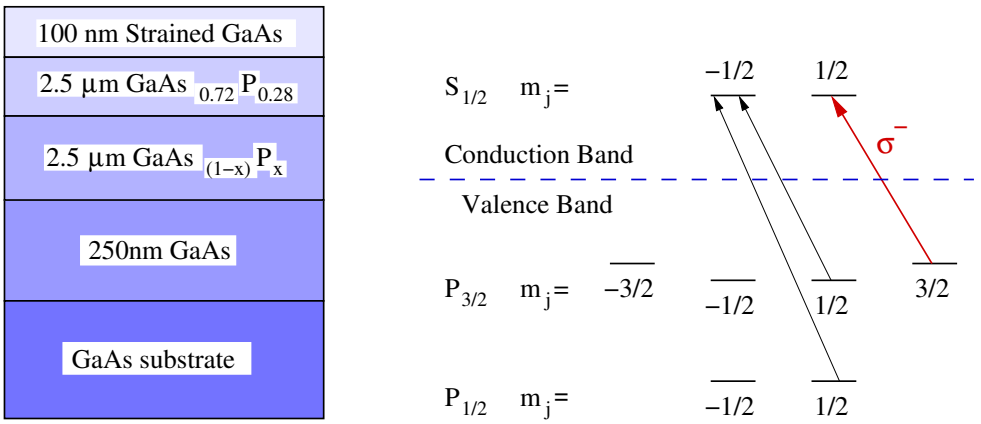

gap between the $P_{3/2}$ sublevels, the electrons from the $P_{3/2}$ $m = 1/2$ state will not be excited by the tuned laser. The consequence is that the electrons leaving the

surface of the cathode are all from the $S_{1/2}$ $m = 1/2$ state and hence are nearly 100% polarized.

3.3 Hall-A Overview

Among the three experimental halls at JLAB, Hall A is the biggest one with a diameter of 53 m. The basic layout of Hall A is shown in Figure 3-5. Figure 3-6 shows

Figure 3-5: Hall-A floor plan during the A_1^n experiment.

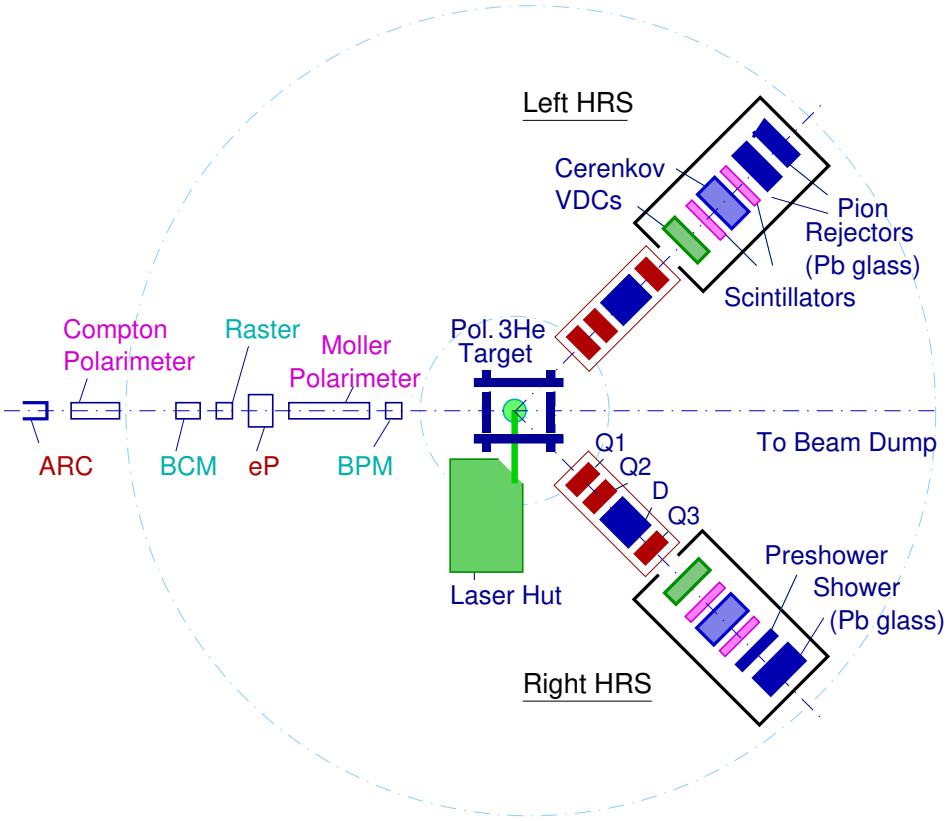

the two coordinate systems [86], the hall frame and the spectrometer frame, that are commonly used in Hall A. The major instrumentation includes beamline equipment, target, and two high resolution spectrometers (HRS).

Figure 3-6: Hall coordinate system (left): Z is the beam direction, Y is vertically pointing up; and the spectrometer coordinate system (right): Z is the HRS central ray direction, X is vertically pointing down and is called the dispersive direction, Y is called the transverse direction, ϕ (θ) is the in-plane (out-of-plane) scattering angle with respective to the HRS central ray direction.

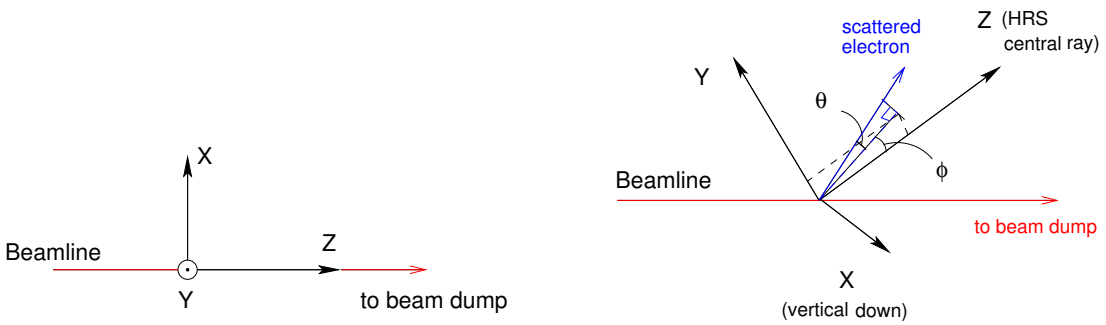

3.4 Beamline

The Hall-A beamline starts after the arc section (for beam energy measurement) and ends at the beam dump. The arc section can be used for beam energy measurement, as will be described in Section 3.5.1. The beamline consists of a Compton beam polarimeter, two Beam Current Monitors (BCM) between which located an Unser monitor (for absolute beam current measurement), a fast raster, the eP device for beam energy measurement, a Møller beam polarimeter, and a number of Beam Position Monitors (BPM). These beamline elements will be described in details in the following sections.

3.5 Beam Energy Measurement

The energy of the beam is measured absolutely by two independent methods [70], the Arc measurement based on beam deflection in a known magnetic field in the arc section of the beamline, and the eP measurement, based on elastic electron-proton scattering. Both methods can provide a precision of $\delta E_{beam}/E_{beam} \sim 2 \times 10^{-4}$.

3.5.1 Arc Measurement

The Arc measurement is based on the principle that an electron in a magnetic field moves in a circular pattern, the radius of which depends on the magnitude of the magnetic field and of the electron's momentum. The Arc method measures the deflection of the beam in the arc section of the beamline, which can be made when

the beam is tuned in either dispersive or non-dispersive mode in the arc section. A detailed description of the instrumentation for the Arc energy measurement can be found in [71]. The nominal bend angle of beam in the arc section is $\phi = 34.3°$, see Figure 3-7. The momentum of electrons (p in GeV/c) is then determined by the field

Figure 3-7: The arc section of the beamline.

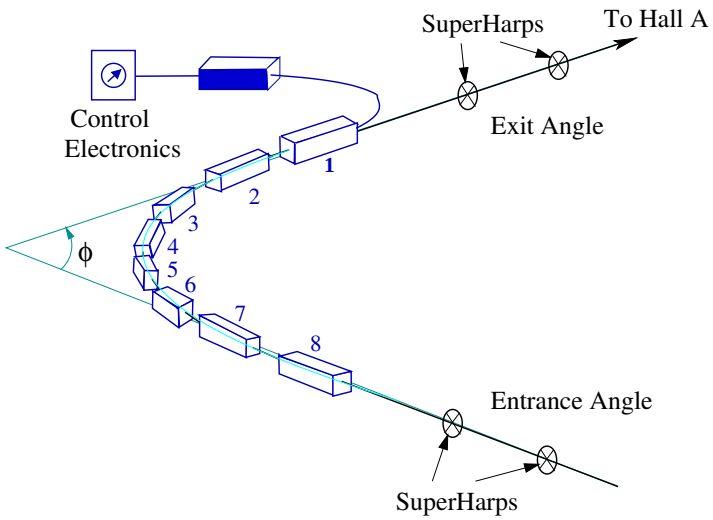

integral of the eight dipoles ($\int \vec{B} \cdot \mathrm{d}\vec{l}$ in T·m), and the net bend angle through the arc section (θ in radians) by

$$p = c\frac{\int \vec{B} \times \mathrm{d}\vec{l}}{\theta} \quad \text{or} \quad c\frac{\int B_{\perp} \cdot \mathrm{d}l}{\theta_{||}}, \tag{3.1}$$

where $c = 0.299792$ GeV· rad/Tm is speed of light, $B_{\perp}$ is the magnetic field component perpendicular to the electron motion, dl is the path length of the electron, and $\theta_{||}$ is the angle by which the electron is deflected. The integral on the right hand side of Eq. (3.1) is called the Bdl value of the arc section. The dispersive (invasive) mode provides better precision ($\delta E_{beam}/E_{beam} \sim 2 \times 10^{-4}$) than non-dispersive (non-invasive) mode ($\delta E_{beam}/E_{beam} \sim 5 \times 10^{-4}$).

The Arc method consists of two simultaneous measurements. One is for the magnetic field integral Bdl of the bending elements (eight dipoles in the arc) based on a reference magnet (9^{th} dipole) measurement. The other measurement is for actual bend angle of the arc, based on superharps (a set of wire scanners). The superharp is moved across the beam path. When the beam strikes a wire, the particles scattering off the wire are collected by a simple ion chamber, hence a current is generated and the beam's position is recorded [72].

3.5.2 eP Measurement

The instrumentation for the eP energy measurement is a stand-alone device along the beamline located 23 m upstream of the target. In the eP method the beam energy is determined by the measurement of the scattered electron angle θ_e and the recoil proton angle θ_p in the H$(e, e'p)$ elastic reaction according to the kinematic formula

$$E = M_p \frac{\cos(\theta_e) + \sin(\theta_e)/\tan(\theta_p) - 1}{1 - \cos(\theta_p)} + O(m_e^2/E'^2) \ . \tag{3.2}$$

A three-dimensional schematic diagram of the eP system [72] is shown in Figure 3-

Figure 3-8: Layout of eP device

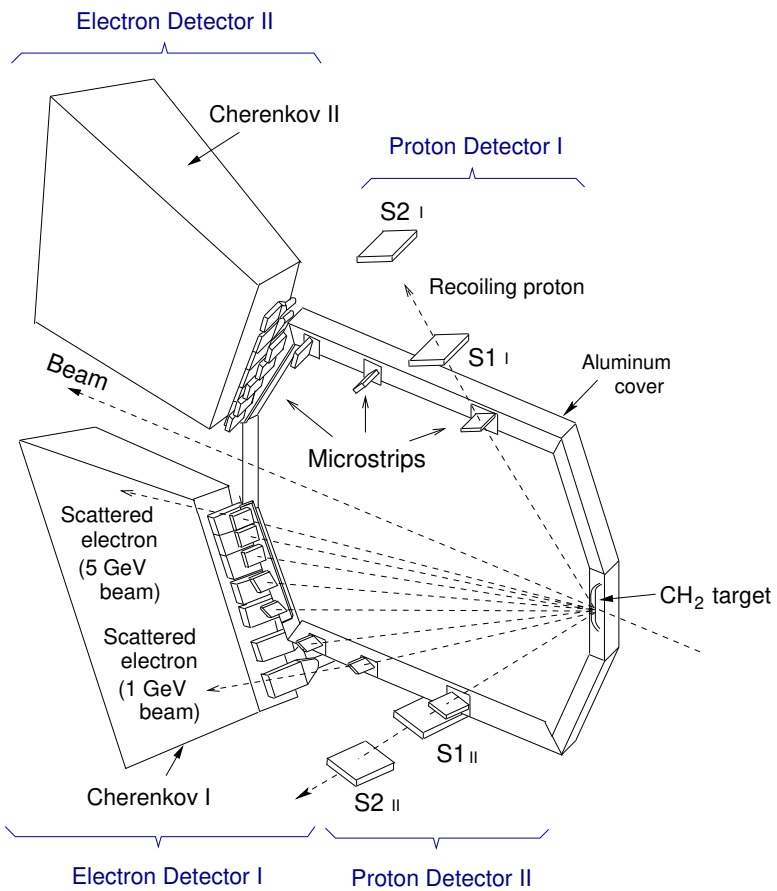

8. A detailed description of the instrumentation for the eP energy measurement can be found in [73]. The target is a CH_2 film enclosed by an aluminum cover. Two identical arms, each consisting of an electron and a proton detector system, are

placed symmetrically with respect to the beam direction along the vertical plane. Each proton detector system is made up of a set of two silicon micro-strip detectors (SSD), called the front and the back SSD. The active area of one SSD for the proton detector is 51.2×25.6 mm^2. Each electron detector system is made up of a set of 7×2 SSD in the reaction plane. The active area of one SSD for the electron detector is 12.8×12.8 mm^2. The trajectories of the scattered electrons and the recoiled protons depend on the beam energy, as well as the position and the direction of the beam. Making simultaneous measurements of the beam energy with both arms cancels to the first order any uncertainty arising from the knowledge of the beam position and direction.

Repeated measurements of the beam energy with both eP and Arc methods show good agreement with each other within their respective uncertainties (discrepancy $\leqslant 3 \times 10^{-4}$) except at around 3 GeV. The discrepancy at 3 GeV originates from the systematic effect related to the position of the silicon micro-strip detector in the eP apparatus corresponding to a beam energy of 3 GeV [72][74].

3.5.3 Beam Energy During the A_1^n Experiment

Table 3.3 shows the result of beam energy measurements during the A_1^n experiment [75].

Table 3.3: Beam energy measurement for the A_1^n experiment, all energies are given in MeV.

Date	Arc	eP	Tiefenbach†	Set Energy‡
06/04/01		1196.84±0.68	1196.52	1197.33
06/06/01		5729.35±1.72	5727.61	5738.42
07/13/01	5727.4±3.3		5726.68	5738.42

† The "Tiefenbach" energy uses the current values of Hall A arc Bdl value and Hall A arc beam position monitors (BPMs) to calculate the beam energy. This number is continuously recorded in the data stream and is calibrated against the Arc energy of the 9th dipole regularly.
‡ The set energy is the beam energy the accelerator is setup to run. This number is based on the field maps of the recirculation magnets and the Hall's energy measurement results.

Two beam energies have been used: 1.2 GeV for commissioning and 5.7 GeV for DIS. For DIS analysis, we will use the weighted average of Arc and eP measurements: $E_b = 5728.94 \pm 1.52$ MeV.

3.6 Beam Polarization Measurement

There are three methods to measure the electron beam polarization: (1) Mott method; (2) Møller polarimetry; and (3) Compton polarimetry. The Mott measurement is performed at the polarized electron source, the other two polarimetries belong to Hall A instrumention and will be discussed in this section.

3.6.1 Møller Polarimetry

The Møller polarimeter [76] measures the process of Møller scattering of the polarized beam electrons off polarized atomic electrons in a magnetized foil $\vec{e^-} + \vec{e^-} \rightarrow e^- + e^-$. Its cross section depends on the beam and target polarizations P_b and P_t as

$$\sigma \propto \left(1 + \sum_{i=X,Y,Z} (A_{ii} P_{b,i} P_{t,i})\right) ,$$

where $i = X, Y, Z$ defines the projections of the polarizations. The analyzing power A_{ii} depends on the scattering angle in the center of mass (CM) frame θ_{CM}. Assuming that the beam direction is along the Z-axis and that the scattering happens in the ZX plane

$$\begin{aligned} A_{ZZ} &= -\frac{\sin^2\theta_{CM} \cdot (7 + \cos^2\theta_{CM})}{(3 + \cos^2\theta_{CM})^2} \quad \text{and} \\ A_{XX} &= -A_{YY} = -\frac{\sin^4\theta_{CM}}{(3 + \cos^2\theta_{CM})^2} \, . \end{aligned} \tag{3.3}$$

At $\theta_{CM} = 90^\circ$ the analyzing power has its maximum $A_{ZZ,max} = 7/9$. A beam polarization transverse to the scattering plane also leads to an asymmetry, though the analyzing power is lower: $A_{XX,max} = A_{ZZ,max}/7$. The main purpose of the polarimeter is to measure the longitudinal component of the beam polarization.

The polarized electron target used by the Møller polarimeter is a ferromagnetic foil. The target polarization can be adjusted to any direction with respect to the beamline. The beam polarization may have a horizontal transverse component, which would couple to the horizontal transverse component of the target polarization. The way to cancel the influence of the transverse component is to take an average of the asymmetries measured at two complimentary target angles, for example 20° and 160°. The target polarization is derived from the foil magnetization measurements. For the supermendur foil used in 1998-2000 a polarization of $7.95 \pm 0.24\%$ was obtained [77].

The Møller scattering events are detected with the help of a magnetic spectrometer, as shown in Figure 3-9. The spectrometer consists of a sequence of three quadrupole magnets and a dipole magnet. The detector consists of scintillators and lead-glass calorimeter modules, split into two arms in order to detect the two scattered electrons in coincidence.

Figure 3-9: Layout of the Møller polarimeter

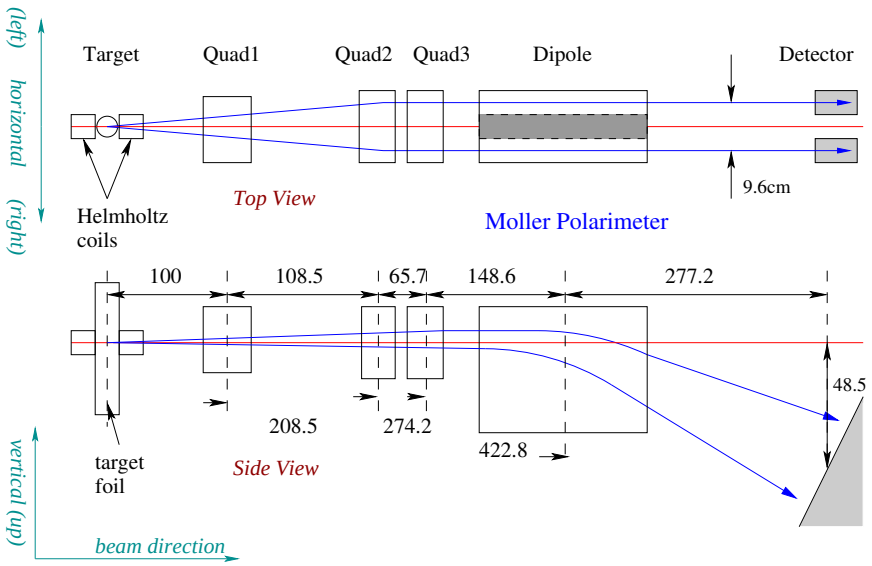

The Møller polarimeter can be used at beam energies from 0.8 to 6 GeV. It has to use a low beam current (~0.5 μA) and is invasive. One measurement typically takes an hour, providing a statistical accuracy of about 0.2%. The systematic error in Møller polarimetry mainly comes from the ferromagnetic foil target polarization. An extra systematic error is due to the fact that the beam current used during a Møller measurement is lower than that used during the real experiment. The total relative systematic error is about 3.4% [77].

3.6.2 Compton Polarimetry

The Compton polarimeter [78] measures the process of Compton scattering. It was designed to measure the beam polarization concurrently with experiments running in the hall. The polarization is extracted from the measurement of the counting rate asymmetry for opposite beam helicities in the scattering of a circularly polarized photon beam off the electron beam. The Compton polarimeter is located at the entrance to the hall. It consists of a magnetic chicane (to deviate the electron beam from the scattered photons), a photon source (not shown in the figure), an electromagnetic calorimeter (photon detector), and an electron detector, as shown in Figure 3-10. The photon source is a 200 mW laser amplified by a resonant Fabry-Perot cavity. The maximum gain of the cavity is determined by the reflectivity R and the transmittivity T of the two ultra-reflecting mirrors used for the cavity. Currently [79] the mirrors are made of several layers of SiO_2, Ta_2O_5 and Si, which have $R = 99.988\%$

Figure 3-10: Layout of the Compton polarimetry.

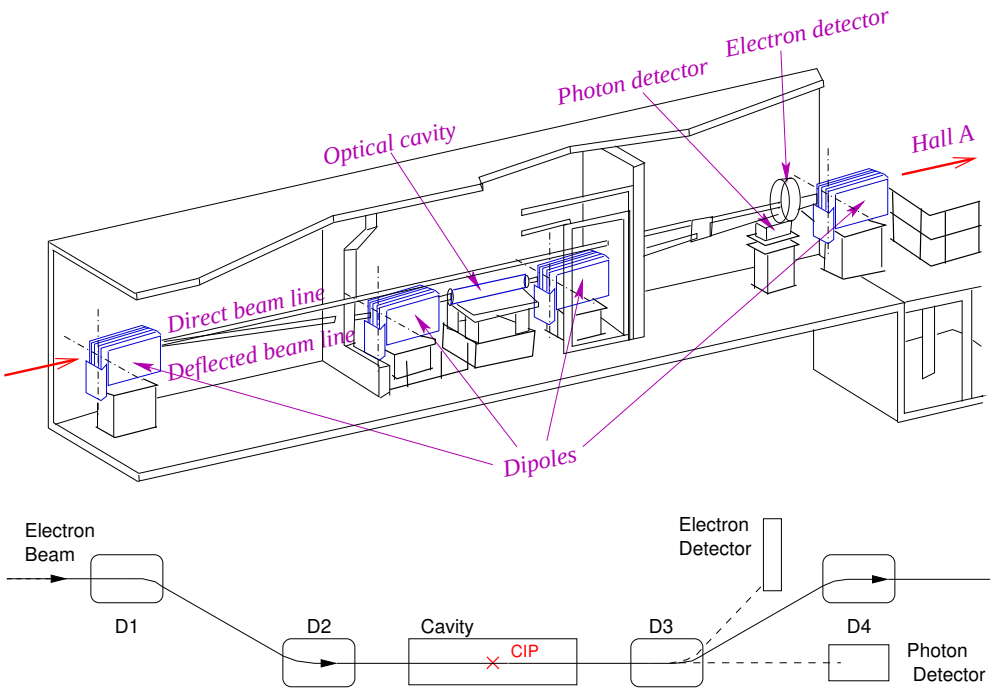

and $T = 95$ ppm. This gives a maximum gain of $G_{max} = T/(1-R)^2 = 7500$. So for an infra-red (IR) photon source of 200 mW, the laser power inside the cavity can reach a power of 1500 W at the Compton Interaction Point (CIP). The circular polarization of the laser beam is $> 99\%$ for each of the right and left photon helicity states. The electron beam is deflected vertically by the four dipoles of the chicane and crosses the photon beam at the CIP. After interaction, the back-scattered photons are detected in the calorimeter and the electrons in the silicon strip electron detector. Electrons that did not interact exit the polarimeter and reach the target in the hall. The asymmetry measured in Compton scattering can vary within a wide range for different beam characteristics. For example, it reaches $\sim 75\%$ for SLAC but only $\sim 1.5\%$ at JLab for a beam energy of 4 GeV (with a 1.165 eV photon beam) [79]. This low asymmetry makes Compton polarimetry measurements at JLab challenging.

The time required to reach a certain statistical error also depends on the beam current, which is determined by the running experiment. During the A_1^n experiment, for a 12 μA beam at 5.7 GeV, one hour was needed to reach a relative statistical accuracy of $(\Delta P_b)_{stat}/P_b \sim 1\%$ [79]. The systematic error on the Compton measurement comes mostly from its low analyzing power. The total systematic error is about $(\Delta P_b)_{sys}/P_b = 1.6\%$ [80].

3.6.3 Beam Polarization Measurements during A_1^n Experiment

During the A_1^n experiment, Møller measurements were performed regularly and the Compton polarimetry was running continuously to monitor the beam polarization. Table 3.4 and 3.5 show the results from Møller [81] and Mott polarimetries [82],

Table 3.4: Møller beam polarization measurements during the A_1^n experiment.

Date	Beam Energy	Beam $\lambda/2$ Plate	Møller Result $\pm$ stat. $\pm$ sys.(%)
06/07/01	1.197 GeV	IN	82.4±0.30±2.4
06/09/01	5.738 GeV	IN	82.9±0.20±2.4
06/14/01	5.731 GeV	OUT	-80.7±0.15±2.4
			-82.3±0.15±2.4
06/18/01	5.731 GeV	IN	82.4±0.15±2.4
07/13/01	5.731 GeV	OUT	-83.0±0.17±2.4
07/29/01	5.731 GeV	IN	82.0±0.15±2.4

Table 3.5: Mott beam polarization measurements during the A_1^n experiment.

Date	Beam Energy	Beam $\lambda/2$ Plate	Mott Result $\pm$ tot.(%)
06/03/01	1.197 GeV	OUT	74.7±2.0
06/11/01	5.738 GeV	IN	-79.1±2.0

respectively. Also listed is the status of the beam half-wave plate which is related to the absolute sign of electron helicity, as will be described in Section 3.6.4.

Figure 3-11 shows results from the Compton continuous monitoring [80]. The beam polarization for DIS measurements is determined from the weighted average of the Compton and Møller results: $P_b = 79.73 \pm 2.4$ %.

Figure 3-11: Beam polarization during the A_1^n experiment.

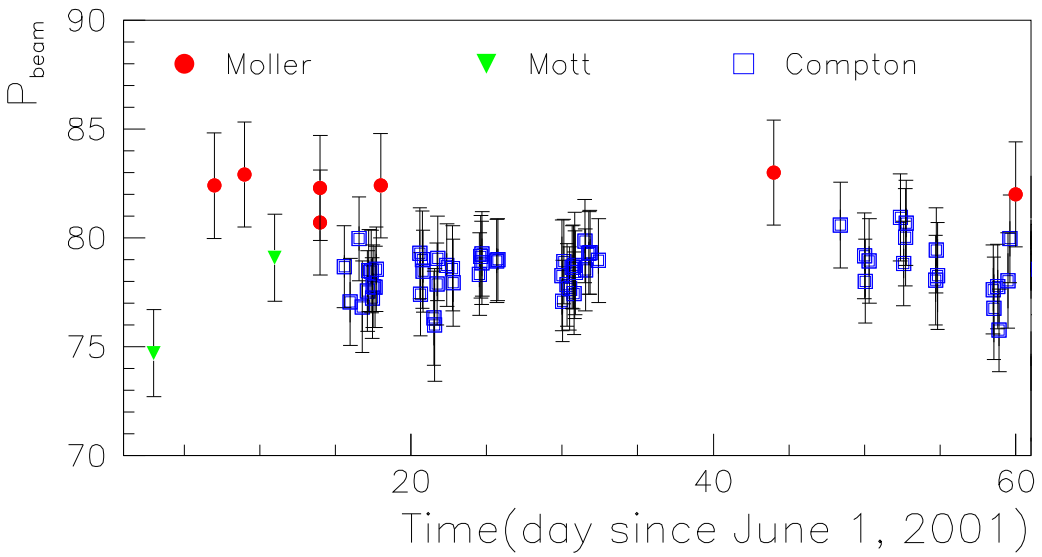

3.6.4 Beam Helicity

Knowing the helicity state of the beam pulse is crucial to any asymmetry experiments. For the A_1^n experiment this was achieved by the Hall A helicity electronics. The helicity circuitry in Hall A uses a helicity '+' signal from Machine Control Center (MCC) as input, generates its complementary (negative) signal and sends both signals down to the two HRS detector stacks. Circuitry in each arm then generates a shortened pulse for each helicity, chops off the leading edge to allow the helicity to stabilize, and sends these stabilized pulses to the detector Data Acquisition (DAQ) System. The data from the detector DAQ and scalers are all gated by these helicity signals. There is a variable *helicity* assigned to all events in the detector data stream, events gated by H+ pulses have $helicity = +1$ and those gated by H− pulses have $helicity = -1$. However they are not necessarily the real helicity state of the electron beam, as will be described later

The helicity signal from MCC has a pulse width of 33 ms. There are two modes – toggle and pseudorandom – which can be used for the pulse sequence. In the toggle mode, the helicity pulse lengths are fixed and the helicity alternates every 33 ms. The signal frequency is therefore 30 Hz for both H+ and H−. In the pseudorandom mode, the helicity alternates with a random probability for each 33 ms. This means one may get two successive pulses of the same helicity, generating a single double length pulse. The net effect of pseudorandom mode is to reduce the frequency by 25%, so the scaler measures 25 Hz for H+ and 25 Hz for H−.

For each helicity signal generated by the HRS circuitry, the leading edge of H+ (H−) is a delayed one of the leading edge of H+ (its complement) from MCC. The

Figure 3-12: Helicity signals in toggle (left) and pseudorandom (right) modes. The four signals are: H+ from MCC, H+ and H− generated by the HRS helicity circuitry, and the DAQ helicity state.

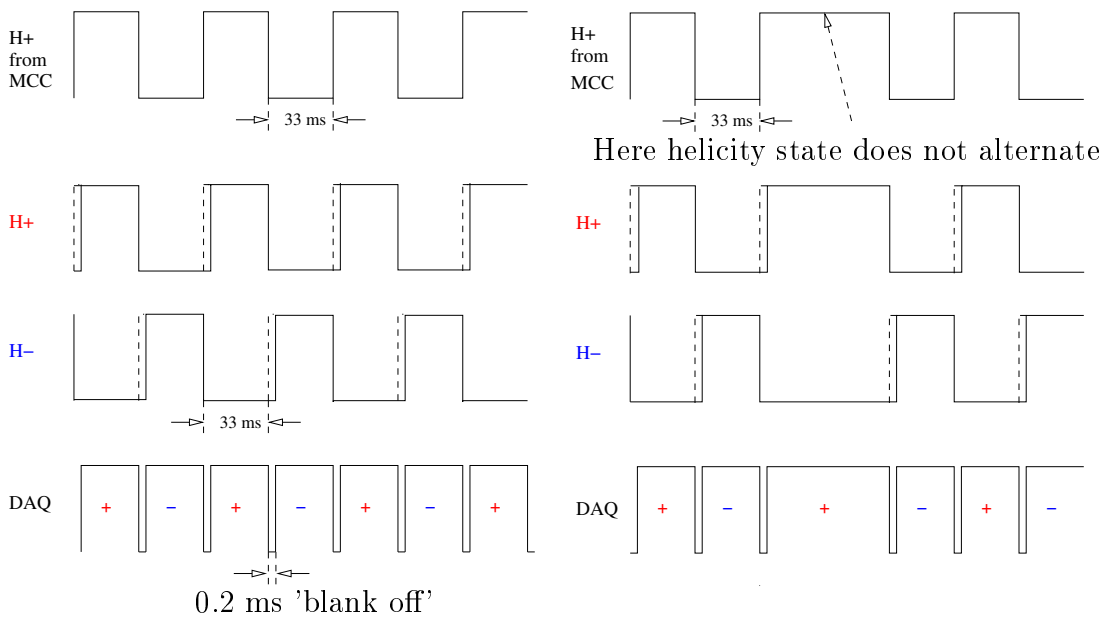

delayed time for each pulse, so called 'blank off' time, is usually 0.2 ms during which the helicity state of DAQ is defined as 'undetermined'. Then the H+ (H−) signal is cleared by the leading edge of the next pulse in the opposite signal H− (H+). Therefore only one of the signals H+ or H− is valid during each 33 ms.

Figure 3-12 shows the helicity H+ signal from MCC, the two shortened (to allow helicity stabilization) signals H+ and H− generated by the HRS helicity circuitry, and the helicity states of the DAQ system.

If the helicity circuitry were ideal, then one would expect the time asymmetry between opposite helicity states to vanish. If the beam current is stable compared to the time scale of the helicity pulses, charge asymmetry vanishes. During the A_1^n experiment, there was a period during which this was not true. The H+ signal on the left HRS was not always cleared by the H− pulse and for every one second, there was about 1.5 ms during which both helicity signals were valid. This caused some *helicity* = +2 events in the data stream and a 1500 ppm charge asymmetry on the left HRS DAQ. Fortunately this can be mostly corrected by the BCM readings and the remaining second order effect is small compared to the statistical error (1300 $\sim$ 2200 ppm) of the measured raw asymmetries. It did not affect the data quality.

As mentioned at the beginning of this section, the variable *helicity* in the detector data stream does not necessarily equal to the real helicity state of the electron beam.

The absolute sign of the electron helicity state can be determined by measuring a well known asymmetry and comparing the measured asymmetry to its prediction. For the A_1^n experiment this was achieved by measuring the parallel asymmetry of $\vec{e}^{\leftarrow} - {}^3\vec{\mathrm{He}}$ elastic scattering; see Section 5.4.

3.7 Beam Charge Measurement

The beam current is measured by the Beam Current Monitor (BCM) in Hall A, which provides a stable, low-noise, non-intercepting measurement [77]. It consists of an Unser monitor and two RF cavities, which are located 25 m upstream of the target. The BCM system is described in details in the Hall A Operations Manual [83]. The Unser monitor is a parametric current transformer which provides an absolute but non-continuous reference. The two resonant RF cavity monitors on both sides of the Unser Monitor are stainless steel cylindrical high Q (~ 3000) waveguides which are tuned to the frequency of the beam (1.497 GHz) resulting in voltage levels at their outputs which are proportional to the beam current. Each of the RF output signals from the two cavities is split into two parts - sampled and integrated data.

The sampled data are processed by a high-precision digital AC voltmeter HP 3458A (Digital Multi-Meter, or DMM), which provides an output representing the RMS value of the input signal once every second. Signals are transported through GPIB [84] cables and are recorded by the data logging process. The integrated data are sent to

Figure 3-13: Schematic of beam current monitors.

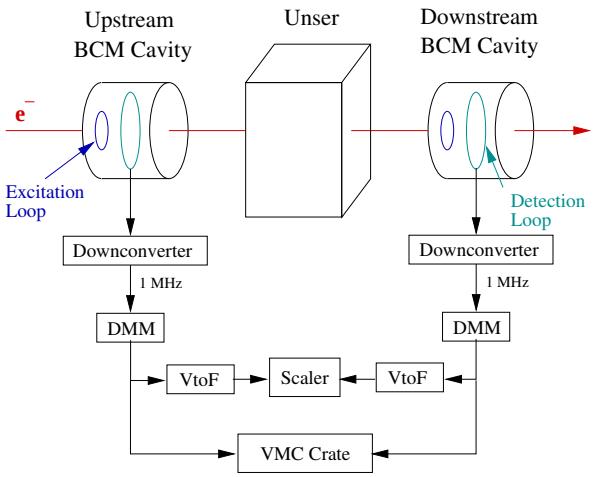

an RMS-to-DC converter and a voltage-to-frequency converter. The output frequency is fed to VME scalers and then injected into the data stream. The scalers accumulate during the run and each gives a number proportional to the time-integrated voltage level and therefore accurately record the integral of the current, i.e., the total beam

charge. The regular RMS to DC output is linear for currents from 5 μA to above 200 μA. A set of amplifiers has been introduced with gain factors of 1, 3 and 10, to extend the linear region to lower currents at the expense of saturating at high currents. Hence there is a set of three signals coming from each BCM. These six signals are fed to scaler inputs of each spectrometer and provide redundant beam charge information for each run.

The beam charge can be derived from BCM scaler reading as

$$Q_{\mathrm{BCM}\times A,H}(\mu C) \;=\; \frac{\frac{N_{\mathrm{BCM}\times A,H}}{\mathrm{clock}_H} - \mathrm{offset}_{\times A,H}}{\mathrm{constant}_{\times A}}\mathrm{clock}_H \;, \tag{3.4}$$

where A=1, 3, 10 is the gain factor of the amplifiers, H=plus, minus, ungated is the beam helicity state, clock_H is the helicity gated clock time for each run (in seconds), $N_{\mathrm{BCM}\times A,H}$ is the helicity gated BCM scaler reading for each gain factor. The offset_H and normalization factors $\mathrm{constant}_{\times A}$ are regularly calibrated from calibration runs. The latest calibration before the A_1^n experiment gave [85]:

Table 3.6: Calibration for BCM's, January 12th, 2001.

upstream				
Ampl.	offsets			constant
	ungated	plus	minus	
1	92.072596	92.21067	92.069586	1345
3	167.05738	167.0949	166.95239	4114
10	102.62361	102.62498	102.46542	12515
downstream				
Ampl.	offsets			constant
	ungated	plus	minus	
1	72.190291	72.309803	72.176298	1303
3	91.080796	91.145465	90.984981	4034
10	199.50698	199.57484	199.34949	12728

3.8 Beam Charge Asymmetry Feedback

The beam charge measured in Hall A is gated by helicity signals and is used to extract raw asymmetries from data, see Eq. (5.29) in Section 5.4.8. The helicity H+ and H− gated beam charge Q^+ and Q^- can be different. This difference is usually

characterized by the beam charge asymmetry, defined as

$$A_Q = \frac{Q^+ - Q^-}{Q^+ + Q^-} . \tag{3.5}$$

$Q^+(Q^-)$ can be written as $Q^+ = I^+t^+$ ($Q^- = I^-t^-$), where $I^+(I^-)$ is the beam intensity, i.e., the beam current, during H+(H−) pulses and $t^+(t^-)$ is the time interval of H+(H−) pulses. There are two sources for beam charge asymmetry. The first one is the time asymmetry of helicity signals, i.e. $t^+ \neq t^-$, caused by the imperfection of the helicity circuitry. The second source is the beam intensity asymmetry, $I^+ \neq I^-$, originated from the polarized electron source. In this section we discuss the beam intensity asymmetry from the polarized electron source, its effect on the measured asymmetries and how to minimize it using charge asymmetry feedback.

3.8.1 Beam Charge Asymmetry

The beam intensity asymmetry at the polarized electron source is due to the fact that the intensity of the circularly polarized laser used to strike the photocathode has an asymmetry between different helicity states. When extracting cross section asymmetries, raw data for different helicity states are normalized by helicity-dependent beam charges, see Eq. (5.29) in Section 5.4.8. After this correction, the helicity-dependent beam intensity asymmetry does not affect the measured physics asymmetries to first order. However, there exist second order effects and the beam intensity asymmetry needs to be minimized because of the following reasons:

- A beam intensity asymmetry at the polarized electron source induces differences in other beam parameters. For example the accelerator turns intensity differences into energy differences through beam loading. In turn, energy differences become beam position drifts due to achromatic transport through the machine.
- Nonlinearity of the BCM system introduces a systematic error in the asymmetry measurement which is proportional to the beam intensity difference.

3.8.2 PITA Effect

The intensity asymmetry in the electron beam that originates from the intensity differences of the circularly polarized laser beam striking the photocathode can be minimized by using the Polarization-Induced Transport Asymmetry (PITA) effect [87].

Consider an optical transport system as shown in Figure 3-14. The laser light is first polarized by a linear polarizer, then the linearly polarized light passes a quarter-wave ($\lambda/4$) plate and becomes circularly polarized. The imperfection of the $\lambda/4$ plate is denoted by a symmetric offset α and an antisymmetric offset Δ, i.e., the retardations for opposite helicities are given by $\theta_\pm = \pm(\pi/2 + \alpha \pm \Delta)$. Next an asymmetric transport system is placed after the $\lambda/4$ plate, with its axis at an angle

θ with respect to the axis of the $\lambda/4$ plate, and a transmission asymmetry given by $\epsilon = \frac{T_x - T_y}{T_x + T_y}$, with T_x (T_y) the transmission coefficient along axis $x(y)$. The asymmetric transport element is also referred to as the analyzer with its transmission asymmetry ϵ giving the analyzing power of the system. The intensity asymmetry, A_{PITA}, of the outgoing light is given to a good approximation by

$$A_{PITA}(\Delta) = \frac{I_+ - I_-}{I_+ + I_-} = 2\epsilon(\Delta - \Delta_0)\sin(2\theta) \ , \tag{3.6}$$

where $I_+(I_-)$ is the intensity of the positive (negative) helicity light that passes through the transport system. Δ_0 is a phase that is caused by any imperfection in various optical components.

In practice, the imperfect $\lambda/4$ plate might be a rotatable birefringent crystal or, a Pockel cell [1]. A Pockel cell is a voltage-controlled retardation plate. The phase Δ, which has the same value for both helicity states, can be adjusted in both cases. For a rotatable birefringent crystal, it can be adjusted by changing the orientation of the crystal. For the case of a Pockel cell, it can be adjusted electro-optically through control of the voltage applied to the cell. Therefore, the helicity correlated intensity asymmetry of the transported light can be controlled by manipulating Δ.

3.8.3 Parity DAQ and Charge Asymmetry Feedback

The laser used to generate photoelectrons at the source is circularly polarized. Laser light first passes a linear polarizer, then is circularly polarized using a Pockel cell, see Figure 3-15. The Pockel cell is pulsed at its positive and negative quarter-wave retardation voltages $\pm V_{\lambda/4}$ so the laser light is either left-handed (helicity minus) or right-handed (helicity plus) circularly polarized. A rotatable half-wave plate is inserted downstream of the Pockel cell, after which the laser light passes a vacuum window and strikes the photocathode. Any imperfection of the optical elements between the linear polarizer and the photocathode can introduce an asymmetric transport effect, which can be controlled either by changing the Pockel cell voltage or by rotating the half-wave plate. The photocathode itself has a sizable transmission asymmetry and is used as an analyzer. However before the strained photocathode was installed in 1998, an additional microscope slide was inserted in front of the vacuum window to increase the analyzing power [88].

The parity DAQ measures the charge asymmetry in Hall A. Assuming the helicity signal of the parity DAQ is perfect, i.e., the time asymmetry is zero, then the beam intensity asymmetry is directly measured.

To control the beam intensity asymmetry, a charge asymmetry feedback system is used between the electron source and Hall A [88]. Either the Pockel cell voltage or

[1] Also written as "Pockel's cell" or "Pockels cell" in some references.

Figure 3-14: The PITA effect.

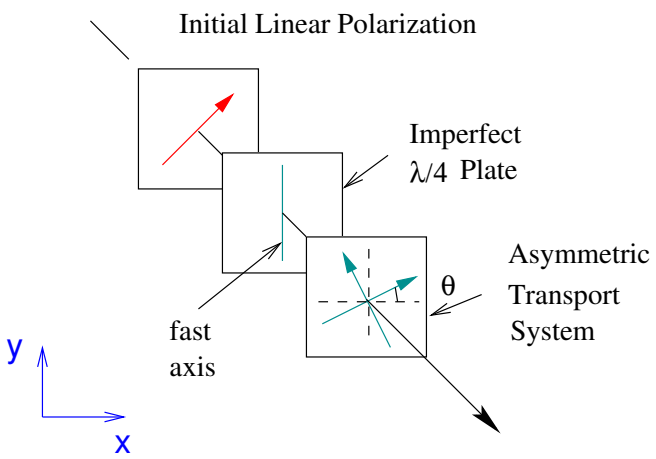

Figure 3-15: Beam charge asymmetry feedback system.

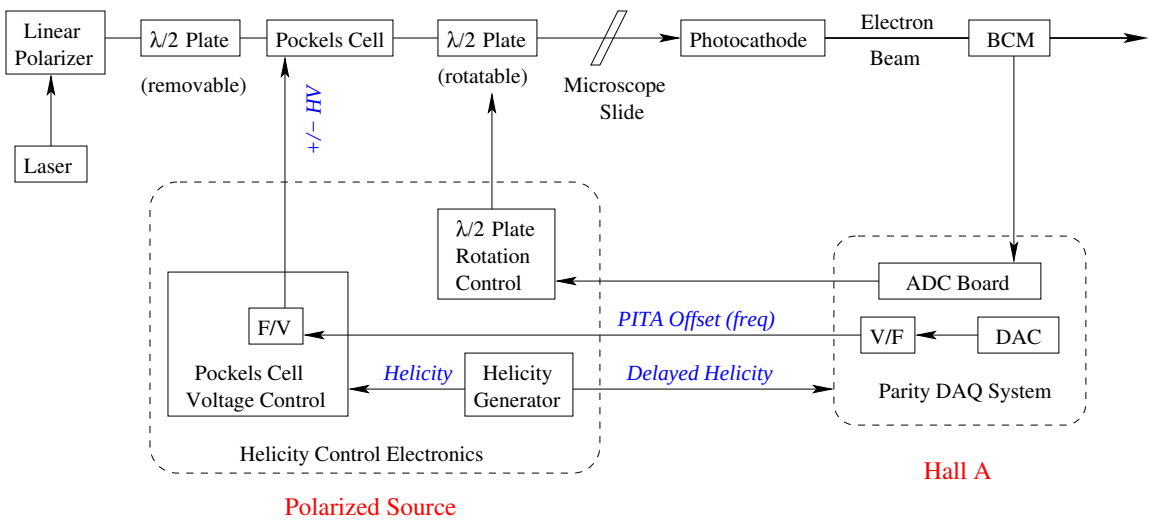

the half-wave plate orientation can be controlled by signals generated by the parity DAQ. Let A_I be the intensity asymmetry of the electron beam measured in Hall A

$$A_I = \frac{I^+ - I^-}{I^+ + I^-} , \tag{3.7}$$

$A_{p.c.}$ and $A_{\lambda/2}$ be the contribution to A_I due to the Pockel cell and the rotatable half-wave plate, and A_0 denotes the contribution from all other sources (for example the vacuum window before photocathode), then

$$A_I = A_0 + A_{PITA} = A_0 + A_{p.c.} + A_{\lambda/2} . \tag{3.8}$$

When the Pockel cell is used to control charge asymmetry, the control electronics gives the Pockel cell voltages $V_\pm = \pm V_{\lambda/4} + V_\Delta$, with $V_{\lambda/4}$ the quarter-wave retardation voltage. The size of the offset V_Δ is given by the *PITA Offset* signal generated by the parity DAQ system. The asymmetry is therefore given by $A_{p.c.} = mV_\Delta$ with m the Pockel cell's PITA slope in unit of ppm/V. In the case where the rotatable half-wave plate is used to control the charge asymmetry, the asymmetry $A_{\lambda/2}$ is given by the sinusoidal function

$$A_{\lambda/2} = 2\epsilon[\Delta \sin(4\psi - 2\theta) + \gamma \sin(2\psi - 2\theta)] , \tag{3.9}$$

where ψ is the orientation of the half-wave plate, γ is the difference between its retardation and π, ϵ and Δ are the analyzing power and the anti-symmetric part of the retardation of the photocathode, θ is the angle between the Pockel cell's fast axis and the photocathode's fast axis.

The feedback system using the Pockel cell voltage control can keep the beam intensity asymmetry to the level of a few ppm. However, this was not necessary for the A_1^n experiment since the measured electron asymmetries were much larger. Using the half-wave plate alone can keep the beam intensity asymmetry below 200 ppm, which was sufficient for the A_1^n experiment. During the run, only the rotatable half-wave plate was used. The measured A_I from the parity DAQ was used to adjust the half-wave plate rotation. The orientation of half-wave plate, ψ, was controlled by the parity DAQ at a PITA slope of $\eta = 17$ ppm/step [89]. The parity DAQ was synchronized with the left and the right HRS DAQs so that the beam intensity asymmetry was monitored for each run.

However, there is a short point of using parity DAQ and charge asymmetry feedback to control the beam charge asymmetry. The intensity asymmetry measured by the parity DAQ is the average value over one run, which usually last one hour. At a beam energy of 5.7 GeV, the beam was not stable and tripped typically every 2 minutes. To smooth the heat impact on the target, beam was ramped at a slope of 0.1 μA/s after each trip. It has been found that the intensity asymmetry during beam trips and rampings was large and cannot be controlled by charge asymmetry

feedback. To make sure that the data are not affected by this short-term intensity asymmetry, data during beam trips and rampings are not used for the analysis. For details, see Section 5.6.1.

3.8.4 Beam Half-wave Plate and Beam Helicity

There is a removable half-wave plate between the linear polarizer and the Pockel cell. It is also called the "beam half-wave plate". When the beam half-wave plate is inserted, the helicity of the electron beam is the opposite to the case when it is not inserted. The beam half-wave plate provides a powerful way to check for a false asymmetry, since the physics asymmetries measured with and without this half-wave plate should have the opposite sign. During the A_1^n experiment this half-wave plate was inserted for half of the statistics for each kinematics and the measured asymmetries were combined together to cancel possible systematic effects coming from the beam intensity differences at the polarized source.

3.9 Raster and Beam Position Monitor

The beam was rastered on the target with an amplitude of several millimeters to prevent damaging the target (overheating). The raster is a pair of horizontal (X) and vertical (Y) air-core dipoles located 24 m upstream of the target. The raster has been used in two different modes, sinusoidal and amplitude modulated. In the sinusoidal mode both the X and Y magnet pairs are driven by pure sine waves with relative 90° phase, and frequencies which do not produce a closed Lissajous pattern. In the amplitude modulated mode both the X and Y magnets are driven at 18 kHz with a 90° phase between X and Y, producing a circular pattern. The radius of this pattern is changed by amplitude modulation at 1 kHz. This radius modulation is controlled by a function generator in order to create a uniform distribution of the area swept out by the beam motion. Switching between the two modes of operation requires hardware changes. The control software for the raster assumes a field-free region between the raster and the target, so it is only approximately correct because there are four quadrupoles in this region.

A circular raster was used for the A_1^n experiment. The radius of the beam spot was 2 mm. To determine the position and the direction of the beam at the target position, two Beam Position Monitors (BPM), called BPMA and BPMB, are used. They are located 7.516 m and 2.378 m upstream of the target, respectively. The relative position of the beam can be determined to within 100 μm for a beam current above 1 μA. The absolute position of the beam can be determined from the BPM's by calibrating them with respect to wire scanners (also called superharps) which are located adjacent to each BPM (at 7.345 m and at 2.214 m upstream of the target). The wire scanners are regularly surveyed absolutely with respect to the Hall A coordinates. At present the results agree with respect to each other at the

level of 200 μm. The position information from the BPM's was recorded at an event-by-event basis in the raw data stream. The real beam position and angle at the target in the Hall A coordinate system, x_{beam}, y_{beam}, θ_{beam} and ϕ_{beam} can then be reconstructed as

$$\begin{aligned} x_{\rm beam} &= \frac{1}{a_3}(x_{\rm bpma}\cdot z_{\rm bpmb} - x_{\rm bpmb}\cdot z_{\rm bpma}) \\ y_{\rm beam} &= \frac{1}{a_3}(y_{\rm bpma}\cdot z_{\rm bpmb} - y_{\rm bpmb}\cdot z_{\rm bpma}) \ , \\ \theta_{\rm beam} &= \frac{a_1}{a_3} \ \text{ and } \ \phi_{\rm beam} = \frac{a_2}{\sqrt{a_1^2+a_3^2}} \ , \end{aligned} \tag{3.10}$$

where $a_1 = x_{\rm bpmb} - x_{\rm bpma}$, $a_2 = y_{\rm bpmb} - y_{\rm bpma}$ and $a_3 = z_{\rm bpmb} - z_{\rm bpma}$. The locations of the wire scanners for BPMA and BPMB are $z_{\rm bpma} = -7.345$ m and $z_{\rm bpmb} = -2.214$ m, respectively.

Figure 3-16 shows the beam position distribution for a circular raster during the A_1^n experiment. The one-dimension distribution of x_{beam} or y_{beam} can be fit by

$$f(x) = H\left[1 - \left(\frac{x-\bar{x}}{R}\right)^2\right] , \tag{3.11}$$

as shown by the red curve, with $R \sim 2$ mm the raster radius and $\bar{x}$ ($\bar{y}$) the beam position offset in x (y) direction. The circular raster pattern can be simulated by

Figure 3-16: Beam position distribution for a circular raster.

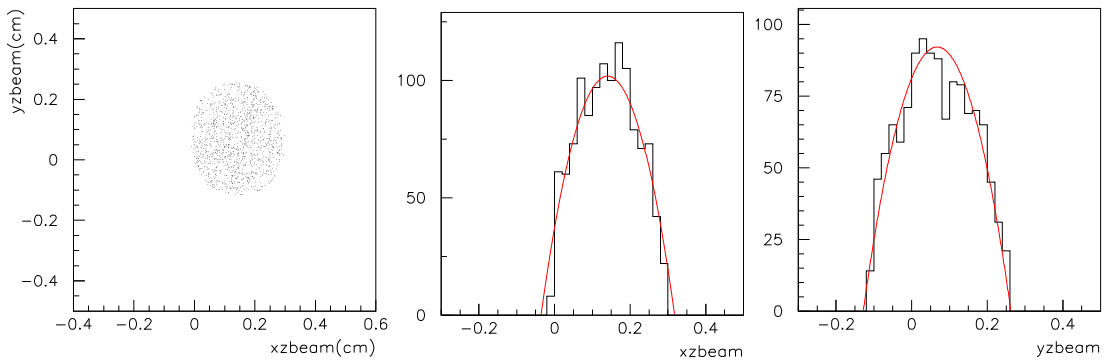

$$\begin{aligned} x &= \cos(2\pi u_1)\sqrt{u_2}\sqrt{(\cos(2\pi u_1)R_x)^2 + (\sin(2\pi u_1)R_x)^2} + x_{offset} \ \text{ and} \\ y &= \sin(2\pi u_1)\sqrt{u_2}\sqrt{(\cos(2\pi u_1)R_y)^2 + (\sin(2\pi u_1)R_y)^2} + y_{offset} \ , \end{aligned} \tag{3.12}$$

where u_1 and u_2 are random numbers between $(0,1)$. The raster phase is $2\pi u_1$ and $\sqrt{u_2}$ gives the radial distribution. Eq. (3.12) have been used in the elastic simulation,

see Section 5.4.

When beam is not centered at $(\bar{x}, \bar{y}) = (0, 0)$, BPM corrections need to be made. This was taken care of in the Hall A analysis software [86].

3.10 Hall A Spectrometers

The Hall A spectrometers have been designed for detailed investigations of the structure of nuclei or nucleons. Therefore, the spectrometers must have a high resolution to be able to isolate the different reaction channels in nuclei so that a clean comparison with theory can be achieved. A high luminosity is also required to achieve a good statistical accuracy. The present instrumentation in Hall A has been used with great success for experiments which require high luminosity and high resolution in momentum and/or angle of the reaction products. The central elements are the two High Resolution Spectrometers (HRS). Both HRSs can provide a momentum resolution better than 2×10^{-4} and a horizontal angular resolution better than 2 mrad with a design maximum central momentum of 4 GeV/c [77].

3.10.1 High Resolution Spectrometers

The basic layout of a spectrometer is shown in Figure 3-17, also shown is the detector hut which will be described later. The vertically bending design includes a pair of super-conducting quadrupoles followed by a 6.6 m long dipole magnet with focusing entrance and exit faces. Further focusing is achieved through the use of a field gradient in the dipole. Subsequent to the dipole is another super-conducting quadrupole. The main design characteristics of the spectrometers are shown in Table 3.7. Details of the spectrometer design can be found in [77].

3.10.2 Detector Package

The detector package [77] is designed to perform various functions in the characterization of charged particles coming through the spectrometer. For the A_1^n experiment the detector package includes:

- Two scintillator planes to provide a trigger to activate the data acquisition electronics;
- A set of two Vertical Drift Chambers (VDC's) to provide tracking information (position and direction);
- A gas Čerenkov detector to provide particle identification (PID) information;
- A set of lead glass counters for additional PID.

Figure 3-17: Schematic layout of HRS spectrometer and the detector hut. Dimensions are in meters.

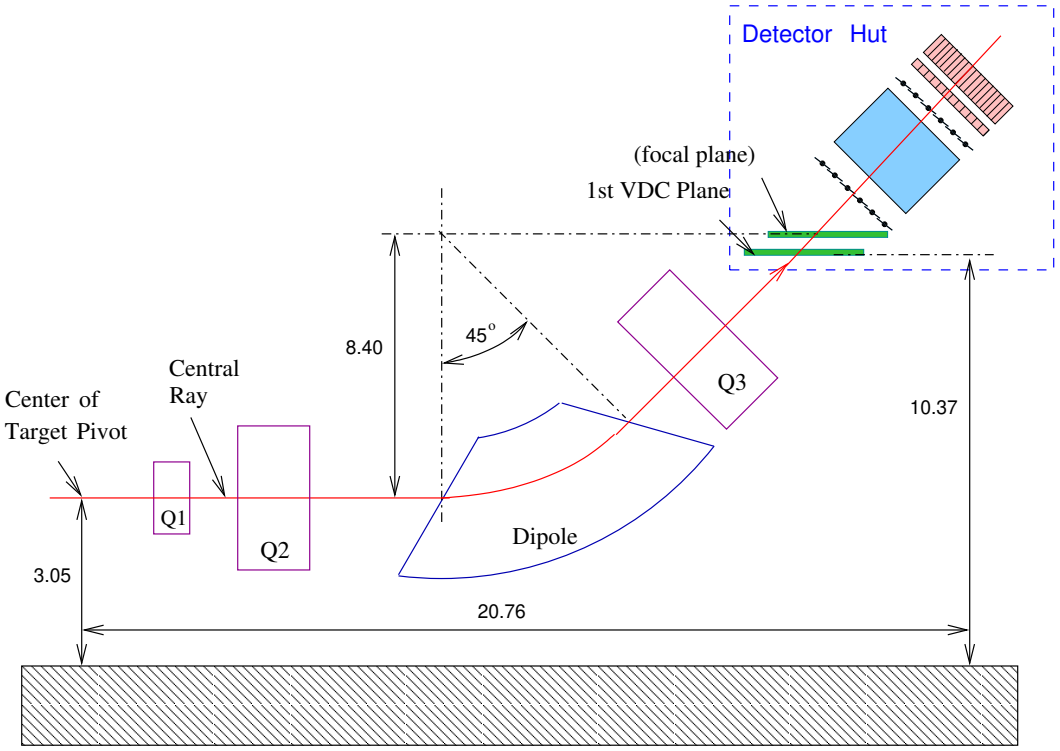

The detector package is located in a large steel and concrete detector hut following the magnet system of the HRS, as shown in Figure 3-17. Figure 3-18 shows a schematic layout of the detector packages for the two spectrometers. The detector packages for the left and right spectrometers are almost identical, except for a slight difference in the gas Čerenkov detector and lead glass counters.

Table 3.7: Hall A HRS general characteristics.

Momentum range p	0.3∼4.0 GeV/c
Configuration	QQDQ
Bend Angle	45°
Optical Length	23.4 m
Momentum Acceptance $\Delta p/p$	±4.5%
Dispersion (D)	12.4 cm/%
Radial Linear Magnification (M)	2.5
D/M	5
Momentum Resolution (FWHM) $\delta p/p$	1×10^{-4}
Angular Acceptance Horizontal	±28 mrad
Angular Acceptance Vertical	±60 mrad
Solid Angle $\Delta\Omega$	∼ 6.7 msr
Angular Resolution (FWHM) Horizontal ϕ	0.6 mrad
Vertical θ	2.0 mrad
Transverse Length Acceptance	± 5 cm
Transverse Position Resolution (FWHM)	1.5 mm
Spectrometer Angle Determination Accuracy	0.1 mrad

Figure 3-18: Configuration of left and right HRS detectors, side view.

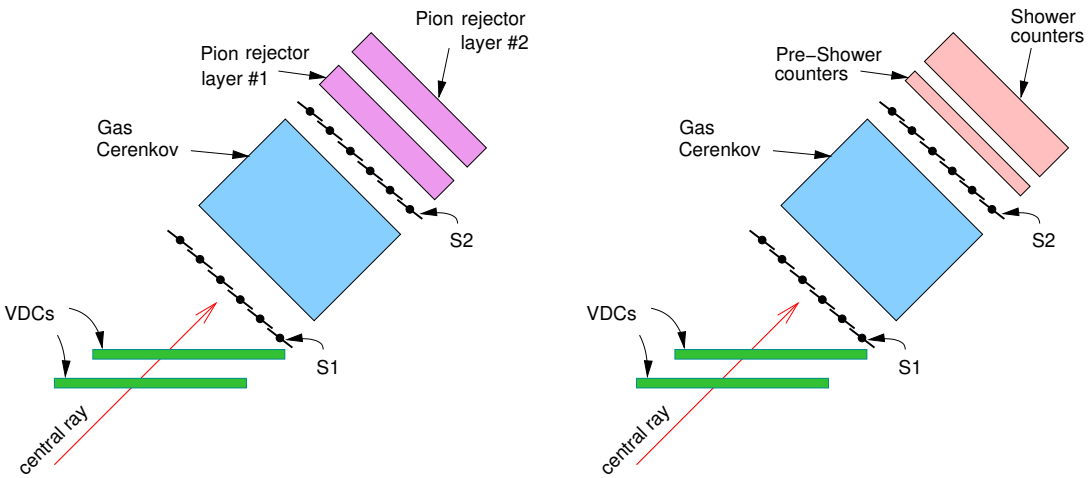

Left HRS detectors Right HRS detectors

3.10.3 Scintillators and Trigger Electronics

There are two primary trigger scintillator planes (S1 and S2), separated by a distance of $\sim$ 2 m. Each plane consists six overlapping paddles made of thin plastic scintillators to minimize hadron absorption. To each scintillator paddle are attached two photo-multiplier tubes (PMT's), called the left and right PMT. Figure 3-19 shows the structure of one scintillator plane. The active volume of scintillator plane S1 is 36.0 cm (transverse direction) $\times$ 29.3 cm (dispersive direction) $\times$ 0.5 cm (thickness) and that of S2 is 60.0 cm $\times$ 37.0 cm $\times$ 0.5 cm. The time resolution of each plane is

Figure 3-19: Configuration of scintillators.

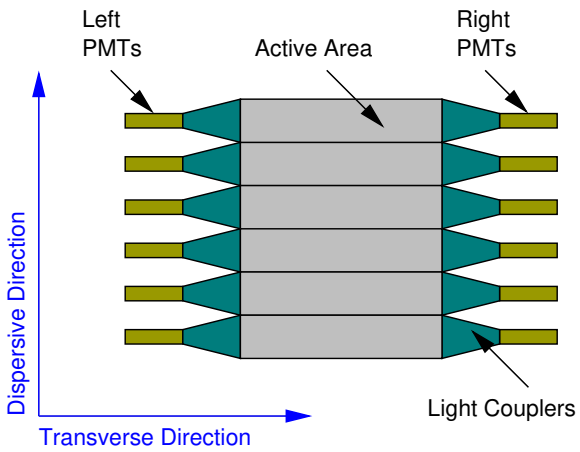

$\sigma \sim 0.30$ ns. Triggers are generated by the PMT signals from the scintillator planes and are sent to all other detectors and DAQ. To make sure that only good events coming from the target are used for the analysis, each event is assigned a variable *event type* based on the signals from scintillator planes for this event. Events with *event type* $= 1, 2, 3, 4$ and 5 are called T1, T2, T3, T4 and T5 events, respectively. The variable *event type* is assigned to each event as follows:

- A T1(T3) event for the right(left) HRS is considered to be a "good event". It satisfies the following conditions:
  - A paddle is said to have fired if there are signals from both its left and right PMT;
  - The N_1^{th} paddle of S1 has fired, at the same time the N_2^{th} paddle of S2 has fired;

  - $N_2^{th} = N_1^{th}$ or $N_1^{th} \pm 1$. This means that the particle trajectory has a very small angle with respect to the central ray of the spectrometer, or approximately 45° with respect to the hall floor.

- A T2(T4) event for the right(left) HRS is formed if one of the following conditions is satisfied:

  - The N_1^{th} paddle of S1 has fired, at the same time the N_2^{th} paddle of S2 has fired, but $N_2^{th} \neq N_1^{th}$ and $N_2^{th} \neq N_1^{th} \pm 1$;
  - One paddle of either S1 or S2 has fired, at the same time Čerenkov has fired.

  T2 (T4) events are either cosmic ray events, or particles rescattered off the edge of the acceptance.

- A T5 event is defined as the coincidence event of T1 and T3. It was not used during the A_1^n experiment.

Triggers T1–T4 are counted by scalers and are sent to the trigger supervisor. The scalers are helicity gated. There are two trigger supervisors, one on each HRS. The trigger supervisor synchronizes all the detector readouts and send them to the data acquisition (DAQ) system.

When the event rate is high, the DAQ system cannot record all the events. We use a quantity – the livetime LT, also called the deadtime correction factor η_{DT} – to describe the fraction of events recorded by the DAQ. The livetime LT is given by

$$LT = \eta_{DT} = \frac{\text{number of events that are recorded by DAQ}}{\text{number of events that are fed to DAQ}} . \qquad (3.13)$$

There is one method to decrease the load of the DAQ system: If the event rate is very high, events can be prescaled by a prescale factor p_{type} at the trigger supervisor. This means that for each set of p_{type} subsequent events, only one is sent to the DAQ system.

Livetime is *event type* and helicity dependent. It can be found by comparing the number of triggers $T_{1(2,3,4)}$ recorded by scalers and the total number of triggers accepted by the DAQ system, $T_{a,1(2,3,4)}$, as

$$LT^H_{\text{type}} = \eta^H_{DT,\text{type}} = \frac{p_{\text{type}} T^H_{a,\text{type}}}{T^H_{\text{type}}} , \qquad (3.14)$$

where type = 1, 2, 3, 4 is the *event type*, p_{type} is the prescale factor of that event type, $H = \pm$ is the helicity. Livetime corrections need to be made when extracting asymmetries from data.

The error on the livetime calculated from scalers is mostly due to the scaler signal quality. During the A_1^n experiment there were 'multi-pulses' in the scaler signals

$T_{1,2,3,4}$. This means each pulse in the scaler signal was followed by multiple pulses with smaller magnitude. This 'multi-pulsing' effect was rate-dependent. It caused double-counting of $T_{1,2,3,4}$ scalers and an overestimation of deadtime (or underestimation of livetime). Since this 'multi-pulsing' problem was independent of beam helicity, it affected both helicity + and − livetimes in the same manner. Therefore the helicity asymmetry of livetime was not affected by the 'multi-pulsing' problem and its contribution to the uncertainty of asymmetry results is negligible. To estimate the uncertainty in the absolute value of deadtime correction factor, two extra copies of scalers $T_{1,3}$ were fed into the main data stream during the later period of the A_1^n experiment and the readings from all three copies were compared. Meanwhile we also used results from electronic deadtime measurement (EDTM) to correct the deadtime from scalers. The EDTM will be described in Section 3.11.2. We estimate a relative uncertainty of ± 1% in the helicity independent deadtime correction for the elastic data, and ± 0.2% for the DIS data. These uncertainties will be taken into account in the cross section analysis, see Chapter 5.

The trigger inefficiency describes the fraction of "good events" that are counted as T2(T4) events. Using scalers from a high yield run (in order to minimize the dilution from cosmic events), the trigger inefficiency for the right (left) HRS is given by

$$\text{Inefficiency} \quad = \quad \frac{T_{2(4)}}{T_{1(3)} + T_{2(4)}} \ , \tag{3.15}$$

from which one can find the trigger efficiency, defined as

$$\eta_{\text{trig.}} = 1 - \text{Inefficiency} = \frac{T_{1(3)}}{T_{1(3)} + T_{2(4)}} \ . \tag{3.16}$$

Trigger inefficiency is not helicity dependent. It does not affect asymmetry results, but it needs to be corrected for when doing cross section analysis. During the A_1^n experiment, trigger inefficiency was less than 1%.

3.10.4 VDCs

Particle tracking for each HRS is provided by the two Vertical Drift Chambers (VDC) [90][91] positioned 23 cm away from each other. The position of the first VDC almost coincides with the spectrometer focal plane [77]. Each VDC is composed of two wire planes in a standard UV configuration – the wires of one plane are perpendicular to that of the other plane – and are oriented at an angle of 45° (−45°) with respect to the dispersive and non-dispersive (transverse) directions, as shown in Figure 3-20. Both wire planes lie in the laboratory horizontal plane and the nominal particle trajectory crosses the wire planes at an angle of 45°.

Each VDC has three high voltage plates at about −4 kV, one between the U and V wire planes and two on opposite sides. The spacing between planes is 26 mm.

Figure 3-20: Schematic diagram (left) and sideview (right) of wire chamber configuration.

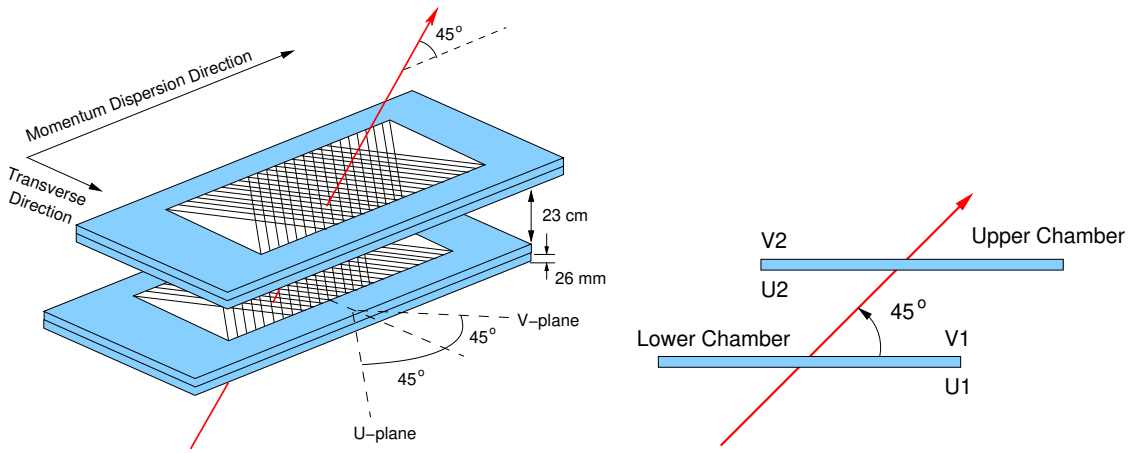

The wires are kept at ground voltage so that the resulting electric field has the configuration shown in Figure 3-21.

Figure 3-21: Configuration of wire chambers.

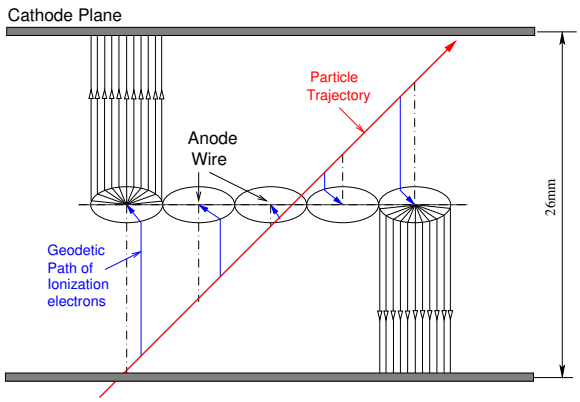

When a charged particle travels through the chamber, it ionizes the gas inside the chamber and leaves behind a track of electrons and ions along its trajectory. The gas supplied to the VDCs is a 62%/38% argon-ethane (C_2H_6) mixture, with a flow rate of 10 liter/hour [77]. The ionization electrons accelerate towards the wires along the path of least time (geodetic path). This time is measured by a Time-to-Digital Converter (TDC), which is started by the triggered wire and stopped by the event trigger supervisor. The basic idea of particle tracking is the following: Since the drift velocity of ionization electrons in the operating gas is known to be 50 μm/ns, the drift distance from the trajectory to each fired wire can then be extracted from the corre-

sponding TDC output. Combining the drift distance of all fired wires together gives the trajectory of the charged particle. A charged particle with a track at the nominal angle of 45° with respect to the lab horizontal plane typically triggers five wires, while those at the extreme angle of 52° trigger three. The position resolution achieved in each direction is 225 μm full width at half maximum (FWHM). Therefore the two VDCs separated by 50 cm are capable of measuring the two angles (in the dispersive plane and transverse directions) of the track with a resolution of approximately 0.3 mrad (FWHM) [91].

The VDC efficiency will be discussed in Section 5.2.1.

3.10.5 Gas Čerenkov Detector

One major task of particle detection is to separate the scattered electrons from background particles, which are particles produced by reactions other than (e, e') scattering. During the A_1^n experiment the highest background came from pions resulting from pion photo-production. In the following sections, we refer to particle identification (PID) as the procedure of separating electrons from pions. PID for each HRS during the A_1^n experiment was accomplished by a CO_2 threshold gas Čerenkov detector and a double-layered lead glass counter.

A threshold Čerenkov detector [92] is based on the Čerenkov effect [93][94]. The Čerenkov effect refers to the effect that when a high energy charged particle travels through transparent materials with a velocity v higher than the velocity of light in the material c/n, a characteristic electromagnetic radiation is emitted, called the Čerenkov radiation (Čerenkov light). Here c is the speed of light in vacuum and n is the refractive index of the material. Čerenkov light is emitted because the charged particle polarizes the atoms along its track so that they become electric dipoles. As long as $v < c/n$, the dipoles are symmetrically arranged around the particle's path, so that the dipole field integrated over all dipoles vanishes and no radiation results. If, however, $v > c/n$, the symmetry is broken resulting in a non-vanishing dipole moment, which leads to the emission of radiation. By detecting whether a given particle emits Čerenkov light, one can know if its velocity is larger than the threshold velocity depending on the material used.

The two threshold gas Čerenkov detectors for the Hall A HRSs are operated with CO_2 at atmospheric pressure. The refraction index is 1.00041 which give a threshold speed and momentum of

$$v_{th} = \frac{c}{n} \quad \text{and} \quad p_{th} = \frac{mv}{\sqrt{1 - \frac{v^2}{c^2}}} \approx \frac{mc}{\sqrt{2\alpha}} \ , \tag{3.17}$$

where $\alpha = n - 1 \ll 1$. The threshold momentum is therefore ~ 17 MeV/c for electrons and ~ 4.8 GeV/c for pions. So within a momentum range of $0.02 \sim 4.8$ GeV/c, which is larger than the HRS designed momentum range $0.30 \sim 4.0$ GeV/c, only electrons

and not pions can emit Čerenkov light and trigger an ADC signal.

The structure of the gas Čerenkov detectors on the two HRSs is very similar. Each one is made of steel with thin entry and exit windows made of tedlar [95]. Ten spherical mirrors positioned as a 2(horizontal)×5(vertical) array are used in each detector to collect Čerenkov light. These mirrors are specially built to be light weight resulting in a very small total thickness (0.23 g/cm^2) [83] traversed by the particles. The position and orientation of these mirrors are designed in a way such that the Čerenkov light emitted by the scattered electrons can be efficiently collected. Each mirror is coupled to a photo-multiplier tube (PMT). The mirrors have radius of curvature of 90 cm, the PMTs are placed at a distance of $90/2 = 45$ cm from the mirrors, where the parallel rays of incident light on the mirrors are approximatively focussed. The light is converted to electronic signals by PMTs and fed to ADCs. The summed signal of all ten ADCs gives information about the total light emitted by the particle and has a different shape for electron and pion events.

In principle pions should not produce any signal in the Čerenkov detector. However they can interact with the matter they pass through and create δ-electrons [96]. These δ-electrons will produce Čerenkov light and trigger the ADCs. Since δ-electrons are in general not moving in the same direction as the scattered electrons, the Čerenkov light emitted by δ-electrons will not be efficiently collected by the mirrors. The summed ADC signals generated by δ-electrons are mostly single photo-electron peaks.

Almost all the Čerenkov light emitted by the scattered electrons is collected by the mirrors, and therefore the signals generated are mainly in a multiple photo-electron peak. The position and the width of this peak depend on the average number of photo-electrons, which is determined by the PMT performance and whether all the Čerenkov light is collected by the mirrors. The number of photo-electrons determines how well one can separate the single photo-electron peak from the multiple one, which subsequently determines the PID quality of Čerenkov detector. The average number of photoelectrons $n_{ph.e.}$ for each PMT can be extracted from detailed mirror-by-mirror analysis for the Čerenkov detector. During the A_1^n experiment $n_{ph.e.} \sim 9$ for the right HRS and $n_{ph.e.} \sim 12$ for the left HRS [97].

The PID efficiency is usually evaluated as a pion contamination or rejection factor at a certain electron detection efficiency (for example 99%). A detailed analysis of PID efficiency will be presented in Section 5.2.2.

3.10.6 Lead Glass Counters

Lead glass counters provide an additional PID. The signal detected by lead glass counters is linearly proportional to the energy deposited by the incoming particle [92]. Electromagnetic showers develop in the counters, whereas hadronic showers do not due to the longer hadronic mean free path. Therefore the longitudinal distribution of the energy deposited in the counter can be used to identify the incident particles. In

our case there are two distributions of energy: low ADC signal for hadrons and high ADC signal for electrons. The limitation on PID efficiency of the lead glass counter comes from separating the tail of the two distributions and hence depends on the energy resolution. At higher energy the relative resolution of a lead glass counter improves and leads to better separation between the two distributions. A double-layered lead glass counter can provide better separation because the second layer can further separate the hadrons which are contaminated with electrons in the first layer.

The two double-layered lead glass counters have different configurations on the left and right HRSs [77]. On the left HRS, they are called 'pion rejectors' and the two layers have the same geometry. Each layer consists 17 short blocks and 17 long blocks of lead glass, forming a 2(transverse)×17(dispersive) array. All lead glass blocks are oriented transversely with respect to the direction of the scattered electrons, as shown in Figure 3-22. Short and long lead glass blocks are arranged interchangeably in the dispersive direction for each row (transverse direction). The gap between blocks of the first layer is covered by a lead glass block of the second layer, and vice versa.

Figure 3-22: Configuration of the pion rejectors on the left HRS.

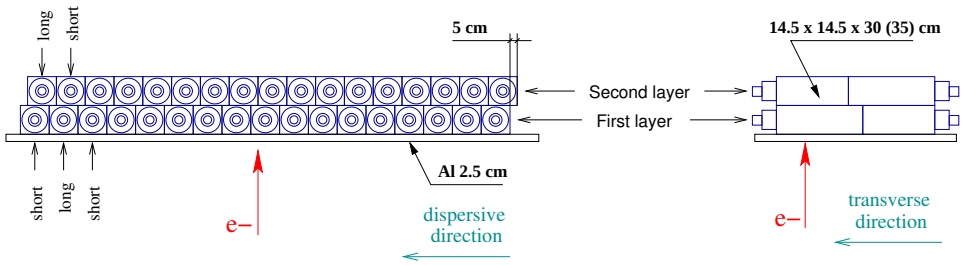

On the right HRS, the first and the second layers of lead glass counters are called 'preshower' and 'shower' detectors, respectively. The preshower detector has $2 \times 24 = 48$ blocks of lead glass oriented transversely with respect to the direction of scattered electrons. The shower detector has 5×20 blocks of lead glass oriented parallelly to the scattered electrons, as shown in Figure 3-23. Preshower and shower together are called 'Total shower' detector.

Due to the different thicknesses of the lead glass layers, the total shower detector on the right HRS has a better PID performance than the pion rejectors on the left HRS. Detailed PID efficiency analysis for lead glass counters will be presented in Section 5.2.2.

Figure 3-23: Configuration of the total shower detector on the right HRS.

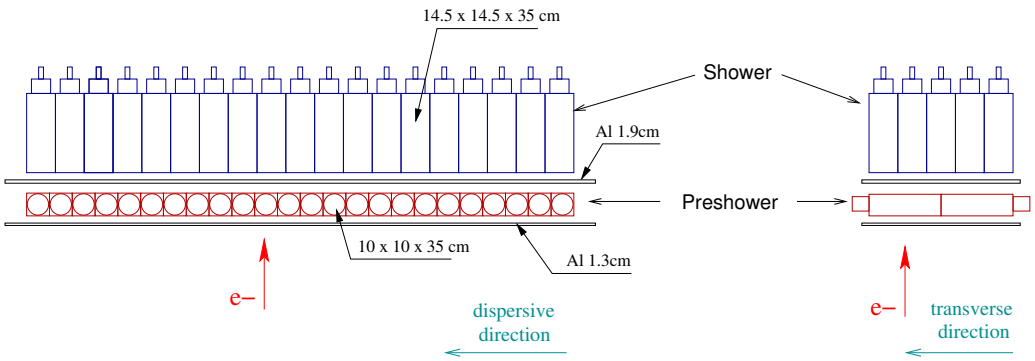

3.11 Data Acquisition System

3.11.1 Data Acquisition System

The A_1^n experiment used the CEBAF Online Data Acquisition (CODA) system [83]. CODA is a toolkit designed for nuclear physics experiments at Jefferson Lab. It is composed of a set of software and hardware packages from which a data acquisition system can be constructed. The recorded data file starts with a header, which consists of information about the event size and the run number. Then the major part consists of:

1. CODA events from the detectors and the beam helicity signal;

2. EPICS [98] data from the slow control software used at JLAB. For example, the spectrometer magnet settings and angles, target temperature and pressure, can all be fed into EPICS data stream and be recorded;

3. CODA scaler events: the DAQ reads the scaler values every 4 seconds and feeds them into the main data stream. The scalers are read from the Trigger Supervisor (TS) so they are not affected by the DAQ deadtime. Therefore one can use scaler readings to correct DAQ deadtime.

The data were first written to a local disk and then transferred to the Mass Storage System (MSS). The total volume of data accumulated during the two months' running period of the A_1^n experiment was about 0.6 TBytes. The data were analyzed using an analysis package called Experiment Scanning Program for hall A Collaboration Experiments (ESPACE) [86]. ESPACE can filter, histogram, ntuplize and/or calibrate variables of the experimental setup while applying conditions on the incoming data. The variables operated within ESPACE range from those at a basic

level, like raw detector signals, to some much more elaborate ones like the calculated location of the reaction point in the target coordinate system.

Scaler events are extracted from raw data files. They are used for deadtime correction and removing data during beam trips and rampings.

3.11.2 Electronic Deadtime Measurement

In addition to using scalers, there is another method to measure the deadtime of the system – Electronic DeadTime Measurement (EDTM) [99]. In this method a well-defined, recognizable pulse is sent into the front-end of the trigger system and the probability that it makes through to the trigger supervisor depends on the electronic deadtime. Then if the DAQ is alive, the trigger supervisor will accept this pulser trigger and it will show up in the data stream as a tagged event. The fraction of such events that get lost is the deadtime of the system.

The EDTM system can be used to check the deadtime measured from scalers, or as an independent deadtime measurement. There are two short points of the EDTM system. The first one is that the pulser frequency is low (~ 1 Hz during the A_1^n experiment) so the statistical error cannot compete with regular deadtime measurement from scalers. Secondly, the pulser signal is not helicity gated so it can only be used for cross section analysis, not asymmetries. However, if the scalers have un-anticipated problems, the EDTM can help to explore the problem and add corrections to the deadtime extracted from scalers. For example, during the A_1^n experiment there was a period during which we observed a $\sim 10\%$ discrepancy between the deadtime from the EDTM and that from scalers. It was found that the scaler signals were affected by multiple pulses due to the instability of the scaler electronic system. Its effect on the deadtime correction has already been discussed in Section 3.10.3. The problem was solved by changing the hardware configuration. For those data taken during this period, the EDTM was used to correct the deadtime from scalers in the cross section analysis.

Chapter 4

The Polarized ^{3}He Target

This chapter describes the polarized ^{3}He target at JLAB Hall A, its principle of operation, setup, polarimetries and the related analysis.

4.1 Principles

Polarized ^{3}He targets are widely used at SLAC, HERMES, MAINZ, MIT-Bates and JLAB to study the electromagnetic structure and the spin structure of the neutron. There exist two major methods of polarizing ^{3}He nuclei. The first one is based on the metastability-exchange optical pumping technique [100]. It polarizes ground state ^{3}He atoms through metastability-exchange collisions with optically pumped ^{3}He metastable atoms. This technique is usually used for internal targets.

The second method is based on spin exchange optical pumping [101]. First alkali metal (rubidium) vapor is polarized by optical pumping and then the polarization is transfered to ^{3}He nuclei through the spin exchange mechanism during ^{3}He-Rb collisions. Targets based on this principle are almost always designed to operate at quite high gas pressures, typically one to ten atmospheres. The polarized ^{3}He target using spin-exchange optical pumping was originally developed at SLAC [102] and has been used in JLAB Hall A since 1998 [103].

4.1.1 Optical Pumping

The first step in polarizing ^{3}He nuclei is to generate a source of polarized electrons that can collide and transfer their spin polarization to the ^{3}He nuclei. These polarized electrons are provided by optically pumped rubidium(Rb) atoms. A review of optical pumping of alkali metals is given in [106][107].

Rb has a single electron in the outer shell ($5S_{1/2}$), whose interaction Hamiltonian with a magnetic field $\vec{B}$ is given by

$$\hat{H} \;=\; A_g \vec{I}\cdot\vec{S} + g_e\mu_B S_z B_z - \frac{\mu_I}{I} I_z B_z \;, \tag{4.1}$$

where the first term is the vector coupling between the electron spin $\vec{S}$ and the nuclear spin $\vec{I}$, the second and the third terms describe the coupling of the electron and nuclear spin to the magnetic field B_z, with a strength related to the electron magnetic moment $\mu_e = g_e\mu_B$ ($g_e = 2.00232$, $\mu_B = 0.57884 \times 10^{-11}$ MeV/T), the nuclear magnetic moment μ_I ($\mu_I = 4.26426 \times 10^{-12}$ MeV/T for ^{85}Rb), and the Rb atom's spin quantum number I ($I = 5/2$ for ^{85}Rb and $I = 3/2$ for ^{87}Rb). Solutions

Figure 4-1: Energy level of ^{85}Rb, the Zeeman splitting is given by ν_Z.

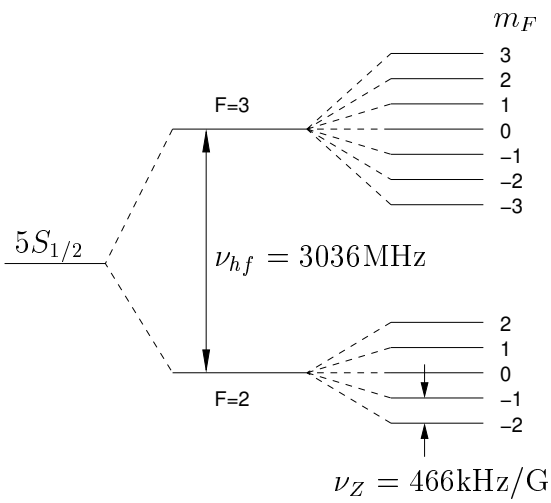

using Eq. (4.1) give the eigenstates of Rb atom, which are labeled by the quantum number $F = I \pm S$ of total spin $\vec{F} = \vec{I} + \vec{S}$. In a magnetic field the F state splits into $2F + 1$ sublevels labeled by $m_F = m_I + m_S$, with $m_I = -I, -I + 1, \cdots, I - 1, I$ and $m_S = -S, -S + 1, \cdots, S - 1, S$, hence $m_F = -F, -F + 1, \cdots, F - 1, F$, as shown in Figure 4-1. Note that for ground state the orbital angular momentum of the electron $L = 0$, so the total angular momentum of the electron $\vec{J} = \vec{S}$. Since electrons have $S = 1/2$, $m_S = \pm 1/2$ and $m_J = \pm 1/2$.

In the process of optical pumping, Rb vapor is exposed to circularly polarized laser tuned to the $5S_{1/2} \rightarrow 5P_{1/2}$ transition, known as the D_1 transition. If the photon helicity is in the same direction as the magnetic field, then electrons from all sub-levels except $m_F = 3$ are excited to the $5P_{1/2}$ state. These excited electrons can then decay to any sub-level of the $5S_{1/2}$ ground state. This procedure is illustrated in Figure 4-2 for a certain m_I. The electrons in the $m_J = -1/2$ level of ground state $5S_{1/2}$ are excited to the $m_J = 1/2$ sublevel of the $5P_{1/2}$ state, then decay either to $m_J = +1/2$, or back to the $m_J = -1/2$ sublevel of ground state. Because a transition from the ground state $m_J = 1/2$ sublevel is prohibited by the selection rule $\Delta m_J = \pm 1$, the electrons will gradually accumulate in this level while the $m_J = -1/2$ sublevel will be depopulated. The net result is that electrons will go from the $m_F = m_I - 1/2$ to

Figure 4-2: Optical pumping of Rb by circularly polarized light.

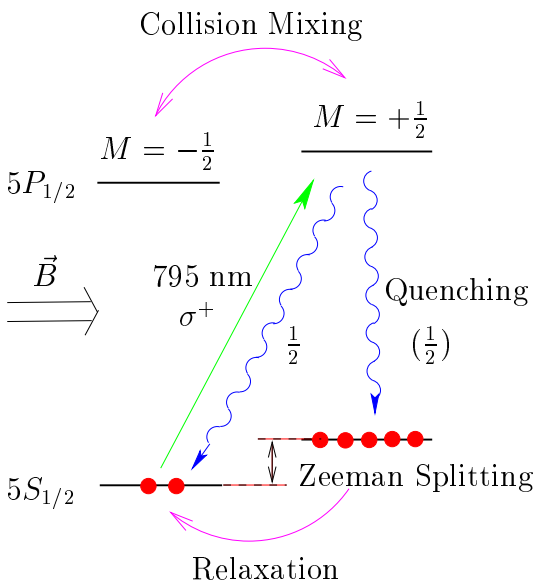

the $m_F = m_I + 1/2$ state. Since this procedure exists for each m_I, finally all electrons will accumulate in the $F = 3,\ m_F = 3$ sublevel.

If the photon helicity is in the opposite direction to that of the magnetic field, all electrons will accumulate in the $m_F = -3$ sublevel. This was the case during the two experiments in the summer of 2001. The first one was the A_1^n experiment and the second one was E97-103 [104], also referred to as the g_2^n experiment. During the A_1^n and g_2^n experiments the lasers were left-handed circularly polarized when the field direction was 0° (parallel to the beam direction) or 270° (perpendicular to the beam direction and pointing to the left side), and right-handed circularly polarized when the field was 180° (anti-parallel to the beam direction) or 90° (perpendicular to the beam direction and pointing to the right side).

When excited electrons decay to the $m_J = -1/2$ sublevel of the ground state they emit photons which have the same D_1 wavelength as the pumping lasers. These photons are not polarized and can excite electrons from the $m_F = 3$ sublevel of the ground state. To minimize this depolarization effect, N_2 buffer gas is introduced to provide a channel for the excited electrons to decay to the ground state without emitting photons. In the presence of N_2, electrons decay through collisions between the Rb atoms and N_2 molecules, usually referred to as non-radiative quenching [107]. The amount of N_2 is chosen to be about two orders of magnitude less in density than that of ^{3}He but a few orders of magnitude higher than that of Rb vapor. In this condition, only about 5% of the excited electrons decay by emitting a photon. Since these N_2 molecules are not polarized, they introduce a dilution effect, as will be discussed in Section 5.4.4.

4.1.2 Spin Exchange

The key process in spin-exchange optical pumping is the collisional transfer of polarization between optically pumped alkali-metal atoms and the nuclei of the noble-gas atoms. The transfer of angular momentum occurs either while the atoms are bound in van der Waals molecules or in simple binary collisions between the atoms [101]. For ^{3}He, binary collisions dominate the spin exchange, and the contribution from

Figure 4-3: Spin exchange between Rb atom and ^{3}He nuclei.

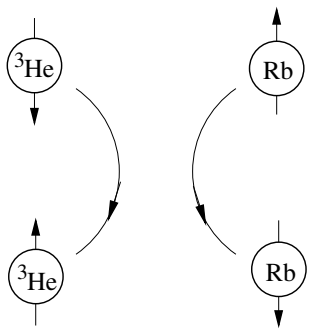

van der Waals molecules is negligible. Spin-dependent interactions, denoted $V_1(\vec{R})$ with R the interatomic separation, produce the spin transfer and relaxation in collisions. For spin-exchange optical pumping, evidence suggests that the spin-exchange process is dominated by two terms, as shown in Eq. (4.2) [101]. The first term is the spin-rotation interaction between the electron spin $\vec{S}$ and the rotational angular momentum $\vec{N}$ of the ^{3}He-Rb system. The second term is the isotropic hyperfine interaction between $\vec{S}$ and the noble-gas nuclear spin $\vec{I}_b$.

$$V_1(\vec{R}) \;=\; \gamma(R)\vec{N}\cdot\vec{S} + A_b(R)\vec{I}_b\cdot\vec{S}\ . \tag{4.2}$$

Simply stated, the spin-rotation interaction arises from magnetic fields produced by the relative motion of the charges of the colliding atoms, while the isotropic hyperfine interaction arises from the magnetic field at the nucleus of the noble-gas atom.

4.1.3 Polarization Evolution

The polarization of the Rb vapor is given by

$$P_{\rm Rb} \;=\; \frac{\mathcal{R}}{\mathcal{R}+\Gamma_{SD}}\ , \tag{4.3}$$

with $\mathcal{R}$ the optical pumping rate defined as

$$\mathcal{R} = \int \Phi(\nu)\sigma(\nu)\mathrm{d}\nu \ , \tag{4.4}$$

where $\Phi(\nu)$ is the laser photon flux per unit frequency and $\sigma(\nu)$ is the light absorption cross-section. The electron spin destruction rate Γ_{SD} is dominated by the spin-rotation interaction $\gamma(R)\vec{N}\cdot\vec{S}$ during collisions among Rb atoms or between Rb atoms and other gases. The spin destruction caused by collisions of Rb atoms with the cell wall, and that caused by the randomly polarized photons emitted from the decay of excited electrons is small [102]. The rate is given by

$$\Gamma_{SD} = k_{\mathrm{Rb}-He}[^3\mathrm{He}] + k_{\mathrm{Rb}-\mathrm{Rb}}[\mathrm{Rb}] + k_{\mathrm{Rb}-\mathrm{N_2}}[\mathrm{N_2}] \ , \tag{4.5}$$

where $[^3\mathrm{He}]$, [Rb] and $[\mathrm{N_2}]$ are densities of each gas component. The spin destruction constants are [105]:

$$k_{\mathrm{Rb}-He} \leqslant 2 \times 10^{-18} \ \mathrm{cm}^3/\mathrm{s} \ , \tag{4.6}$$

$$k_{\mathrm{Rb}-\mathrm{Rb}} = 8 \times 10^{-13} \ \mathrm{cm}^3/\mathrm{s} \ \text{ and} \tag{4.7}$$

$$k_{\mathrm{Rb}-\mathrm{N_2}} = 8 \times 10^{-18} \ \mathrm{cm}^3/\mathrm{s} \ . \tag{4.8}$$

The gas densities for a typical cell used in JLAB Hall A are [He] = 10 amg[1] = $2.69 \times 10^{+20}$ cm^{-3}, and $[\mathrm{N_2}] = 0.08$ amg $= 2.15 \times 10^{+18}$ cm^{-3}. The Rb density can be given by the Killian formula [108]: $\log(p_{\mathrm{Rb}}) = 10.53 - 4132/T$ with p_{Rb} the Rb gas pressure in bar (1 bar = 10^5 Pa), T the temperature where Rb condensates, i.e. the coldest spot inside the pumping chamber [2]. However, Killian did not quote an error for his data. A more commonly used formula is [109]

$$[\mathrm{Rb}] \ (\text{in cm}^{-3}) = (10^{26.178-4040/T})/T \ , \tag{4.9}$$

with a quoted accuracy of 5%. This gives [Rb] $\approx 2.60 \times 10^{14}$ cm^{-3} for $T = 170$ °C. The spin destruction rate is therefore

$$\Gamma_{SD} = 538_{\mathrm{Rb}-He} + 206_{\mathrm{Rb}-\mathrm{Rb}} + 17_{\mathrm{Rb}-\mathrm{N_2}} \approx 761 \ \mathrm{s}^{-1} = (1.3 \ \mathrm{ms})^{-1} \tag{4.10}$$

The Rb relaxation due to spin exchange with ^{3}He comes from the hyperfine interaction $A_b(R)\vec{I}_b\cdot\vec{S}$ between the Rb electron and the ^{3}He nucleus. This interaction causes the polarization transfer from Rb to ^{3}He and a shift of the Rb Zeeman frequency due to the ^{3}He polarization. The latter is used for ^{3}He polarimetry and will

[1] 1 amg$= 2.6894 \times 10^{+19}$ cm^{-3}, it corresponds to the gas density at a pressure of one atmosphere and a temperature of 0 °C.

[2] Usually it is the temperature of the oven heating the pumping chamber, during the A_1^n and g_2^n experiments it was 170°C.

be described in Section 4.6. There have been two measurements of the spin exchange rate constant k_{SE}, the results of which differ by a factor of two. One gives [111]

$$k_{SE} = (6.1 \pm 0.2) \times 10^{-20} \text{ [cm}^3\text{/s]} , \tag{4.11}$$

and the other gives [112]

$$k_{SE} = (1.2 \pm 0.2) \times 10^{-19} \text{ [cm}^3\text{/s]} . \tag{4.12}$$

Using the average value of these two measurements, spin exchange with ^{3}He contributes

$$\Gamma_{SE} = k_{SE}[^3\text{He}] \approx 24 \text{ s}^{-1} \tag{4.13}$$

to the relaxation of Rb spin, so about $24/761 \approx 3\%$ of the Rb atoms transfer their polarization to ^{3}He, while the rest lose it in other spin destruction processes.

The excitation rate of the $m_J = -1/2$ sublevel of the ground state is on the order of 10^{-6} s^{-1}. So in principle in the region where optical absorption occurs the Rb polarization can be close to 100%. Rb polarization has been studied at Princeton University [114] and was found to be above 90%.

A measurement of polarization versus time with optical pumping is called a spin-up measurement. The spin-up curve is determined by the evolution of the ^{3}He polarization $P_{\text{He}}(t)$ given by

$$P_{\text{He}}(t) = \langle P_{\text{Rb}} \rangle \frac{\gamma_{SE}}{\gamma_{SE} + \Gamma} \left(1 - e^{-(\gamma_{SE}+\Gamma)t} \right) , \tag{4.14}$$

where $\langle P_{\text{Rb}} \rangle$ is the Rb polarization averaged over volume, $\langle P_{\text{Rb}} \rangle > 90\%$. γ_{SE} is the Rb-^{3}He spin exchange rate per ^{3}He nuclei given by

$$\gamma_{SE} = k_{SE}[\text{Rb}] , \tag{4.15}$$

with [Rb] from Eq. (4.9), k_{SE} from Eq. (4.11) and (4.12). Under regular operating conditions γ_{SE} is about $1/(6 \sim 8$ hours). Figure 4-4 shows a typical spin-up curve, from which the maximum polarization and the spin-up time constant $\tau = 1/(\gamma_{SE}+\Gamma)$ can be extracted [113].

Γ is the ^{3}He nuclear spin relaxation rate which can be obtained from a spin-down measurement, which measures polarization versus time in the absence of optical pumping and an electron beam. Γ is related to the time constant of the spin-down measurement as $\Gamma = 1/\tau_{spindown}$, where $\tau_{spindown}$ is called the lifetime of the cell describing how fast the polarization drops during a spin-down measurement. Note that Γ depends on density so a correction should be applied if the spin-down measurement is performed under a temperature different from that during a spin-up measurement.

Cell lifetime is one of the main characteristics to evaluate the quality of the cell.

Figure 4-4: Spin up curve measured in the polarized ^{3}He target lab at JLAB [113].

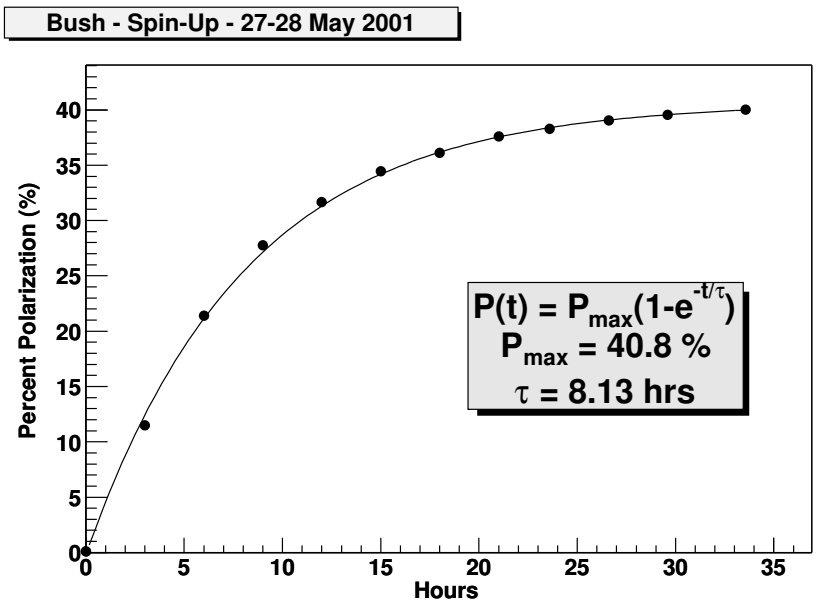

This can be seen from Eq. (4.14). Once the optical pumping conditions ($\langle P_{\rm Rb}\rangle$, [Rb]) are fixed, the maximum polarization of the cell depends solely on its lifetime. The longer the lifetime is, the higher polarization can be reached. Cell lifetime is determined by

$$1/\tau_{spindown} = \Gamma \;\; = \;\; \Gamma_{\rm He} + \Gamma_{wall} + \Gamma_{beam} + \Gamma_{\Delta B} \;, \tag{4.16}$$

where $\Gamma_{\rm He}$ (hour)$^{-1}$ = (744/[He])$^{-1}$ [115] is the relaxation rate of magnetic dipolar interaction among ^{3}He nucleus, with [He] the ^{3}He density in amg. $\Gamma_{wall} \approx$ (90 hour)$^{-1}$ is the relaxation due to collisions between the ^{3}He nucleus and the cell glass wall. Γ_{beam} is the relaxation due to the beam depolarization effect. Following the procedure in [116], we found for a 25 cm cell used during the A_1^n experiment, Γ_{beam}(hour)$^{-1}$ = (622/I)$^{-1}$ with I the beam current in μA. $\Gamma_{\Delta B}$ (hour)$^{-1}$ = $D\frac{|\nabla B_x|^2+|\nabla B_y|^2}{B_z^2}$ [117] is the relaxation due to the magnetic field gradient, with $D \approx 0.2$ cm^2/s the ^{3}He self-diffusion coefficient. After optimizing the Helmholtz coil setup, $\Gamma_{\Delta B} \approx$ (2000 hour)$^{-1}$ and thus is negligible compared to other relaxation terms.

4.2 Target Cell

4.2.1 ^{3}He Cell at JLAB

The target cells used at JLAB are highly pressurized glass cells with $\sim$ 130 μm thick end windows. There have been four experiments performed at JLAB using the polarized ^{3}He target, three of them (E94-010 [103], E95-001 [118], E97-103 [104]) used 40 cm long cells, while 25 cm long cells were used for the A_1^n experiment. Except for the difference in cell length, they all have the some shape. A typical cell consists of two chambers, a circular upper chamber which holds Rb vapor and in which optical pumping occurs, and a long cylindrical chamber where the electron beam passes through and interacts with the polarized ^{3}He nuclei. Figure 4-5 is a picture of a 40 cm long JLAB target cell. Dimensions in the figure are given in mm for a 25 cm long cell used during the A_1^n experiment.

Figure 4-5: A regular JLAB target cell, dimensions are given in mm for a cell used during the A_1^n experiment. The name of the cell is "Tilghman".

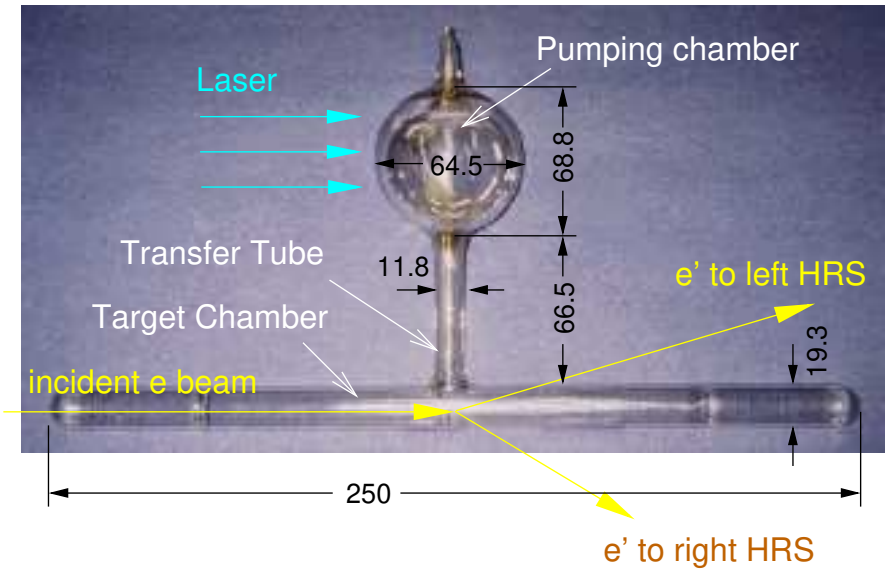

4.2.2 Target Cell Characteristics

Target cell volumes and densities are crucial for polarimetry analysis. The two cells used during the A_1^n experiment were characterized both at University of Virginia (UVa) [119] and at JLAB [120]. The main characteristics are shown in Table 4.1.

The data on target chamber wall thickness were used for radiative corrections in the data analysis described in Chapter 5.

Table 4.1: Main characteristics of the two cells used during the A_1^n experiment. V_p is pumping chamber volume in cm^3; V_t is target chamber volume in cm^3; V_{tr} is transfer tube volume in cm^3; V_0 is total volume in cm^3; L_{tr} is transfer tube length in cm; n_0 is ^{3}He density in amg at room temperature.

Name	V_p	V_t	V_{tr}	V_0	L_{tr}	n_0	lifetime
Gore	116.7	51.1	3.8	171.6	6.574	9.10	49
Tilghman	116.1	53.5	3.9	173.5	6.46	8.28	44
uncertainty	1.5	1.0	0.25	1.8	0.020	2%	1

4.3 Target Setup

Figure 4-6 is a schematic diagram of the target setup. There are two pairs of Helmholtz coils to provide the main holding field. The coils are powered by two KEPCO power supplies [121] in constant current mode. During the A_1^n experiment the coil currents were continuously measured and were sent to the slow control EPICS [98] data stream.

The cell was held in the center of the target, with the pumping chamber mounted inside an oven heated to 170°C to vaporize the Rb. The lasers used for optical pumping were six 30 W diode lasers tuned to 795 nm, three for longitudinal pumping and three for transverse pumping. The target polarization was measured by two independent polarimetries - NMR (Nuclear Magnetic Resonance) and EPR (Electron Paramagnetic Resonance). The NMR system consists of one pair of pick-up coils, one on each side of the target chamber, one pair of RF coils and the associated electronics. The RF coils are placed at the top and the bottom of the scattering chamber, oriented in the horizontal plane. The EPR system shares the RF coils with the NMR system. It consists of a photodiode and the related optics to collect the EPR light signal, one EPR RF coil and the associated electronics.

The orientation of the two Helmholtz coils during the A_1^n experiment is shown in Figure 4-7. The smaller coils were oriented perpendicular and the larger coils

Figure 4-6: Target setup overview (schematic).

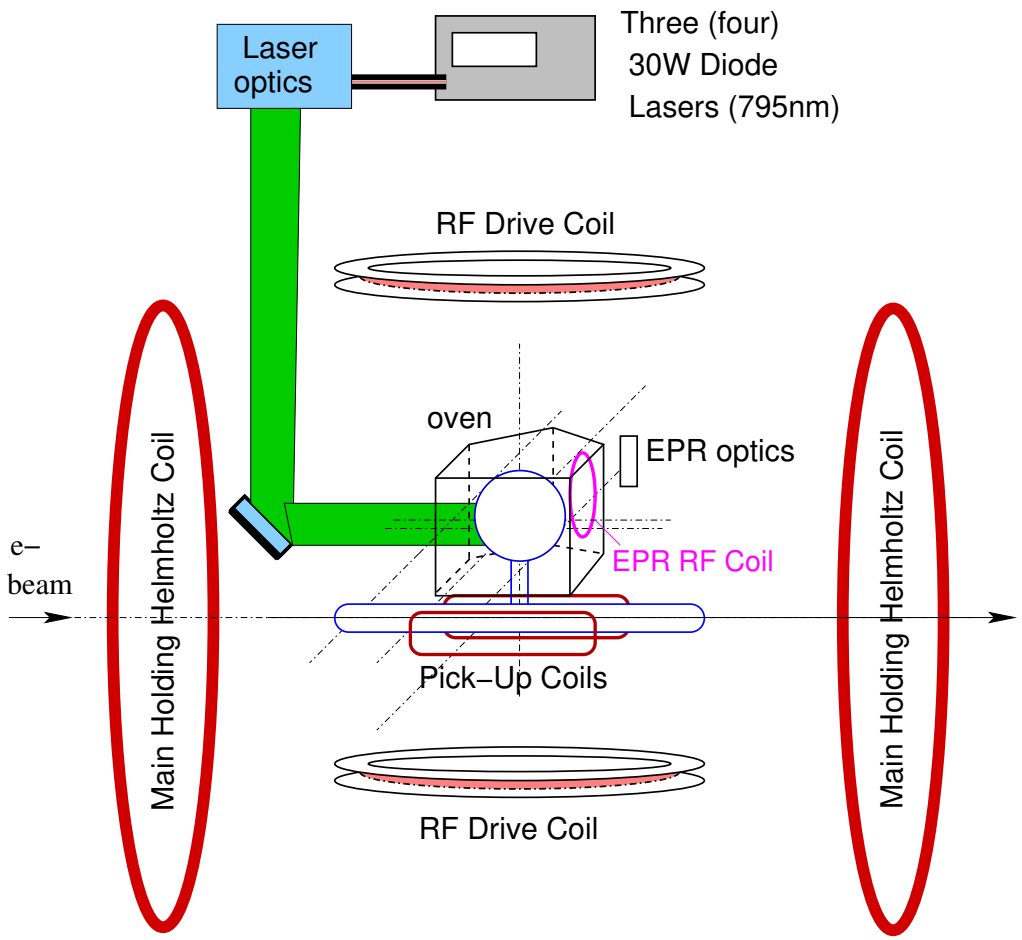

parallel to the beamline. So the holding field can be configured in any direction in the horizontal plane with respect to the incident electron beam.

The target setup in the hall is shown in Figure 4-8. To protect the diode lasers from radiation damage due to the electron beam, as well as to minimize the safety issue related to the laser hazard, the diode lasers and associated optics system were enclosed in a concrete hut located on the right side of the beamline. This concrete hut is usually called "the laser hut". Viewing from the top, see Figure 4-9, the right HRS was limited to a maximum scattering angle of about 50° because of the laser hut. This maximum angle was sufficient for the A_1^n experiment.

Figure 4-7: Helmholtz coil orientation and the field coordinate system (topview).

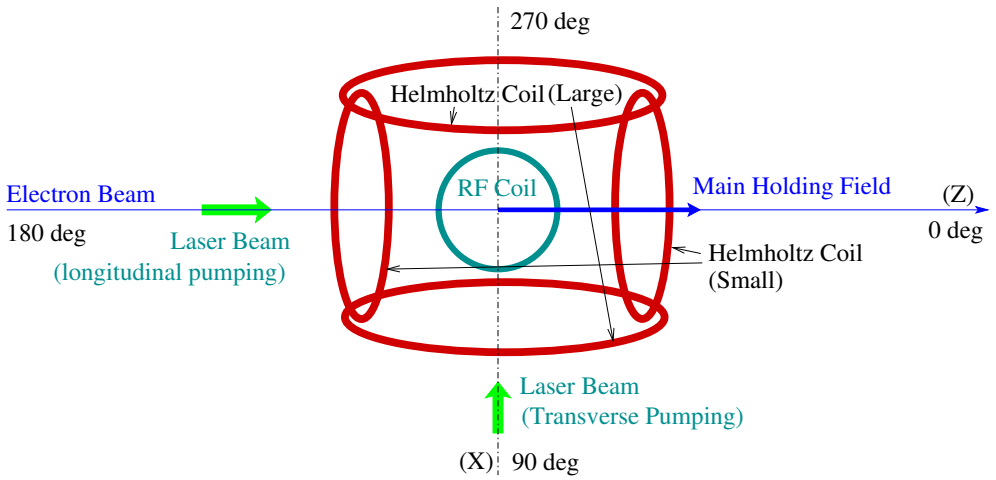

Figure 4-8: Target setup in Hall A, the laser hut and the target.

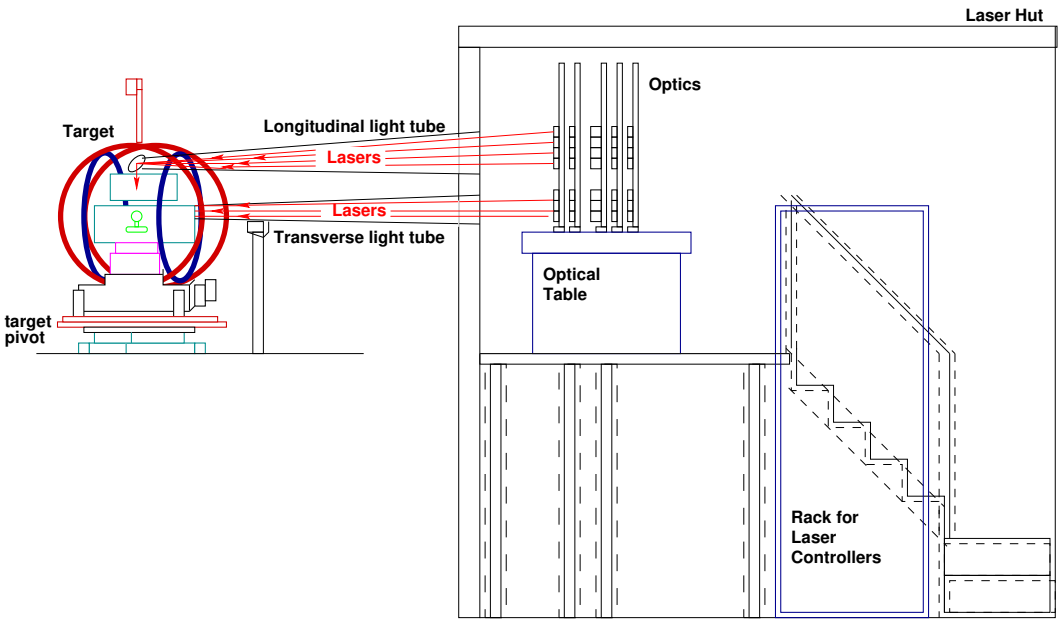

Figure 4-9: Target setup in Hall A, the laser hut and the right spectrometer (topview)

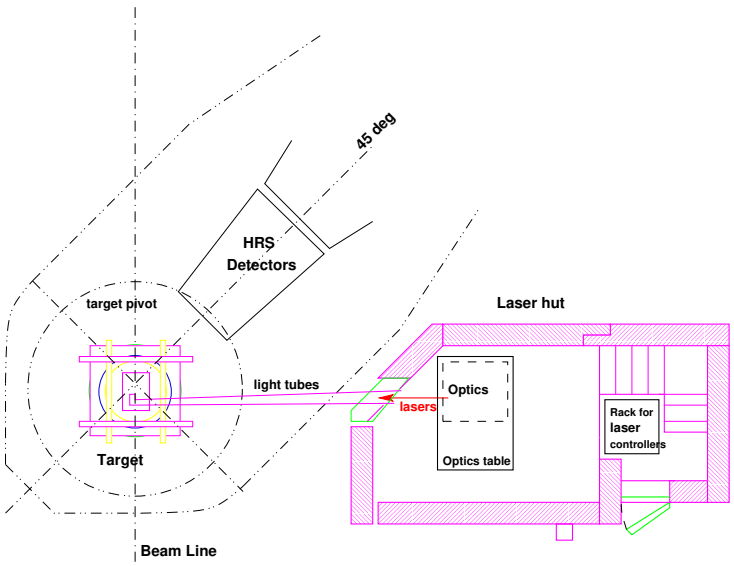

4.4 Laser System

The laser system used during the A_1^n and g_2^n experiments consists of seven 30 W diode lasers, three for longitudinal pumping, three for transverse pumping and one spare. Therefore the laser optics had seven individual lines, each associated with one diode laser. All these seven lines were identical and were placed one on top of the other (see Figure 4-8). Figure 4-10 shows the schematic diagram for the laser optics of one line. The laser beam going out from the laser fiber has an angular divergence of $\sim \pm 15°$. A focusing lens is placed at a distance equals to its focal length (8.83 cm) away from the laser fiber, such that the laser becomes a parallel beam with a diameter of ~ 1.6" after passing through the lens. Then the beam is split into two linearly polarized beams by a beam-splitter. The beam passing through the beam splitter is the P light which means its $\vec{E}$ component is polarized in the horizontal plane. This beam is reflected by a 3" diameter mirror and is circularly polarized by a quarter-wave ($\lambda/4$) plate (the right polarizing $\lambda/4$ plate). This is the beam path on the right side, as shown in Figure 4-10. The beam reflected by the beam splitter is the S light which means its $\vec{E}$ component is polarized in the vertical plane. A $\lambda/4$ plate and a mirror are used to change the polarization direction of the S light and reflect it back to the beam splitter. We refer to this $\lambda/4$ plate as the "back" $\lambda/4$ plate The fast and slow axes of the back $\lambda/4$ plate are oriented at an angle of 45° with respect to the horizontal plane. After passing through the back $\lambda/4$ plate, being reflected by the mirror, and passing through the back $\lambda/4$ plate the second time, the S light becomes P light and

Figure 4-10: Laser optics setup (schematic).

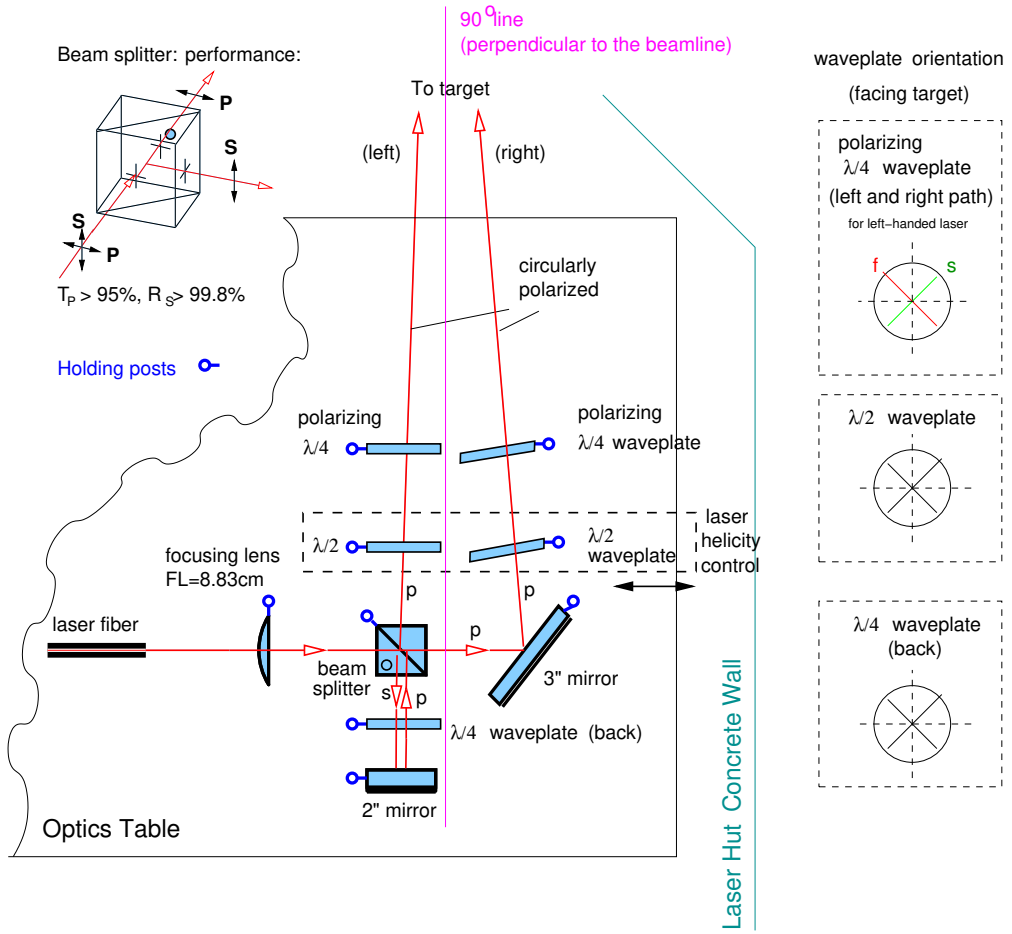

can pass through the beam splitter. It is then circularly polarized by a $\lambda/4$ plate (the left polarizing $\lambda/4$ plate) and forms the beam path on the left side, as shown in Figure 4-10. Both left and right beams are then going towards the target. To generate a left-handed circularly polarized laser beam, the slow axis of the right and the left polarizing $\lambda/4$ plates should be aligned to the 1:30 o'clock direction and the fast axis should be at the 4:30 o'clock, when viewing from the optics to the target. For a right-handed circularly polarized laser, the slow axis should be at the 4:30 o'clock direction and the fast axis should be at the 1:30 o'clock. There is one removable half-wave ($\lambda/2$) plate placed before the polarizing $\lambda/4$ plate for each path. It can be inserted into the laser beam path by remote control. The axes of this $\lambda/2$ plate are oriented at an angle of 45° with respect to the horizontal plane, so a left-handed circularly polarized laser beam becomes right-handed circularly polarized after passing through

the $\lambda/2$ plate. These $\lambda/2$ plates were used to rotate the target spin direction. For example, during the A_1^n experiment left-handed laser beams were needed to polarize the target in the 0° direction (parallel to the beamline) or 270° (perpendicular to the beamline and pointing to the left); while right-handed lasers were needed for 180° (anti-parallel to the beamline) or 90° (perpendicular to the beamline and pointing to the right). During the A_1^n experiment, these $\lambda/2$ plates were inserted for half of the data taking period so as to cancel possible systematic effects related to the target spin direction.

All optics components were placed on a optics table inside the laser hut. Under the operating conditions for either longitudinal or transverse pumping, the original beam of each diode laser was split into two beams so there are a total of six polarized laser beams going to the target. For transverse pumping, all these laser beams went directly towards the pumping chamber of the cell through a window on the side of target scattering chamber enclosure. For longitudinal pumping, they were guided towards the top of the scattering chamber, where they were reflected two times and finally reached the cell pumping chamber. The target was about 5 m away from the optical table. For longitudinal pumping the laser beam traversed a distance of about 6 m before they reached the cell. This made the focusing a little more difficult than in the case of transverse pumping.

4.5 NMR Polarimetry

The polarization of ^{3}He can be determined by measuring the ^{3}He Nuclear Magnetic Resonance (NMR) signal. The principle of NMR polarimetry is the spin reversal of ^{3}He nuclei using the Adiabatic Fast Passage (AFP) [122] technique. This spin reversal will induce an electromagnetic field and a signal in a pair of pick-up coils. The signal magnitude is proportional to the polarization of ^{3}He and can be calibrated by performing the same measurement on a water sample, whose thermal polarization can be calculated.

4.5.1 Principle

Classically, NMR-AFP is described by considering one free particle with spin $\vec{I}$ and magnetic moment $\vec{M} = \gamma\vec{I}$, where γ is the gyro-magnetic ratio. When this particle is placed in a magnetic field $\vec{H}$, its moment experiences a torque

$$\frac{\mathrm{d}\vec{M}}{\mathrm{d}t} = \gamma\vec{M} \times \vec{H} \ . \tag{4.17}$$

To simplify the procedure, it is useful to transform this equation into a frame that is rotating at a frequency and direction given by $-\vec{\omega}$. In this rotating frame Eq. (4.17)

becomes [123]

$$\frac{\partial \vec{M}}{\partial t} = \gamma \vec{M} \times \left(\vec{H} - \frac{\vec{\omega}}{\gamma} \right) . \tag{4.18}$$

The magnetic field $\vec{H}$ in Eq. (4.17) is now replaced by an effective field comprised of the laboratory field and a fictitious field, $\vec{H}_e = (\vec{H} - \frac{\vec{\omega}}{\gamma})$.

When performing an NMR measurement during the experiment, the holding field was always oriented parallel to the beamline, which is in the z-direction of the laboratory frame and can be written as $H_z \hat{e}_z$. An RF field was applied in the x (vertical) direction, $\vec{H}_{RF} = 2H_1 \cos(\omega_0 t)\vec{e}_x$. The RF field can be expressed in terms of two counter-rotating components

$$\vec{H}_{RF} = H_1 \hat{e}'_+ + H_1 \hat{e}'_- , \tag{4.19}$$

where $\hat{e}'_\pm = \cos(\omega_0 t)\hat{e}_x \pm \sin(\omega_0 t)\hat{e}_y$. One of these two components, for example $\hat{e}'_-$, rotates in the opposite direction to that of the magnetic moment. It does not play any role and will not be considered anymore.

If $\vec{\omega}$ is set to $\omega_0 \hat{e}_z$, then the effective field in the rotating system becomes

$$\vec{H}_e = \left(H_z - \frac{\omega_0}{\gamma} \right) \hat{e}_z + H_1 \hat{e}'_+ , \tag{4.20}$$

where $\langle \vec{M} \rangle$ is the ^{3}He average magnetic moment which aligns itself with the effective field.

During AFP, the holding field changes in magnitude such that it passes through the value $|\omega_0/\gamma|$. The angle between $\langle \vec{M} \rangle$ and the z-axis increases until $H_z = \omega_0/\gamma$ and the spins are at an angle of 90° with respect to the z-axis. The RF field has a magnitude of $H_1 = 100$ mGauss and its frequency is $f_{RF} = 91$ kHz. From $\omega_0 = 2\pi f_{RF}$ and $\gamma = -20378$ Hz/Gauss for ^{3}He, one obtains $|\omega_0/\gamma| = 28.06$ Gauss. When this resonance condition is met, the ^{3}He average magnetic moment $\langle \vec{M} \rangle$ induces an electromagnetic force and generates a signal in the pickup coils located on both sides of the target chamber. As the holding field increases further and beyond $|\omega_0/\gamma|$, the spins end up pointing in the opposite direction. This process is called a spin flip. Figure 4-11 shows the principle of the AFP technique described above.

A measurement of the ^{3}He polarization is performed by scanning the holding field from 25 to 32 Gauss and back, resulting in two spin flips, inducing an electromotive forced (EMF) signal twice. The signal height is proportional to the transverse component of the magnetization:

$$S_{\mathrm{He}}^{\mathrm{NMR}}(t) \propto \frac{\langle \vec{M} \rangle H_1}{\sqrt{(H_0(t) - \frac{\nu_{RF}}{\gamma_{^3\mathrm{He}}})^2 + H_1^2}} , \tag{4.21}$$

Figure 4-11: Principle of ^{3}He spin reversal using Adiabatic Fast Passage (AFP).

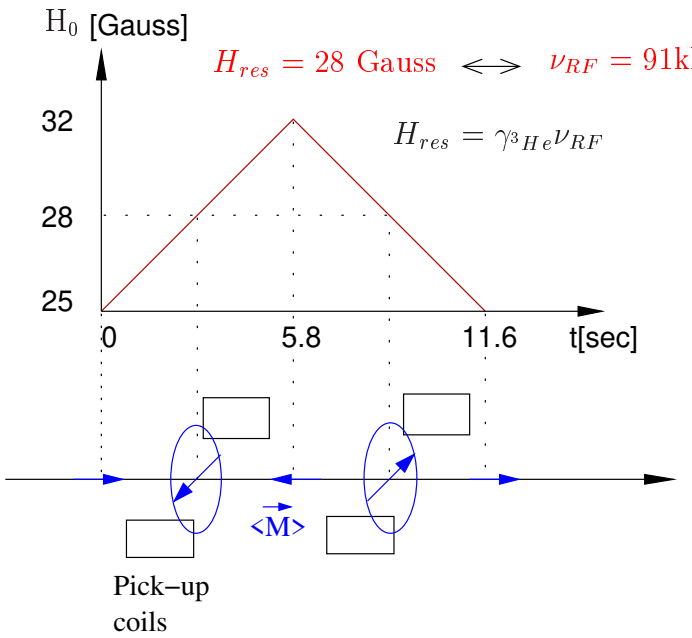

where

$$\langle \vec{M} \rangle \quad = \quad P_{\rm He}\mu_{\rm He}[^3{\rm He}] \ , \tag{4.22}$$

where $P_{\rm He}$ is the ^{3}He polarization and $\mu_{\rm He} = 6.706984 \times 10^{-14}$ MeV/T is the ^{3}He magnetic moment. A typical NMR signal $S(t)$ from the pick-up coil is shown in Figure 4-12. The resonance frequency is not exact 28.06 Gauss because of the drift in the RF field. Signals are fitted using Eq. (4.21) and the fitted amplitude is considered to be proportional to the polarization. The signal amplitude can be calibrated by performing the same measurement on a sample for which the polarization is well known, for example, a water sample, as will be described in the next two sections.

The change in the main holding field must satisfy the AFP condition – slow (adiabatic) enough so the ^{3}He spins can follow the magnetic field while sweeping, and fast enough so the ^{3}He spins do not relax. This can be described as

$$\frac{1}{T_{1r}} = \frac{D|\bigtriangledown H_z|^2}{H_1^2} \quad \ll \quad \frac{\dot{H}_z}{H_1} \ll \omega_0 \ , \tag{4.23}$$

where $T_{1r} \approx 100$ s is the relaxation rate, D is the ^{3}He diffusion rate, $\omega_0 = 9100$ s^{-1} is the RF field frequency and $\frac{\dot{H}_0}{H_1} \approx 24$ s^{-1}. Conditions described by (4.23) can be easily

Figure 4-12: A typical NMR signal for ^{3}He. The resonance frequency is not exact 28.06 Gauss because of the field drifting.

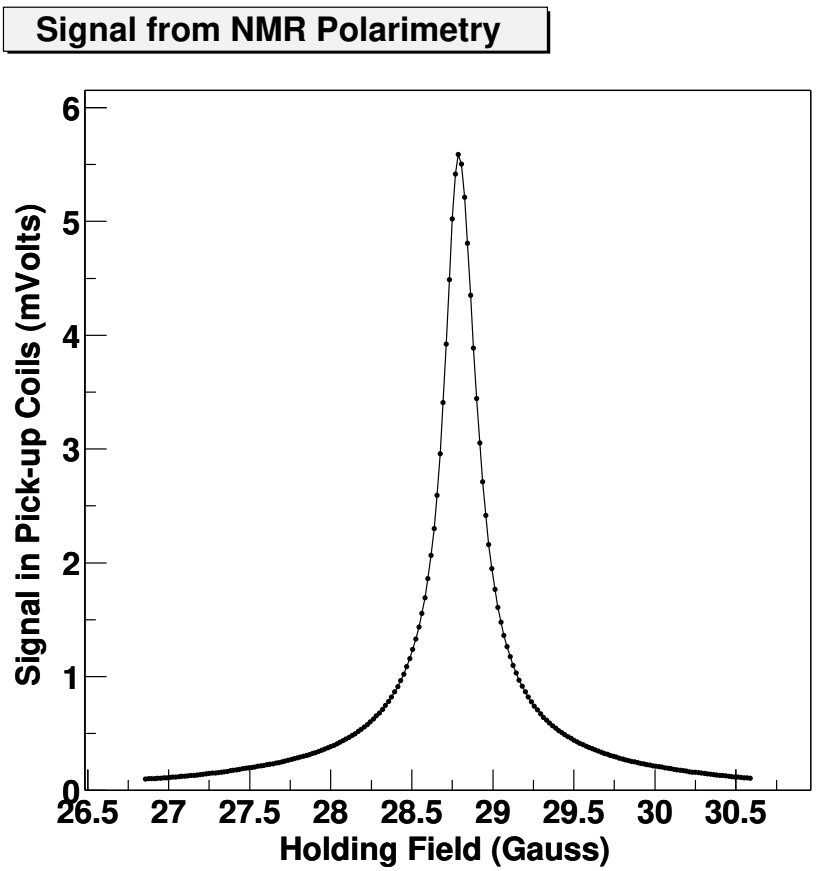

satisfied. More information about the NMR system can be found in [125].

4.5.2 Calibration

The calibration of the NMR system is aimed at finding the constant of proportionality, $\kappa_{\rm NMR}$, between the NMR signal height and the ^{3}He polarization

$$S_{\rm He} \;=\; \kappa_{\rm NMR} P_{\rm He}\ . \tag{4.24}$$

The constant of proportionality depends on several factors. Some of them are cell related, for example, the position, density and geometry of the cell. Other factors are independent of the target cell and measures the amount of signal seen by the NMR system for a given spin, or the responsiveness of the system. Therefore $\kappa_{\rm NMR}$ can be

divided into two parts

$$\kappa_{\rm NMR} \;=\; \kappa^* \Phi_{\rm He} G^Q_{\rm He} n_0 \left(\frac{n_c}{n_0}\right) \;, \tag{4.25}$$

where κ^* is the responsiveness of the system, $\Phi_{\rm He}$ is the geometrical flux produced by a particular cell, $G^Q_{\rm He}$ is a measure of the gain of the electronics, n_0 is the ^{3}He density of the cell at room temperature, and n_c is the average ^{3}He density between the pick-up coils under operating conditions. The purpose of the calibration is to determine κ^*, usually performed by measuring the thermal polarization of the protons in water.

4.5.3 Water Calibration

To do a water calibration, a cell with the same geometry as the ^{3}He cell was filled with de-oxygenated, de-ionized water. This water cell was mounted in the same setup as the ^{3}He cell, and NMR measurements were taken. The thermal polarization of protons in water is given by $P_{\rm thermal} = \tanh(\frac{\mu_p B}{k_B T})$, where $\mu_p = 2.793\mu_N$ is the proton magnetic moment, $\mu_N = 3.152454 \times 10^{-14}$ MeV/T is the nuclear magneton, $k_B = 1.38 \times 10^{-23}$ J/K is the Boltzmann constant and T is the temperature of water sample in K. For a holding field $B = 18$ Gauss and room temperature $T = 395$ K, $P_{\rm thermal} \approx 6.23 \times 10^{-9}$. This polarization can induce an AFP signal large enough to be used to calibrate the ^{3}He AFP signals. The AFP condition for the water sample is slightly different from that for ^{3}He. Since $\gamma = 26752$ Hz/Gauss for the proton, the resonance field for an RF frequency of 91 kHz is $H_{res} = 21.27$ Gauss. The holding field is therefore changing from 18 to 25 Gauss for the water sample. To increase the signal-to-noise ratio, usually several hundreds of sweeps are performed and the average signal is used for calibration. Figure 4-13 shows an AFP signal for a water calibration performed during the A_1^n experiment. It is the average signal from 500 sweeps.

Since the thermal relaxation time for a water sample is about 3 s, which is of the same order of magnitude as the holding field sweep time $T_{sweep} = 5.83$ s, water AFP signals cannot be described by Eq. (4.21). Relaxation during the sweep affects both the height and the shape of the AFP signal. It also makes the signal be dependent on the speed and the direction of the magnetic field sweep. In order to relate the water AFP signal with its thermal polarization, the Bloch equations are used to describe the time evolution of the three components of the polarization (P_x, P_y, P_z) in the rotating frame [122]

$$\begin{cases} \frac{{\rm d}P_x}{{\rm d}t} = \gamma P_y (H - H_0) - \frac{(P_x - \chi H_1)}{T_{2r}(H_1)} \\ \frac{{\rm d}P_y}{{\rm d}t} = -\gamma P_x (H - H_0) + \gamma P_z H_1 - \frac{P_y}{T_{2r}(H_1)} \\ \frac{{\rm d}P_z}{{\rm d}t} = -\gamma P_y H_1 - \frac{P_z - \chi H}{T_{1r}} \\ H = H_0 + \alpha t \end{cases}$$

where T_{1r} is the longitudinal relaxation time, $T_{2r}(H_1)$ is the transverse relaxation

Figure 4-13: NMR signal on a water sample.

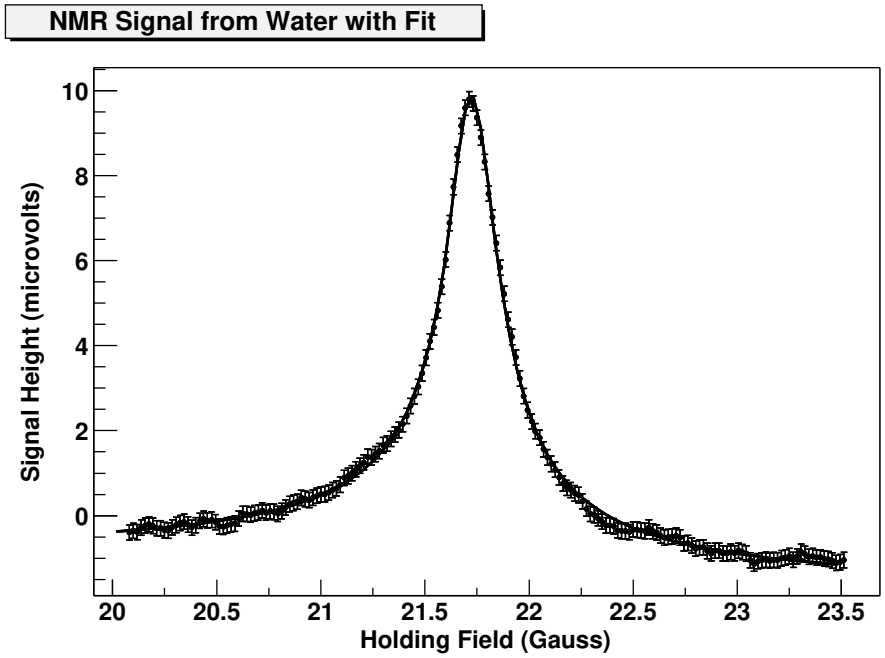

time in the presence of the rotating magnetic field H_1, and $\chi = \mu_p/k_BT = 3.4616 \pm 0.0117 \times 10^{-10}$ G^{-1} at 22°C is the magnetic susceptibility of the proton. Because of the presence of ^{17}O isotope in natural water, T_{2r} is slightly smaller than T_{1r}. For neutral (i.e. pH = 7.0) water $1/T_{2r} = 1/T_{1r} + 0.125$ s^{-1} [124].

The Bloch equations do not have an analytic solution. However, they can be solved numerically in order to determine the shape and the height of the resonance signal under different conditions. It was found that T_{2r} does not significantly affect the shape of the signal but it does affect the height. In order to find an analytic solution to fit the data, we first assume $T_{1r} = T_{2r}$ and the polarization follows the effective magnetic field $\vec{H}_{eff} = (H - H_0)\hat{e}_z + H_1\hat{e}'_+$ provided that the adiabatic conditions are satisfied. In this case the set of Bloch equations reduces to one equation

$$\begin{aligned} \frac{\mathrm{d}P_{eff}}{\mathrm{d}t} &= \frac{1}{T_1}\Big(P_{eq}(t) - P_{eff}\Big) \ , \\ \text{where } P_{eq}(t) &= \chi\left(\frac{H(H-H_0)+H_1^2}{\sqrt{H_1^2+(H-H_0)^2}}\right) \ . \end{aligned} \tag{4.26}$$

The integral form of the solution is

$$P(t) = e^{-(t-t_0)/T_1}\left(P(t_0) + \frac{1}{T_1}\int_{t_0}^{t} e^{(t'-t_0)/T_1}P_{eq}(t)\mathrm{d}t'\right) \ . \tag{4.27}$$

By expanding the exponential and the denominator of $P_{eq}(t)$ to the first order in t', the integral can be solved, which gives an approximate analytic solution to the Bloch equations. The analytic solution allows one to fit the water signal and determine the signal height. Since the AFP signal is proportional to the spin magnetization, one can scale the water signal to calculate the calibration constant C_w between the ^{3}He signal height $S_{\rm He}$ and the polarization $P_{\rm He}$ using $P_{\rm He} = \kappa_w S_{\rm He}$, where w stands for water calibration. A complete water calibration analysis can be found in [125].

4.5.4 NMR with Field Gradient

The field gradient should always be kept small in order to maintain a high target polarization, see Eq. (4.16). However, during the A_1^n and g_2^n experiments, a field gradient was introduced intentionally to prevent the polarization from being destroyed by the masing effect, as will be described in Section 4.7.2. With a large field gradient, the spin relaxation time of ^{3}He is smaller and is comparable to the AFP sweep time. In this case, Eq. (4.21) cannot describe the AFP signal shape. Similar to water signal analysis, one can use the Bloch equations to describe the behavior of ^{3}He spins in the presence of a large field gradient and find an analytic solution. A detailed analysis can be found in [125].

4.6 EPR Polarimetry

4.6.1 Principle

In the presence of a magnetic field $\vec{B}$, the $F = 3$ state of Rb splits into seven sublevels $M_F = -3, -2, \cdots, 2, 3$. The Zeeman splitting between $F = 3, M_F = -3$ and $F = 3, M_F = -2$ sublevels, described by the Electron-Paramagnetic Resonance frequency ν_{EPR}, is proportional to the magnitude of the $\vec{B}$ field. When ^{3}He nuclei are polarized ($P \sim 40\%$), their spins can generate a small magnetic field $B_{^3\rm He}$, of an order of ~ 0.1 Gauss, in addition to the main holding field $B_H = 25$ Gauss. The EPR polarimetry [133] measures this small component of the Zeeman splitting $\delta\nu_{EPR}$, which is proportional to the polarization of ^{3}He. The EPR frequency can be decomposed as

$$\nu_{EPR} \;=\; \nu_0 \pm \delta\nu_{EPR} \;, \tag{4.28}$$

where $\nu_0 \propto B_H$ and $\delta\nu_{EPR} \propto B_{^3\rm He} \propto P_{^3\rm He}$, with $+(-)$ sign corresponds to the ^{3}He spin being antiparallel (parallel) to the main holding field.

Since the measured frequency shift $\delta\nu_{EPR}$ is a small component compared to the main component ν_0 generated by the main holding field, during an EPR measurement the ^{3}He spins are reversed by AFP. During a spin reversal the large component ν_0 cancel and the frequency shift $\delta\nu_{EPR}$ is measured directly.

4.6.2 Setup

Two major techniques of an EPR measurement are the ^{3}He spin reversal and the measurement of the Rb EPR resonance frequency. The EPR polarimetry shares the RF coils with NMR for AFP spin reversal. Unlike NMR, during an EPR measurement the frequency of the vertical RF field is ramped through the ^{3}He resonance (81 KHz for a 25 Gauss field) and the main holding field stays unchanged.

The measurement of the Rb Zeeman transition resonance frequency is based on an assumption that under regular operating conditions the Rb polarization is very high ($> 90\%$), so most of the electrons stay in the $F = 3, M = -3$ state and cannot absorb polarized light. If an additional magnetic field is applied at the EPR resonance frequency, then the electrons will try to be equally distributed between $F = 3, M = -3$ and $F = 3, M = -2$ states under this perturbation. Electrons in the $F = 3, M = -2$ state can further undergo an optical transition and emit D_2 light with a wavelength of 785 nm. This perturbation field, also called the EPR RF field, greatly increases the electron population in the $F = 3, M = -2$ state. The increase in D_2 light is large enough to be measured by a photodiode [126]. One can therefore modulate the frequency of EPR RF field around the Rb EPR resonance frequency, and determine the Rb EPR resonance frequency by detecting the correlation between the strength of D_2 light and the modulated frequency, as will be described in Section 4.6.3.

The small perturbation field is generated by an EPR RF coil. During the A_1^n

Figure 4-14: EPR Optics setup in hall, during summer 2001.

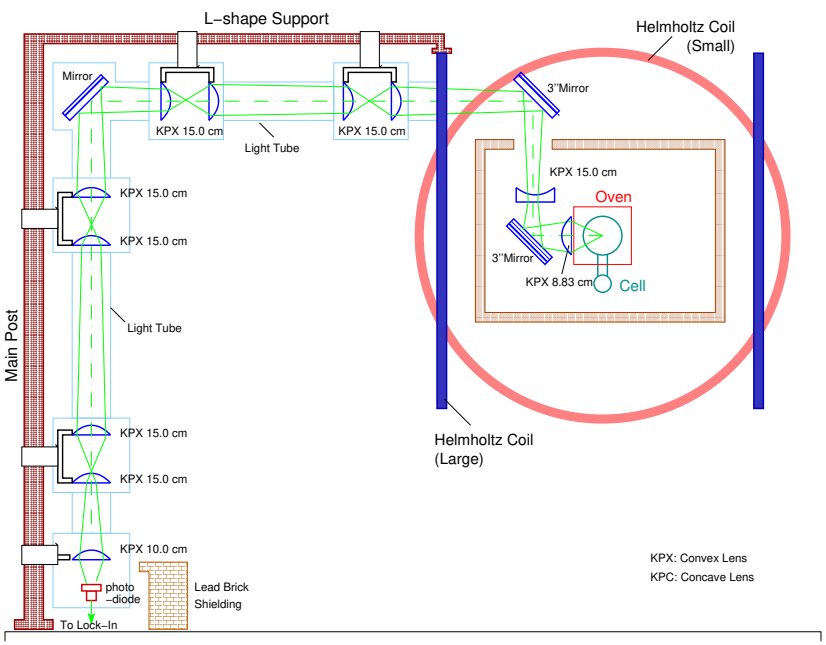

and g_2^n experiments it was a 10 turns coil with a diameter of about 3 inches, attached vertically to a window at the right downstream side of the oven. The EPR RF coil was connected to a function generator (Wavetek80) [128], which was set at voltage controlled output (VCO) mode and was modulated by a function generator (DS345) [128]. The EPR RF field is swept at a frequency of 200 Hz around 11.85 MHz. The D_2 light from target cell has a wavelength of 785 nm. To minimize the radiation damage to the photodiode, the D_2 light from the target cell was focused and guided by an EPR optics system, as shown in Figure 4-14, to 5 m away from the target. Lead bricks were placed around the photodiode to protect it from radiation damage. To detect the D_2 light under a strong D_1 (795 nm) background, a D_2 filter [127] was attached to the photodiode. The signal from the photodiode was sent to a lock-in amplifier (SR844) [128] from which the D_2 signal is extracted.

4.6.3 EPR Frequency Modulation Sweep

The EPR Frequency Modulation (FM) Sweep is used to find the D_2 signal, measure the Rb EPR resonance shape and determine the resonance frequency. It is not for the polarization measurement but was regularly performed during the experiment to monitor changes in the D_2 signal and the Rb resonance frequency. Usually the main

Figure 4-15: EPR frequency modulation sweep setup.

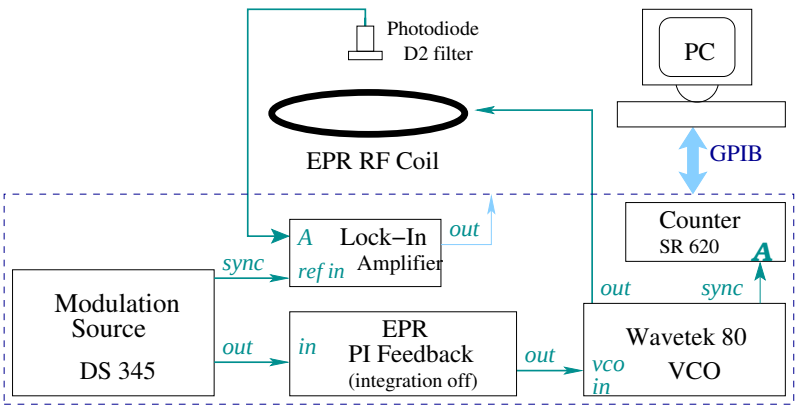

holding field is stable and so is the value of the resonance frequency. However, after target configuration changes, for example, field rotation, cell change, replacement of the photodiode, adjustment of the laser or EPR optics system, an FM sweep is necessary to check possible changes. Figure 4-15 shows the setup for the FM sweep measurement. The signal from the photodiode is fed into a lock-in amplifier and is recorded by the computer. There is no feedback from this signal to the modulation source for the EPR RF field frequency. The output of lock-in amplifier directly shows

Figure 4-16: A typical frequency modulation sweep spectrum.

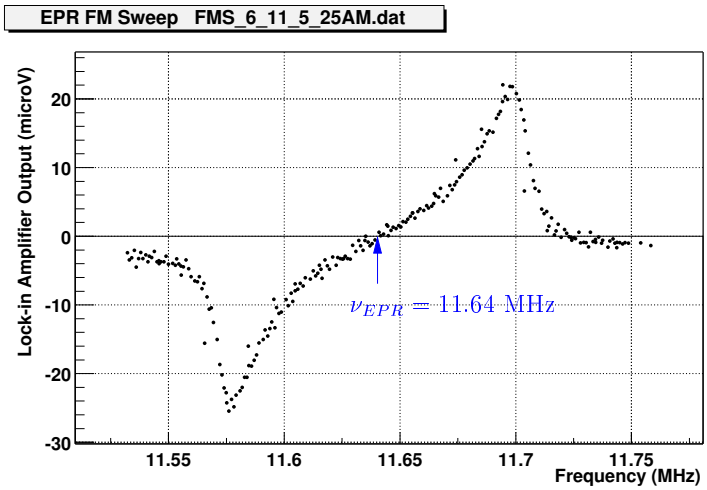

the shape of the Rb resonance. Figure 4-16 shows a typical spectrum of an FM sweep measurement, of which the zero crossing point gives the Rb resonance frequency.

4.6.4 EPR AFP Sweep

The EPR AFP sweep is used to measure the ^{3}He polarization. During an EPR AFP sweep measurement, the signal from the photodiode is sent to a lock-in amplifier, by which the D_2 signal is extracted. The D_2 signal is then fed to a Proportional-Integral (PI) feedback unit and is mixed with the modulation source output. The mixed signal from the PI unit is used to modulate the Wavetek80 frequency, which is the frequency of the EPR RF field. This way the system forms a closed feedback loop, so the Wavetek80 frequency is locked to the EPR resonance frequency of the Rb. Once this lock is formed, the ^{3}He spins are reversed by sweeping the frequency of the vertical RF field from 71 MHz to 91 MHz. Figure 4-17 shows the setup of AFP sweep and Figure 4-18 shows a typical spectrum of an AFP sweep measurement.

Settings for the instruments are given below. Details of each device can be found in [128].

1. RF generator (HP3324A)

   - Sweep frequency: 71 kHz $\sim$ 91 kHz;
   - Amplitude: 2.4 V_{rms};
   - Sweep time: 6$\sim$8 s.

Figure 4-17: EPR AFP sweep setup.

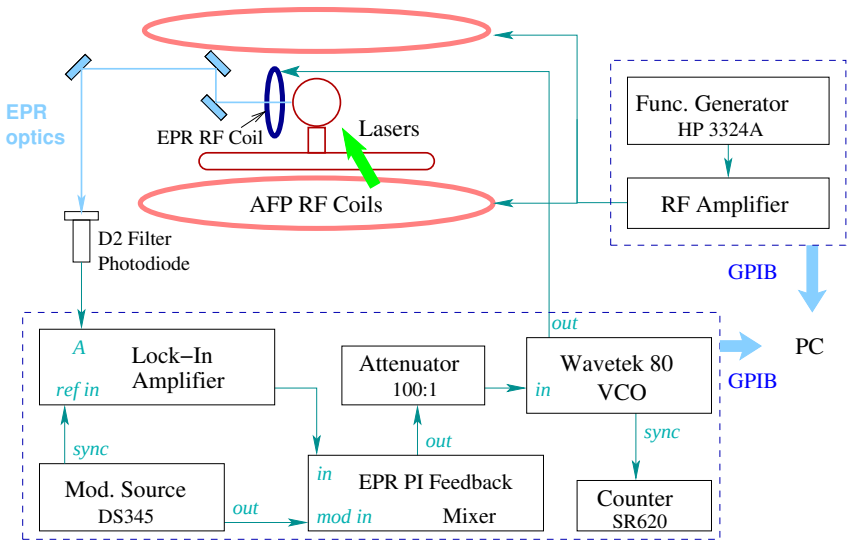

2. Modulation source (DS345)

   - Frequency: 200 Hz;
   - Amplitude: $>$ 0.4 Vpp for polarization $\sim$ 30%, 1.0 Vpp for $>$ 40%;
   - Function: sine wave;
   - Sweep/modulate: LIN SWP.

   At high polarization the EPR frequency shift is large. If the amplitude of the modulation source is not large enough then the PI feedback cannot lock to the EPR frequency when it changes very fast or changes by a large amount.

3. Sweep generator (Wavetek80)

   - Frequency: 11.65 MHz;
     It should be close to the resonance frequency but has a non-zero value in the EPR line-shape. Usually it was set to be 200 KHz below the resonance, which was $11.85 - 0.20 = 11.65$ MHz during A_1^n experiment;
   - Amplitude: 16.00 V;
     The EPR RF field is proportional to this value. It also depends on the configuration of the EPR coil;
   - Modulation Mode: VCO;
   - Output: sine wave;

Figure 4-18: A typical spectrum of EPR AFP sweep measurement.

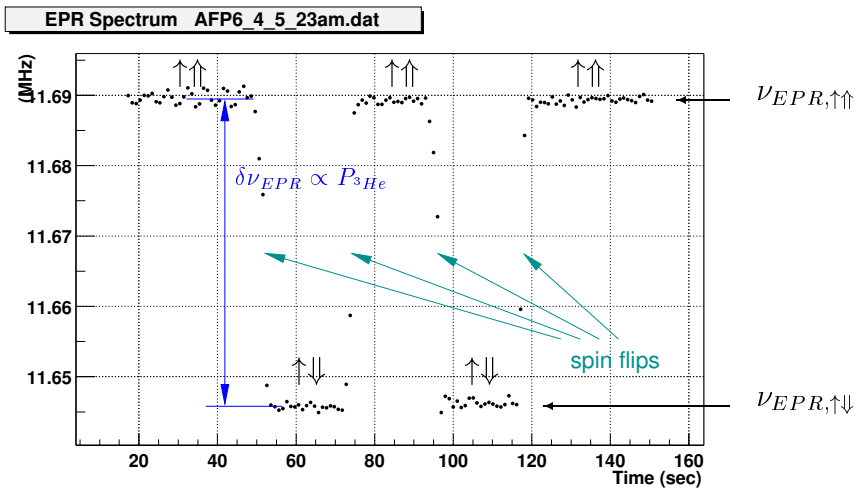

- Operating mode: FUNC.

4. Lock-in Amplifier (SR844)

   - AC Gain: 50 dB;
   - Input Limit: 10 mV;
   - Sensitivity: 1 mV;
   - DR 16;
   - Time Constant: 100 ms;
   - Osc: 0.000 Hz;
   - Reference source: ext.;

   The time constant should be small so the lock-in can follow the input signal, and should be much larger than the period of the modulation source, $1/(200\text{ Hz}) = 5$ ms.

4.6.5 EPR Analysis

The energy spectrum of the Rb ($I_{Rb} = 5/2$) atoms in a magnetic field can be described exactly by the Breit-Rabi formula [129]

$$E_{F=I\pm\frac{1}{2},m_F} = -\frac{\Delta E_{hf}}{2(2I+1)} + g_N\mu_N B m_F$$

$$\pm\frac{\Delta E_{hf}}{2}(1+\frac{4m_F}{2I+1}x+x^2)^{\frac{1}{2}} \ ,$$

where $x \equiv (g_S\mu_B - g_{\rm Rb}\mu_N)B/\Delta E_{hf}$.

During the A_1^n and g_2^n experiments, Rb atoms were always polarized to the $F = 3, m_F = -3$ state. The EPR resonance frequency is given by the energy splitting between $F = 3, m_F = -3$ and $F = 3, m_F = -2$ states as

$$\nu_{EPR} \ = \ E_{F=3,m_F=-2} - E_{F=3,m_F=-3} \ . \tag{4.29}$$

The EPR full frequency shift during the measurement is given by the difference in ν_{EPR} before and after the spin flip. It is related to the pumping chamber ^{3}He polarization P_p as

$$2\Delta\nu \ = \ 2\times\frac{2\mu_0}{3}\frac{{\rm d}\nu_{EPR}}{{\rm d}B}\kappa\mu_{\rm He}n_pP_p \ . \tag{4.30}$$

In the following we describe how to obtain the quantities on the right hand side of Eq. (4.30).

EPR Frequency Shift $2\Delta\nu$

The EPR frequency shift $2\Delta\nu$ can be obtained by fitting to an EPR AFP sweep spectrum, using either a constant or a linear function. The main component of the EPR resonance frequency associated with the main holding field is

$$\nu_{EPR} = \frac{\nu_{EPR,\uparrow\Uparrow} + \nu_{EPR,\downarrow\Uparrow}}{2} \ , \tag{4.31}$$

where $\nu_{EPR,\uparrow\Uparrow}$ and $\nu_{EPR,\downarrow\Uparrow}$ are the fitted frequencies before and after the spin flip, as shown in Figure 4-19. We denote $\Delta\nu_1$ and $\Delta\nu_2$ half of the frequency shifts of the first and the second spin flips, respectively:

$$\begin{cases} 2\Delta\nu_1 = \nu_{EPR,\uparrow\Uparrow} - \nu_{EPR,\downarrow\Uparrow} & \text{first flip} \\ 2\Delta\nu_2 = \nu_{EPR,\uparrow\Uparrow} - \nu_{EPR,\downarrow\Uparrow} & \text{second flip} \ . \end{cases}$$

We take the average of these two as the EPR resonance frequency shift

$$2\Delta\nu \ = \ \frac{\frac{\Delta\nu_1}{\left(\delta(\Delta\nu_1)\right)^2} + \frac{\Delta\nu_2}{\left(\delta(\Delta\nu_2)\right)^2}}{\frac{1}{\left(\delta(\Delta\nu_1)\right)^2} + \frac{1}{\left(\delta(\Delta\nu_2)\right)^2}} \ , \tag{4.32}$$

where $\delta(\Delta\nu_1)$ and $\delta(\Delta\nu_2)$ are the errors of $\Delta\nu_1$ and $\Delta\nu_2$, respectively. The error in

$\Delta\nu$ is given by

$$2\delta(\Delta\nu) = \frac{1}{\frac{1}{\left(\delta(\Delta\nu_1)\right)^2} + \frac{1}{\left(\delta(\Delta\nu_2)\right)^2}} . \tag{4.33}$$

Figure 4-19: EPR frequency shift spectrum

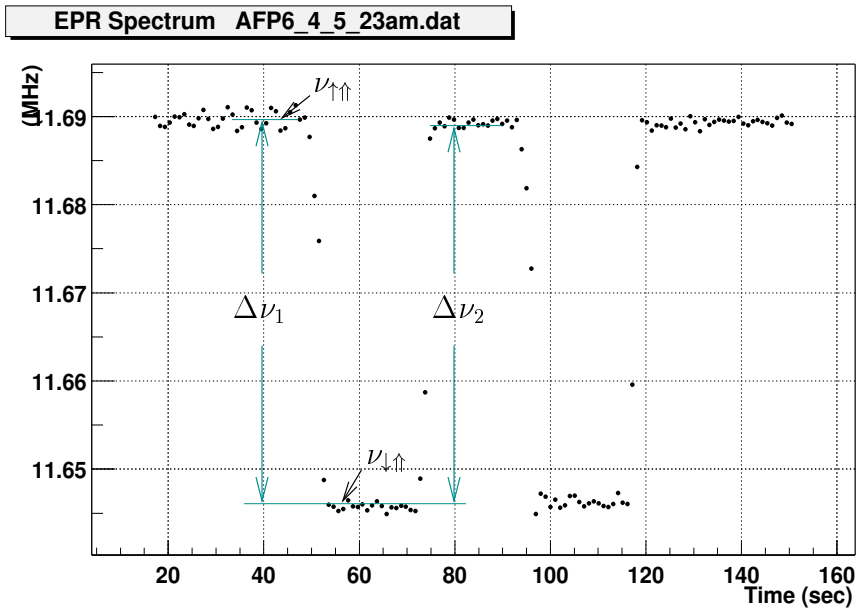

Cell Densities n_p and n_t

The pumping chamber and target chamber densities, n_p and n_t, respectively, can be calculated from the cell density at room temperature n_0, the pumping chamber and target chamber interior temperatures T_p and T_t, the pumping chamber and target chamber volumes V_p and V_t, and the cell total volume V_{tot} as

$$n_p = \frac{n_0}{1 + \frac{V_t}{V_{tot}}(\frac{T_p}{T_t} - 1)} \quad \text{and} \tag{4.34}$$

$$n_t = \frac{n_0}{1 + \frac{V_p}{V_{tot}}(\frac{T_t}{T_p} - 1)} . \tag{4.35}$$

The interior temperature T_p can be measured by the cell temperature test. There were seven temperature sensors (RTD) mounted on the cell during the experiment. RTD 1 to 5 were evenly placed on the target chamber, RTD 6 was placed at the top and RTD 7 at the bottom of pumping chamber, as shown in Figure 4-20. We denote the temperature measured by the i^{th} sensor as RTD_i in Kelvin. For the two cells

Figure 4-20: Location of temperature sensors on a 25 cm cell.

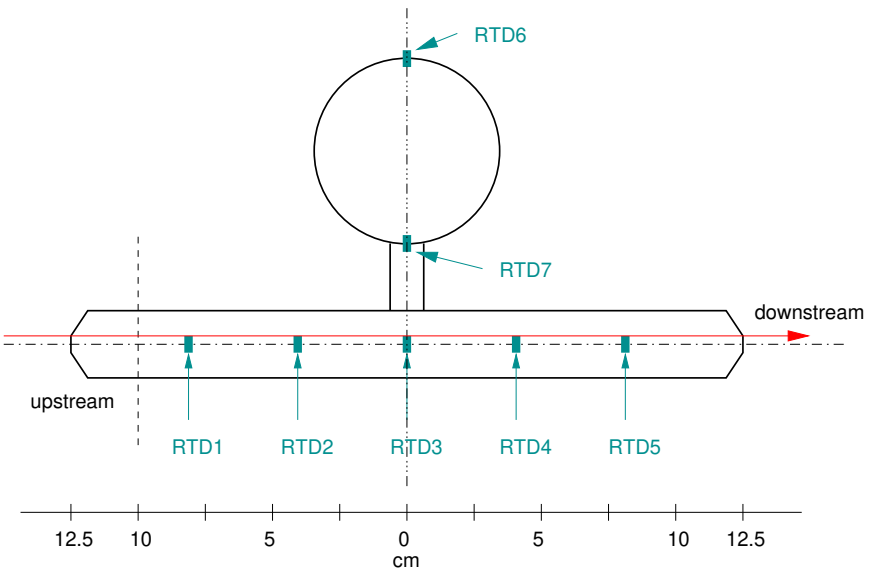

used during the A_1^n experiment the interior temperatures of the cell are given by [130]

$$\begin{aligned} T_p(K) &= 2.319\frac{RTD_6 + RTD_7}{2} - 569.9 \quad \text{for Gore ,} \\ &= 3.333\frac{RTD_6 + RTD_7}{2} - 1015. \quad \text{for Tilghman , and} \qquad (4.36) \\ T_t(K) &= \frac{3}{13}(RTD_2 + RTD_3 + RTD_4) + \frac{2}{13}(RTD_1 + RTD_5) \ . \qquad (4.37) \end{aligned}$$

The errors in the interior temperatures are $\Delta T_p = 10°\text{C}$ and $\Delta T_t = 2°\text{C}$.

The Holding Field B

The holding field B provided by the Helmholtz coils has been calibrated two times during during the A_1^n experiment. The field magnitude for longitudinal orientation is given by [131]

$$\begin{aligned} B_{\|} &= -3.4826 I_{\text{small}} - 0.0073 \ \text{ and} \\ B_{\perp} &= -3.3439 I_{\text{large}} - 0.2777 \ ; \qquad (4.38) \end{aligned}$$

and for transverse orientation

$$\begin{aligned} B_{\|} &= -3.5400 I_{\text{small}} - 0.0007 \ \text{ and} \\ B_{\perp} &= -3.4394 I_{\text{large}} - 0.2934 \ , \qquad (4.39) \end{aligned}$$

where $B_{\|}$ ($B_{\perp}$) is the field component parallel (perpendicular) to the beamline direction in Gauss, $I_{\rm small}$ ($I_{\rm large}$) is the current of the small (large) Helmholtz coils in Ampere. However, in addition to the main holding field, there exists a background field (from the natural earth field, field generated by spectrometers, etc.) which changes with time and cannot be calculated. A more precise way to determine the field magnitude B is to use EPR resonance frequency ν_{EPR}, which is directly related to the absolute value of B. We start from

$$\begin{aligned}
\nu_{EPR} &= E_{F=3,m_F=-2} - E_{F=3,m_F=-3} \\
&= g_N\mu_N B + \frac{\Delta E_{hf}}{2}\Big[(1+\frac{-8}{6}x+x^2)^{\frac{1}{2}} - (1+\frac{-12}{6}x+x^2)^{\frac{1}{2}}\Big] \ , \\
\text{obtain} \quad (\nu_{EPR} - g_N\mu_N B)\frac{1}{\Delta E_{hf}/2} &= \frac{2}{2I+1}x - \frac{2}{(2I+1)^2}(2m_F-1)x^2 \\
&\quad +(\frac{4(3m_F^2-3m_F+1}{(2I+1)^3} - \frac{1}{2I+1})x^3 + O(x^4) \ .
\end{aligned}$$

Neglecting $O(x^4)$ terms, B can be solved by iteration

$$\begin{aligned}
B^{(i)} &= (\frac{2I+1}{2\alpha})\Big[\frac{\nu_{EPR} - g_N\mu_N B^{(i-1)}}{\Delta E_{hf}/2} \\
&\quad +\frac{2(2m_F-1)}{(2I+1)^2}x_{(i-1)}^2 + (\frac{1}{2I+1} - \frac{4(3m_F^2-3m_F+1)}{(2I+1)^3})x_{(i-1)}^3\Big] \ , \quad (4.40)
\end{aligned}$$

with $\alpha \equiv (g_S\mu_B - g_{\rm Rb}\mu_N)/(\Delta E_{hf})$ and $x = \alpha B = 0.0023$ for a 25 Gauss holding field. Results for the field magnitude from the EPR resonance frequency are shown in Figure 4-21, along with field magnitude calculated from Eq. (4.38) and (4.39). The differences between the two show the effect of the background field.

The Derivative $\mathrm{d}\nu/\mathrm{d}B$

The derivative $\mathrm{d}\nu/\mathrm{d}B$ in Eq. (4.30) can be calculated from the absolute EPR resonance frequency ν_{EPR}. They can be fitted by linear functions and the results are [132]

$$\frac{\mathrm{d}\nu}{\mathrm{d}B} = \begin{cases}
0.4670779 + 7.37904\times10^{-4}B & \text{if } M_0 = -2 \\
0.4670779 + 4.25140\times10^{-4}B & M_0 = -1 \\
0.4670779 + 1.26135\times10^{-4}B & M_0 = 0 \\
0.4670779 - 1.59878\times10^{-4}B & M_0 = 1 \\
0.4670779 - 4.33604\times10^{-4}B & M_0 = 2 \\
0.4670779 - 6.95702\times10^{-4}B & M_0 = 3 \ ,
\end{cases}$$

where B is the field magnitude in Gauss, $\mathrm{d}\nu/\mathrm{d}B$ is in MHz/G. The error of the fit is negligible. The error of $\frac{d\nu}{dB}$ comes solely from the uncertainty in the field magnitudeΔB, which is of the order of $\Delta B/B = 1\times10^{-6}$, from Eq. (4.40).

Figure 4-21: Holding field magnitude during E99-117.

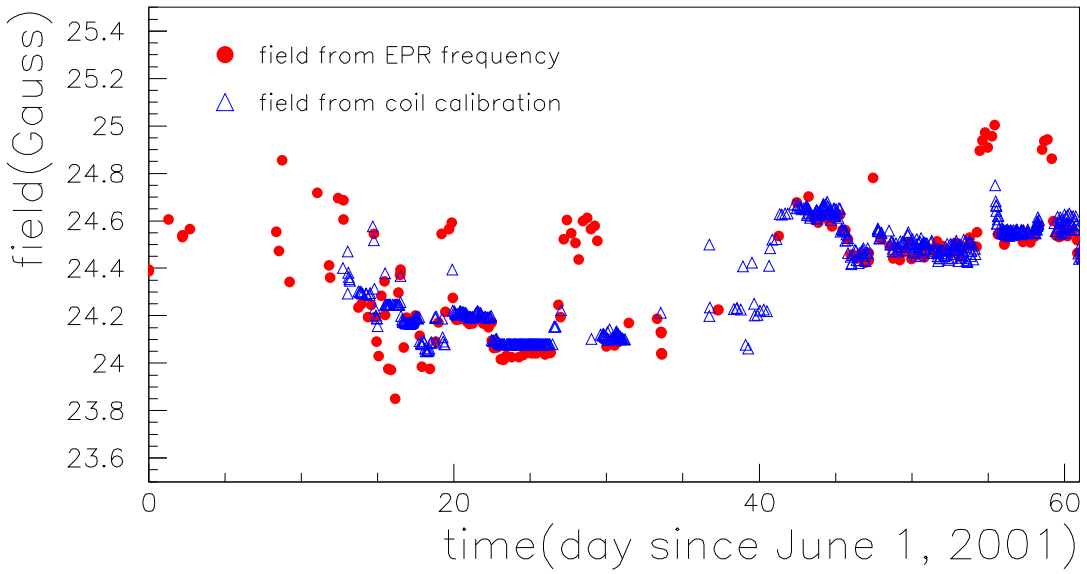

The Constant κ

The constant κ in Eq. (4.30) has been measured to be [133] $\kappa = 4.52 + 0.00934\ T_p$, where T_p is the pumping chamber temperature in °C. The systematic error of this measurement is $\delta\kappa/\kappa = 1.4\%$.

From the information listed in this section, one can calculate the statistical error (from the fits of AFP sweep spectrum) and the systematic error (from all sources above) for the pumping chamber polarization P_p.

4.6.6 Polarization Gradient

The EPR frequency shift is a measure of the polarization in the pumping chamber, while the electron beam interacts with ^{3}He in the target chamber. Since the ^{3}He gas is polarized in the pumping chamber and diffuses down, there is a constant polarization gradient between the two chambers. The evolution of the polarization with time is governed by a set of differential equations that includes spin exchange, spin relaxation and diffusion terms. We assume that the flux is constant along the transfer tube, i.e., neglect the volume of the transfer tube compared with the volume of the cell. We also assume that the temperature changes linearly along the tube and that the diffusion constant $D(T) = D(T_0)(T/T_0)^m$, with $T_0 = 80.0$°C and m a parameter to be determined empirically. One can show that the polarization evolutions in the pumping and target chambers due to diffusion are given by [102]

$$\frac{dP_t}{dt} = \frac{A_{Tr}D_t}{V_t L_{Tr}} K(P_p - P_t) \quad \text{and} \tag{4.41}$$

$$\frac{dP_p}{dt} = \frac{A_{Tr} D_t n_t}{V_p L_{Tr} n_p} K (P_p - P_t) \ , \tag{4.42}$$

where A_{Tr} and L_{Tr} are the cross section and the length of the transfer tube, $A_{Tr} = V_{Tr}/L_{Tr}$ with V_{Tr} the transfer tube volume, D_t is the diffusion constant in the target chamber and is inversely proportional to the pressure

$$D_t = D_{t,\ 1\ \mathrm{atm}} \frac{1\ \mathrm{atm}}{p_t} \ , \tag{4.43}$$

where p_t is the target chamber pressure given by $p_t = n_t R T_t$, $R = 8.3145$ J/(K·mol) is the molar gas constant. p_t can also be written as: $(1\ \mathrm{atm})/p_t = (1\ \mathrm{atm})/(n_t R T_t) = (n_0 R T_0)/(n_t R T_t)$, with $n_0 = 1\ \mathrm{atm}/(R T_0) = (1\ \mathrm{amg})(273.14\ \mathrm{K}/T_0) = 0.7733$ amg The diffusion constant at 1 atm $D_{t,1\ \mathrm{atm}}$ is obtained by fitting to diffusion constant data D_t [134]. A function

$$D_t = D_{t_0} (T_t/T_0)^m \tag{4.44}$$

has been used and the results are

$$\begin{aligned} D_{t_0}^{^3\mathrm{He}} &= D_{t_0}^{^4\mathrm{He}} \times \frac{\sqrt{M_{^4\mathrm{He}}}}{\sqrt{M_{^3\mathrm{He}}}} = (2.4153 \pm 0.0060) \times \sqrt{\frac{4}{3}}\ \mathrm{cm}^2/\mathrm{s} \\ &= 2.7889 \pm 0.0069\ \mathrm{cm}^2/\mathrm{s} \ \text{ at } T_0 = 80.0^\circ\mathrm{C} = 353.14\ \mathrm{K} \ , \ \text{ and} \qquad (4.45) \\ m &= 1.7048 \pm 0.0025 \ . \qquad (4.46) \end{aligned}$$

Note that only ^{4}He data are available and ^{3}He data can be deduced by applying a scaling factor $1/\sqrt{M}$. Now one obtains

$$D_t = D_{T_0} (T_t/T_0)^{m-1} \frac{n_0}{n_t} \ . \tag{4.47}$$

The dimensionless parameter K in Eq. (4.41) and (4.42) is given by

$$K = \frac{(m-2)(T_t - T_p) T_t}{\left[(\frac{T_t}{T_p})^m T_p^2 \right] - T_t^2} \ . \tag{4.48}$$

Combining Eq.(4.41) and (4.42) with the spin exchange and relaxation terms one finds

$$\begin{aligned} \frac{dP_p}{dt} &= d_p (P_t - P_p) + \bar{\gamma}_{SE} (P_{\mathrm{Rb}} - P_p) - \Gamma_p P_p \ \text{ and} \qquad (4.49) \\ \frac{dP_t}{dt} &= d_t (P_p - P_t) - \Gamma_t P_t \ , \qquad (4.50) \end{aligned}$$

where d_p and d_t are the reduced diffusion constants given by

$$d_p = \frac{A_{Tr} D_t n_t}{V_p L_{Tr} n_p} K \quad \text{and} \tag{4.51}$$

$$d_t = \frac{A_{Tr} D_t}{V_t L_{Tr}} K \ . \tag{4.52}$$

The volume averaged spin exchange rate $\bar{\gamma}_{SE}$ is given by

$$\bar{\gamma}_{SE} = \gamma_{SE} \frac{n_p V_p}{n_p V_p + n_t V_t} \ , \tag{4.53}$$

with γ_{SE} from Eq. (4.15). Since the value of $\bar{\gamma}_{SE}$ is sensitive to the Rb density and polarization, of which we do not have a good measurement, in the following I will use a method to calculate P_t independently of the values of $n_{\rm Rb}$, γ_{SE}, and $P_{\rm Rb}$.

The spin relaxation time constants of the two chambers Γ_p and Γ_t differ from the spin relaxation time measured by a spin-down measurement. This is because the pumping and the target chamber temperatures are not the same as the value during a spin-down measurement (which is usually performed at room temperature). However, one can make corrections to this temperature effect based on Eq. (4.16). The spin relaxation rate from a spin-down measurement is

$$\Gamma_{20^\circ{\rm C}} = \frac{1}{\tau} = (\frac{744}{n_0})^{-1} + \Gamma_{wall} + \Gamma_{\Delta B} \ , \tag{4.54}$$

where n_0 is the cell density at room temperature. The spin relaxation rates under operating conditions are

$$\Gamma_p = (\frac{744}{n_p})^{-1} + \Gamma_{wall} + \Gamma_{\Delta B} \ , \text{ and} \tag{4.55}$$

$$\Gamma_t = (\frac{744}{n_t})^{-1} + \Gamma_{wall} + \Gamma_{\Delta B} + \Gamma_{beam} \ . \tag{4.56}$$

Assuming the wall and field gradient depolarization effects do not change with time, then

$$\Gamma_p = \frac{1}{\tau} - \frac{n_0}{744} + \frac{n_p}{744} \ , \text{ and} \tag{4.57}$$

$$\Gamma_t = \frac{1}{\tau} - \frac{n_0}{744} + \frac{n_t}{744} + \frac{I}{622} \ , \tag{4.58}$$

where I is the beam current in μA.

There are two ways of obtaining the target chamber polarization P_t – Equilibrium solution and dynamic solution.

Equilibrium solution

Assuming that the diffusion between P_t and P_p are in equilibrium at the time EPR was performed, then P_t can be obtained by forcing $\mathrm{d}P_t/\mathrm{d}t = 0$, which gives

$$P_t = \frac{d_t}{d_t + \Gamma_t} P_p \ , \tag{4.59}$$

where d_t and Γ_t are calculated using the cell temperatures and the beam current at the time EPR was performed. Results of the target chamber polarizations from equilibrium method are shown in Table 4.2.

Dynamic solution

For most of EPRs during the A_1^n experiment, two (out of three) lasers were turned off and the beam conditions were different. Since d_t is of the order of ~ 1 hour^{-1}, P_t and P_p are not necessarily in equilibrium during each measurement. The target chamber polarization P_t can be determined from the dynamic differential equations $\mathrm{d}P_t/\mathrm{d}t$, using the pumping chamber polarization, cell densities, temperatures, geometries, and the average beam current between two measurements as

$$\begin{aligned} \frac{dP_t}{dt} &= d_t(P_p - P_t) - \Gamma_t P_t \\ \Rightarrow P_t^{(i)} &= \frac{P_t^{(i-1)} + \Delta t \ d_t (P_p^{(i)} + P_p^{(i-1)})/2}{1 + (d_t + \Gamma_t)\Delta t} \ , \end{aligned} \tag{4.60}$$

where $P_p^{(i)}$ is the pumping chamber polarization from the i^{th} EPR measurement, Δt is the time interval between the i^{th} and the $(i-1)^{th}$ EPR measurements, Γ_t is calculated from the average beam current $I^{(i)}$ between the two measurements, and $\Delta t(P_p^{(i)} + P_p^{(i-1)})/2$ is approximately the integral of P_p between the two measurements.

We use the diffusion model to estimate the error of P_t due to the polarization gradient. The error from the model itself is not considered here.

The systematic uncertainties for diffusion parameters have been calculated and the results are

$$\frac{\Delta D_t}{D_t} = 2.1\%, \quad \frac{\Delta K}{K} = 0.4\% \ , \tag{4.61}$$

$$\frac{\Delta d_t}{d_t} \approx \frac{\Delta d_p}{d_p} \approx 7.3\% \ \text{ and } \frac{\Delta \Gamma_p}{\Gamma_p} \approx 2.3\% \ . \tag{4.62}$$

Uncertainties in P_t due to diffusion are shown in Table 4.3.

Finally, by fitting P_t and P_p with a second order polynomial, one obtains

$$P_t = a_2 P_p^2 + a_1 P_p + a_0 \ , \tag{4.63}$$

where both P_t and P_p are in %. Five measurements of $P_p < 29\%$ (due to masing

effect) are excluded in the fit. The results are $a_2 = -0.0030 \pm 0.0004$, $a_1 = 1.17 \pm 0.03$ and and $a_0 = -2.8 \pm 0.6$.

4.7 Target Polarization

4.7.1 Target Polarization During the A_1^n Experiment

The average polarizations for each cell from EPR measurements are listed in Table 4.2 and 4.3, for equilibrium and dynamic solutions, respectively.

Table 4.2: The average polarization for each cell from equilibrium solution of EPR measurements. Polarizations and errors are given as absolute values in %.

Cell	P_t±stat.±sys.	P_p±stat.±sys.	$P_p - P_t$
Gore	36.319±1.166±0.833	37.185±1.194±0.851	0.866
Tilghman	42.171±1.116±0.970	42.972±1.137±0.986	0.801

Table 4.3: The average polarization for each cell, dynamic solution. Polarizations and errors are given as absolute values in %.

Cell	P_t±stat.±sys.±diff.	P_p±stat.±sys.	$P_p - P_t$
Gore	36.377±1.451±1.062±0.125	37.185±1.194±0.851	0.809
Tilghman	41.902±1.558±1.305±0.131	42.972±1.137±0.986	1.070

Figure 4-22 shows the target polarization from EPR measurements (equilibrium solution) and from NMR measurements during the A_1^n experiment.

For the data analysis of the A_1^n experiment, we first interpolate in time the target chamber polarizations from EPR measurements using the equilibrium solution, and interpolate in time the polarizations from NMR measurements, then take the average of these two values as the target polarization P_t. The target polarization P_t will be used in Eq. (5.30), (5.32) and (5.33) in Chapter 5 to correct the measured raw asymmetries.

4.7.2 Masing Effect

This section describes a nonlinear polarization evolution effect called 'masing', its effect on the target performance and how we minimized it during the experiment.

Among the four cells used during summer 2001 (two for A_1^n, two for g_2^n), two cells, "Gore" and "Virginia One", showed the so called masing effect. During the first two

Figure 4-22: Target performance during the A_1^n experiments. Data of EPR measurements are obtained from equilibrium solutions.

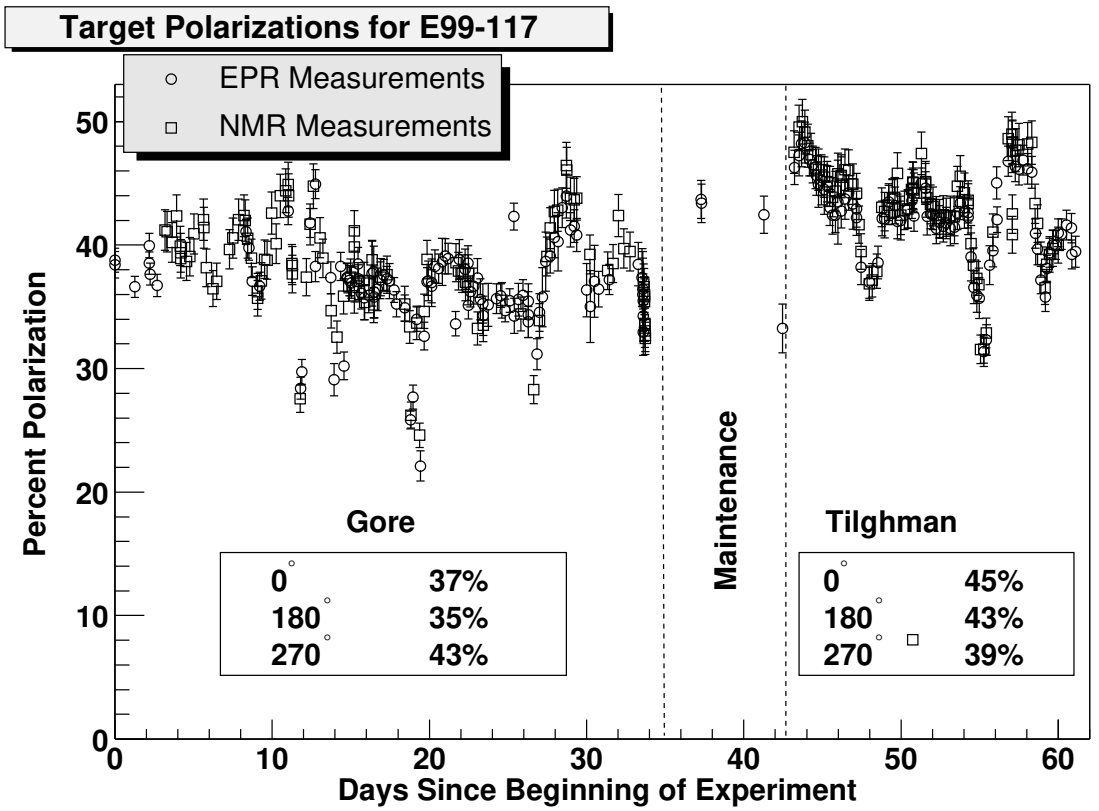

weeks of running, for a couple of times, the polarization of "Gore" dropped abruptly from 37% to $\sim$ 25% after polarization measurements (day 10 $\sim$ 25 of Figure 4-22). Later this effect was suppressed by adding extra field gradients in two directions, parallel to the beamline ($\mathrm{d}B/\mathrm{d}z$) and perpendicular to the beamline ($\mathrm{d}B/\mathrm{d}y$), using two pairs of coils attached to the main Helmholtz coils. These two pairs of coils were called 'gradient coils' and the field generated was 'gradient field'. Cell "Virginia One" showed a similar behavior but the polarization loss was well controlled by the gradient field. This abrupt polarization loss during a polarization measurement cannot be explained in terms of linear relaxation rates or AFP loss and is known to be a non-linear effect called masing [102]. It is caused by the coupling between ^{3}He spins and some close-loop conductor adjacent to the cell. In most cases these elements are identified as NMR pick-up coils. During an NMR measurement, the cell is positioned between pick-up coils and a masing effect may occur. It could also be the 'Rb ring' [3]

[3]When the cell is made, the transfer tube does not connect simply to the pumping chamber as for the SLAC cells but is pushed slightly inside the pumping chamber so that a ring-shaped reservoir is created. It contains the Rb and forbids it to drip inside the scattering chamber when the cell is warmed up for the optical pumping. It is also informally called the "Souder ring".

inside the cell.

Assuming that it is the pick-up coils which couple to the ^{3}He spins, then the masing effect can be described as follows. Consider a polarized cell in a holding magnetic field along the z direction. The cell is placed inside or close to a coil which is part of an LC circuit. We assume that the ^{3}He magnetization has a small transverse component and the spins are precessing around the magnetic field. This precession induces a voltage in the coil. The voltage induced in the coil causes a current to flow through it. This current produces a magnetic field transverse to the holding field. Under certain conditions this induced transverse field can cause the spins to tip away from the z axis and increase the voltage induced in the coil. That in turn increases the transverse field and causes a runaway situation. The longitudinal polarization of the spins will decrease until the coupling between the transverse field and the coil breaks down. Thereafter it will remain stable at the so-called masing threshold. The masing effect described above can be simulated using non-linear Bloch equations [102].

The uncertainty of holding field direction is $\pm 1^\circ$ [130]. During regular operations the transverse component of polarization is very small: $|P_{trans}/P_{long}| < 1^\circ = 0.017$ so the major condition required by masing is not satisfied. But an AFP flip of polarization measurement creates a large transverse spin component that satisfies the transverse condition and masing may occur. In this case AFP flip plays the role of triggering.

Pick-up coils are not the only devices which couple to the transverse component of the ^{3}He spin and produce masing. For a few times (both during the experimental running and in the JLAB target lab) it has been observed that EPR measurements alone triggered the masing effect, which cannot be caused by coupling to the pick-up coils since the cell was positioned far away from them. It is very likely that some other elements inside the target enclosure or the 'Rb ring' satisfied the conditions for nonlinear coupling to the ^{3}He spins. In this case the masing effect can be clearly seen from the EPR spectrum. Figure 4-23 shows an EPR measurement on cell "Virginia One" during the g_2^n experiment. The EPR resonance frequency shift dropped from 43.34 KHz (first flip) to 32.31 KHz (second flip) within 16 seconds, which corresponds to a relative 25% drop in polarization.

To maintain a high polarization of the target the masing effect should be minimized. There are a few ways to suppress masing or to avoid it completely. One solution is to apply a gradient field $(\mathrm{d}B/\mathrm{d}y)$ and $(\mathrm{d}B/\mathrm{d}z)$. The extra field gradient can destroy the conditions which produce the masing effect. However, a large field gradient can distort the NMR signal which makes the analysis for NMR polarimetry challenging [125]. Nevertheless, to protect the polarization from being destroyed by the masing effect, a magnetic field gradient was applied by attaching two pairs of gradient field coils to the main holding field Helmholtz coils. After optimizing the gradient field settings this indeed caused the polarization of cell "Gore" to rise sharply during the experimental running. The same magnetic field gradient was applied to "Virginia One" as soon as the masing effect was observed on this cell. Since the

Figure 4-23: Masing during an EPR measurement.

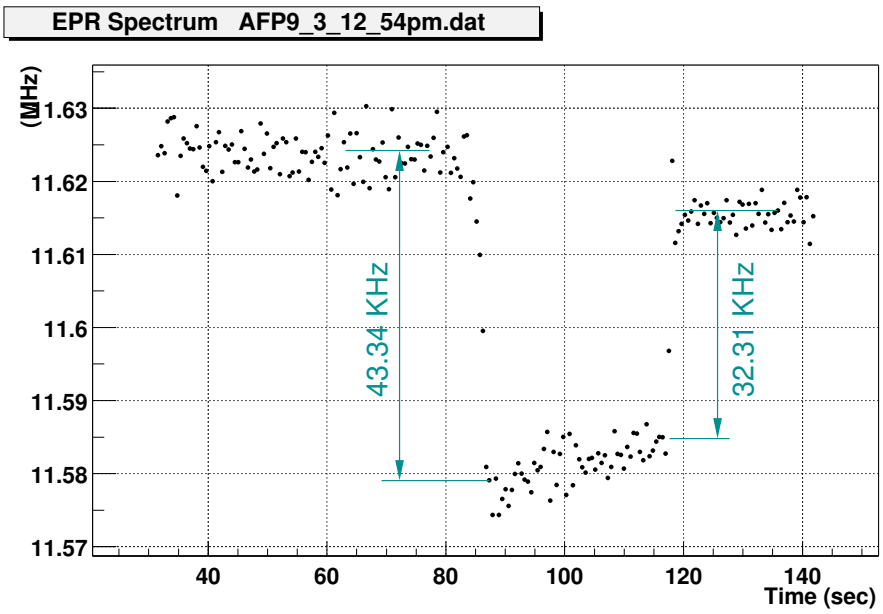

gradient setting was optimized during "Gore" running, the masing effect of "Virginia One" did not affect the data taking of the g_2 experiment. The masing effect was not observed on the other two cells, "Tilghman" and "Shapiro".

A second way to reduce masing is to decrease the main holding field magnitude. This was demonstrated during target tests at SLAC, during which the holding field was decreased from 19 Gauss to 9 Gauss [102]. However, a decrease in the field affects both NMR and EPR polarimetries so this method was not used during the A_1^n and g_2^n experiments.

Chapter 5

Data Analysis

In this chapter we discuss the data analysis which leads to the physics results in Chapter 6.

5.1 Analysis Procedure

The main goal of the data analysis is to extract the electron asymmetries $A_{\parallel}$ and $A_{\perp}$ for $\vec{e} - {}^3\vec{\mathrm{He}}$ deep inelastic scattering, from which one can calculate the virtual photon asymmetries A_1^n and A_2^n and the structure function ratios g_1^n/F_1^n and g_2^n/F_1^n. This procedure is shown in Figure 5-1. To extract the asymmetries, one needs to know the

Figure 5-1: Procedure for asymmetry analysis.

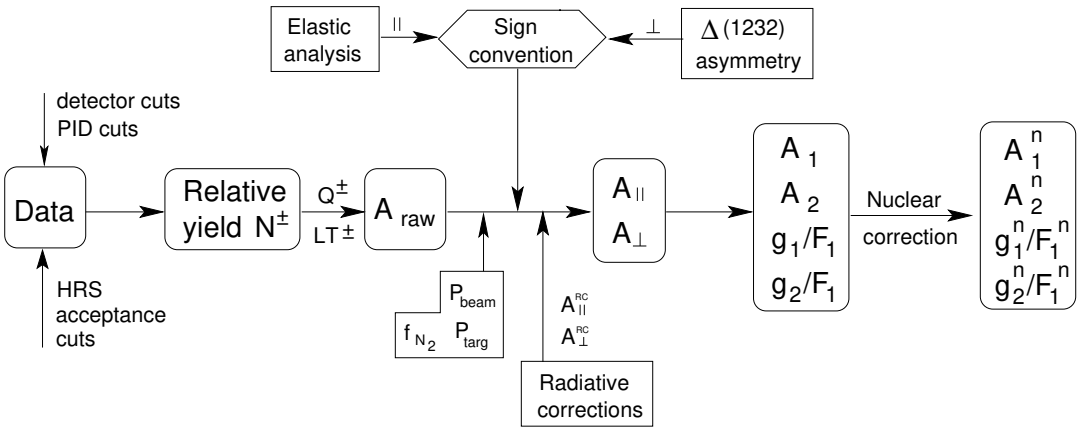

cross section ratio of opposite electron helicity states, as can be seen from Eq. (1.45) and (1.46). To do this, one first needs to obtain the helicity dependent electron yield $N^{\pm}$ from the raw data, during which detector cuts, particle identification cuts and

spectrometer acceptance cuts need to be applied. The efficiencies associated with these cuts will be described in Section 5.2. However, since these efficiencies are not helicity dependent, it is not necessary to correct the yields $N^{\pm}$ for these efficiencies in the asymmetry analysis. The yield is then corrected by the helicity dependent integrated beam charge and the deadtime of the data acquisition (DAQ) system, which has been discussed in Sections 3.7 and 3.10.3, respectively. The corrected yields are proportional to the cross sections. The raw asymmetry A_{raw} can be obtained by taking the difference of the corrected yields for opposite helicity states, and dividing it by the sum of the two. Next, to go from raw asymmetries to physics asymmetries $A_{\parallel}$ and $A_{\perp}$, four factors need to be taken into account: the beam polarization P_b, the target polarization P_t, the nitrogen dilution factor f_{N_2} due to the unpolarized nitrogen nuclei mixed with the polarized ^{3}He gas, and a sign based on the knowledge of the absolute sign of the electron helicity and the target spin direction. The beam and the target polarizations P_b and P_t have been presented in the last two chapters. The nitrogen dilution factor will be discussed in this chapter. The fourth factor is usually referred to as "the sign convention". The sign convention for parallel asymmetries is obtained from the elastic scattering asymmetry and that for perpendicular asymmetries is obtained from the $\Delta(1232)$ asymmetry analysis, as will be described in Sections 5.4 and 5.5. The physics asymmetries $A_{\parallel}$ and $A_{\perp}$, after corrections for the radiative effects, are used to calculate A_1 and A_2 and the structure function ratios g_1/F_1 and g_2/F_1. This step involves kinematic factors and the ratio $R = \sigma_L/\sigma_T$ discussed in Chapter 1. Finally, all the results described above are for the ^{3}He nuclei. The last step is to extract the neutron asymmetries and the structure function ratios from ^{3}He results. This is called "nuclear corrections" and will be presented in Section 5.7.

Although the major goal of the A_1^n experiment is to provide precise data on the asymmetries, cross sections have also been extracted from the data. The procedure for the cross section analysis is shown in Figure 5-2.

To extract cross sections, one first needs to determine the absolute yield of $\vec{e}-\vec{^3\mathrm{He}}$ inclusive scattering from the raw data. Unlike the asymmetry analysis, corrections need to be made for the detector efficiencies, particle identification (PID) efficiencies and the spectrometer acceptance effect. A Monte-Carlo simulation is used to calculate the spectrometer acceptance based on a transport model for the Hall A HRS. One also needs to subtract the yield of $e-\mathrm{N}$ scattering caused by the N_2 nuclei mixed with the ^{3}He gas. The absolute $\vec{e}-\vec{^3\mathrm{He}}$ yield is then corrected for the integrated beam charge and DAQ deadtime to give the final cross section results. Using world fits for the unpolarized structure functions (form factors) of ^{3}He, one can calculate the expected deep inelastic (elastic) scattering cross section in the Monte-Carlo simulation. Moreover, if the polarized structure functions are known, one can calculate the expected asymmetries. For the analysis of the A_1^n experiment, the parallel asymmetry of $\vec{e}-\vec{^3\mathrm{He}}$ elastic scattering was simulated and compared with data.

Figure 5-2: Procedure for cross section analysis.

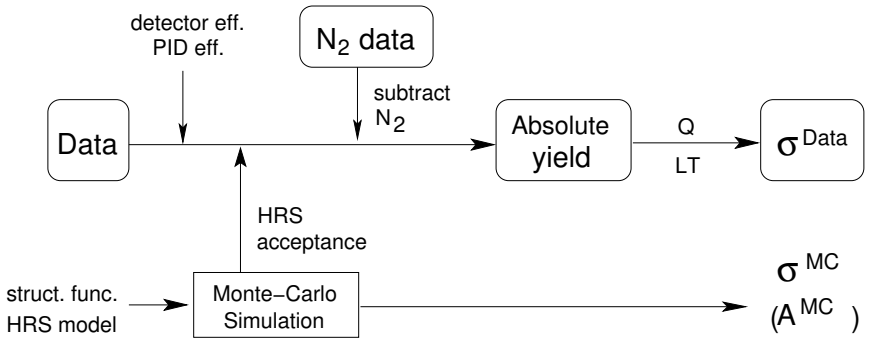

In this chapter we first describe the detector analysis, including VDC efficiency, particle identification efficiencies, and the HRS acceptance. Then in Section 5.3 we describe the Monte-Carlo program developed for the A_1^n experiment. The elastic analysis will be presented in Section 5.4. The elastic asymmetry results provide an additional way to check the product of beam and target polarizations. The elastic cross section results are used to check the target density and N_2 fill pressure, as well as to help understand the apparatus. The $\Delta(1232)$ transverse asymmetry will be presented in Section 5.5. The deep inelastic scattering (DIS) analysis will be described in Section 5.6. The DIS asymmetry analysis will provide the main results of this experiment - the neutron asymmetries A_1^n and A_2^n and the structure function ratios g_1^n/F_1^n and g_2^n/F_1^n. The results for the DIS cross sections, together with the world fit for $R = \sigma_L/\sigma_T$, will determine the unpolarized structure function F_1, and thus allow one to calculate the polarized structure functions g_1 and g_2 from the results for g_1/F_1 and g_2/F_1.

5.2 Detector Analysis

The trigger efficiency has been presented in Section 3.10.3. In this section we will discuss the VDC efficiency, particle identification efficiencies and the HRS acceptance effect.

5.2.1 VDC Efficiency

The hardware efficiency of the VDC wires is almost 100%. VDC inefficiency comes mainly from the software misreconstruction of particle tracks. Only one track events will be used for data analysis in the following sections, so the VDC inefficiency can be characterized by the fraction of zero-track and multiple-track events generated by

non-cosmic particles. A proper way to analyze the VDC efficiency is to use data with low cosmic background, then apply $\beta \equiv v/c$ and particle identification (PID) cuts to select non-cosmic particles. For our case, electrons were detected. The β distribution of scattered electrons is a Gaussian centered at $\beta = 1$. Hence we applied a cut $0.5 < \beta < 1.5$ and electron PID cuts in the VDC efficiency analysis. Figure 5-3

Figure 5-3: Right HRS VDC track number distribution.

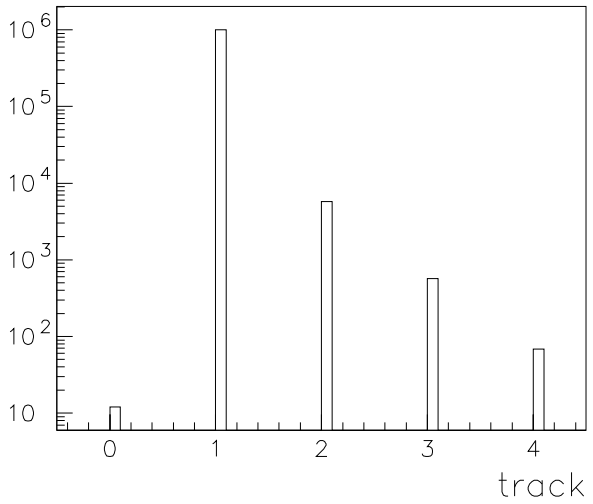

Table 5.1: Fraction of zero-, one- and multiple-track events from elastic scattering data, $E_b = 1.196$ GeV, $E' = 1.191$ GeV, $\theta = 19.985°$.

Number of tracks	0	1	2	3	4
Left HRS	0.0	0.98768	0.01094	0.00126	1.28×10^{-4}
Right HRS	1.18×10^{-5}	0.99371	0.00565	0.00056	0.68×10^{-4}

shows the distribution of the number of reconstructed tracks in the right HRS from elastic scattering data, with a cut $0.5 < \beta < 1.5$ and electron PID cuts applied. As already mentioned, only one-track events will be used. The VDC efficiency that should be used to correct the results, is therefore defined by the fraction of one-track events as $\eta_{VDC} \equiv N_{one}/N_{tot}$, where N_{one} is number of events with only one-track and N_{tot} is the total number of events. The fractions of zero-, one- and multiple-track events from elastic scattering data are shown in Table 5.1. One obtains $\eta_{VDC} = 98.77\%$ for the left HRS and $\eta_{VDC} = 99.37\%$ for the right HRS.

5.2.2 Particle Identification Efficiency

As described in Sections 3.10.5 and 3.10.6, particle identification (PID) was achieved by a threshold CO_2 Čerenkov detector and a double-layered lead glass counter. Their PID efficiencies are usually characterized by two variables: electron efficiency η_e and pion rejection factor η_π. Electron efficiency η_e is defined as the ratio of the number of electrons identified by the detector and the total number of electrons that enter the detector. The pion rejection factor η_π is defined as the ratio of number of pions that are rejected by the detector and the number of pions that are mis-identified as electrons by the detector.

PID efficiencies can be obtained by two methods. The first method is to fit the detector data by expected distributions for electrons and pions. For example, one can fit the summed ADC spectrum of the Čerenkov detector by the photo-multiplier tube's (PMT) response functions [138]. Then one can deduce the PID efficiency of the Čerenkov detector from the fitting results. This method is not ideal since in the real situation there are background events and the ADC spectrum cannot be fully described by the knowledge of the hardware. The second method is to use sample electron and pion events and study their distributions in the detector. This way the results are closer to reality, but the difficulty is how to select real electron and pion sample events. Since the particle identification of the Čerenkov detector and the lead glass counters is based on different mechanisms, the PID efficiencies of these two are not correlated. We therefore used the second method and extracted the PID efficiency of lead glass counters by using the sample electron events selected by the Čerenkov detector, and vice versa.

Figure 5-4 shows a spectrum of summed ADC signal of the left HRS gas Čerenkov detector, before and after the lead glass counter electron and pion cuts. The spectrum from the right HRS is similar. As described in Section 3.10.5, electrons and pions have different distributions. The peak around $\sum$ADC=1400 is the multiple photo-electron peak triggered by the electrons. The peak centered at $\sum$ADC=250 is the single photo-electron peak triggered mostly by the pions. In order to perform a precise PID efficiency analysis, the sample electron and pion events need to have the least contamination. To do this, the lead glass counter electron and pion cuts applied here are very tight, which means we apply an electron (pion) cut which rejects more than 99% of the pions (electrons) with the cost of losing electrons (pions). This explains the drop in the multiple photo-electron peak after applying the electron cut and the drop in the single photo-electron peak after applying the pion cut.

As can be seen, electrons can be separated from pions by using a cut in the summed ADC signal. A cut $\sum$ADC>400 is shown in Figure 5-4.

Figure 5-4: Summed ADC signal of left HRS gas Čerenkov detector, without cut (black), after lead glass counters' electron cut (red) and pion cut (blue). The vertical line shows a cut $\sum \mathrm{ADC}_i > 400$ for selecting electrons.

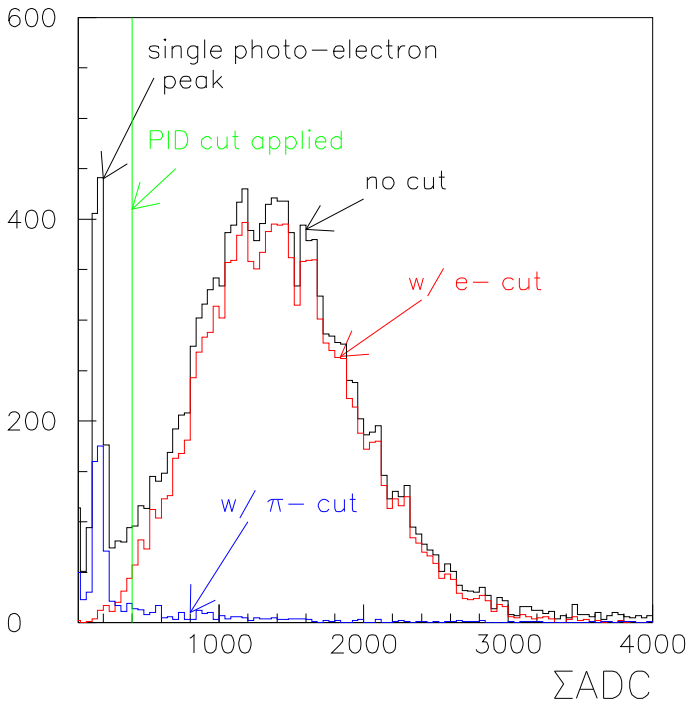

When crossing the double-layered lead glass counter, electrons lose part of their energy in the first layer and deposit the rest in the second layer, while pions deposit only a small part of their energy in either layer. Therefore one can separate pions from electrons by applying a two-dimensional cut in the energy deposits. Figure 5-5 shows a two-dimensional (2D) distribution of the energy deposits in the pion rejectors in the left HRS and a typical 2D cut applied to separate pions from electrons.

Lead glass has a density of 5.18 g/cm^3 and a radiation length of 1.68 cm. The thickness for the lead glass counter in the left HRS is 14.5 cm for both the first and the second layer, which corresponds to 8.6 radiation lengths. Thus the electron's energy deposits in the first and the second layer are comparable. In the right HRS, the first layer of lead glass counter is 10 cm thick and the second layer is 35 cm thick, which corresponds to 6.0 and 20.8 radiation lengths, respectively. Thus the electrons' energy deposit in the first layer is much smaller than that in the second layer. As a result, the total shower detector in the right HRS has a better PID performance than the pion rejectors in the left HRS. Figure 5-6 shows the 2D distribution of the energy deposits in the preshower and shower detectors, before and after Čerenkov electron and pion cuts.

Figure 5-5: Two-dimensional distribution of energy deposits in the two layers of lead glass counter in the left HRS, after the gas Čerenkov electron cut (red) and the pion cut (blue). Black straight lines show the boundary of the 2D cut for selecting electrons.

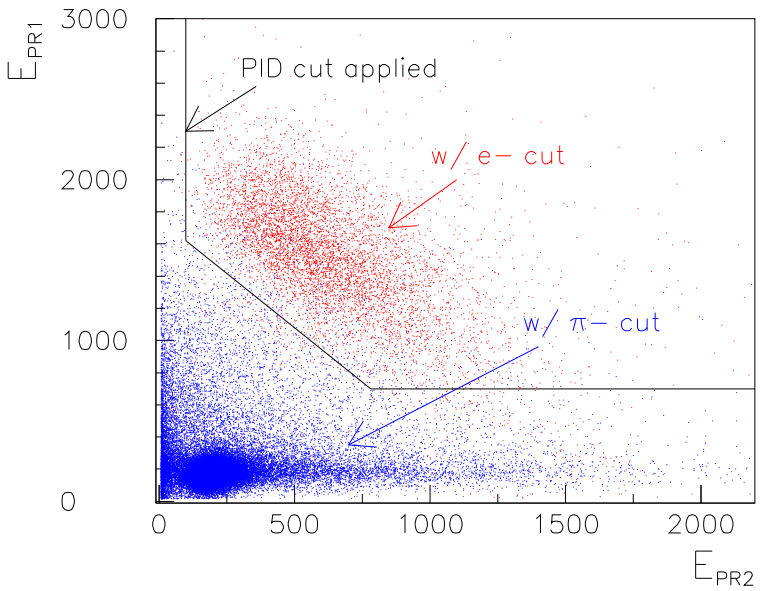

Figure 5-6: Two-dimensional distribution of energy deposits in the two layers of lead glass counter in the right HRS, after the gas Čerenkov ADC electron cut (red) and the pion cut (blue). Black straight lines show the boundary of the 2D cut to select electrons.

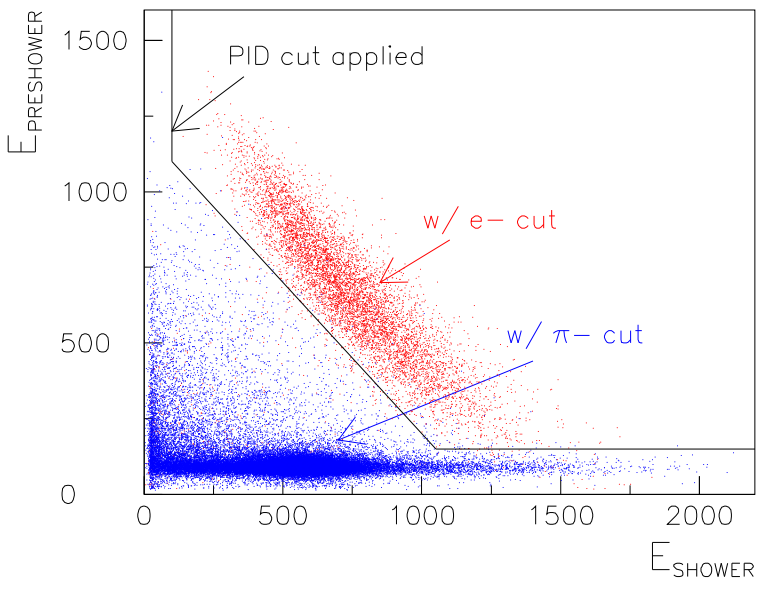

We have done detailed analysis for electron efficiencies and pion contaminations for the Čerenkov detector and the lead glass counters [97][136]. Figure 5-7 shows results of PID efficiencies for the left and the right HRS detectors. The PID cuts and efficiency

Figure 5-7: PID efficiencies of the left and the right HRS detectors in the range of $0.8 < p_0 < 2.0$ (GeV/c).
The horizontal axis for the gas Čerenkov efficiency is the value of the cut in the summed ADC signal. The horizontal axis for the lead glass counter's efficiency is the value of the cut in the ratio E_1/p_0, with E_1 the energy deposit in the first layer in arbitrary unit and p_0 the HRS central momentum in GeV/c. Numbers on the left vertical axis are for electron efficiencies η_e in %. Numbers on the right vertical axis are for pion rejection factors η_π.

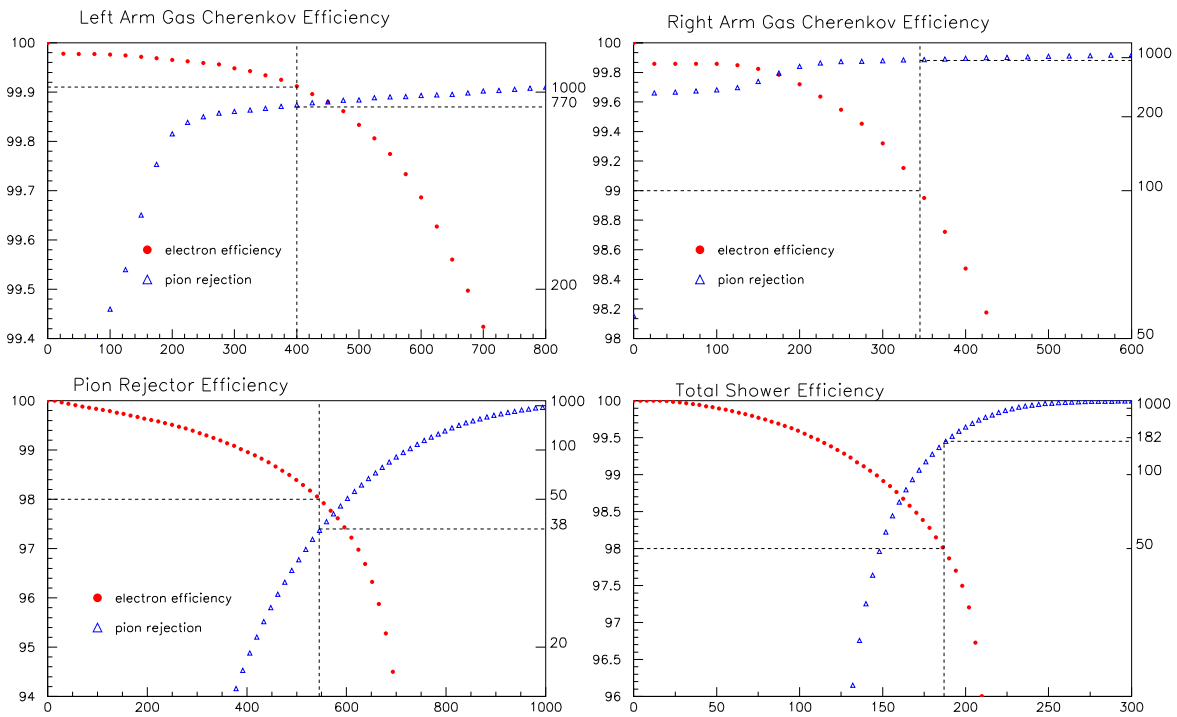

of each detector, in the HRS central momentum range $0.8 < p_0 < 1.4$ (GeV/c), are:

- Left HRS:
  - Gas Čerenkov: $\sum$ADC >400; $\eta_{\pi,\mathrm{rej}} > 770$, $\eta_e = 99.9\%$.
  - Lead glass counters:
    $E_{PR1} > 0.42\ p_0$, $E_{PR2} > 100$, $0.75E_{PR1} + E_{PR2} > 0.8\ p_0$;
    $\eta_\pi \sim 38$, $\eta_e = 98\%$.
  - Combined pion rejection factor: $\eta_\pi > 3 \times 10^4$ at $\eta_e = 98\%$.

- Right HRS:
  - Gas Čerenkov: $\sum$ADC >342; $\eta_\pi = 900$ at $\eta_e = 99\%$.
  - Lead glass counters:
    $E_{psh} > 0.14\ p_0$, $E_{sh} > 100$, $E_{psh} + E_{sh} > 0.75\ p_0$;
    $\eta_\pi \sim 182$ at $\eta_e = 98\%$.
  - Combined pion rejection factor: $\eta_\pi > 1.6 \times 10^5$ at $\eta_e = 97\%$.

  where $\sum$ADC is the summed ADC signal of the gas Čerenkov detector. E_{PR1} and E_{PR2} are the energy deposits in the first and second layers of the pion rejector in arbitrary units. E_{psh} and E_{sh} are the energy deposits in the preshower and the shower counters in arbitrary units, p_0 is the HRS central momentum in MeV/c.

5.2.3 HRS Acceptance

Not all the events being detected can be used for data analysis. Each High Resolution Spectrometer (HRS) does not have a clear cut in acceptance. Only events going well within the acceptance can be considered to be good events. Events from the edge of the acceptance may be particles scattered from the inside of the spectrometers. This section describes the features of HRS acceptance, how to define the boundary of acceptance and how to select good events.

For a fixed beam position (x, y), the acceptance of Hall A HRS depends on four target variables: in-plane angle $\phi_{\rm tg}$, out-of-plane angle $\theta_{\rm tg}$, position of the reaction point in the HRS frame $y_{\rm tg}$ and momentum fraction $\delta_{\rm tg} \equiv ({\rm d}p/p)_{\rm tg}$. Their design acceptance ranges are listed in Table 3.7. In most cases simple one dimensional cuts like $|\phi_{\rm tg}| < 30$ mrad are good enough to select good events. But if the statistics are low, then one needs to use a four-dimensional boundary function to select events from as large good acceptance region as possible. For the Hall A spectrometers an acceptance boundary function has been developed for such purpose using the so called 'R-function' method [135].

An R-function is a real-valued function whose sign is completely determined by its arguments. An R-function can be used to defined a geometric object by the boundary equations of this object. The resulting function is equal to 0 on the boundary of the geometrical object, greater than 0 inside the object and less than 0 outside the object. Moreover, the absolute value of the resulting function can be made approximately equal to the distance to the nearest boundary of the geometrical object. For example, the function $f(x, y) = 1 - (x^2 + y^2)$ can be used to define a circle with a radius of 1, since $f = 0$ on the circle, $f > 0$ inside the circle and $f < 0$ outside the circle.

With a given $x_{\rm tg}$, the spectrometer acceptance is a 4-dimensional region of variables $\phi_{\rm tg}$, $\theta_{\rm tg}$, $y_{\rm tg}$ and $\delta_{\rm tg}$. Its main features can be seen in the $(\theta_{\rm tg}, \delta_{\rm tg})$, $(\phi_{\rm tg}, \delta_{\rm tg})$, $(\phi_{\rm tg}, y_{\rm tg})$ and $(\theta_{\rm tg}, \phi_{\rm tg})$ distributions of single arm data that cover as much geometrical

Figure 5-8: Boundary of acceptance. Top left: $\phi_{\rm tg}$ vs. $y_{\rm tg}$; top right: $\theta_{\rm tg}$ vs. $\delta_{\rm tg}$; bottom left: $\phi_{\rm tg}$ vs. $\theta_{\rm tg}$; bottom right: $\delta_{\rm tg}$ vs. $\phi_{\rm tg}$.
Black dots show event distribution without R-cut and contour plots show events with a cut $R > 0$. Blue lines show roughly the boundary of acceptance for which $R = 0$.

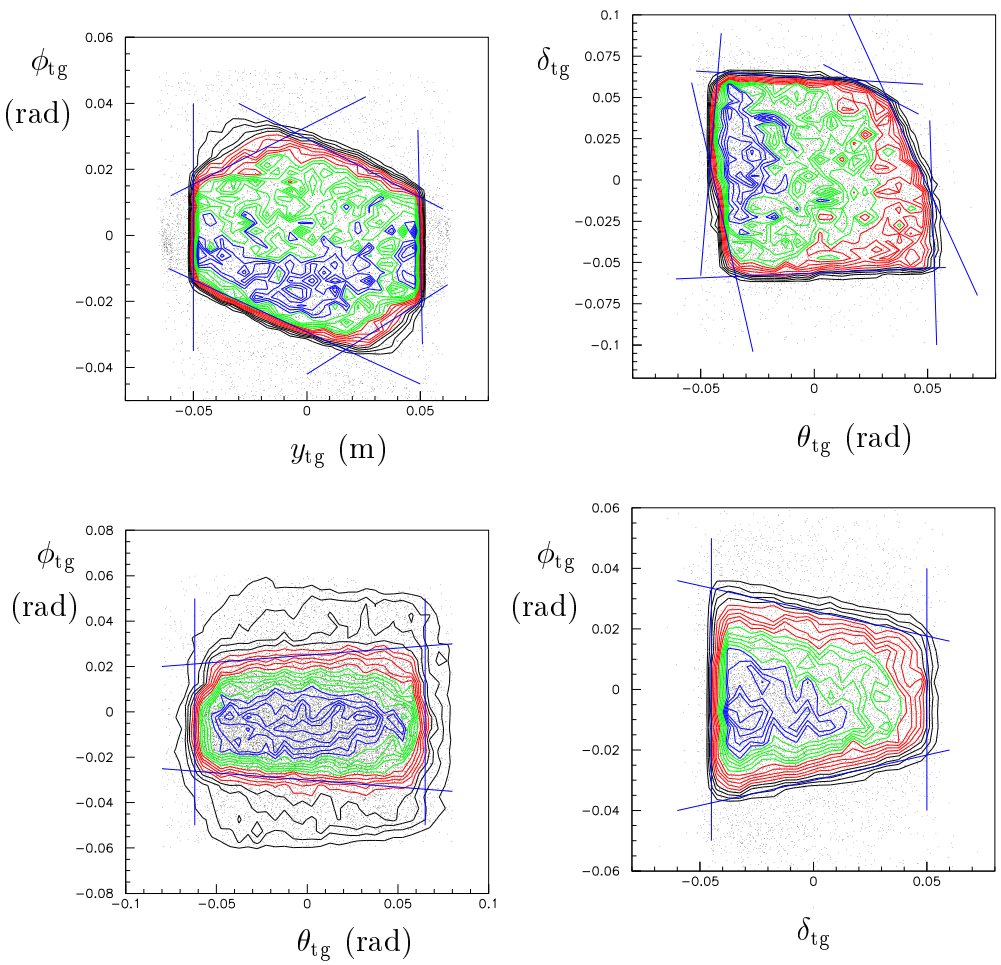

acceptance as possible, see Figure 5-8. The boundary of the acceptance is defined as $R = 0$.

Usually a cut $R > 0$ or $R > 0.005$ is used to define the flat region of acceptance and to select good events. Since the acceptance affects both helicity '+' and '−' cross sections in the same way, the ratio of cross sections with the opposite helicities is not sensitive to the acceptance effect. We thus used a cut $R > 0$ in the asymmetry analysis to maximize the statistics. For the cross section analysis, we applied a cut $R > 0.005$ for both the data and the simulation.

5.3 Monte-Carlo Simulation - SAMC

A Monte-Carlo program was developed for single arm polarized ^{3}He experiments at JLAB Hall A in 1998 [140]. This program, known as mce94010, has been renamed as SAMC (Single Arm Monte-Carlo) after some improvements. SAMC was used for the elastic and DIS simulations for the A_1^n experiment. The main features of SAMC are listed as follows:

- It contains the Hall A HRS geometry. For each HRS the latest version of the particle transport models [141] has been used. The R-function is used for acceptance evaluation;
- The reference frame used inside the spectrometer is the usual spectrometer coordinates. The frame used for target quantities is the Hall A coordinates [86];
- Incoming and scattered electron energy losses (ionization, external and internal bremsstrahlung) are taken into account according to the setup of polarized ^{3}He experiments in 2001;
- A raster (circular or squared pattern) option can be set to simulate the beam raster. The circular raster is implemented using Eq. (3.12) in Section 3.9 to generate an evenly distributed radial pattern of the beam position;
- There is a 6 msr collimator located at the spectrometer entrance on each HRS. It is used to calibrate the optical properties of the spectrometers. When running an experiment it can either be inserted or be left open, called "collimator IN" and "OPEN collimator", respectively. This collimator is being simulated in SAMC;
- ^{3}He elastic cross sections and asymmetries are calculated using a world fit of the ^{3}He elastic form factors [139].
- For the case of elastic scattering, the ^{3}He quasi-elastic contribution can be calculated based on a PWIA model. This was implemented in the program mce94010. However the calculation was found to be rough [72]. In the elastic

analysis for the A_1^n experiment, the quasi-elastic contamination is estimated by taking the difference between data and the elastic simulation.

- The unpolarized ^{3}He deep inelastic computation uses the ^{3}He structure functions $F_1^{^3\mathrm{He}}$ and $F_2^{^3\mathrm{He}}$ calculated from world fits of the proton and deuteron F_2 structure functions [142], a world fit of the ratio $R = \sigma_L/\sigma_T$ [143], and with nuclear EMC effects included [144]. Details of the calculation of $F_1^{^3\mathrm{He}}$ and $F_2^{^3\mathrm{He}}$ can be found in Appendix A. The polarized cross section is computed using internally radiated polarized structure functions g_1 and g_2 generated by POLRAD2.0 [145], see Section 5.6.6.

- For the case of DIS analysis, the elastic and quasi-elastic tail contributions are simulated by the peaking approximation [158][159]. In the peaking approximation for elastic tail, we used the latest world fit of the ^{3}He elastic form factors [139]. In the peaking approximation for the quasi-elastic tail, proton and neutron form factors are needed. We use the proton electric form factor G_E^p from [160]. The proton magnetic form factor G_M^p was computed by multiplying G_E^p with ratio G_E^p/G_M^p [42]. For the neutron form factors, we use a dipole fit for G_M^n [161] and Galster's fit for G_E^n [162].

The structure of SAMC is shown in Figure 5-9 and is described as follows: A large number of trial events are generated at the beginning. For the A_1^n analysis we used 1M events. We call each event a 'trial event' and the simulated electron a 'trial electron'. The initial energy of the trial electron is determined by the beam energy and its uncertainty. The energy loss of the trial electron – including that due to ionization, external and internal radiations - before scattering is calculated based on the knowledge of the material passed through by the incoming electrons in the hall. The position of the reaction point along the target z, the in-plane and out-of-plane scattering angles ϕ and θ, and the outgoing electron's energy E' are generated randomly within their illumination ranges for each trial event. The illumination range of each variable should be large enough to include all the events that are possible in reality. For example, the illumination range of z needs to be longer than the target length; the illumination ranges of ϕ, θ and E' should be larger than the acceptance range of the HRS given in Table 3.7. The cross section and the asymmetries are calculated for each trial event using the simulated incoming and outgoing energies and the scattering angle. Then the energy loss of the trial electron after scattering is calculated based on the knowledge of the material passed through by the outgoing electrons in the hall. The trial electron is then simulated to go through the spectrometer and reach the focal plane using an HRS transport model. For each trial event, the position of the reaction point and the momentum of the scattered electron at the target are reconstructed using the simulated focal plane information, based on the HRS transport model. These reconstructed target variables are the ones that should be compared with real data. After applying the same acceptance cuts (and invariant

Figure 5-9: Flow chart for the single arm Monte-Carlo simulation program SAMC

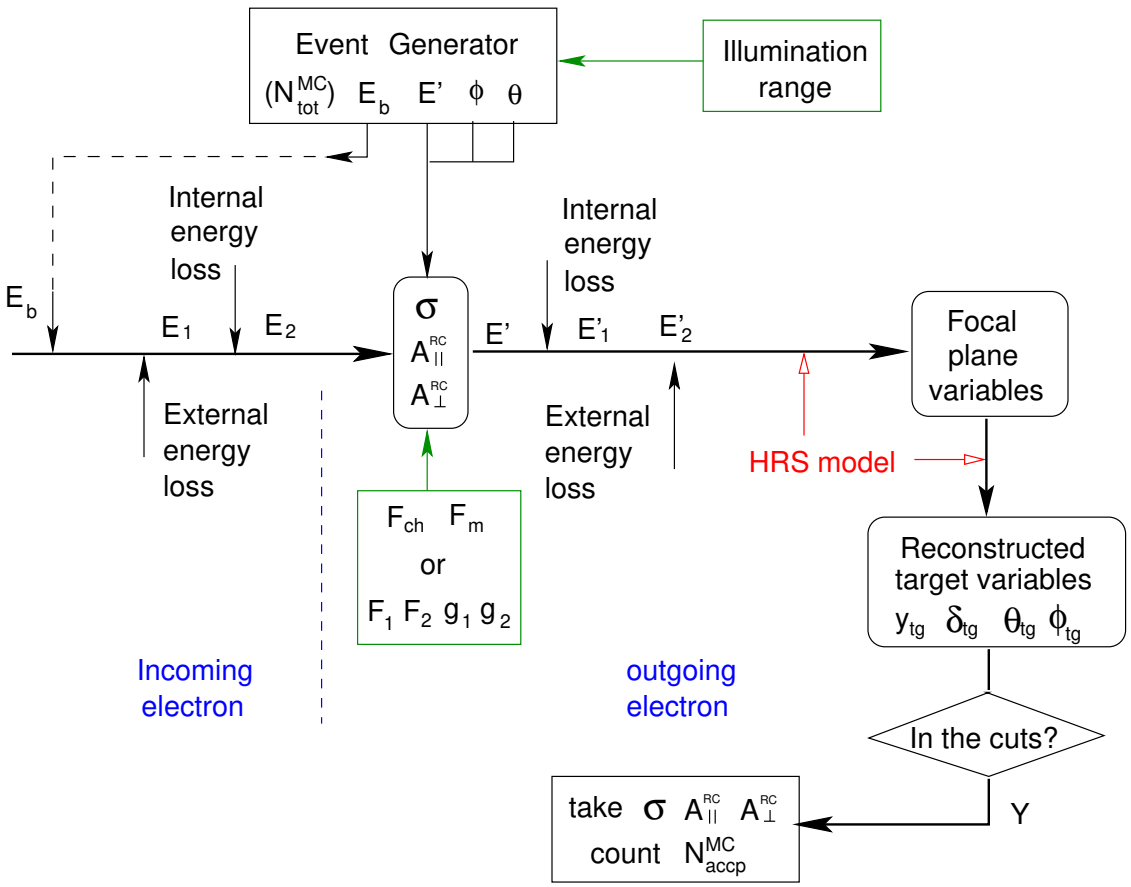

mass W cut in the case of elastic scattering) as those applied to the real data in the analysis, the simulated reconstructed target variables are expected to have the same distribution as the data.

A detailed description of all the material passed through by the incoming and outgoing electrons for the A_1^n experiment is given in Appendix B.

5.4 Elastic Analysis

Elastic $\vec{e}-{}^3\vec{\text{He}}$ scattering data have been taken on the cell "Gore" polarized longitudinally with respect to the beam direction. A Monte-Carlo simulation was performed from which the acceptance, the expected cross section and longitudinal asymmetry were evaluated. The simulated acceptance was then used to extract cross sections

from the data. To eliminate possible systematic effects, a beam half-wave plate was inserted to reverse the beam helicity for half of the statistics. For each beam half-wave plate configuration (not inserted or inserted), the target spin direction was also reversed for half of the statistics. As a result there are four combinations of beam helicity and target spin directions and the sign of the raw asymmetry flips for each beam and/or target spin reversal. Because the calculated elastic asymmetry is significantly non-zero compared to the statistical error of the measured asymmetry, the sign convention for each beam and target helicity configuration can be determined by comparing the sign of the measured raw asymmetry with the expected value. The measured elastic longitudinal asymmetry was also used to check the product of beam and target polarizations. The measured elastic cross section was used to check the target density.

In this section the formalism of elastic $\vec{e} - {}^3\vec{\mathrm{He}}$ scattering will be reviewed first. Then the method of elastic simulation using SAMC will be described, followed by the simulation results for various reconstructed target quantities to show the quality of simulation. Next, results for the N_2 and ^{3}He pressure curves will be presented which were used to determine the N_2 dilution factor and to check the ^{3}He and N_2 densities of the polarized cell "Gore". The systematic uncertainties in the elastic cross section and asymmetry will be discussed next. In the end we present the results on the elastic cross section and longitudinal asymmetry. The cross section and asymmetry results agree with the simulation at a level of 5% and 4%, respectively. This level of agreement is within the expected systematic and statistical uncertainties. We therefore conclude that the experimental apparatus was well understood and that the ^{3}He and N_2 densities used in the analysis are correct. Also deduced is the sign convention for the asymmetry of a longitudinally polarized target.

5.4.1 Physics Formulae for $\vec{e} - {}^3\vec{\mathrm{He}}$ Elastic Scattering

The elastic cross section for the unpolarized case is given by the Rosenbluth formula [6][12]:

$$\left(\frac{\mathrm{d}\sigma}{\mathrm{d}\Omega \mathrm{d}E'}\right)^u = \sigma_{Mott}\left[W_2^{el}(Q^2) + 2W_1^{el}(Q^2)\tan^2(\theta/2)\right] , \tag{5.1}$$

where Q^2 is determined by Eq. (1.14) and the elastic kinematic:

$$E' = \frac{E}{1 + \frac{2E}{M_T}\sin^2(\theta/2)} , \tag{5.2}$$

with M_T the target (^{3}He) mass, E the beam energy, and θ the scattering angle. σ_{Mott} is the Mott cross section

$$\left(\frac{\mathrm{d}^2\sigma}{\mathrm{d}\Omega}\right)_{Mott} = \frac{Z^2\alpha^2\cos^2\frac{\theta}{2}}{4E^2\sin^4\frac{\theta}{2}} . \tag{5.3}$$

Compared with Eq. (1.15) which is for a nucleon target, Eq. (5.3) has an extra factor of Z^2, with Z the charge of the target nucleus. The invariant mass W, defined by Eq. (1.2) satisfies $W = M_T$ in the case of elastic scattering. This means that the target does not acquire any energy from the incident electron (aside from recoil energy) and thus is not excited. $W_1^{el}(Q^2)$ and $W_2^{el}(Q^2)$ are the form factors for elastic scattering. In this dissertation a superscript 'el' is used to distinguish them from structure functions in deep inelastic scattering. But in some textbooks this superscript is dropped. The form factors $W_1^{el}(Q^2)$ and $W_2^{el}(Q^2)$ are often parameterized with the Sachs form factors $G_E(Q^2)$ and $G_M(Q^2)$, also referred to as the electric and magnetic form factors, as

$$W_1^{el}(Q^2) = \tau G_M^2(Q^2) \text{ and} \tag{5.4}$$

$$W_2^{el}(Q^2) = \frac{G_E^2(Q^2)+\tau G_M^2(Q^2)}{1+\tau} \tag{5.5}$$

with $\tau \equiv Q^2/(4M_T^2) = \nu/(2M_T)$ the recoil factor. Eq. (5.1) is then given in terms of $G_E(Q^2)$ and $G_M(Q^2)$ as

$$\left(\frac{\mathrm{d}\sigma}{\mathrm{d}\Omega\mathrm{d}E'}\right)^u = \sigma_{Mott}\left\{\frac{G_E^2(Q^2)+\tau G_M^2(Q^2)}{1+\tau} + 2\tau G_M^2(Q^2)\tan^2(\theta/2)\right\} . \tag{5.6}$$

Dirac and Pauli form factors $F_1^{el}(Q^2)$ and $F_2^{el}(Q^2)$ are often introduced for convenience, which are related to the Sachs form factors as

$$G_E(Q^2) = F_1^{el}(Q^2) - \tau F_2^{el}(Q^2) \text{ and} \tag{5.7}$$

$$G_M(Q^2) = F_1^{el}(Q^2) + F_2^{el}(Q^2) . \tag{5.8}$$

Then the cross section becomes

$$\left(\frac{\mathrm{d}\sigma}{\mathrm{d}\Omega\mathrm{d}E'}\right)^u = \sigma_{Mott} \left\{F_1^{el}(Q^2)^2 + \tau\left[F_2^{el}(Q^2)^2 + 2\left(F_1^{el}(Q^2)+F_2^{el}(Q^2)\right)^2\tan^2(\theta/2)\right]\right\} . \tag{5.9}$$

At low Q^2 such that the relativistic effect of the recoiled target is negligible, and in the Breit frame, the electric form factor can be interpreted as the Fourier transform

of the charge distribution of the target, i.e.

$$\rho(\vec{r}) \;=\; \int \frac{d^3\vec{q}}{(2\pi)^3} e^{-i\vec{q}\cdot\vec{r}} \frac{M_T}{E(\vec{q})} G_E(\vec{q}^2) \;, \tag{5.10}$$

where $\rho(\vec{r})$ is the charge density of the target. Similarly, the magnetic form factor can be related to the magnetization density of the target.

The ^{3}He charge and magnetic form factors have been measured to a good precision [139]. The elastic unpolarized cross section is given by

$$\left(\frac{\mathrm{d}\sigma}{\mathrm{d}\Omega \mathrm{d}E'}\right)^u \;=\; \frac{\sigma_{Mott}}{\eta}\left\{\frac{Q^2}{|\vec{q}|^2}F_c^2(Q) + \frac{\mu^2 Q^2}{2M_T^2}\left(\frac{1}{2}\frac{Q^2}{|\vec{q}|^2} - \tan^2(\theta/2)\right)F_m^2(Q)\right\} \;, \tag{5.11}$$

where μ is the ^{3}He magnetic moment, $\eta = 1 - Q^2/4M_T^2$ is a factor taking into account the target mass effect, and $Q(\vec{q})$ is the four (three) momentum transfer. F_c and F_m are the nuclear charge and magnetic form factors of ^{3}He.

The elastic cross section for a polarized target can be written as [137]

$$\left(\frac{\mathrm{d}\sigma}{\mathrm{d}\Omega \mathrm{d}E'}\right)^h \;=\; \left(\frac{\mathrm{d}\sigma}{\mathrm{d}\Omega \mathrm{d}E'}\right)^u + h\Delta(\theta^*, \phi^*, E, \theta, Q^2) \;, \tag{5.12}$$

where h is the helicity of the incident electron beam, θ^* and ϕ^* are the polar angle and the azimuthal angle of the target spin direction, as shown in Figure 5-10. Following

Figure 5-10: Polar and azimuthal angles of the target spin.

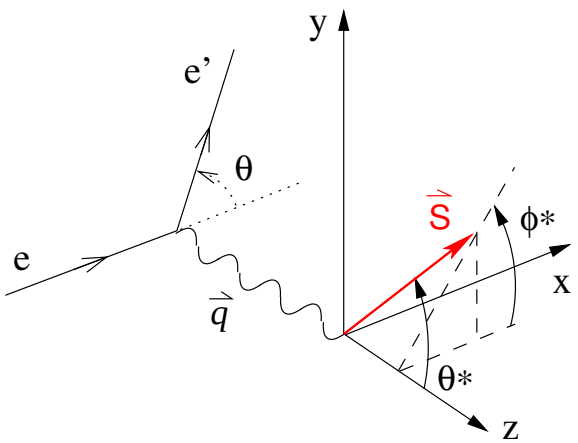

the convention in [137], one can write them explicitly for a target with spin parallel

to the beam direction as

$$\cos\theta^* = (E - E'\cos\theta)/|\vec{q}| \ ; \tag{5.13}$$

$$\phi^* = 0 \ . \tag{5.14}$$

The asymmetry term in the cross section can be written as

$$\left(\frac{\mathrm{d}\sigma}{\mathrm{d}\Omega \mathrm{d}E'}\right)^{h=+1} - \left(\frac{\mathrm{d}\sigma}{\mathrm{d}\Omega \mathrm{d}E'}\right)^{h=-1} = - \sigma_{Mott}\Big(V_{T'}R_{T'}(Q^2)\cos\theta^* + V_{TL'}R_{TL'}(Q^2)\sin\theta^*\cos\phi^*\Big) \ , \tag{5.15}$$

with kinematic factors

$$V_{T'} \equiv \tan\frac{\theta}{2}\sqrt{\frac{Q^2}{|\vec{q}|^2} + \tan^2\frac{\theta}{2}} \ ; \tag{5.16}$$

$$V_{TL'} \equiv -\frac{Q^2}{\sqrt{2}|\vec{q}|^2}\tan\frac{\theta}{2} \ . \tag{5.17}$$

$R_{T'}$, $R_{TL'}$ can be related to the ^{3}He charge and magnetic form factors F_c, F_m as

$$R_{T'}(Q^2) = \frac{2\tau E'}{E}(\mu_A F_m)^2 \ ; \tag{5.18}$$

$$R_{TL'}(Q^2) = -\frac{2\sqrt{2\tau(1+\tau)}E'}{E}(ZF_c)(\mu_A F_m) \ . \tag{5.19}$$

Therefore the elastic asymmetry can be calculated from Eq. (5.9) and (5.15) as

$$A_{\|}^{el} \equiv \frac{(\frac{\mathrm{d}\sigma}{\mathrm{d}\Omega \mathrm{d}E'})^{h=+1} - (\frac{\mathrm{d}\sigma}{\mathrm{d}\Omega \mathrm{d}E'})^{h=-1}}{(\frac{\mathrm{d}\sigma}{\mathrm{d}\Omega \mathrm{d}E'})^{h=+1} + (\frac{\mathrm{d}\sigma}{\mathrm{d}\Omega \mathrm{d}E'})^{h=-1}} \tag{5.20}$$

$$= -\frac{\Big(V_{T'}R_{T'}(Q^2)\cos\theta^* + V_{TL'}R_{TL'}(Q^2)\sin\theta^*\cos\phi^*\Big)}{\frac{1}{\eta}\left\{\frac{Q^2}{|\vec{q}|^2}F_c^2(q) + \frac{\mu^2Q^2}{2M^2}\Big(\frac{1}{2}\frac{Q^2}{|\vec{q}|^2} - \tan^2(\theta/2)\Big)F_m^2(q)\right\}} \ . \tag{5.21}$$

5.4.2 Elastic Simulation

Using the simulation results one can extract the elastic cross section from the data as

$$\sigma^{data} = \frac{N^{data}}{Q\ \eta_{DT}\ \eta_{PID}\ \eta_{VDC}\ \eta_{trig.}}\frac{N_{tot}^{MC}}{N_{accp}^{MC}\ \rho_{\mathrm{tg}}d_{\mathrm{tg},il}\ \Delta\Omega_{il}} \ , \tag{5.22}$$

where N^{data} is the number of events from the data, Q is the accumulated beam charge from the BCM scalers, η_{DT} is the deadtime correction, η_{PID} is the electron particle

identification (PID) efficiency, η_{VDC} is the VDC tracking efficiency, and $\eta_{trig.}$ is the trigger efficiency. $N_{tot}^{MC} = 10^6$ is the total number of trials for the simulation, N_{accp}^{MC} is the number of trial events in the simulation whose reconstructed target variables and invariant mass $W_{^3\mathrm{He}}$ fall into the same cuts as those applied to data. ρ_{tg} is the target density, $d_{\mathrm{tg},il}$ is the target length being illuminated in the simulation and $\Delta\Omega_{il} = \Delta\theta_{il}\Delta\phi_{il}$ is the illuminated range of the solid angle for outgoing electrons. For elastic simulation we used $d_{\mathrm{tg},il} = 25$ cm, $\Delta\theta_{il} = 150$ mrad and $\Delta\phi_{il} = 80$ mrad. To compare with data, we used acceptance cut $R > 0.005$, $|\Delta p_{\mathrm{tg}}/p_{\mathrm{tg}}| < 4.5\%$, and invariant mass cut $0 < W_{^3\mathrm{He}} - M_{^3\mathrm{He}} < 0.006$ GeV/c^2.

5.4.3 Kinematics, Parameters and Simulation Quality

During elastic running, the beam energy was 1.19684 ± 0.68 GeV from the eP measurement, see Table 3.3. The central momentum of each HRS is calculated from the spectrometer dipole field B_{Dipole} as $p_0 = \Gamma B_{Dipole}$, where Γ is the spectrometer's 'gamma constant' [147]. We adjusted Γ slightly to match data and simulation. From this analysis the values of Γ are found to be

$$\Gamma_{left} = 270.0 \text{ (MeV/kG)} ; \tag{5.23}$$

$$\Gamma_{right} = 269.8 \text{ (MeV/kG)} . \tag{5.24}$$

Γ_{left} is smaller than the value given in [147] by a factor of 3.8×10^{-4} (relative), which is within its uncertainty.

The central angle of each HRS is obtained from the Hall A survey report [148], which gives 19.985° for the left and 19.998° for the right HRS. The error in the survey results for the HRS central angle was estimated to be ±0.06° [149].

The imperfection of the VDCs causes a smearing effect in the reconstructed VDC variables x, y, θ and ϕ, i.e., each quantity has a Gaussian distribution. It further affects the distribution of the calculated variables, for example, the particle momentum and the invariant mass W. This smearing effect is usually referred to as the VDC resolution and is characterized by the width of Gaussian distribution for each quantity. The VDC resolution of each HRS was checked using data on elastic scattering on a ^{12}C foil target with open collimator. By comparing the width of invariant mass W peak from the simulation with the data, the VDC resolution in x, y, θ and ϕ was found to be:

$$\begin{cases} \delta_x = 0.01 \text{ cm} \\ \delta_y = 0.01 \text{ cm} \\ \delta_\theta = 0.12 \text{ mrad} \\ \delta_\phi = 0.12 \text{ mrad} . \end{cases}$$

The widening of $\delta \equiv \Delta p/p$ is dominated by the VDC resolution. These results are consistent with the values given in [91].

The glass wall of the target cell causes the largest external radiation effect to the

scattered electrons, which affects the shape, width and the position of the W peak. By comparing the W peak with the data, the cell glass wall thickness on the right side is found to be 1.44 mm for both "Gore" and the reference cell, while on the left side the cell wall is 1.70 mm for "Gore" and 1.60 mm for the reference cell. Compared with the results of optical measurements performed at University of Virginia (UVa) and JLAB (given in Appendix C), there is a ~ 0.3 mm discrepancy on the left side wall thickness. This means there might exist extra material in the path of the outgoing electrons on the left HRS. This uncertainty in cell wall thickness has been taken into account in the external radiative corrections to the DIS data; see Section 5.6.6.

Comparisons between simulation and data for the reconstructed target variables in the spectrometer coordinate system $y_{\rm tg}$, $\delta_{\rm tg}$, $\theta_{\rm tg}$ and $\phi_{\rm tg}$ are shown in Figure 5-11. The R-function is shown in Figure 5-12. Figure 5-13 contains the $y_{\rm tg}$ distribution, showing that the contamination from the glass cell windows is negligible after applying a cut $|y_{\rm tg}| < 2.0$ cm. Comparisons between simulation and data for the ^{3}He invariant mass

Figure 5-11: Reconstructed target variables $\theta_{\rm tg}$, $\phi_{\rm tg}$, $\delta_{\rm tg}$ and $y_{\rm tg}$, for the left and right HRS, with an acceptance cut $R > 0$ applied.
black: data; red: N_2 contamination; yellow: simulation, quasi-elastic; blue: simulation, sum of elastic and quasi-elastic;

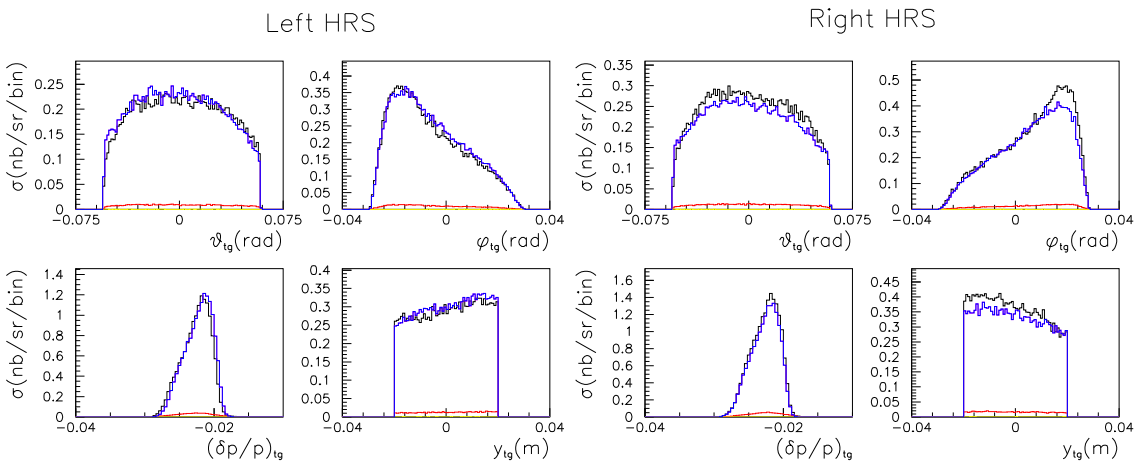

$W_{^3\rm He}$ is shown in Figure 5-14. A cut $0 < (W_{^3\rm He} - M_{^3\rm He}) < 0.006$ GeV/c^2 is applied to select elastic events. The quasi-elastic contamination is at the level of 1%. From the simulation, the quasi-elastic asymmetry is smaller than the elastic asymmetry by more than one order of magnitude, and therefore is negligible and quasi-elastic events are considered to cause a dilution effect.

Figure 5-12: R-function distribution. An acceptance cut1 $R > 0$ is used for the asymmetry analysis and cut2 $R > 0.005$ is used for cross section analysis.
black: data; red: N_2 contamination in data; yellow: simulation, quasi-elastic; blue: simulation, sum of elastic and quasi-elastic.

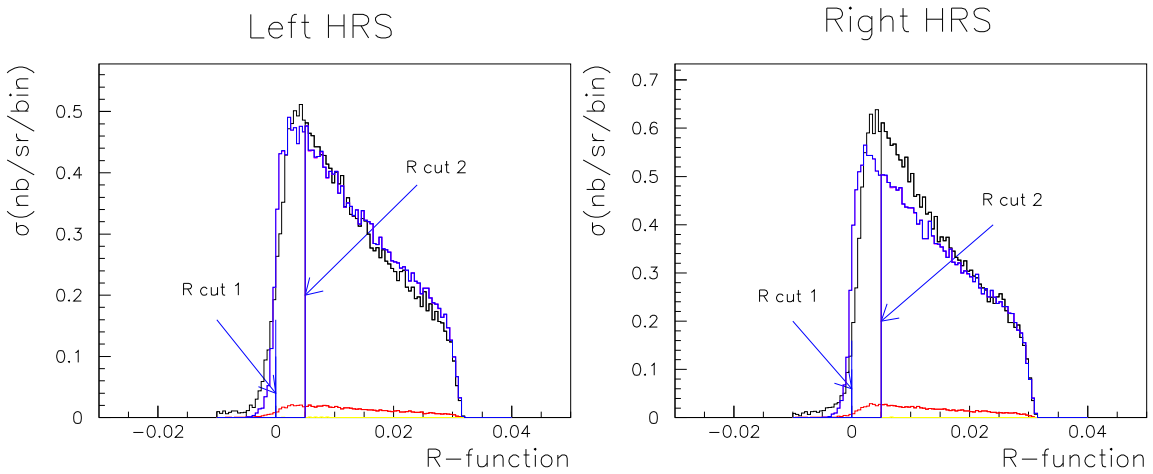

Figure 5-13: Cell window contamination. Cut $|y_{tg}| < 0.02$ m is used in the elastic analysis to exclude events scattered from cell windows.
black: data; red: N_2 contamination; yellow: quasi-elastic simulation; blue: sum of elastic and quasi-elastic simulation; green: data(black)-simulation(blue), showing the net contribution from windows.

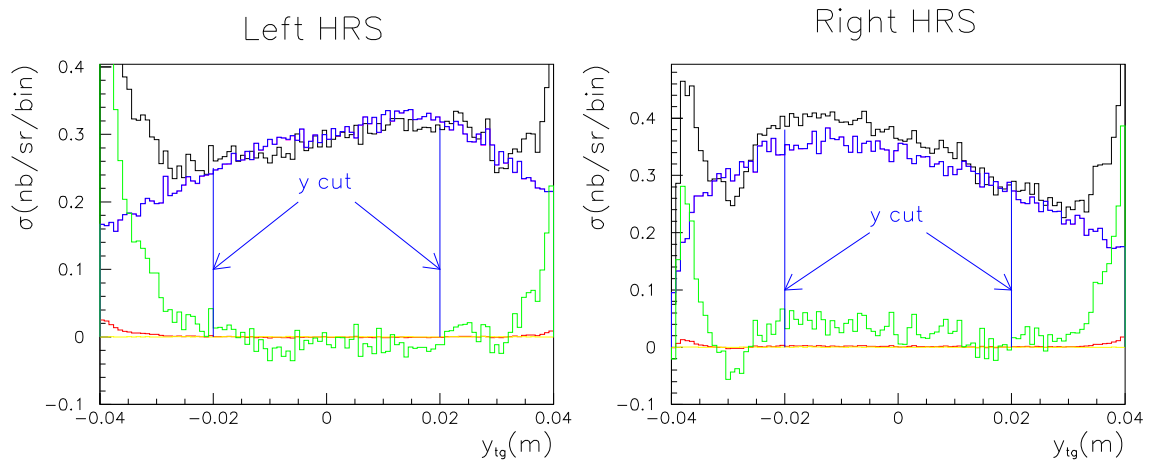

Figure 5-14: $W_{^3\mathrm{He}}$ spectrum of ^{3}He elastic peak.
black: data; red: N_2 contamination; purple: elastic simulation; cyan: difference between data and elastic simulation, which shows the quasi-elastic contamination in the region of $(W - M_{^3\mathrm{He}}) > 0.006$ GeV/c^2;
A cut $0 < (W_{^3\mathrm{He}} - M_{^3\mathrm{He}}) < 0.006$ GeV/c^2 is used to select elastic events in the analysis.

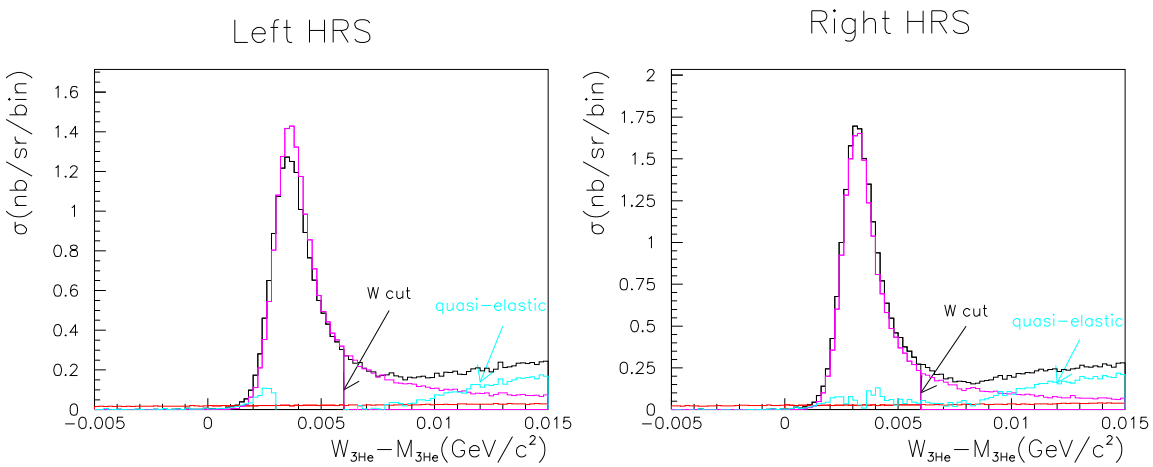

5.4.4 N_2 Dilution for Elastic Data

To estimate the dilution effect caused by ∼1% unpolarized N_2 mixed in the ^{3}He cell, data were taken on a reference cell filled with N_2. The N_2 dilution factor f_{N_2} is defined by

$$1 - f_{N_2} = \frac{N_{N_2}}{N_{^3\mathrm{He}}} = \frac{\sigma_{N_2}}{\sigma_{^3\mathrm{He}}} \frac{n_{N_2}}{n_{^3\mathrm{He}}} , \tag{5.25}$$

where $N_{N_2}(N_{^3\mathrm{He}})$ is the N_2 (^{3}He) yield, $\sigma_{^3\mathrm{He}}$ is the ^{3}He cross section from the polarized ^{3}He cell data, σ_{N_2} is the N_2 cross section from reference cell N_2 data, and n_{N_2} ($n_{^3\mathrm{He}}$) is the N_2 (^{3}He) density inside the polarized ^{3}He cell under running conditions. Since temperature affects both N_2 and ^{3}He densities of the cell in the same way, one can use the ^{3}He density measurement results (performed at room temperature) and the N_2 fill density measured when the cell was made (also given at room temperature). The cross sections $\sigma_{^3\mathrm{He}}$ and σ_{N_2} were obtained from data with exactly the same acceptance, $W_{^3\mathrm{He}}$ and particle identification (PID) cuts.

The N_2 fill density was checked by ^{3}He elastic scattering. The N_2 density n_{N_2} of the cell under running conditions can be obtained by two methods from the elastic data. The first one is to compare the N_2 elastic peak from data taken on a polarized ^{3}He cell with that on a reference cell filled with N_2. The ratio of these two peaks equals the ratio of the N_2 density of the polarized ^{3}He cell to that of the reference

cell.

Figure 5-15: $(W_{N_2} - M_{N_2})$ spectrum of the N_2 elastic peak from the left and right HRS data, with cuts $(W_{^3He} - M_{^3He}) < 0$ & $-0.02 < (W_{N_2} - M_{N_2}) < 0.05$ GeV/c^2 applied.
A cut $0 < (W_{N_2} - M_{N_2}) < 0.006$ GeV/c^2 is used to select the elastic peak. green: data from polarized ^{3}He runs; red: data from reference cell N_2 runs, scaled; black: residual of N_2 matching.

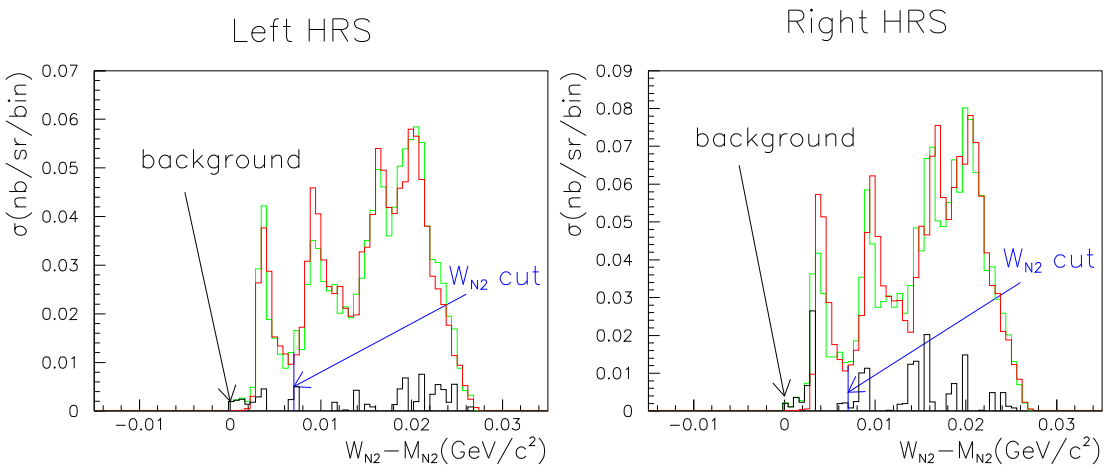

The N_2 elastic peak can be separated from ^{3}He elastic scattering events using cuts $(W_{^3He} - M_{^3He}) < -0.002$ GeV/c^2 and $-0.02 < (W_{N_2} - M_{N_2}) < 0.04$ GeV/c^2, where $W_{^3He}(W_{N_2})$ is the invariant mass for ^{3}He(N_2) nucleus. Figure 5-15 shows the $(W_{N_2} - M_{N_2})$ spectrum with these two cuts applied. The first peak at $(W_{N_2} - M_{N_2}) \approx 0.004$ GeV/c^2 is the elastic peak, the other peaks correspond to the three nuclear excitation levels of N_2. We further applied a cut $0 < (W_{N_2} - M_{N_2}) < 0.006$ GeV/c^2 to select the elastic peak. Assuming that the N_2 elastic yield is $N_{N_2,Gore}$ from the polarized cell and $N_{N_2,refcell}$ from the reference cell filled with N_2 of density $n_{N_2,refcell}$, the N_2 density in "Gore" can be determined by

$$n_{N_2,Gore} = \frac{N_{N_2,Gore}}{N_{N_2,refcell}} n_{N_2,refcell} \ . \tag{5.26}$$

A more precise way to find the N_2 density in "Gore" is to measure the N_2 pressure curve, i.e., a curve of yield vs. N_2 pressure. Such a curve is obtained on a reference cell filled with N_2 with different pressures. In principle the N_2 elastic yield is proportional to the N_2 pressure, so an ideal pressure curve is a straight line crossing zero. Figure 5-16 shows a N_2 pressure curve from reference cell runs with N_2 pressure -12.293 [1],

[1] empty cell runs, pressure is from slow control EPICS data recorded after the run ended, which

Figure 5-16: N_2 pressure curves from the left and right HRS data. Each curve is zoomed in on the right side.

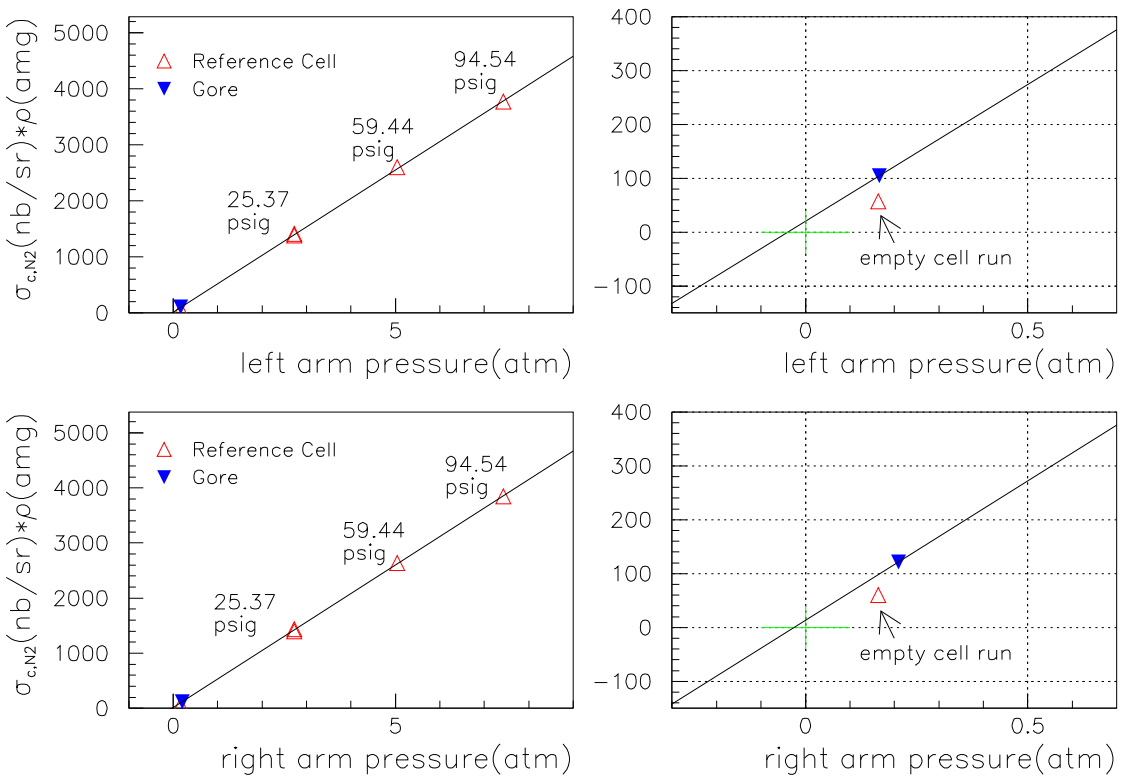

25.3715, 59.4463, and 94.5383 [2] psig.[3]. Data are plotted as $\sigma^{data}_{c,refcell} = \sigma^{data}_{refcell} \frac{\sigma^{MC}_{Gore}}{\sigma^{MC}_{refcell}}$ to correct for radiation effects caused by the fact that the reference cell has a different glass wall thickness than "Gore". Pressure curves were fitted using non-empty cell runs, giving

$$p = -0.0385(\pm 0.0895) + 0.001970(\pm 0.000036)\ \sigma\rho \quad \text{for left HRS ;} \qquad (5.27)$$

$$p = -0.0235(\pm 0.0883) + 0.001932(\pm 0.000035)\ \sigma\rho \quad \text{for right HRS ,} \qquad (5.28)$$

with p the cell pressure in atm, $\sigma\rho$ the yield in (amg·nb/GeV/sr), number in brackets are the error of fit parameters. Empty cell runs do not agree with the curve, which shows that the pressure recorded in EPICS is incorrect. The N_2 pressure in "Gore" is determined by the N_2 yield in"Gore" data, shown as blue markers in Figure 5-16. It gives 0.169 ± 0.088 atm from left HRS data and 0.210 ± 0.088 atm from right

was not necessarily the real pressure during the run.

[2]from target logbook, recorded by hand during data taking.

[3]1 psig $\equiv$ 1 pound/(inch)^2 above 1 atm. Numbers are from data taking logbook.

HRS. Taking the average of the results from the left and right HRS the N_2 density is 0.160 ± 0.074 amg under running conditions; the N_2 fill density at room temperature is then determined to be 0.120 ± 0.056 amg. This result agrees with the N_2 fill pressure 0.0773 ± 0.0023 amg from UVa [146]. The overestimation is mostly due to the background contamination under the N_2 elastic peak in the cell "Gore", as can be seen in Figure 5-15. In the following sections the UVa fill pressure will be used for the N_2 density.

The cross section ratio $\sigma_{N_2}/\sigma_{^3He}$ is found to be 3.006 in the left HRS and 2.813 in the right. Using the UVa fill pressure $n_{N_2} = 0.0773$ amg, $n_{^3He} = 9.08$ amg, the N_2 dilution factor for elastic analysis is $f_{N_2} = 1 - \frac{\sigma_{N_2}}{\sigma_{^3He}} \frac{n_{N_2}}{n_{^3He}} = 0.9753$, averaged over two HRSs.

5.4.5 ^{3}He Pressure Curve

Figure 5-17: Elastic ^{3}He pressure curve.

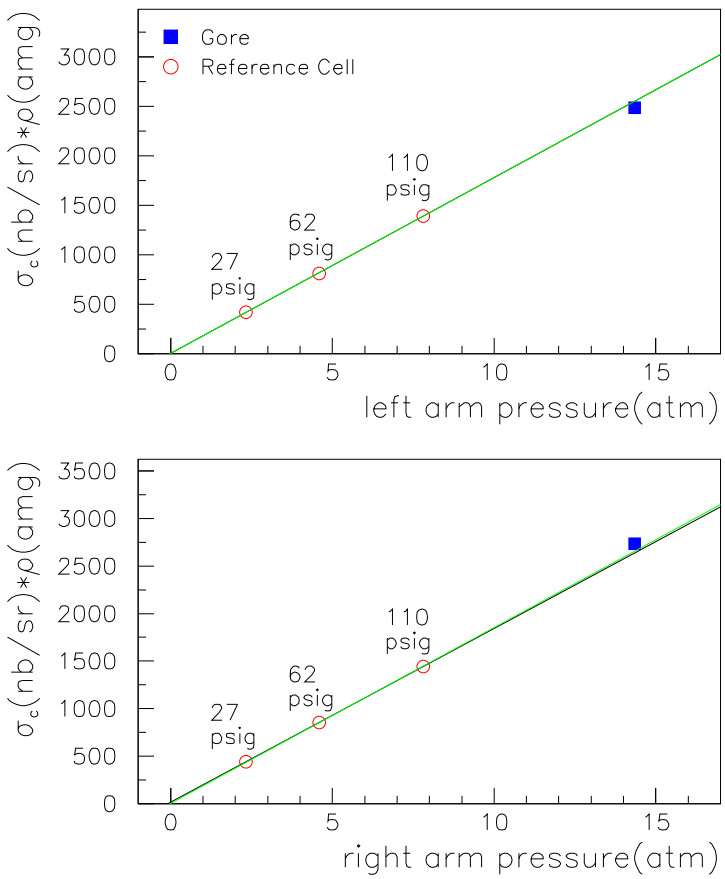

Data were taken using the reference cell with different ^{3}He fill pressures to precisely determine the ^{3}He cross section and to check the ^{3}He density of the polarized cell

under operating conditions. Figure 5-17 shows a ^{3}He pressure curve from reference cell runs with ^{3}He fill pressure 27, 62 and 110 psig [4]. Reference cell data are plotted as $\sigma^{data}_{c,refcell} = \sigma^{data}_{refcell}\frac{\sigma^{MC}_{Gore}}{\sigma^{MC}_{refcell}}$ to correct for the radiation effect caused by the fact that reference cell has a different glass wall thickness from "Gore". The ^{3}He cross sections were extracted from the polarized cell "Gore" data using the ^{3}He density from target density measurements. They are shown as blue squares in the Figure. The results agree with the ^{3}He pressure curve within their systematic uncertainty of 6.7% (see next Section). This indicates that the ^{3}He density from the target density measurement is correct.

5.4.6 Systematic Error Estimate for Elastic Analysis

Systematic Error for Asymmetries

The sources of systematic uncertainties for the asymmetry results are:

- Target polarization: 3% [125];
- Beam polarization: 2.5% (Table 3.4);
- The error on the nitrogen dilution factor comes from the uncertainties in N_2 and ^{3}He pressure, and the ratio of N_2 and ^{3}He cross sections. We estimate $\pm$ 10% on the cross section ratio, compared with which the uncertainties of N_2 and ^{3}He pressure are negligible. We obtain from Eq. (5.30) in the next section the uncertainty in the asymmetry

$$\frac{\Delta A}{A} = \frac{\Delta f_{N_2}}{f_{N_2}} = \frac{\Delta(\frac{\sigma^{N_2}}{\sigma^{^3He}})\frac{n_{N_2}}{n_{^3He}}}{f_{N_2}} = \frac{(\pm 10\%)(1-f_{N_2})}{f_{N_2}} \approx \pm 0.3\% \ ;$$

- We estimate the uncertainty in the quasi-elastic dilution to be 0.5%;
- The error in the helicity dependent deadtime corrections is negligible, as described in Section 3.10.3;
- For our elastic analysis, $Q^2 = 0.174$ (GeV/c)^2 = 0.45 fm^{-2}, the errors in the ^{3}He elastic form factors are $\Delta F_c \approx 0.001$ and $\Delta F_m \approx 0.001$ [139]. We obtain an uncertainty of $\pm$1.2% for the elastic longitudinal asymmetry;
- The uncertainty due to the HRS transport model has been studied in SAMC by using different versions of the HRS transport functions. The uncertainty is found to be 0.23%;

[4] Numbers are from the shift logbook, recorded by hand during data taking.

- We used the SAMC simulation to study the uncertainty in the asymmetry due to uncertainties in the beam energy ($\Delta E_b = \pm 0.7$ MeV, from Table 3.3), HRS central momentum ($\Delta p_0/p_0 = \pm 5 \times 10^{-4}$ [147]), HRS central angle ($\Delta\theta_0 = \pm 0.06^\circ$ [149]), target spin direction ($\pm 1^\circ$ [131]), and the radiation length of the material traversed by the scattered electrons (± 0.2 mm glass, this study). The uncertainty is found to be at a level of 1.3%.

Systematic Error for Cross Sections

The relative systematic errors on the cross sections come from the following sources:

- Target density under operating conditions: 3% [119]. This is the quadratic sum of a 2% uncertainty for the ^{3}He density at room temperature and a 2% uncertainty for the cell temperature under operating conditions;
- The uncertainty due to the nitrogen dilution factor is the same as that for the asymmetry: 0.3%;
- We estimate a 1% uncertainty due to the error in VDC and trigger efficiencies;
- We estimate a 1% uncertainty due to the error in PID efficiencies;
- The uncertainty due to the error in beam charge is 1% [85];
- The uncertainty due to the error in R-function acceptance cut is estimated to be 1%;
- The uncertainty due to the absolute deadtime corrections is 1%, as described in Section 3.10.3;
- Using $\Delta F_c \approx 0.001$ and $\Delta F_m \approx 0.001$, the uncertainty in the cross section due to the errors in the ^{3}He elastic form factors is 3.4% ;
- Target length: the error in the reconstructed $y_{\rm tg}$ is ± 0.5 mm, our software cut is $|y_{\rm tg}| < 2$ cm. This gives a 2.5% uncertainty in the cross section;
- The uncertainty due to the HRS transport model has been studied in SAMC by using different versions of the HRS transport functions. The uncertainty is found to be 1.6%;
- The uncertainties due to kinematics have been studied in SAMC. The uncertainty in the asymmetry due to the uncertainty in the beam energy ($\Delta E_b = \pm 0.7$ MeV, from Table 3.3), HRS central momentum ($\Delta p_0/p_0 = \pm 5\times 10^{-4}$ [147]), HRS central angle ($\Delta\theta_0 = \pm\ 0.06^\circ$ [149]), and the radiation length of the material traversed by the scattered electrons (± 0.2 mm glass, this study), is found to be $\sim$3.5%.

The uncertainties are added in quadrature. We obtain a systematic error of 4.5% for the longitudinal asymmetry and 6.7% for the cross section. These systematic uncertainties are larger than the error in the beam polarimetry, target polarimetry and the target density measurement; we therefore did not use the elastic analysis results as a calibration.

5.4.7 Elastic Cross Section Results

Elastic cross sections extracted using Eq. (5.22) from $\sim$ 20 runs are shown in Figure 5-18. The results agree with the simulation at a level of 5%, which is within its systematic uncertainty. We conclude from this result that the target density used in the analysis is accurate within its uncertainty and the helicity-independent part of the experimental apparatus is well understood.

Figure 5-18: Elastic cross section results. A systematic error of 6.7% has been added to each data point.

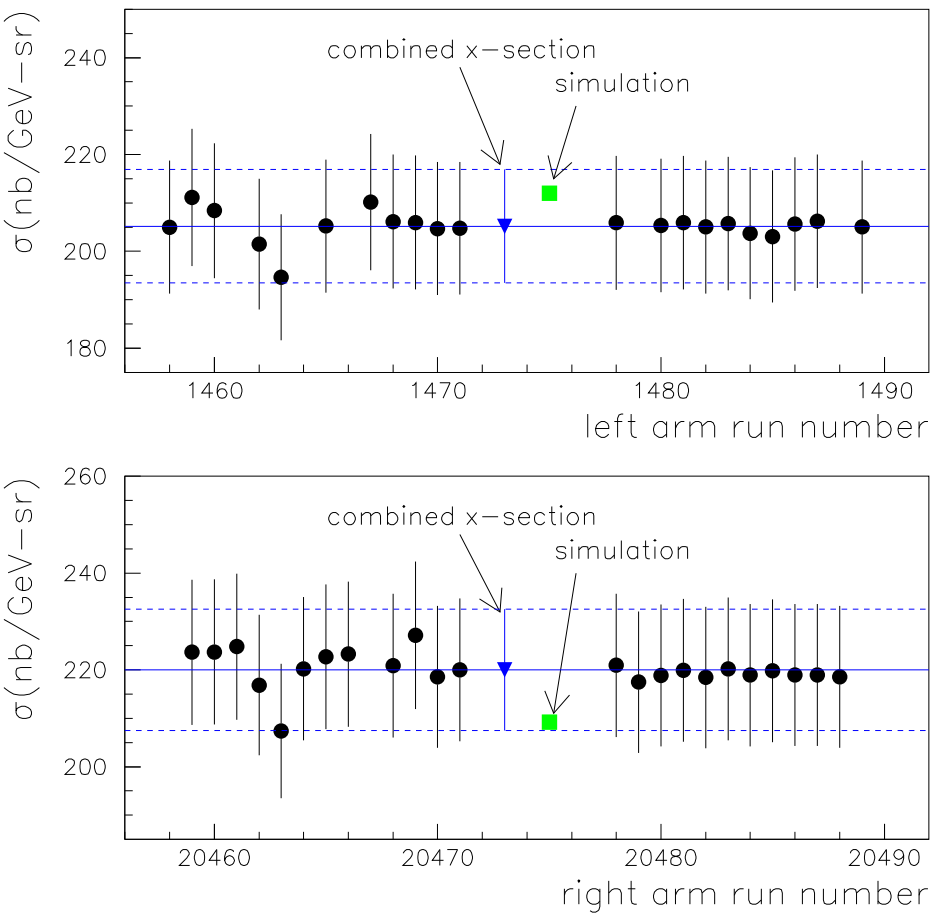

5.4.8 Elastic Asymmetry Results

The raw asymmetry is extracted from data using

$$A_{raw} = \frac{\frac{N^+}{Q^+DT^+} - \frac{N^-}{Q^+DT^-}}{\frac{N^+}{Q^+DT^+} + \frac{N^-}{Q^+DT^-}}, \tag{5.29}$$

where $N^\pm$, $Q^\pm$, $DT^\pm$ are the helicity-dependent yield, beam charge and deadtime correction, respectively. The elastic asymmetry is

$$A_\parallel^{el} = \pm\frac{A_{raw}}{f_{N_2} f_{QE} P_b P_t}, \tag{5.30}$$

where $f_{N_2} = 0.9753$ is the N_2 dilution factor obtained in Section 5.4.4, $f_{QE} \approx 99\%$ is the quasi-elastic dilution. The beam polarization P_b was 82.4±0.30(stat.)±2.4(sys.)%

Figure 5-19: Elastic longitudinal asymmetry results. A 4.5% systematic uncertainty has been included in the total error. The combined asymmetry and its total error from ∼ 20 elastic runs are shown by the horizontal solid and dashed lines, respectively.

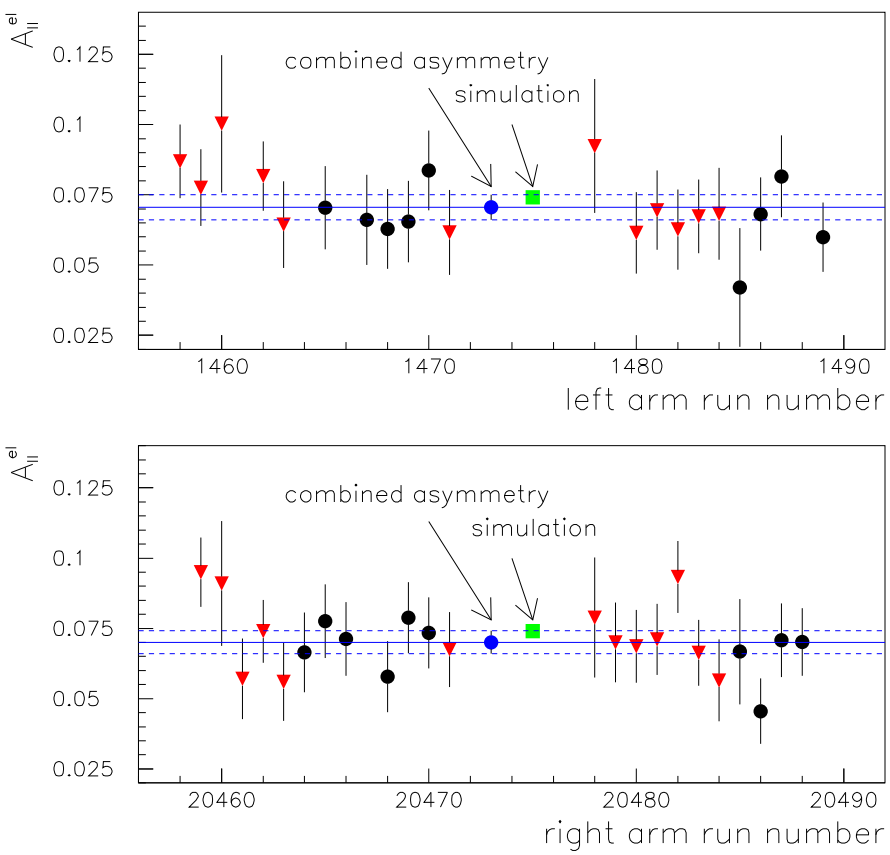

measured by the Møller polarimeter. [5]. For the target polarization P_t we used the average value of NMR and EPR measurements, interpolated in time for each run. The sign on the right hand side of Eq. (5.30) depends on the configuration of the beam half-wave plate and target spin direction. We denote the status of the beam half-wave plate to be 'IN' if it is inserted, and 'OUT' if not. The target spin direction is always aligned to the holding field direction, e.g., parallel to the beam direction for 0° field, and anti-parallel to beam for 180° field. The measured raw asymmetries are positive for (beam half-wave plate, target spin) = (OUT, 0°) or (IN, 180°), and are negative for (OUT, 180°) or (IN, 0°). The expected asymmetry from Eq. (5.20) is found to be positive. Therefore from Eq. (5.20) the absolute helicity state of the electron beam is determined to be +1 during H+ pulses, and −1 during H− pulses, in the case of the beam half-wave plate not inserted (OUT), and opposite to the helicity signal if the beam half-wave plate is inserted (IN). The elastic asymmetry results are shown in Figure 5-19. The sign for results from runs with (OUT, 180°) and (IN, 0°) has been reversed and the data points are shown as red triangles. The combined asymmetries from all runs agree with the simulation at a level of 4%, which is within its total uncertainty (4.5%). We conclude from this result that the beam and target polarizations from polarimetry measurements are correct within their uncertainties. Also the helicity-dependent part of experimental apparatus is well under control.

5.5 $\Delta(1232)$ Transverse Asymmetry

The transverse asymmetry of the $\Delta(1232)$ was measured to determine the sign convention for perpendicular electron asymmetries. The kinematics for the measurement was: $E_b = 1.196$ GeV, $E' = 0.796$ GeV/c and $\theta = 20°$.

The perpendicular asymmetry in electron scattering is defined by Eq. (1.46):

$$A_\perp = \frac{\frac{d\sigma_{\downarrow\Rightarrow}}{d\Omega dE'} - \frac{d\sigma_{\uparrow\Rightarrow}}{d\Omega dE'}}{\frac{d\sigma_{\downarrow\Rightarrow}}{d\Omega dE'} + \frac{d\sigma_{\uparrow\Rightarrow}}{d\Omega dE'}} ,$$

where $\frac{d\sigma_{\downarrow\Rightarrow}}{d\Omega dE'}$ ($\frac{d\sigma_{\uparrow\Rightarrow}}{d\Omega dE'}$) is the cross section for scattering off a target polarized perpendicular to the beamline, with incident electron spin anti-parallel (parallel) to the beam direction, and the scattered electrons being detected on the same side of the beamline as that to which the target spin is pointing. $A_\perp$ can be extracted from raw asymmetry given by Eq. (5.29) as

$$A_\perp = \pm\frac{A_{raw}}{f_{N_2} P_b P_t} . \tag{5.31}$$

[5] Elastic data were taken on June 5th and 6th, 2001; Compton polarimetry was not available until June 15th, 2001.

The sign on the right hand side depends on the beam half-wave plate status, target spin direction, and in which (left or right) HRS the asymmetry is measured. The asymmetries of the $\Delta(1232)$ resonance have been measured in about the same Q^2 range during a previous experiment in 1998 [150]. Their final results give the $\Delta(1232)$ transverse asymmetry without being corrected for the radiative effect and N_2 dilution, denoted by $A^{\Delta}_{\perp,raw}/(P_b P_t)$, to be [151]

- At $Q^2 = 0.03$ (GeV/c)^2, $A^{\Delta}_{\perp,raw}/(P_b P_t)$=0.79%;
- At $Q^2 = 0.16$ (GeV/c)^2, $A^{\Delta}_{\perp,raw}/(P_b P_t)$=1.81%.

We interpolate these data to our kinematics $Q^2 = 0.115$ (GeV/c)^2, and obtained $A^{\Delta}_{\perp,raw}/(P_b P_t)$=1.45%. Figure 5-20 shows the results for $A^{\Delta}_{\perp,raw}/(P_b P_t)$ from our data. This is the transverse asymmetry before being corrected for the sign, radiation effect and the N_2 dilution. A cut $|W_{^3\mathrm{He}} - M_{\Delta}| < 0.02$ GeV/c^2 has been applied to select events from the $\Delta(1232)$ resonance, where $M_{\Delta} = 1.232$ GeV/c^2 is the mass of the

Figure 5-20: Measured $\Delta(1232)$ transverse raw asymmetry $A^{\Delta}_{\perp,raw}/(P_b P_t)$ without sign correction. No correction for radiative effect and N_2 dilution has been applied. A cut $|W_{^3\mathrm{He}} - M_{\Delta}| < 0.02$ GeV/c^2 has been used to select events from $\Delta(1232)$ resonance. The beam half-wave plate was inserted and target spin direction was 270°. The expected value $A^{\Delta}_{\perp,raw}/(P_b P_t)$=1.45% is shown as a blue line.

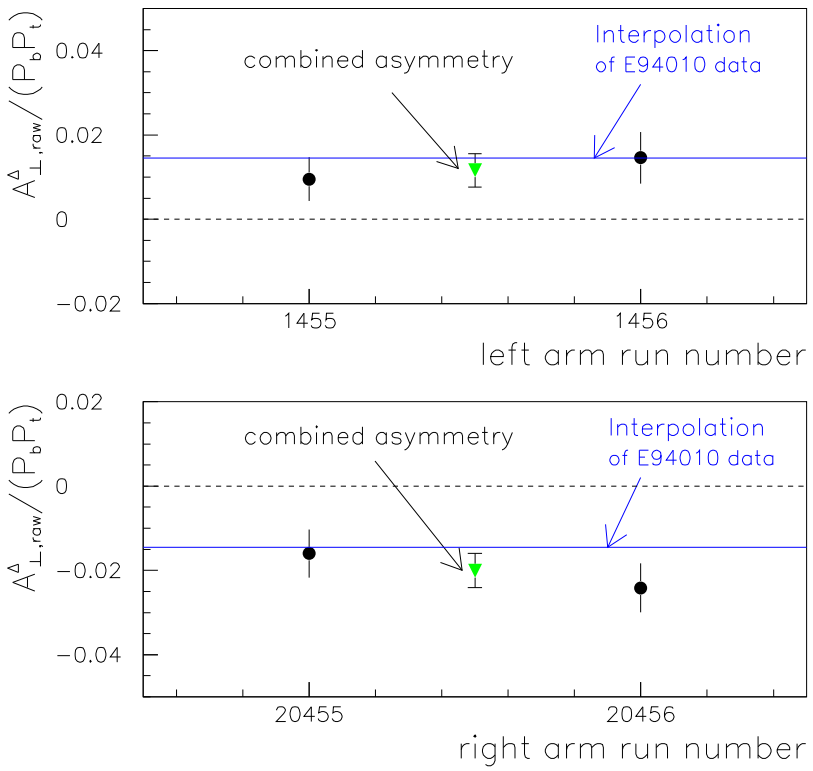

$\Delta(1232)$. The asymmetries from the left and the right HRS data have the opposite sign, both are very close to the expected value. We therefore conclude that the measurement is reliable and one can use $A_\perp^\Delta$ to determine the sign convention for measured transverse asymmetries.

The raw $\Delta(1232)$ transverse asymmetry measured during the A_1^n experiment was positive in the left HRS, with beam half-wave plate IN and target spin at 270°. The sign on the right hand side of Eq. (5.31) should be '+' for (beam half-wave plate, target, HRS)=(IN, 270°, left), (OUT, 90°, left) or (IN, 90°, right), (OUT, 270°, right); and '−' for (beam half-wave plate, target, HRS)=(IN, 90°, left), (OUT, 270°, left) or (IN, 270°, right), (OUT, 90°, right).

5.6 DIS Analysis

The asymmetry and cross section analysis for DIS data is discussed in this section. First, the procedure of removing data collected during beam trips and rampings is described. Then the sign conventions for the longitudinal and transverse asymmetries are clarified. The results of false asymmetry and positron background tests are presented. Next the procedure and results for radiative corrections to the asymmetries will be given. The systematic uncertainties in the DIS cross sections and asymmetries will be discussed. The systematic uncertainties in the asymmetry A_1^n will be presented in detail. The results for the DIS cross sections will be presented at the end. The DIS asymmetry results will be presented in Chapter 6.

5.6.1 Charge Asymmetry and Beam Trips

As described in Section 3.8.3, the average charge asymmetry during one run was controlled to below 200 ppm by the charge asymmetry feedback system. However, for the deep inelastic data taking in the A_1^n experiment, the electron beam was used at an energy of 5.7 GeV. At this energy the beam is not stable and trips typically every 2 minutes. To smooth the heat impact to the target, the beam was ramped on at a slope of 0.1 μA/sec after each trip. During these beam trips and beam rampings, the beam intensity asymmetry measured in Hall A was not stable, which can be explained by the unstable asymmetry from the electron source. To make sure that the beam intensity asymmetries do not affect the results, data during beam trip and rampings were removed, as shown in Figure 5-21. This procedure is called "beam trip removal".

5.6.2 Sign Convention for Asymmetries

The parallel asymmetry is defined by Eq. (1.45) and is repeated here

$$A_\parallel = \frac{\frac{d\sigma_{\downarrow\Uparrow}}{d\Omega dE'} - \frac{d\sigma_{\uparrow\Uparrow}}{d\Omega dE'}}{\frac{d\sigma_{\downarrow\Uparrow}}{d\Omega dE'} + \frac{d\sigma_{\uparrow\Uparrow}}{d\Omega dE'}},$$

Figure 5-21: Beam trip removal at 5.7 GeV running.
Red: events during stable beam, used for the analysis; Green: events during beam trips and rampings, removed.

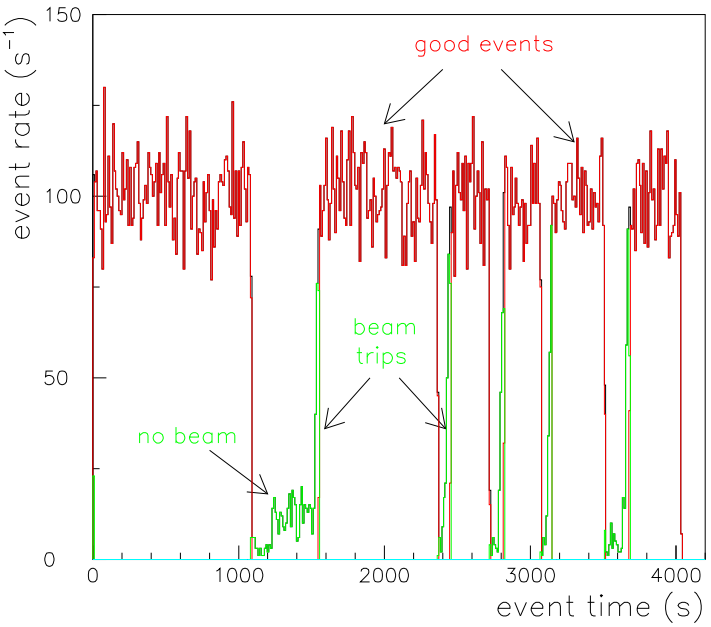

where $\frac{d\sigma_{\downarrow\Uparrow}}{d\Omega dE'}$ ($\frac{d\sigma_{\uparrow\Uparrow}}{d\Omega dE'}$) is the cross section for scattering off a longitudinally polarized target, with incident electron spin anti-parallel (parallel) to the target spin. $A_{\parallel}$ can be extracted from the raw asymmetry of Eq. (5.29) as

$$A_{\parallel} = \pm\frac{A_{\parallel,raw}}{f_{N_2}P_bP_t} + \Delta A_{\parallel}^{RC} , \tag{5.32}$$

where $\Delta A_{\parallel}^{RC}$ is the radiative correction; it will be given in Section 5.6.6. The sign on the right hand side depends on the configuration of the beam half-wave plate and the target spin direction. From the definition of $A_{\parallel}$ and the electron beam helicity states found in Section 5.4.8, it should be '+' for (beam,target)=(IN, 0°) or (OUT, 180°) and '−' for (IN, 180°) or (OUT, 0°).

The perpendicular asymmetry is defined by Eq. (1.46) and can be extracted from the raw asymmetry of Eq. (5.29) as

$$A_{\perp} = \pm\frac{A_{\perp,raw}}{f_{N_2}P_bP_t} + \Delta A_{\perp}^{RC} , \tag{5.33}$$

where $\Delta A_{\perp}^{RC}$ is the radiative correction; it will be given in Section 5.6.6. The first term on the right hand side is the same as the $\Delta(1232)$ transverse asymmetry, and therefore it follows the same sign convention as given in Section 5.5.

5.6.3 False Asymmetries

To make sure that the data were not affected by false asymmetries, we performed a false asymmetry check at the kinematics of $x = 0.33$ using an unpolarized ^{12}C foil

Figure 5-22: False asymmetry results for four different combinations of beam half-wave plate status and beam helicity signal mode. Data were taken on an unpolarized ^{12}C foil target; The kinematics was $E_b = 5.73$ GeV, $E' = 1.32$ GeV and $\theta = 35°$.

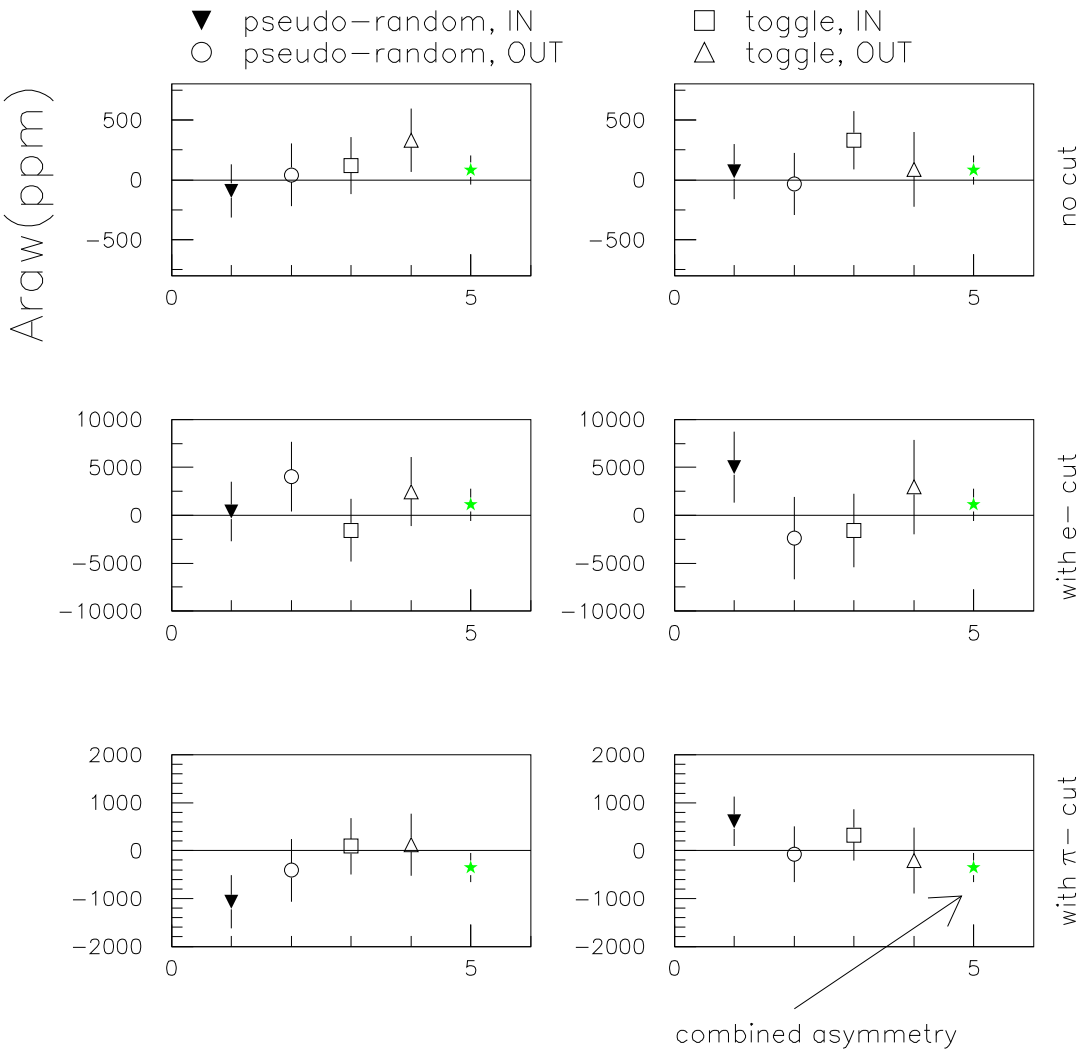

target. The beam half-wave plate was inserted for half of the statistics and the two beam helicity signal modes (pseudo-random and toggle, see Section 3.6.4) were both tested. The asymmetries from the data were checked both with and without PID cuts. The results are shown in Figure 5-22. The asymmetries for each combination of beam half-wave plate and helicity mode, as well as their combined asymmetries, are consistent with zero within their error bars. In addition, the statistical errors in

the measured ^{3}He DIS longitudinal (transverse) asymmetries are 1340 (2693) ppm, 1343 (2363) ppm and 2213 (4640) ppm for $x = 0.33$, 0.47 and 0.60, respectively. The magnitude of the false asymmetry is negligible compared with the statistical error in the measured DIS ^{3}He asymmetries for all three kinematics.

5.6.4 Positron Background

In addition to pion photo-production background, one of the background processes contributing to the inelastic (e, e') scattering is pair production $\gamma \to e^- + e^+$, where γ comes from the decay of photo-produced pions. The electrons produced by this process cannot be separated from those from (e, e') inclusive scattering. However, one can measure the positron (e^+) yield at the same kinematics and subtract it from the data, because the yield of e^- and e^+ are the same in the pair production process. This is the reason why this background contribution is also called 'positron background'. During the A_1^n experiment we measured the positron background at the kinematics $x = 0.33$. The positron yield was found to contribute 5.5% to the total yield. We did not measure the positron background at the other two kinematics. However, the positron background was estimated [152] to contribute $\sim 0.2\%$, $\sim 0.5\%$ and $\sim 3\%$ to the total yield at $x = 0.60$, 0.47 and 0.33, respectively. Therefore we concluded that the positron background contributes less than 1% at $x = 0.60$ and 0.47 (from estimation), and contributes 5.5% at $x = 0.60$ (from data). The positron asymmetries were found to be consistent with zero within their error bars. So the positron background is considered to be a dilution effect.

5.6.5 N_2 Dilution for DIS Data

The N_2 dilution is obtained by the ratio of N_2 and ^{3}He fill pressure of the polarized cell and the cross section ratio $\sigma_{N_2}/\sigma_{^3He}$ obtained from reference cell data filled with N_2 and ^{3}He. The results are shown in Table 5.6.5.

Table 5.2: N_2 dilution factor for DIS analysis.

x	Cell Name	n_{N_2} (amg)	$n_{^3He}$ (amg)	$\sigma_{N_2}/\sigma_{^3He}$	$f_{N_2} = 1 - \frac{n_{N_2}}{n_{^3He}} \frac{\sigma_{N_2}}{\sigma_{^3He}}$
0.33	Tilghman	0.075	8.28	6.720	0.9390
0.47	Tilghman	0.075	8.28	6.870	0.9376
0.60	Gore	0.0773	9.10	7.231	0.9386

5.6.6 Radiative Corrections

Radiative corrections were performed for the ^{3}He asymmetries $A_{\parallel}^{^3\mathrm{He}}$ and $A_{\perp}^{^3\mathrm{He}}$ directly. We denote by A^{obs} the observed asymmetry, i.e., the measured asymmetry from the data; A^{Born} the non-radiated (Born) asymmetry; ΔA^{ir} the correction due to internal radiation effects and ΔA^{er} the correction due to external radiation effects. One has

$$A^{Born} = A^{obs} + \Delta A^{ir} + \Delta A^{er} \tag{5.34}$$

for a specific target spin orientation. Comparing with Eq. (5.32) and (5.33), one obtains the full radiative corrections $\Delta A_{\parallel}^{RC} = \Delta A_{\parallel}^{ir} + \Delta A_{\parallel}^{er}$, and $\Delta A_{\perp}^{RC} = \Delta A_{\perp}^{ir} + \Delta A_{\perp}^{er}$.

Internal and external radiative corrections were performed separately for the A_1^n experiment.

Internal corrections were calculated using an improved version of POLRAD 2.0 [145]. This program calculates both the non-radiated (Born) asymmetry A^{Born} and the internally radiated asymmetry $A^{ir} = A^{Born} - \Delta A^{ir}$. The difference of these two asymmetries is the internal radiative correction ΔA^{ir}.

External corrections were calculated in SAMC simulation (see Section 5.3) based on the procedure first described by Mo & Tsai [154]. SAMC calculates both the internally radiated asymmetry A^{ir} and the observed asymmetry $A^{obs} = A^{ir} - \Delta A^{er}$ The difference of these two asymmetries is the external radiative correction ΔA^{er}.

Since the theory for radiative corrections is well established [154], the quality of the radiative corrections depends mainly on the quality of the structure functions used in the procedure. Both the polarized and unpolarized structure functions in POLRAD 2.0 were updated; see Appendix D. A comparison among the radiative correction results using different structure functions was made to estimate the systematic error of the corrections. The error in the external corrections was estimated in a similar manner in SAMC, plus an extra contribution from the uncertainty in the cell glass wall thickness.

Internal Radiative Correction Results

Both non-radiated (Born) asymmetry A^{Born} and internally radiated asymmetry A^{ir} are given by POLRAD 2.0, for either a longitudinally or a transversely polarized target [6]. Four different fits of unpolarized structure functions [142][155][156][157] have been used to estimate the full uncertainty. Details of each fit can be found in Appendix D. We obtain from POLRAD 2.0 an internal radiative correction using

[6] Here I want to mention one technical thing for POLRAD 2.0 outputs. The asymmetries given in the output file asm.out for longitudinally and transversely polarized targets are $A_{\parallel}/D$ and $A_{\perp}/D$, respectively, where D is a factor given by $D = y(2-y)/[y^2 + 2(1-y)(1+R)]$. $R = \sigma_L/\sigma_T$ is defined in Section 1.12 and $y = \nu/E_b$ is the fractional energy loss of the incident electron defined in Section 1.5. This was not clarified in the POLRAD 2.0 manual.

Table 5.3: Internal radiative corrections to $A_{\parallel}^{^3\mathrm{He}}$ and $A_{\perp}^{^3\mathrm{He}}$, given as absolute values (not percentage).

x	$\Delta A_{\parallel}^{ir} = A_{\parallel,Born} - A_{\parallel}^{ir}$	$\Delta A_{\perp}^{ir} = A_{\perp,Born} - A_{\perp}^{ir}$
0.327	-0.00577 $\pm$ 0.00047	0.00266 $\pm$ 0.00003
0.466	-0.00328 $\pm$ 0.00013	0.00147 $\pm$ 0.00005
0.601	-0.00266 $\pm$ 0.00015	0.00128 $\pm$ 0.00007

each fit; then the full uncertainty is given by $\delta(\Delta A^{ir}) = \Delta A^{ir}_{\max} - \Delta A^{ir}_{\min}$, where ΔA^{ir}_{max} and ΔA^{ir}_{min} are the maximum and the minimum values of all four results.

Internal radiative correction results are shown in Table 5.3.

External Radiative Correction Results

The external radiative correction is calculated by SAMC. It uses internally radiated structure functions g_1 and g_2 to calculate the asymmetry A^{ir}. Then the procedure described by Mo & Tsai [154] is used to calculate the external radiation effect, thus obtaining the observed asymmetry $A^{obs} = A^{ir} - \Delta A^{er}$.

The internally radiated structure functions g_1 and g_2 were generated using POLRAD 2.0. We first computed the kinematic ranges of g_1 and g_2 needed for the external radiative corrections, as will be presented in Appendix D. Then we created a three-dimensional grid of (E_b, x, y) which covers the required kinematic range, and ran POLRAD 2.0 for each kinematics of this grid. Here E_b is the beam energy, x is the Bjorken variable and $y = \nu/E_b$ is the fractional energy loss of the incident electron. Since POLRAD 2.0 calculates the polarized and unpolarized cross sections with internal radiation effects included, we thus obtained the internally radiated structure functions g_1 and g_2 within the kinematics range required by the external radiative corrections.

Table 5.4: External radiative corrections to $A_{\parallel}^{^3\mathrm{He}}$ and $A_{\perp}^{^3\mathrm{He}}$, given as absolute values (not percentage). Errors are from the uncertainties in the structure functions and the cell wall thickness.

x	$\Delta A_{\parallel}^{er} = A_{\parallel}^{obs} - A_{\parallel}^{ir}$	$\Delta A_{\perp}^{er} = A_{\perp}^{obs} - A_{\perp}^{ir}$
0.327	-0.00067 $\pm$ 0.00010	-0.00005 $\pm$ 0.00011
0.466	-0.00116 $\pm$ 0.00015	0.00080 $\pm$ 0.00046
0.601	-0.00039 $\pm$ 0.00003	0.00029 $\pm$ 0.00004

The results for the external radiative correction are given in Table 5.4. Similar to the case of internal radiative corrections, four different fits of unpolarized structure

functions [142][155][156][157] were used to estimate the uncertainty in the correction due to the quality of the structure functions. The cell wall thickness was varied from 1.3 mm to 1.7 mm to estimate the uncertainty due to the error in cell wall thickness found in the elastic analysis.

Corrections to Data

Using Eq. (5.32), (5.33), (5.34) and the results for internal and external radiative corrections given in Table 5.3 and 5.4, the asymmetries $A_{\parallel}^{^3\mathrm{He}}$ and $A_{\perp}^{^3\mathrm{He}}$ were calculated from the measured asymmetries obtained in the DIS analysis as

$$\begin{aligned} A_{\parallel}^{^3\mathrm{He}} &= \pm\frac{A_{\parallel,raw}^{^3\mathrm{He}}}{f_{\mathrm{N}_2}P_bP_t} + \Delta A_{\parallel}^{ir} + \Delta A_{\parallel}^{er} \ ; \\ A_{\perp}^{^3\mathrm{He}} &= \pm\frac{A_{\perp,raw}^{^3\mathrm{He}}}{f_{\mathrm{N}_2}P_bP_t} + \Delta A_{\perp}^{ir} + \Delta A_{\perp}^{er} \ . \end{aligned}$$

5.6.7 Systematic Error Estimate for DIS Analysis

In DIS analysis, we used the average value of the Compton and the Møller measurements given in Section 3.6.3 for the beam polarization. For the target polarization we used the average value of the EPR and the NMR measurements, interpolated in time for each run.

Systematic Error for DIS Asymmetries

The systematic uncertainty in the measured DIS asymmetries comes from the following sources:

- Target polarization: 3% [125];
- Beam polarization: 2.5%, as given in Section 3.6.3;
- The error in the nitrogen dilution factor comes from the uncertainties in N_2 and ^{3}He pressure, and the ratio of the N_2 and ^{3}He cross sections. We estimate $\pm 10\%$ in the cross section ratio, and obtain the uncertainty in the asymmetry

$$\frac{\Delta A}{A} = \frac{\Delta f_{\mathrm{N}_2}}{f_{\mathrm{N}_2}} = \frac{\Delta(\frac{\sigma^{\mathrm{N}_2}}{\sigma^{^3\mathrm{He}}})\frac{n_{\mathrm{N}_2}}{n_{^3\mathrm{He}}}}{f_{\mathrm{N}_2}} = \frac{(\pm 10\%)(1-f_{\mathrm{N}_2})}{f_{\mathrm{N}_2}} \approx \pm 0.7\% \ ;$$

- We estimate the uncertainty in the positron background cross section to be 10% at $x = 0.33$. The positron background contributes $\sim 5\%$ to the total cross section at $x = 0.33$. Therefore the uncertainty due to the error in positron background dilution is $5\% \times 10\% = 0.5\%$ at $x = 0.33$, and is negligible at $x = 0.47$ and 0.60;
- The error in the helicity dependent deadtime corrections is negligible, as described in Section 3.10.3;

- The uncertainty due to kinematics has been evaluated using the error propagation method [153]. It includes the uncertainties of beam energy $\Delta E_b/E_b \leqslant 5 \times 10^{-4}$, HRS central momentum $\Delta E_e/E_e \leqslant 5 \times 10^{-4}$, HRS central angle $\Delta\theta_e \leqslant 0.06^\circ$, and the target spin direction $\Delta\alpha_{\rm tg} \leqslant 1^\circ$;

The total systematic uncertainty from the sources listed above will be presented in Section 5.8 as "experimental systematics".

Systematic Error for DIS Cross Sections

The relative systematic errors in the cross sections come from the following sources:

- Target density: 3% [119];
- The error in the nitrogen dilution factor is the same as that for the DIS asymmetry, $\sim 0.7\%$;
- The uncertainty due to the absolute deadtime corrections is 0.2%, as described in Section 3.10.3;
- We estimate 1% uncertainty due to the error in VDC and trigger efficiencies;
- We estimate 2% uncertainty due to the error in PID efficiencies. This is due to the fact that the PID efficiency analysis was performed at a kinematics ($E' = 1.12$ GeV) different from the running conditions ($E' = 1.32$, 1.72 and 1.45 GeV for x =0.33, 0.47 and 0.60, respectively);
- The uncertainty due to the error in the beam charge is 1% [85];
- The uncertainty due to the error in the R-function acceptance cut is estimated to be 1%;
- The uncertainty in the cross section due to the error in the ^{3}He structure function $F_1^{^3\rm He}$ is 2.6%. This can be decomposed into three sources: the structure function F_2 for the proton ($\pm$ 2.3%) and the neutron ($\pm$ 2.4%) [142], the ratio $R = \sigma_L/\sigma_T$ ($\pm$ 1%) [143], and ^{3}He EMC effect ($\pm$ 1%) [144];
- We estimate the radiative correction procedure in the simulation has a relative error of 20%. By "radiative correction" we refer to the sum of elastic, quasi-elastic and inelastic radiative tails. The uncertainties in the total cross sections due to this error are 1.4%, 0.47% and 0.5%, at $x = 0.33$, 0.47 and 0.60, respectively;
- Similar to the case of DIS asymmetries, we estimate the uncertainty in the DIS cross section due to the error in the positron background dilution to be 0.5% at $x = 0.33$, and is negligible at $x = 0.47$ and 0.60;

- The uncertainty due to the HRS transport model has been studied in SAMC by using different versions of the HRS transport functions. The uncertainty is found to be 0.1%;

- The uncertainty due to kinematics has been studied in SAMC. The uncertainty in the asymmetry due to beam energy ($\Delta E_b = \pm 1.52$ MeV, from Table 3.3), HRS central momentum ($\Delta p_0/p_0 = \pm 5 \times 10^{-4}$ [147]), HRS central angle ($\Delta\theta_0 = \pm 0.06^\circ$ [149]), and the radiation length of the material traversed by the scattered electrons (± 0.2 mm glass, this study), is found to be at the level of 3%.

The uncertainties are added in quadrature. We obtained a systematic error of 6% for the DIS cross sections.

5.6.8 DIS Cross Section Analysis

If the DIS cross sections are measured and the ratio $R = \sigma_L/\sigma_T$ is known, one can obtain the unpolarized structure function F_1 and thus determine the polarized structure functions g_1 and g_2 from Eq. (1.56) and (1.57).

Simulation for DIS Data

To obtain the Born cross section from the data, SAMC was used to perform the DIS simulation. The HRS acceptance effect, the internal and external radiations were included.

Elastic and quasi-elastic radiative tails were simulated based on the peaking approximation [158][159]. A description of the form factors used in the peaking approximation was given in Section 5.3. We found that elastic radiative tails are negligible for all three kinematics, but quasi-elastic tails are not. The ratios of the quasi-elastic tail to the total cross section are $< 1\%$, 2.5% and 5% at x =0.60, 0.47 and 0.33, respectively.

The DIS cross sections can be extracted from data using

$$\left(\frac{\mathrm{d}\sigma}{\mathrm{d}E'\mathrm{d}\Omega}\right)^{data} = \frac{N^{data}}{Q\ \eta_{DT}\ \eta_{PID}\ \eta_{VDC}\ \eta_{trig.}} \frac{N^{MC}_{tot}}{N^{MC}_{accp}\ \rho_{\mathrm{tg}} d_{\mathrm{tg},il}\ \Delta p_{il} \Delta\Omega_{il}}\ , \quad (5.35)$$

where Δp_{il} is the illuminated range of the outgoing electron's momentum. Δp_{il} needs to be large enough to include the elastic and quasi-elastic scattering, such that the full radiation effect of the scattered electrons can be included. Other quantities are the same as those in Eq. (5.22). For the DIS simulation we used $-0.06 < \Delta p_{il}/p_0 < 2.0$, $d_{\mathrm{tg},il} = 25$ cm, $\Delta\theta_{il} = 150$ mrad and $\phi_{il} = 80$ mrad, where p_0 is the HRS central momentum. We used acceptance cuts $R > 0.005$ and $|\Delta p_{\mathrm{tg}}/p_0| < 4.5\%$ for both data and the simulation.

DIS Cross Section Results

Figure 5-23 shows cross section results obtained from Eq. (5.35) compared with the

Figure 5-23: DIS cross sections. The simulation is performed using world fits of unpolarized structure functions [142][143] for the DIS evaluation, the peaking approximation for the evaluation of the elastic and quasi-elastic elastic tails. A 6% error bar has been plotted for each data point for the cross sections and the ratio of $\sigma^{data}/\sigma^{MC}$.

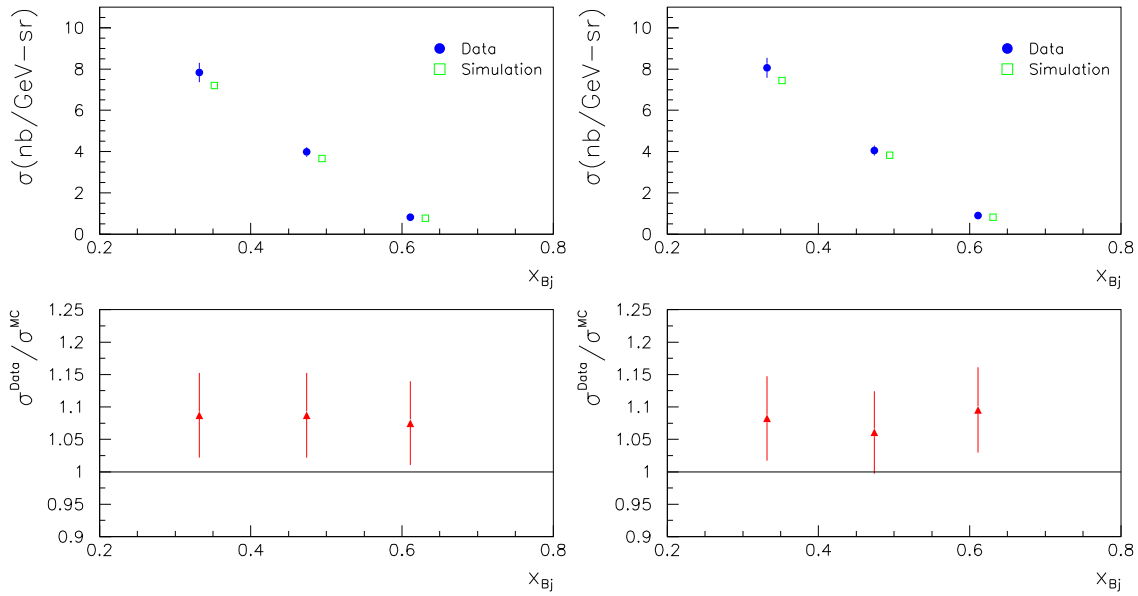

simulated observed cross sections σ^{MC}. The results agree with simulation at the level of 8%. This difference is larger than the 6% systematic uncertainty obtained in the last section, which indicates that there are unknown systematic uncertainties which have not been taken into account in our analysis. However, the goal of the DIS cross section analysis is to obtain g_1 and g_2 from results for the measured structure function ratios g_1/F_1 and g_2/F_1. In the following we will show that a 10% uncertainty in the DIS cross sections will not significantly affect the final results of g_1 and g_2.

For the ^{3}He results, assuming the structure function ratio obtained from DIS asymmetry analysis is $(g_1^{^3\mathrm{He}}/F_1^{^3\mathrm{He}})^{\mathrm{m}}$, where 'm' stands for 'measured'. The unpolarized structure function obtained from the DIS cross section results is $F_1^{^3\mathrm{He,m}}$. Then the polarized structure function $g_1^{^3\mathrm{He}}$ is given by $g_1^{^3\mathrm{He}} = F_1^{^3\mathrm{He,m}}(g_1^{^3\mathrm{He}}/F_1^{^3\mathrm{He}})^{\mathrm{m}}$. Its uncertainty is given by

$$\Delta g_1^{^3\mathrm{He}} = \sqrt{\left[\Delta F_1^{^3\mathrm{He,m}}(g_1^{^3\mathrm{He}}/F_1^{^3\mathrm{He}})^{\mathrm{m}}\right]^2 + \left[F_1^{^3\mathrm{He,m}}\Delta(g_1^{^3\mathrm{He}}/F_1^{^3\mathrm{He}})^{\mathrm{m}}\right]^2}, \quad (5.36)$$

where $\Delta F_1^{^3\mathrm{He,m}}$ and $\Delta(g_1^{^3\mathrm{He}}/F_1^{^3\mathrm{He}})$ are the total uncertainties of $F_1^{^3\mathrm{He,m}}$ and $g_1^{^3\mathrm{He}}/F_1^{^3\mathrm{He}}$,

respectively. We compare the two terms on the right hand side of Eq. (5.36):

$$\frac{\text{1st term}}{\text{2nd term}} = \left\{ \frac{\Delta F_1^{^3\text{He,m}}}{F_1^{^3\text{He,m}}} \frac{(g_1^{^3\text{He}}/F_1^{^3\text{He}})^{\text{m}}}{\Delta(g_1^{^3\text{He}}/F_1^{^3\text{He}})^{\text{m}}} \right\}^2 . \tag{5.37}$$

The total error in $(g_1^{^3\text{He}}/F_1^{^3\text{He}})^{\text{m}}$ is dominated by statistical uncertainties, which give $\Delta(g_1^{^3\text{He}}/F_1^{^3\text{He}})^{\text{m}}_{\text{stat.}}/(g_1^{^3\text{He}}/F_1^{^3\text{He}})^{\text{m}} = 0.23,\ 0.98$, and 2.79 for $x = 0.33,\ 0.47$ and 0.60, respectively. The total error in the cross section is dominated by systematic uncertainties. Assuming the systematic uncertainty is 10% for all three kinematics, one obtains

$$\frac{\text{1st term}}{\text{2nd term}} = 0.18,\ 0.01,\ 0.0013 \ \text{ at } x = 0.33,\ 0.47,\ 0.60, \text{ respectively.}$$

Therefore the total error $\Delta g_1^{^3\text{He}}$ is dominated by the uncertainty in the measured structure function ratio $(g_1^{^3\text{He}}/F_1^{^3\text{He}})^m$.

Similarly, the total errors in the neutron results for g_1^n and g_2^n are dominated by the uncertainties in g_1^n/F_1^n and g_2^n/F_1^n.

We conclude that a 10% systematic uncertainty in the DIS cross section results will not affect the final results for g_1 and g_2 at a significant level. Hence the 8% difference between data and simulation shown in Figure 5-23 will not significantly affect the final results for g_1 and g_2. To minimize the total uncertainties of g_1 and g_2, we used the unpolarized structure function $F_1^{^3\text{He}}$ and F_1^n from world fits of unpolarized data [142][143][144] to calculate g_1 and g_2 from our g_1/F_1 and g_2/F_1 results. The results for g_1 and g_2 for the ^{3}He and the neutron will be presented in Sections 6.1.4 and 6.2.3, respectively.

5.7 From ^{3}He to Neutron

This section describes how to extract neutron information from a ^{3}He target in DIS experiments [165].

The properties of protons and neutrons embedded in nuclei are expected to be different from those in free space. In particular the neutron spin structure function g_1^n is not equal to the ^{3}He spin structure function $g_1^{^3\text{He}}$ because of a variety of nuclear effects. These effects include spin depolarization, nuclear binding and Fermi motion of the nucleons, the off-shellness of the nucleons, the presence of non-nucleonic degrees of freedom, and nuclear shadowing and antishadowing. In this section we first describe the convolution approach of the ^{3}He model, which was used by most of the previous polarized ^{3}He experiments. We then present a "complete" ^{3}He model which takes into account the effect of pre-existing $\Delta(1232)$ isobar in the ^{3}He ground state. In the end we show how to extract neutron asymmetries and structure function ratios from ^{3}He data and the inputs we used in the analysis. This procedure is usually referred

to as the "^{3}He nuclear correction".

5.7.1 ^{3}He Model - Convolution Approach

The nuclear effects of spin depolarization, binding and Fermi motion are traditionally described within the framework of the convolution approach [164]. In this approximation, nuclear structure functions are in general given by the convolution of the off-shell nucleon structure functions with the light-cone nucleon momentum distributions. Thus, $g_1^{^3\mathrm{He}}$ can be represented as the convolution of the off-shell neutron $\tilde{g}_1^n$ and the off-shell proton $\tilde{g}_1^p$ spin structure functions with the spin-dependent nucleon light-cone momentum distributions $\Delta f_{N/^3\mathrm{He}}(y)$, where y is the ratio of the struck nucleon's light-cone plus component of the momenta to that of the nucleus

$$\begin{aligned} g_1^{^3\mathrm{He}}(x,Q^2) &= \int_x^3 \frac{\mathrm{d}y}{y}\Delta f_{n/^3\mathrm{He}}(y)\tilde{g}_1^n(x/y,Q^2) \\ &\quad + \int_x^3 \frac{\mathrm{d}y}{y}\Delta f_{p/^3\mathrm{He}}(y)\tilde{g}_1^p(x/y,Q^2) \ . \end{aligned} \tag{5.38}$$

The motion of the nucleons inside the nucleus (Fermi motion) and their binding are parameterized through the distributions $\Delta f_{N/^3\mathrm{He}}(y)$, which can be readily calculated using the ground-state wave functions of ^{3}He. Calculations by various groups using different ground-state wavefunctions of ^{3}He came to a similar conclusion that $\Delta f_{N/^3\mathrm{He}}(y)$ is sharply peaked around $y \approx 1$ due to the small average separation energy per nucleon. Thus, Eq. (5.38) is often approximated by

$$g_1^{^3\mathrm{He}}(x,Q^2) = P_n\tilde{g}_1^n(x,Q^2) + 2P_p\tilde{g}_1^p(x,Q^2) \ . \tag{5.39}$$

A similar equation exists for $g_2^{^3\mathrm{He}}$

$$g_1^{^3\mathrm{He}}(x,Q^2) = P_n\tilde{g}_1^n(x,Q^2) + 2P_p\tilde{g}_1^p(x,Q^2) \ , \tag{5.40}$$

where $P_n(P_p)$ are the effective polarizations of the neutron (proton) inside the polarized ^{3}He nucleus, defined as

$$P_{n,p} = \int_0^3 \mathrm{d}y\Delta f_{n,p/^3\mathrm{He}}(y) \ . \tag{5.41}$$

In the first approximation to the ground-state wave function of ^{3}He, only the neutron is polarized, which corresponds to the S-wave type interaction between any pair of the nucleons of ^{3}He. In this case, $P_n = 1$ and $P_p = 0$. Realistic approaches to the wave function of ^{3}He include also higher partial waves, notably the D and S' partial waves that arise due to the tensor component of the nucleon-nucleon (N-N) force. This leads to the depolarization of the neutron and the polarization of the

protons in ^{3}He. The average of calculations with several models of N-N interactions and 3N forces can be summarized as $P_n = 0.86 \pm 0.02$ and $P_p = -0.028 \pm 0.004$ [166]. The calculations using the Paris N-N potential give similar values: $P_n = 0.879$ and $P_p = -0.021$ [167]. One should note that most of the uncertainty in the values for P_n and P_p comes from the uncertainty in the D-wave component of the ^{3}He wave function.

Assuming that one can use the on-shell neutron and proton structure functions g_1^n and g_1^p in Eq. (5.39), by dividing this equation by F_1^n and using Eq. (1.18), one obtains

$$\frac{g_1^n}{F_1^n} = \frac{1}{P_n}\frac{F_2^{^3\mathrm{He}}}{F_2^n}\Big(\frac{g_1^{^3\mathrm{He}}}{F_1^{^3\mathrm{He}}} - 2P_p\frac{F_2^p}{F_2^{^3\mathrm{He}}}\frac{g_1^p}{F_1^p}\Big) \; ; \tag{5.42}$$

Similarly, one has

$$A_1^n = \frac{1}{P_n}\frac{F_2^{^3\mathrm{He}}}{F_2^n}\Big(A_1^{^3\mathrm{He}} - 2P_p\frac{F_2^p}{F_2^{^3\mathrm{He}}}A_1^p\Big) \; . \tag{5.43}$$

5.7.2 ^{3}He Model - Complete Analysis

The above convolution model gives a simple picture of how polarized ^{3}He behaves as an effective polarized neutron target. A more comprehensive model is summarized in [165], which takes into account the off-shellness of the nucleons, the presence of non-nucleonic degrees of freedom, and nuclear shadowing and antishadowing. Then the spin structure function of ^{3}He can be written as

$$\begin{aligned} g_1^{^3\mathrm{He}}(x,Q^2) = & \int_x^3 \frac{\mathrm{d}y}{y}\Delta f_{n/^3\mathrm{He}}(y)\tilde{g}_1^n(x/y,Q^2) + \int_x^3 \frac{\mathrm{d}y}{y}\Delta f_{p/^3\mathrm{He}}(y)\tilde{g}_1^p(x/y,Q^2) \\ & -0.014(\tilde{g}_1^p(x) - 4\tilde{g}_1^n(x) + a(x)g_1^n(x) + b(x)g_1^p(x) \; , \end{aligned} \tag{5.44}$$

where $\tilde{g}_1^N$ are off-shell nucleon spin structure functions. The third term on the right hand side of Eq. (5.44) shows contributions from the Δ isobars pre-existing in ^{3}He. a and b are functions of x and Q^2 describing nuclear shadowing and antishadowing effects. The shadowing effect refers to the observation that the ratio $2F_2^A/(AF_2^D)$ is smaller than unity for $0.0035 \leqslant x \leqslant 0.03 \sim 0.07$ and the anti-shadowing effect refers to the fact that the ratio $2F_2^A/(AF_2^D)$ is larger than unity for $0.03 \sim 0.07 \leqslant x \leqslant 0.2$ [163]. a and b satisfy the following integral:

$$\int_{10^{-4}}^{0.2} \mathrm{d}x\Big(a(x) - b(x)\Big)\Big(g_1^p(x) - g_1^n(x)\Big) = 0 \; . \tag{5.45}$$

5.7.3 Extracting g_1^n and A_1^n from E99-117 ^{3}He Data

The approximate calculation given by Eq. (5.38) gives a clear picture of behavior of ^{3}He, and has been frequently used in the analysis of many polarized ^{3}He DIS experiments. But for this experiment we use Eq. (5.44) to extract neutron information from the ^{3}He results. For g_1 it gives

$$g_1^{^3\mathrm{He}} = P_n g_1^n + 2P_p g_1^p - 0.014\Big(g_1^p(x) - 4g_1^n(x)\Big) + a(x)g_1^n(x) + b(x)g_1^p(x) \quad (5.46)$$

Note that since shadowing and antishadowing are not present in the large x region, the last two terms on the right hand side can be neglected. One obtains

$$\begin{aligned} g_1^{^3\mathrm{He}} &= P_n g_1^n + 2P_p g_1^p - 0.014\Big(g_1^p(x) - 4g_1^n(x)\Big) \\ &= (P_n + 0.056)g_1^n + (2P_p - 0.014)g_1^p \ ; \end{aligned} \quad (5.47)$$

The same equation is valid for the structure functions g_2, i.e.,

$$g_2^{^3\mathrm{He}} = (P_n + 0.056)g_2^n + (2P_p - 0.014)g_2^p \ ; \quad (5.48)$$

Dividing both sides of Eq. (5.47) by the ^{3}He structure function $F_1^{^3\mathrm{He}}$, one obtains

$$\frac{g_1^{^3\mathrm{He}}}{F_1^{^3\mathrm{He}}} = (P_n + 0.056)\frac{g_1^n}{F_1^{^3\mathrm{He}}} + (2P_p - 0.014)\frac{g_1^p}{F_1^{^3\mathrm{He}}} \ . \quad (5.49)$$

Using Eq. (1.18) and assuming R is the same for proton and ^{3}He, one obtains

$$\frac{g_1^{^3\mathrm{He}}}{F_1^{^3\mathrm{He}}} = (P_n + 0.056)\frac{g_1^n}{F_1^n}\frac{F_2^n}{F_2^{^3\mathrm{He}}} + (2P_p - 0.014)\frac{g_1^p}{F_1^p}\frac{F_2^p}{F_2^{^3\mathrm{He}}} \quad (5.50)$$

$$\Rightarrow \frac{g_1^n}{F_1^n} = \frac{F_2^{^3\mathrm{He}}}{P_n F_2^n(1+\frac{0.056}{P_n})}\Big(\frac{g_1^{^3\mathrm{He}}}{F_1^{^3\mathrm{He}}} - 2\frac{F_2^p}{F_2^{^3\mathrm{He}}}P_p(1-\frac{0.014}{2P_p})\frac{g_1^p}{F_1^p}\Big) \ ; \quad (5.51)$$

Similarly, for g_2/F_1 one has

$$\frac{g_2^n}{F_1^n} = \frac{F_2^{^3\mathrm{He}}}{P_n F_2^n(1+\frac{0.056}{P_n})}\Big(\frac{g_2^{^3\mathrm{He}}}{F_1^{^3\mathrm{He}}} - 2\frac{F_2^p}{F_2^{^3\mathrm{He}}}P_p(1-\frac{0.014}{2P_p})\frac{g_2^p}{F_1^p}\Big) \ . \quad (5.52)$$

Using Eq. (1.41) and (1.42), one obtains

$$A_1^n = \frac{F_2^{^3\mathrm{He}}}{P_n F_2^n(1+\frac{0.056}{P_n})}\Big(A_1^{^3\mathrm{He}} - 2\frac{F_2^p}{F_2^{^3\mathrm{He}}}P_p(1-\frac{0.014}{2P_p})A_1^p\Big) \ ; \quad (5.53)$$

$$A_2^n = \frac{F_2^{^3\mathrm{He}}}{P_n F_2^n(1+\frac{0.056}{P_n})}\Big(A_2^{^3\mathrm{He}} - 2\frac{F_2^p}{F_2^{^3\mathrm{He}}}P_p(1-\frac{0.014}{2P_p})A_2^p\Big) \ . \quad (5.54)$$

The two terms $\frac{0.056}{P_n}$ and $\frac{0.014}{2P_p}$ represent the corrections to the neutron asymmetries or structure function ratios associated with the pre-existing Δ isobar. In Eq. (5.53), both terms make A_1^n turn positive at lower values of x compared to the convolution approach.

5.7.4 Inputs for Nuclear Corrections

From Eq. (5.53), the inputs needed for the nuclear corrections are the unpolarized structure functions F_2^p, F_2^n and $F_2^{^3\mathrm{He}}$ in the deep inelastic region, the proton asymmetry A_1^p (or A_2^p, g_1^p/F_1^p and g_2^p/F_1^p), and the effective nucleon polarization P_n and P_p.

F_2 Structure Functions

We used a world fit of proton and deuteron structure functions F_2^p and F_2^D [142] to calculate F_2^p, F_2^n and $F_2^{^3\mathrm{He}}$ in the deep inelastic region. The deuteron and the ^{3}He nuclear EMC effects are included [144]. Details of these calculations will be given in Appendix A.

Proton Asymmetries

There exists a world fit of g_1/F_1 data for both the proton and the neutron performed by the E155 collaboration at SLAC [20]. It is usually referred to as the "E155 fit". However their proton fit is not well constrained in the large x region, which is not ideal for the purpose of the data analysis of this A_1^n experiment. We did a new fit to the world data for g_1^p/F_1^p and obtained

$$g_1^p/F_1^p \;=\; x^{0.813}(1.231 - 0.413x)(1 + \frac{0.030}{Q^2}) \;, \tag{5.55}$$

where Q^2 is in $(\mathrm{GeV/c})^2$. The data set used by this fit includes g_1^p/F_1^p data from the E143 [23] and E155 [20] experiments at SLAC and the HERMES experiment [30] at DESY. Details of this fit will be presented in Appendix F.

There are two methods to obtain A_1^p. In the first method, we construct A_1^p from the g_1^p/F_1^p fit given by Eq. (5.55), assuming that the higher twist effect is small, i.e., $g_2 = g_2^{WW}$ with g_2^{WW} the twist-2 term defined by Eq. (1.37). This is a reasonable assumption since the data on g_2^p from experiment E155x at SLAC [168] show good agreement with $g_2^{p,WW}$. We then follow the procedure below:

- Construct F_1^p using Eq. (1.18) and world fits of F_2^p [142] and R [143];
- Multiply Eq. (5.55) by F_1^p, obtain g_1^p;
- At a constant Q^2, obtain $g_2^{p,WW}$ using Eq. (1.37);
- Compute A_1^p using Eq. (1.41) and the F_1^p, g_1^p, $g_2^{p,WW}$ constructed above.

However, the A_1^p value calculated from this procedure is in general higher than the world A_1^p data. The second method is to fit the world A_1^p data directly; we obtain

$$A_1^p = x^{0.771}(1.126 - 0.189x)(1 - \frac{0.09}{Q^2}) \ . \tag{5.56}$$

The fitted data set includes A_1^p data from the E143 [23] and E155 [20] experiments at SLAC, the EMC [24] and the SMC experiments [25] at CERN.

We take the average of the results from these two methods as the central value for A_1^p, and take their difference as the uncertainty in A_1^p.

For the structure function ratio g_2^p/F_1^p and the asymmetry A_2^p, we used Eq. (1.41) and (1.43) to compute their values using the F_1^p, g_1^p and A_1^p constructed above. The value of A_2^p is checked with the A_1^p fitted results to make sure that it does not exceed Soffer's bound given by Eq. (1.40).

Effective Nucleon Polarization P_n and P_p in ^{3}He

In the following we present the values of the effective nucleon polarization P_p and P_n from various calculations.

The effective nucleon polarizations P_n and P_p are given by

$$P_p = p^+ - p^- = -\frac{1}{3}\Big[P(D) - P(S')\Big] \ ; \tag{5.57}$$

$$P_n = n^+ - n^- = 1 - \frac{2}{3}\Big[P(S') + 2P(D)\Big] \ , \tag{5.58}$$

where $n^\pm$ ($p^\pm$) are the probabilities to find a neutron (proton) with a given momentum fraction y of the nucleus with spin aligned (+) or anti-aligned (−) along the spin of the nucleus.

Averaging over available world calculations gives [167]

$$P_n = 0.86 \pm 0.02 \text{ and } P_p = -0.028 \pm 0.004 \ . \tag{5.59}$$

To estimate the full uncertainty of P_n and P_p, nine more models have been investigated [165] [169]. The probabilities of S, S', P, and D states for the ^{3}He wave functions and the effective nucleon polarizations P_n and P_p for each model are listed in Table 5.7.4. The extreme values, given by the model CD-Bonn, have been combined with Eq. (5.59) to give the full uncertainty that is used in the nuclear corrections of the A_1^n experiment:

$$P_n = 0.86^{+0.036}_{-0.02}, \qquad P_p = -0.028 \pm^{+0.094}_{-0.004} \ . \tag{5.60}$$

Table 5.5: More calculations of the effective nucleon polarizations P_n and P_p.

N-N	S	S'	D	P	P_n	P_p
PEST-5	89.3%	1.88%	8.11%	0.79%	0.879	-0.0208
CD-Bonn 2000	91.35%	1.56%	7.04%	0.047%	0.896	-0.0183
CD-Bonn 2000+TM	91.46%	1.42%	7.01%	0.100%	0.897	-0.0186
CD-Bonn	91.38%	1.55%	7.02%	0.046%	0.896	-0.0182
CD-Bonn + TM	91.50%	1.42%	6.97%	0.098%	0.898	-0.0185
AV18	89.93%	1.53%	8.46%	0.065%	0.877	-0.0231
AV18 + TM	89.93%	1.26%	8.75%	0.150%	0.875	-0.0250
AV18 + TM'	89.44%	1.26%	9.16%	0.130%	0.869	-0.0263
AV18 + Urb IX	89.37%	1.24%	9.25%	0.132%	0.866	-0.0267

5.7.5 Comparison of Two Models

We used the complete analysis described in 5.7.2 for the nuclear corrections of the A_1^n experiment, while existing measurements using a ^{3}He target prior to this experiment used the convolution approach described in 5.7.1. In this section we estimate the effect on the final neutron results due to the difference between the two approaches.

We denote by $(A_1^n)^{conv}$ the results from the convolution approach described by Eq. (5.43) and $(A_1^n)^{cmplt}$ the results from the complete analysis described by Eq. (5.53); one has

$$(A_1^n)^{cmplt} - (A_1^n)^{conv} \approx \frac{F_2^{^3\mathrm{He}}}{F_2^n}\frac{0.056}{{P_n}^2}A_1^{^3\mathrm{He}} - \frac{0.014F_2^p}{P_nF_2^n}A_1^p \ .$$

Using the fits of g_1^p/F_1^p and g_1^n/F_1^n in Appendix F, P_n and P_p from Eq. (5.59) and world fits for the F_2 structure functions [142], one finds $0 < (A_1^n)^{cmplt} - (A_1^n)^{conv} < 0.02$ in the range $0.2 < x < 0.7$, as shown in Figure 5-24.

Figure 5-24: Difference in A_1^n between using the complete analysis and the convolution approach.

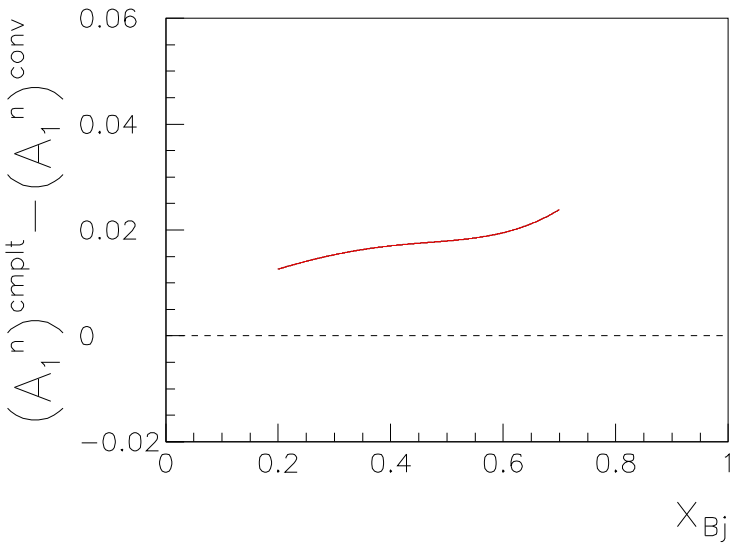

5.8 Systematic Uncertainty of Neutron Asymmetries and Structure Function Ratios

The systematic uncertainties in the neutron asymmetries and structure function ratios come from the systematic uncertainties in the measured ^{3}He asymmetries listed in Section 5.6.7, and the uncertainties in the radiative corrections and nuclear corrections. Since the systematic errors given in Section 5.6.7 are associated with the experimental technique, in the following they are referred to as "experimental uncertainties", so as to be distinguished from the uncertainties of radiative and nuclear corrections.

The uncertainties in the radiative corrections were presented in Section 5.6.6. The uncertainties in the nuclear corrections come from the following sources:

- The uncertainty due to the error of the proton and the deuteron structure functions F_2^p, F_2^D [142];
- The uncertainty due to the error of the deuteron and the ^{3}He EMC effect $\mathcal{R}^D \equiv (2F_2^D)/(F_2^p + F_2^n)$ and $\mathcal{R}^{^3\mathrm{He}} \equiv (3F_2^{^3\mathrm{He}})/(2F_2^p + F_2^n)$ [144];
- The uncertainty due to the proton asymmetry A_1^p was estimated in Section 5.7.4;
- The uncertainty due to the error of the nucleon effective polarizations P_p and P_n inside the ^{3}He nucleus was given in Section 5.7.4.

The total errors for A_1^n including experimental systematics, radiative corrections and nuclear corrections are shown in Table 5.6, where $\Delta A_1^{n,ir}$ is the error in the internal

radiative corrections and $\Delta A_1^{n,er}$ is the error in the external radiative corrections.

Table 5.6: Total errors for A_1^n, all numbers are absolute values given in %.

x	0.327	0.466	0.601
Statistics	2.43	2.67	4.78
Experimental systematics	0.42	0.32	0.35
$\Delta A_1^{n,ir}$	1.19	1.31	1.50
$\Delta A_1^{n,er}$	0.22	0.24	0.28
F_2^p, F_2^d	$^{+0.55}_{-0.59}$	$^{+0.78}_{-0.75}$	$^{+0.48}_{-0.93}$
EMC effect	0.13	0.03	0.92
A_1^p	0.13	0.51	1.12
P_n, P_p	$^{+0.50}_{-1.15}$	$^{+0.93}_{-2.04}$	$^{+1.78}_{-3.74}$

As shown in Figure 5-25, the total error of A_1^n is dominated by the statistical uncertainty. The three main sources of the systematic error are those due to the uncertainties in the effective nucleon polarization P_n and P_p, the radiative corrections and the proton asymmetry A_1^p.

Figure 5-25: Sources of error in A_1^n. The total errors are dominated by the statistical uncertainty. The three main sources of the systematic error are those due to the uncertainties in the effective nucleon polarization P_n and P_p, the radiative corrections and the proton asymmetry A_1^p.

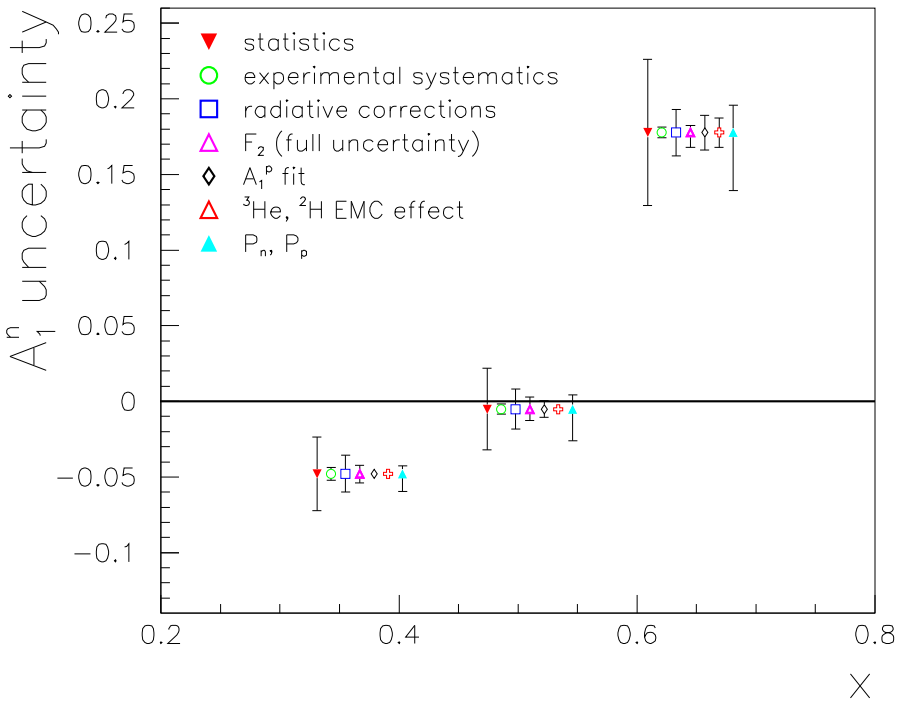

Chapter 6

Results and Conclusions

In this chapter we first present the ^{3}He results for $A_{\parallel}^{^3\mathrm{He}}$, $A_{\perp}^{^3\mathrm{He}}$, $g_1^{^3\mathrm{He}}/F_1^{^3\mathrm{He}}$, $g_2^{^3\mathrm{He}}/F_1^{^3\mathrm{He}}$, $A_1^{^3\mathrm{He}}$, $A_2^{^3\mathrm{He}}$, $g_1^{^3\mathrm{He}}$, and $g_2^{^3\mathrm{He}}$. Neutron results for A_1^n, A_2^n, g_1^n/F_1^n, g_2^n/F_1^n, g_1^n, and g_2^n are presented in Section 6.2. Results for the flavor decomposition of polarized parton distribution functions $(\Delta u + \Delta\bar{u})/(u + \bar{u})$ and $(\Delta d + \Delta\bar{d})/(d + \bar{d})$ are presented in Section 6.3. Pion asymmetry results as a by-product of the experiment are given in Section 6.4. The impact of data on the understanding of the nucleon spin structure is discussed in Section 6.5. We will conclude this dissertation in Section 6.6.

Results from this experiment will be compared with existing world data. World ^{3}He data are from E142 [26] and E154 [27] experiments at the Stanford Linear Accelerator (SLAC) and the HERMES [29] experiment at the Deutsches Elektronen-Synchrotron (DESY).

World neutron data on A_1^n are from E142 [26], E154 [27] experiments at SLAC using a ^{3}He target, the Spin Muon Collaboration (SMC) [28] experiment at CERN using a deuteron (^{2}H) target, and the HERMES [29] experiment at DESY using a ^{3}He target. World neutron data on g_1^n/F_1^n are from E143 [23] and E155 [20] experiments at SLAC using a ^{2}H target. The neutron data obtained from a ^{3}He target are taken from the original publications or web sites and have not been re-analyzed using the complete ^{3}He nuclear corrections. However in Section 5.7.5 we have shown that the difference in A_1^n between the two nuclear corrections is less than 2%. This difference will not affect the final conclusions.

When comparing existing data with the new results of A_1 or g_1/F_1 from this experiment, the existing data have *not* been evolved to the same Q^2 range. This Q^2 evolution of the data is not critical since A_1 and g_1/F_1 are nearly Q^2 independent, as was described in Section 1.11.

6.1 ^{3}He Results

6.1.1 ^{3}He Electron Asymmetries $A_{\parallel}^{^3\mathrm{He}}$ and $A_{\perp}^{^3\mathrm{He}}$

Results for the electron asymmetries of $\vec{e} - {}^3\vec{\mathrm{He}}$ scattering, $A_{\parallel}^{^3\mathrm{He}}$ and $A_{\perp}^{^3\mathrm{He}}$, defined respectively by Eq. (1.45), are given in Table 6.1.

Table 6.1: ^{3}He results – $A_{\parallel}^{^3\mathrm{He}}$ and $A_{\perp}^{^3\mathrm{He}}$.

x	Q^2	$A_{\parallel}^{^3\mathrm{He}}\pm$stat.$\pm$sys.	$A_{\perp}^{^3\mathrm{He}}\pm$stat.$\pm$sys.
0.327	2.709	$-0.01397 \pm 0.00475 \pm 0.00071$	$-0.00216 \pm 0.00955 \pm 0.00011$
0.466	3.516	$-0.00722 \pm 0.00449 \pm 0.00036$	$0.01359 \pm 0.00790 \pm 0.00069$
0.601	4.833	$0.01036 \pm 0.00739 \pm 0.00052$	$-0.01173 \pm 0.01550 \pm 0.00059$

6.1.2 ^{3}He Structure Function Ratios $g_1^{^3\mathrm{He}}/F_1^{^3\mathrm{He}}$ and $g_2^{^3\mathrm{He}}/F_1^{^3\mathrm{He}}$

Using Eq. (1.56), (1.57) and the ^{3}He results presented in Table 6.1, we obtained results for the ^{3}He structure function ratios $g_1^{^3\mathrm{He}}/F_1^{^3\mathrm{He}}$ and $g_2^{^3\mathrm{He}}/F_1^{^3\mathrm{He}}$, as shown in Table 6.2.

Table 6.2: ^{3}He results – $g_1^{^3\mathrm{He}}/F_1^{^3\mathrm{He}}$ and $g_2^{^3\mathrm{He}}/F_1^{^3\mathrm{He}}$.

x	Q^2	$g_1^{^3\mathrm{He}}/F_1^{^3\mathrm{He}}\pm$stat.$\pm$sys.	$g_2^{^3\mathrm{He}}/F_1^{^3\mathrm{He}}\pm$stat.$\pm$sys.
0.327	2.709	$-0.0223 \pm 0.0052 \pm 0.0009$	$0.0103 \pm 0.0362 \pm 0.0016$
0.466	3.516	$-0.0077 \pm 0.0075 \pm 0.0006$	$0.0497 \pm 0.0222 \pm 0.0027$
0.601	4.833	$0.0031 \pm 0.0085 \pm 0.0006$	$-0.0276 \pm 0.0384 \pm 0.0016$

6.1.3 ^{3}He Asymmetries $A_1^{^3\mathrm{He}}$ and $A_2^{^3\mathrm{He}}$

Using the ^{3}He results presented in Table 6.1 and Eq. (1.56) and (1.57), we obtained

Table 6.3: ^{3}He results – $A_1^{^3\mathrm{He}}$ and $A_2^{^3\mathrm{He}}$.

x	Q^2	$A_1^{^3\mathrm{He}}\pm$stat.$\pm$sys.	$A_2^{^3\mathrm{He}}\pm$stat.$\pm$sys.
0.327	2.709	$-0.0237 \pm 0.0057 \pm 0.0010$	$-0.0044 \pm 0.0149 \pm 0.0007$
0.466	3.516	$-0.0187 \pm 0.0058 \pm 0.0007$	$0.0199 \pm 0.0119 \pm 0.0014$
0.601	4.833	$0.0104 \pm 0.0090 \pm 0.0007$	$-0.0128 \pm 0.0233 \pm 0.0009$

Figure 6-1: ^{3}He results – $A_1^{^3\mathrm{He}}$.

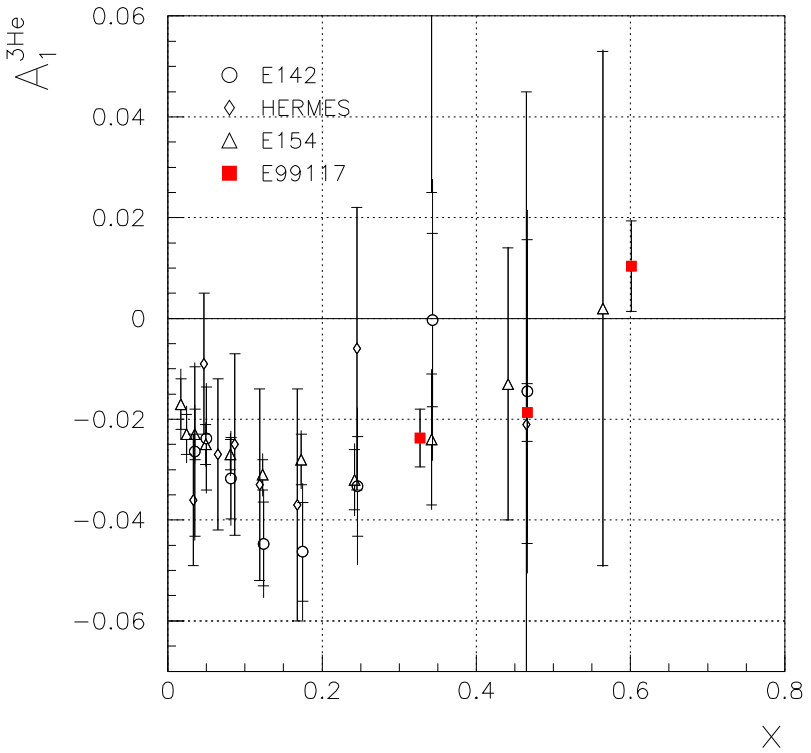

results for the ^{3}He asymmetries $A_1^{^3\mathrm{He}}$ and $A_2^{^3\mathrm{He}}$, as shown in Table 6.3. The $A_1^{^3\mathrm{He}}$ results are plotted in Figure 6-1. Also shown in Figure 6-1 are data from the E142 [26] and E154 [27] experiments at SLAC and the HERMES experiment [29] at DESY. The error bars on the experimental results from E142 and HERMES are large and cannot provide any constraining information about the value of $A_1^{^3\mathrm{He}}$ at $x > 0.3$. The new data at all three x points are in good agreement with the data from E154, but have much better precision. The new data at $x = 0.47$ and $x = 0.60$ have improved the precision by about one order of magnitude.

6.1.4 ^{3}He Polarized Structure Functions $g_1^{^3\mathrm{He}}$ and $g_2^{^3\mathrm{He}}$

The unpolarized structure function $F_1^{^3\mathrm{He}}$ was constructed using a world fit of the ratio $R = \sigma_L/\sigma_T$ [143] and the proton and deuteron unpolarized structure functions [142], with nuclear EMC effects included [144]. Details of the calculation of $F_1^{^3\mathrm{He}}$ is given in Appendix A. Results for the ^{3}He polarized structure functions $g_1^{^3\mathrm{He}}$ and $g_2^{^3\mathrm{He}}$ are obtained by multiplying the $g_1^{^3\mathrm{He}}/F_1^{^3\mathrm{He}}$ and $g_2^{^3\mathrm{He}}/F_1^{^3\mathrm{He}}$ results by the constructed $F_1^{^3\mathrm{He}}$. Results for $g_1^{^3\mathrm{He}}$ and $g_2^{^3\mathrm{He}}$ are listed in Table 6.4. Figure 6-2 shows the $g_1^{^3\mathrm{He}}$ results along with data from the E142 [26] and E154 [27] experiments at SLAC.

Table 6.4: ^{3}He results – $g_1^{^3\mathrm{He}}$ and $g_2^{^3\mathrm{He}}$.

x	Q^2	$g_1^{^3\mathrm{He}}\pm$stat.$\pm$sys.	$g_2^{^3\mathrm{He}}\pm$stat.$\pm$sys.
0.327	2.709	$-0.0240 \pm 0.0056 \pm 0.0010$	$0.0111 \pm 0.0389 \pm 0.0009$
0.466	3.516	$-0.0040 \pm 0.0040 \pm 0.0004$	$0.0263 \pm 0.0117 \pm 0.0019$
0.601	4.833	$0.0007 \pm 0.0019 \pm 0.0003$	$-0.0062 \pm 0.0086 \pm 0.0007$

Figure 6-2: ^{3}He results - $g_1^{^3\mathrm{He}}$.

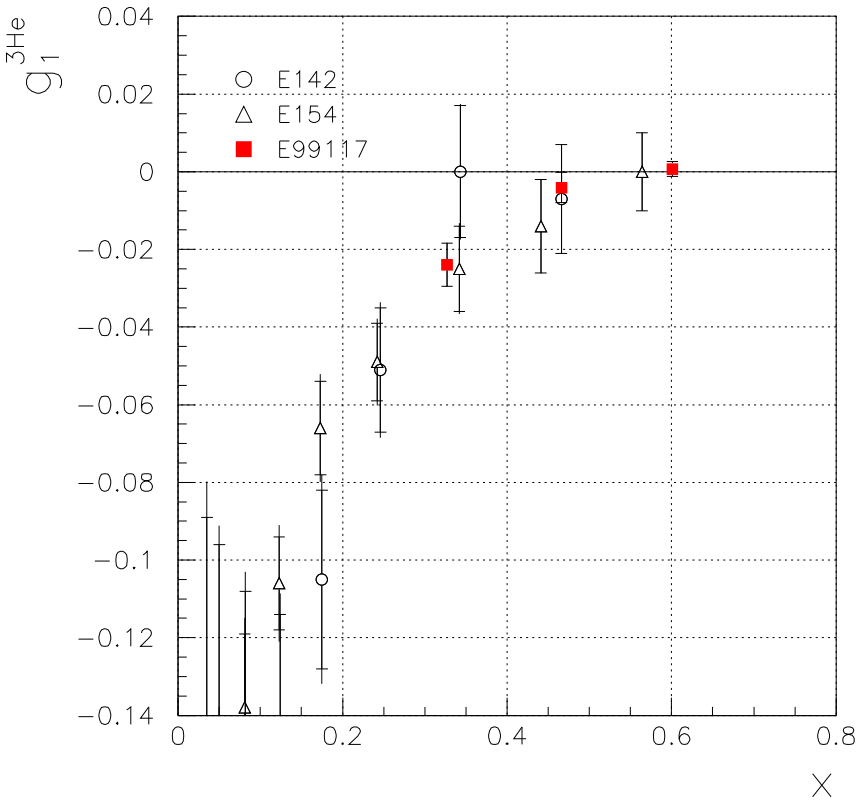

Similar to the results for $A_1^{^3\mathrm{He}}$, the new data are in good agreement with existing world data, but have improved the precision by about one order of magnitude.

6.2 Neutron Results

In this section we present results for the neutron asymmetries A_1^n and A_2^n, the structure function ratios g_1^n/F_1^n and g_2^n/F_1^n, and the polarized structure functions g_1^n and g_2^n. The data will be compared with the latest world fit performed by the E155 collaboration at SLAC [20], usually referred to as the "E155 fit". Details of this fit are given in Appendix E.

6.2.1 Neutron Asymmetries A_1^n and A_2^n

To obtain the neutron asymmetries, we applied nuclear corrections to the ^{3}He asymmetry results $A_1^{^3\mathrm{He}}$ and $A_2^{^3\mathrm{He}}$ using the procedure described in Section 5.7. Results for the neutron asymmetries A_1^n and A_2^n are shown in Table 6.5.

Table 6.5: Neutron results – A_1^n and A_2^n.

x	Q^2	$A_1^n \pm$stat.$\pm$sys.	$A_2^n \pm$stat.$\pm$sys.
0.327	2.709	$-0.048 \pm 0.024^{+0.015}_{-0.016}$	$-0.004 \pm 0.063^{+0.005}_{-0.005}$
0.466	3.516	$-0.006 \pm 0.027^{+0.019}_{-0.019}$	$0.117 \pm 0.055^{+0.012}_{-0.012}$
0.601	4.833	$0.175 \pm 0.048^{+0.026}_{-0.028}$	$-0.034 \pm 0.124^{+0.014}_{-0.014}$

The A_1^n results are plotted in Figure 6-3, along with data from the SMC [28] experiment at CERN, the HERMES [29] experiment at DESY, and the E142 [26] and E154 [27] experiments at SLAC. Also shown in Figure 6-3 is the A_1^n curve obtained from the E155 fit using the procedure described in Appendix E. The curve is calculated at a constant $Q^2 = 4$ (GeV/c)^2, which is about the average Q^2 value of the three kinematics of this experiment.

The new data in the low x region are in good agreement with existing world data. This can also be seen from the fact that the two data points at $x = 0.33$ and $x = 0.47$ lie on the E155 curve. The new datum at the highest x point has improved the precision of the world data at $x = 0.60$ by one order of magnitude. Moreover, this datum is slightly above the E155 curve which means that the current world fit for g_1^n/F_1^n can be improved. We will present a new fit for g_1^n/F_1^n in Appendix F. This new fit has been used for the data analysis in this experiment. We will compare these results with theoretical predictions in Section 6.5.

Figure 6-3: Neutron A_1^n results. Curve: E155 fit at $Q^2 = 4$ (GeV/c)^2.

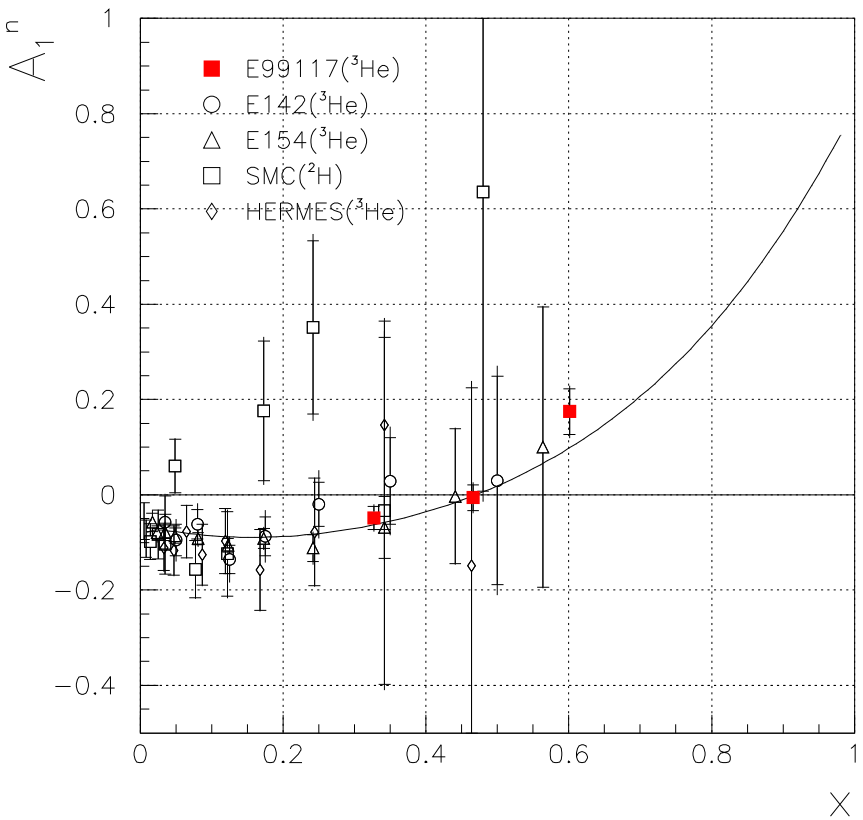

The A_2^n results are plotted in Figure 6-4 along with data from the E142 [26], E143 [23], E154 [27] and E155x [168] experiments at SLAC along with the twist-two $A_2^{n,WW}$ curve obtained from the E155 fit at constant $Q^2 = 4$ (GeV/c)^2 following the procedure described in Section E. Although the transverse asymmetry A_2^n was not the main goal of this experiment, the uncertainties in the A_2^n results are comparable to those in the best world data from E155x [168] experiment at SLAC. The curve in Figure 6-4 shows the twist-two term $A_2^{n,WW}$ from the E155 fit using the procedure described in Appendix E. The data at $x = 0.33$ and $x = 0.60$ agree with the E155 $A_2^{n,WW}$ curve, while the datum at $x = 0.47$ is about two standard deviations (2σ) above the curve. The existing E155x [168] data in the region of $x > 0.4$ are also above the E155 $A_2^{n,WW}$ curve. A deviation from $A_2^{n,WW}$ might indicate that there exist higher twist effects. However, the data have relatively large uncertainties and are not conclusive.

Figure 6-4: A_2^n results; Curve: $A_2^{n,WW}$ using E155 fit at $Q^2 = 4$ (GeV/c)^2.

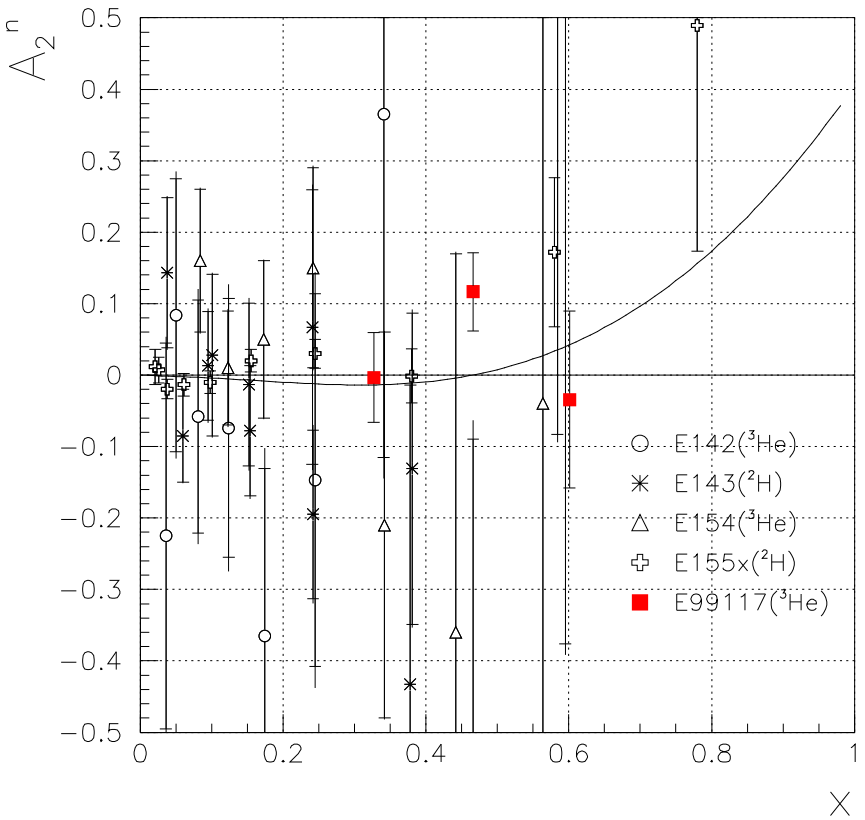

6.2.2 Neutron Structure Function Ratios g_1^n/F_1^n and g_2^n/F_1^n

Using Eq. (5.51) and (5.52), neutron structure function ratios g_1^n/F_1^n and g_2^n/F_1^n are extracted from the ^{3}He data. The results are shown in Table 6.6.

The results for g_1^n/F_1^n are plotted in Figure 6-5 along with existing data from the E143 [23] and E155 [20] experiments at SLAC and the E155 fit at $Q^2 = 4$ (GeV/c)^2. Similar to the A_1^n results, the new data from this experiment have improved the precision of the world data at $x > 0.4$ by about one order of magnitude. The new data at all three x points are consistent with the E155 fit but systematically higher. This can be partly explained by the difference in nuclear corrections used for the data analysis, as described in Section 5.7.5.

Table 6.6: Neutron results – g_1^n/F_1^n and g_2^n/F_1^n.

x	Q^2	$g_1^n/F_1^n \pm$stat.$\pm$sys.	$g_2^n/F_1^n \pm$stat.$\pm$sys.
0.327	2.709	$-0.043 \pm 0.022^{+0.009}_{-0.009}$	$0.034 \pm 0.153^{+0.010}_{-0.010}$
0.466	3.516	$0.040 \pm 0.035^{+0.011}_{-0.011}$	$0.207 \pm 0.103^{+0.022}_{-0.021}$
0.601	4.833	$0.124 \pm 0.045^{+0.016}_{-0.017}$	$-0.190 \pm 0.204^{+0.027}_{-0.026}$

Figure 6-5: Neutron $(g_1/F_1)^n$ results. Curve: E155 fit at $Q^2 = 4$ (GeV/c)^2.

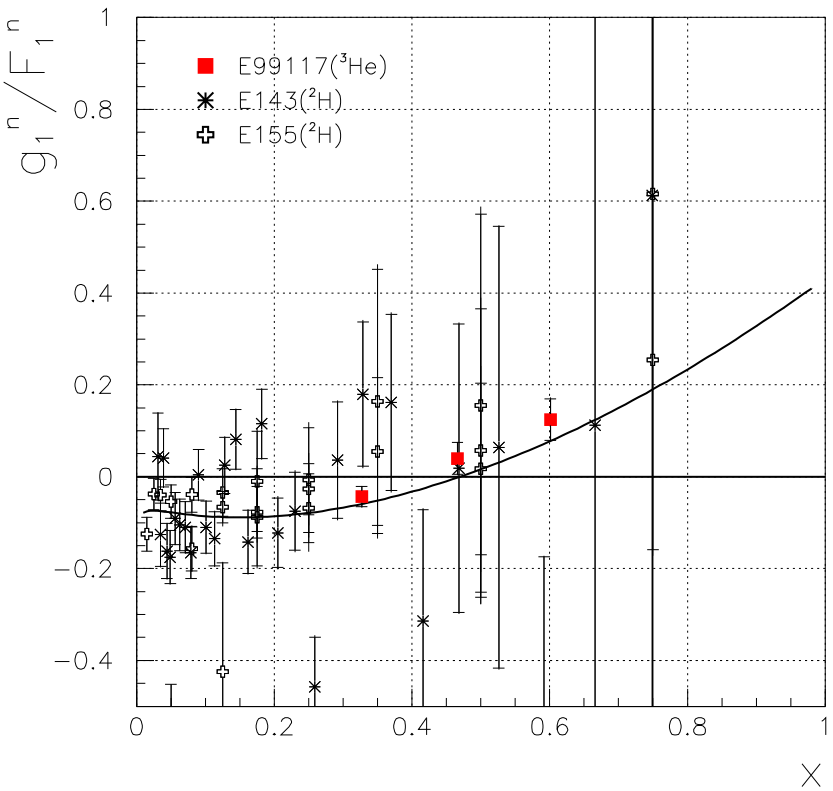

6.2.3 Neutron Polarized Structure Functions g_1^n and g_2^n

The neutron polarized structure functions g_1^n and g_2^n are obtained by multiplying the g_1^n/F_1^n and g_2^n/F_1^n results by the unpolarized structure function F_1^n, where F_1^n is

Table 6.7: Neutron results – g_1^n and g_2^n.

x	Q^2	$g_1^n \pm$stat.$\pm$sys.	$g_2^n \pm$stat.$\pm$sys.
0.327	2.709	$-0.012 \pm 0.006^{+0.003}_{-0.003}$	$0.009 \pm 0.043^{+0.003}_{-0.003}$
0.466	3.516	$0.005 \pm 0.004^{+0.001}_{-0.001}$	$0.026 \pm 0.013^{+0.003}_{-0.003}$
0.601	4.833	$0.006 \pm 0.002^{+0.001}_{-0.001}$	$-0.009 \pm 0.009^{+0.001}_{-0.001}$

calculated using Eq. (1.18), Eq. (A.3) and the world fits [142][143][144]. Results for g_1^n and g_2^n are listed in Table 6.7. The g_1^n results are shown in Figure 6-6. Similar to the A_1^n results, the new g_1^n data from this experiment have improved the precision of the world data at $x > 0.4$ by about one order of magnitude. The new data at $x = 0.33$ and $x = 0.60$ agree well with the E155 fit, but the new datum at $x = 0.47$ is higher than the value from the E155 fit by one standard deviation (1σ).

The results for xg_2^n are shown in Figure 6-7. Similar to the A_2^n results, the precision of the new xg_2^n data is slightly better than the best world data from the E155x [168] experiment at SLAC. The two data points at $x = 0.33$ and $x = 0.60$ agree with the $xg_2^{n,WW}$ curve from the E155 fit. The new datum at $x = 0.47$ is higher than the $xg_2^{n,WW}$ curve. This might indicate the existence of higher twist effects, but the indication is not conclusive because of the size of the error bar.

Figure 6-6: g_1^n results. Curve: g_1^n from E155 fit at $Q^2 = 4$ (GeV/c)^2.

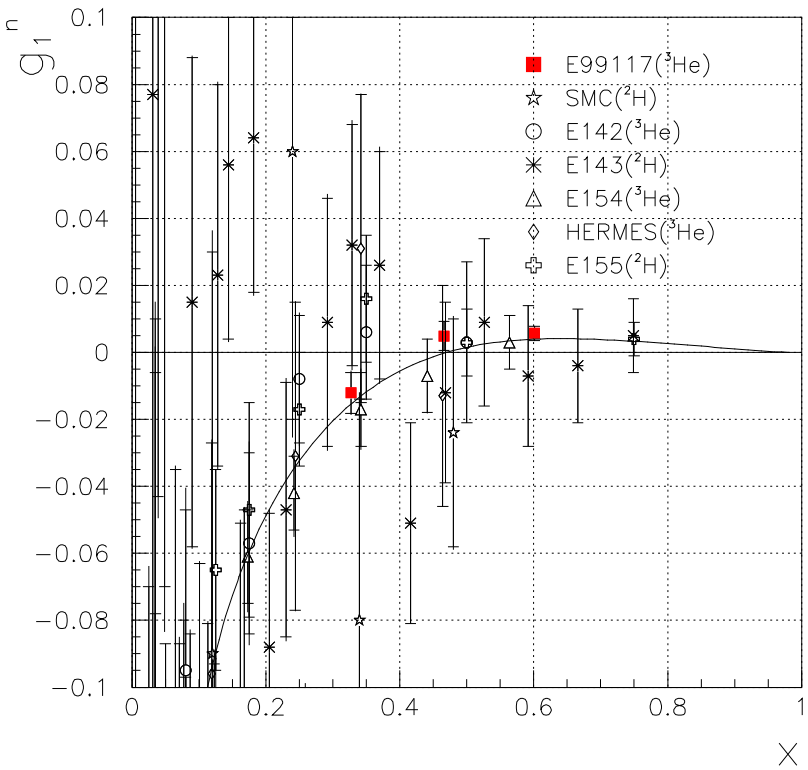

Figure 6-7: Results for xg_2^n. Curve: $xg_2^{n,WW}$ from E155 fit at $Q^2 = 4$ (GeV/c)^2.

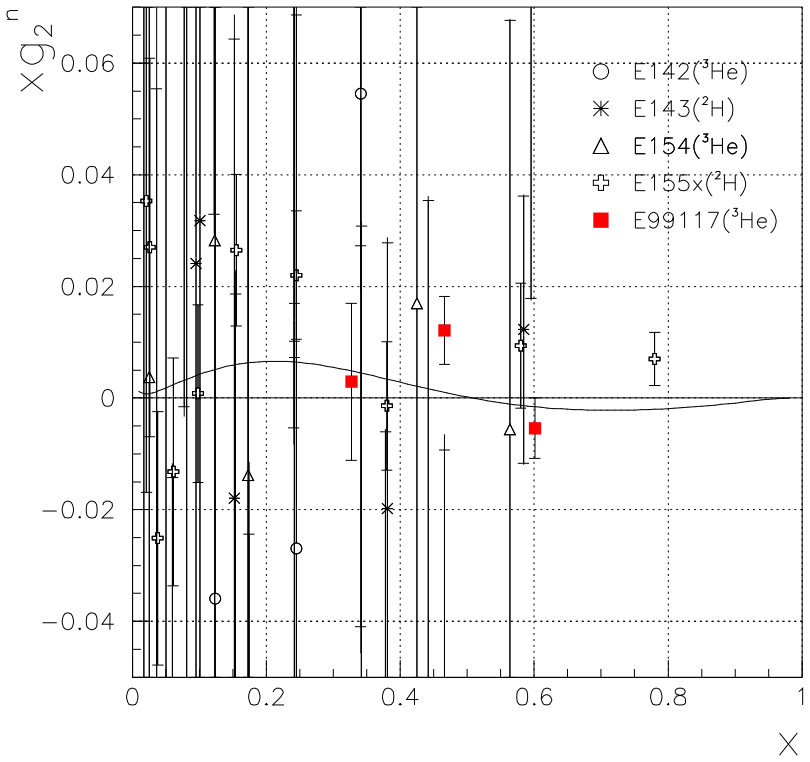

6.3 Flavor Decomposition of Polarized Quark Distribution Functions

As described in Chapter 1, the major goal of polarized deep inelastic scattering experiments is to understand the spin structure of the nucleon. How exactly do constituent partons (quarks or gluons) form the nucleon and contribute to the nucleon spin? To answer this question, one needs to determine the unpolarized and the polarized parton distribution functions (pdf), $q(x)$ and $\Delta q(x)$, respectively. They were introduced in Section 1.8. Here we assume isospin symmetry and denote $q(x)$ and $\Delta q(x)$ as the pdf's of the proton.

As shown in Figure 2-1, in the region $x > 0.4$ strange quarks and gluons are rare. So only a few pdf's remain sizable in this region: $u(x)$, $d(x)$, $\bar{u}(x)$, $\bar{d}(x)$ and their polarized counterparts $\Delta u(x)$, $\Delta d(x)$, $\Delta\bar{u}(x)$ and $\Delta\bar{d}(x)$. The common way to determine these pdf's is to assume isospin symmetry and combine the proton and the neutron polarized DIS data. However, so far little is known about the polarized pdf's in the large x region due to the lack of precise neutron data.

In this section we show how to extract the polarized quark distributions $(\Delta u + \Delta\bar{u})/(u + \bar{u})$ and $(\Delta d + \Delta\bar{d})/(d + \bar{d})$ from the results of this experiment. Results of $(\Delta u+\Delta\bar{u})/(u+\bar{u})$ and $(\Delta d+\Delta\bar{d})/(d+\bar{d})$ will be compared with the preliminary data from the HERMES experiment [172], the prediction from the constituent quark model (CQM) and the prediction from pQCD based hadron helicity conservation (HHC).

Assuming that the strange quark distributions $s(x)$ and $\bar{s}(x)$ are negligible in the region $x > 0.3$, one can use Eq. (1.31) and (1.32) to write g_1^p/F_1^p and g_1^n/F_1^n in terms of polarized quark distribution functions as

$$\frac{g_1^p}{F_1^p} = \frac{4\Delta u + \Delta d + 4\Delta\bar{u} + \Delta\bar{d}}{4u + d + 4\bar{u} + \bar{d}} , \quad \text{and} \tag{6.1}$$

$$\frac{g_1^n}{F_1^n} = \frac{\Delta u + 4\Delta d + \Delta\bar{u} + 4\Delta\bar{d}}{u + 4d + \bar{u} + 4\bar{d}} . \tag{6.2}$$

Combining Eq. (6.1) and (6.2), one can extract

$$\frac{\Delta u + \Delta\bar{u}}{u + \bar{u}} = \frac{4}{15}\frac{g_1^p}{F_1^p}(4 + \frac{d + \bar{d}}{u + \bar{u}}) - \frac{1}{15}\frac{g_1^n}{F_1^n}(1 + 4\frac{d + \bar{d}}{u + \bar{u}}) \quad \text{and} \tag{6.3}$$

$$\frac{\Delta d + \Delta\bar{d}}{d + \bar{d}} = \frac{4}{15}\frac{g_1^n}{F_1^n}(4 + 1/\frac{d + \bar{d}}{u + \bar{u}}) - \frac{1}{15}\frac{g_1^p}{F_1^p}(1 + 4/\frac{d + \bar{d}}{u + \bar{u}}) . \tag{6.4}$$

For g_1^p/F_1^p we use a fit to the world proton data, see Appendix F. For the ratio $(d + \bar{d})/(u + \bar{u})$ we used the values extracted from proton and deuteron structure function data with nuclear EMC effects included [173]. Moreover, one can see from Figure 2-1 that in the region $x > 0.3$, sea quarks $\bar{u}$ and $\bar{d}$ are rare. Therefore one has $(d + \bar{d})/(u + \bar{u}) \approx d/u$ for $x > 0.3$. In the following we will not distinguish between

these two ratios.

An estimation for the uncertainty in the d/u ratio is obtained by comparing the d/u results from the off-shell and the on-shell deuteron calculations presented in [173]. We use the off-shell calculation results as the central value $(d/u)_{\rm central}$ and the on-shell calculation results as the minimal value $(d/u)_{\rm min}$. Then we make a conservative estimate for the maximal value as $(d/u)_{\rm max} = (d/u)_{\rm central} + [(d/u)_{\rm central} - (d/u)_{\rm min}]/4$, as shown in Figure 6-8.

Figure 6-8: d/u ratio extracted from proton and deuteron data from SLAC, using the off-shell deuteron calculation (solid circles) and using the on-shell calculation (open circles) [173]. Also shown is the ratio extracted from neutrino measurements by the CDHS collaboration [175]. The three curves show the d/u central values (black curve), the minimal (lower red curve), and the maximal values (higher red curve) used in the analysis presented in this section.

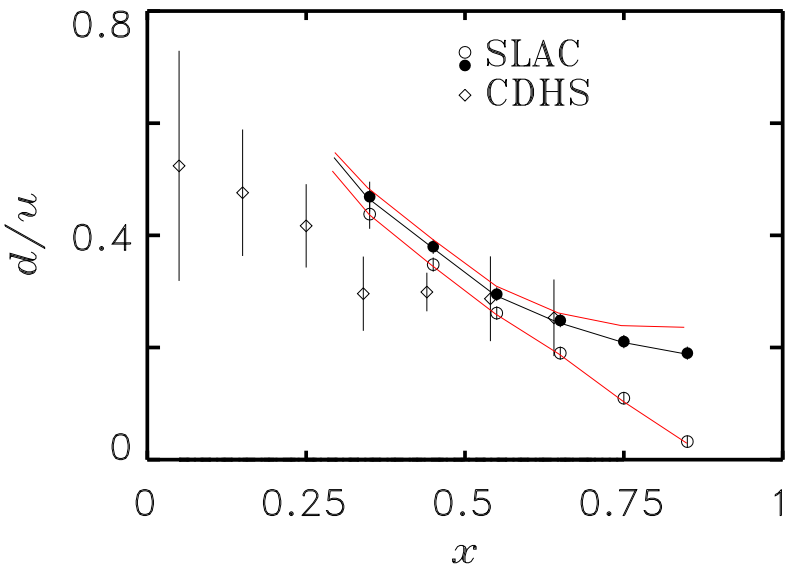

Figure 6-9 shows results for $(\Delta u + \Delta\bar{u})/(u + \bar{u})$ and $(\Delta d + \Delta\bar{d})/(d + \bar{d})$ from g_1^n/F_1^n data in comparison with the preliminary data from the HERMES experiment [172], CQM predictions [36] and pQCD based hadron helicity conservation (HHC) predictions using the LSS(BBS) parameterization [39]. Table 6.8 gives the numerical results, the statistical error (stat.), systematic error (sys.) and the model uncertainty (mod.) due to the uncertainties in the fits for g_1^p/F_1^p and d/u.

In Eq. (6.1) and (6.2), the strangeness contributions s, $\bar{s}$, Δs and $\Delta\bar{s}$ were neglected. Now we estimate the error in $(\Delta u + \Delta\bar{u})/(u + \bar{u})$ and $(\Delta d + \Delta\bar{d})/(d + \bar{d})$

Table 6.8: Polarized quark distribution results for $(\Delta u + \Delta\bar{u})/(u + \bar{u})$ and $(\Delta d + \Delta\bar{d})/(d + \bar{d})$. The three error bars are the statistical error (stat.), systematic error (sys.) and the model uncertainty (mod.) due to the uncertainties in the fits for g_1^p/F_1^p data and the d/u ratio.

x	$(\Delta u + \Delta\bar{u})/(u + \bar{u})\pm$stat.$\pm$sys.$\pm$mod.	$(\Delta d + \Delta\bar{d})/(d + \bar{d})\pm$stat.$\pm$sys.$\pm$mod.
0.327	$0.535 \pm 0.005^{+0.002\ +0.008}_{-0.002\ -0.005}$	$-0.271 \pm 0.031^{+0.013\ +0.004}_{-0.013\ -0.016}$
0.466	$0.642 \pm 0.007^{+0.002\ +0.013}_{-0.002\ -0.013}$	$-0.303 \pm 0.054^{+0.018\ +0.008}_{-0.017\ -0.014}$
0.601	$0.733 \pm 0.007^{+0.003\ +0.026}_{-0.003\ -0.026}$	$-0.363 \pm 0.081^{+0.029\ +0.021}_{-0.030\ -0.036}$

due to neglecting the strangeness contributions.

The full expressions for g_1^p/F_1^p and g_1^n/F_1^n in the quark parton model are

$$\frac{g_1^p}{F_1^p} = \frac{4\Delta u + \Delta d + 4\Delta\bar{u} + \Delta\bar{d} + \Delta s + \Delta\bar{s}}{4u + d + 4\bar{u} + \bar{d} + s + \bar{s}} \quad \text{and} \tag{6.5}$$

$$\frac{g_1^n}{F_1^n} = \frac{\Delta u + 4\Delta d + \Delta\bar{u} + 4\Delta\bar{d} + \Delta s + \Delta\bar{s}}{u + 4d + \bar{u} + 4\bar{d} + s + \bar{s}} \,. \tag{6.6}$$

Comparing Eq. (6.5) and (6.6) with Eq. (6.1) and (6.2), one obtains

$$\begin{aligned} \frac{\Delta u + \Delta\bar{u}}{u + \bar{u}} &= \Big(\frac{\Delta u + \Delta\bar{u}}{u + \bar{u}}\Big)_{s,\bar{s}=0} \\ &\quad + \frac{s + \bar{s}}{u}\Big[\frac{4}{15}\frac{g_1^p}{F_1^p} - \frac{1}{15}\frac{g_1^n}{F_1^n} - \frac{1}{5}\frac{\Delta s + \Delta\bar{s}}{s + \bar{s}}\Big] \quad \text{and} \end{aligned} \tag{6.7}$$

$$\begin{aligned} \frac{\Delta d + \Delta\bar{d}}{d + \bar{d}} &= \Big(\frac{\Delta d + \Delta\bar{d}}{d + \bar{d}}\Big)_{s,\bar{s}=0} \\ &\quad + \frac{s + \bar{s}}{d}\Big[\frac{4}{15}\frac{g_1^n}{F_1^n} - \frac{1}{15}\frac{g_1^p}{F_1^p} - \frac{1}{5}\frac{\Delta s + \Delta\bar{s}}{s + \bar{s}}\Big] \,, \end{aligned} \tag{6.8}$$

where $(\frac{\Delta u+\Delta\bar{u}}{u+\bar{u}})_{s,\bar{s}=0}$ and $(\frac{\Delta d+\Delta\bar{d}}{d+\bar{d}})_{s,\bar{s}=0}$ are the approximate values assuming that the strangeness contributions are zero. Assuming $s = \bar{s}$ and using the positivity constraints that $|\Delta s/s| \leqslant 1$ and $|\Delta\bar{s}/\bar{s}| \leqslant 1$, errors due to neglecting the strangeness contributions can be estimated using the unpolarized parton distribution functions from a

Figure 6-9: Results for $(\Delta u + \Delta\bar{u})/(u + \bar{u})$ and $(\Delta d + \Delta\bar{d})/(d + \bar{d})$, The error bars on the HERMES preliminary data are statistical uncertainties [172]. The error band in the middle shows the uncertainty due to neglecting s and $\bar{s}$ contributions.

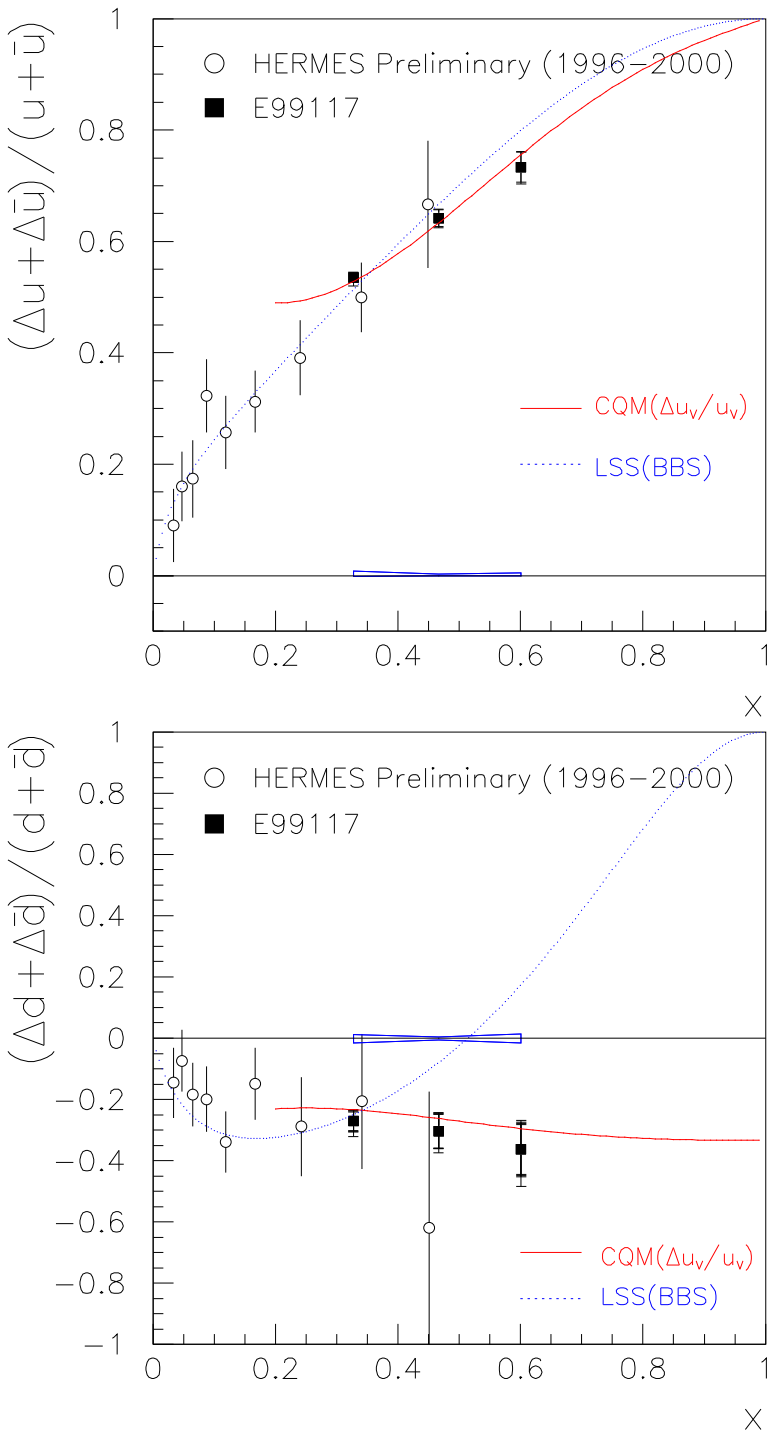

global fit – CTEQ6M [21] – performed by the Coordinated Theoretical-Experimental Project on QCD (CTEQ) collaboration. The results are shown as the blue error bands in Figure 6-9.

To compare with CQM predictions, which are only given for valence quark distributions $\Delta q_V/q_V$, we have estimated the difference between $(\Delta q + \Delta\bar{q})/(q + \bar{q})$ and $\Delta q_V/q_V$. For each quark flavor, one can decompose $(q + \bar{q})$ as $q + \bar{q} = q_V + q_{sea} + \bar{q}$, where q_V is the valence quark distribution and $q_{sea} = \bar{q}$ is the sea quark distribution. Then one can write

$$\frac{\Delta u_V}{u_V} = \frac{\Delta u + \Delta\bar{u}}{u + \bar{u}} + \frac{u_{sea} + \bar{u}}{u_V}\Big(\frac{\Delta\bar{u}}{\bar{u}} - \frac{\Delta u_V}{u_V}\Big) \quad \text{and} \tag{6.9}$$

$$\frac{\Delta d_V}{d_V} = \frac{\Delta d + \Delta\bar{d}}{d + \bar{d}} + \frac{d_{sea} + \bar{d}}{d_V}\Big(\frac{\Delta\bar{d}}{\bar{d}} - \frac{\Delta d_V}{d_V}\Big)\ . \tag{6.10}$$

Again using the unpolarized parton distribution functions from the global fit CTEQ6M [21], one obtains

$$\Delta u_V/u_V = \Big(\frac{\Delta u + \Delta\bar{u}}{u + \bar{u}}\Big)^{+0.03}_{-0.015} \quad \text{and} \tag{6.11}$$

$$\Delta d_V/d_V = \Big(\frac{\Delta d + \Delta\bar{d}}{d + \bar{d}}\Big)^{+0.069}_{-0.035}\ . \tag{6.12}$$

In the equations above, we have used the current knowledge that inside a polarized proton, the u quark polarization is aligned to the proton spin and the d quark polarization is anti-aligned to the proton spin: $0 < \Delta u/u < 1$ and $-1 < \Delta d/d < 0$ [4]. We also assume that the polarization of the sea quarks is unknown and only use the positivity constraints that $|\Delta\bar{u}/\bar{u}| \leqslant 1$ and $|\Delta\bar{d}/\bar{d}| \leqslant 1$.

From Figure 6-9, the results for $(\Delta u + \Delta\bar{u})/(u + \bar{u})$ are in good agreement with the HERMES preliminary data and have better precision. The $(\Delta u + \Delta\bar{u})/(u + \bar{u})$ results agree with the predictions from the pQCD based LSS(BBS) parameterization. The results also agree well with the prediction from the CQM in the region of $x > 0.3$. For $x < 0.3$, however, the $q - \bar{q}$ sea and the gluons contribute and the CQM is not expected to work well.

The physics implied by the $(\Delta d + \Delta\bar{d})/(d + \bar{d})$ results is more interesting, since the CQM predictions differ from the pQCD based predictions and they even have the opposite sign in the region $x > 0.5$. The total uncertainties in the new results of $(\Delta d + \Delta\bar{d})/(d + \bar{d})$ from this experiment are smaller than those in the HERMES data by about a factor of 5, which allows one to distinguish between the two predictions in the region $x > 0.3$. Clearly the new results agree well with the CQM predictions, but do not agree with the pQCD based predictions. We will discuss these two predictions further in Section 6.5.

6.4 Pion Asymmetries

In addition to polarization asymmetries in electron scattering, polarization asymmetries are also observed in photo-production of pions in our polarized DIS experiments. Here we define the parallel and the perpendicular pion asymmetries to be

$$A_{\parallel}^{\pi^-} \equiv \frac{\sigma_{\downarrow\Uparrow}^{\pi^-} - \sigma_{\uparrow\Uparrow}^{\pi^-}}{\sigma_{\downarrow\Uparrow}^{\pi^-} + \sigma_{\uparrow\Uparrow}^{\pi^-}} \quad \text{and} \tag{6.13}$$

$$A_{\perp}^{\pi^-} \equiv \frac{\sigma_{\downarrow\Rightarrow}^{\pi^-} - \sigma_{\uparrow\Rightarrow}^{\pi^-}}{\sigma_{\downarrow\Rightarrow}^{\pi^-} + \sigma_{\uparrow\Rightarrow}^{\pi^-}} , \tag{6.14}$$

where $\sigma_{\downarrow\Uparrow}^{\pi^-}(\sigma_{\uparrow\Uparrow}^{\pi^-})$ is the cross section for π^- photo-production on a longitudinally polarized target, with incident electron spin anti-parallel (parallel) to the target spin; and $\sigma_{\downarrow\Rightarrow}^{\pi^-}(\sigma_{\uparrow\Rightarrow}^{\pi^-})$ is the cross section for π^- photo-production on a transversely polarized target, with incident electron spin anti-parallel (parallel) to the beam direction, and the scattered electrons being detected on the same side of the beam as that to which the target spin is pointing.

Figure 6-10: Pion asymmetry A^{π^-} results.

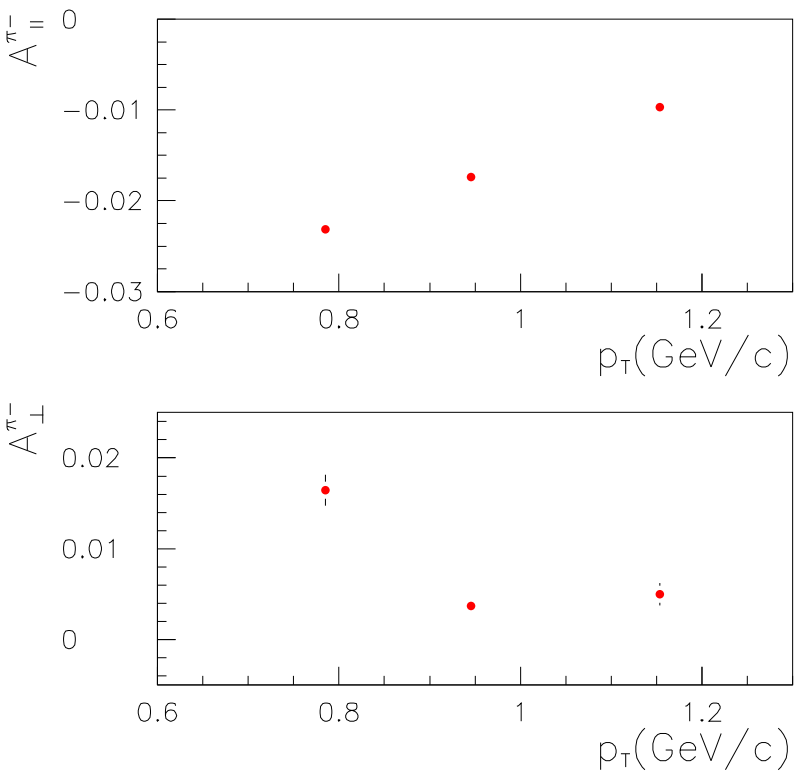

Because of the relatively high cross section for pion photo-production, data on pion asymmetries usually have better statistics than data on electron asymmetries. These pion asymmetries are often not small and, as recently pointed out, can be of some value to the understanding of polarization distribution of quarks and gluons in nucleons [170]. Results for A_{π^-} from this experiment are shown in Fig. 6-10. p_T is the transverse momentum of the produced pion in a direction perpendicular to the momentum transfer $\vec{q}$. Unfortunately, the calculation [170] was performed in the kinematic range of $8 < p_T < 40$ (GeV/c). The A_{π^-} results from this experiment are in the range $0.8 < p_T < 1.2$ (GeV/c) and thus we cannot compare our data with the calculation. Further theoretical calculations are needed to interpret the pion results within the JLAB kinematic range.

6.5 Discussion

In this section we compare the new data with the theoretical predictions for A_1^n presented in Chapter 2.

The A_1^n predictions can be divided into two categories. The first one includes calculations based on models without fitting to the world A_1 data, for example, the SU(6) prediction [22], the constituent quark models [36], the perturbative QCD based BBS parameterization [38], the local duality method [52] and the chiral soliton model [62]. The local duality method cannot be applied to the region below the pion threshold $x = x_{\rm th} \approx 0.8$ and will not be discussed here. The chiral soliton model calculation [63] is not available in the kinematic range of our data and will also not be discussed. The other three models will be discussed in Section 6.5.1. The second category of A_1^n predictions refers to those being developed particularly for constructing parton distribution functions (pdf) and are fitted to a large amount of world data. This latter group includes the LSS(BBS) parameterization [39], the LSS parameterization [44] and the statistical model prediction [46]. They will be discussed in Section 6.5.2. In Section 6.5.3 we will give an outlook on possible measurements of A_1^n in the future and conclude the dissertation.

6.5.1 A_1^n and Models

In Figure 6-11 we compare the A_1^n results with existing world data and the three models described in Chapter 2: the SU(6) model [22], the constituent quark model (CQM) [36] and the perturbative QCD (pQCD) based BBS parameterization [38]. We itemize the discussion as follows:

- The new datum at $x = 0.33$ agrees with world data. The three new data points show a zero crossing point at $x \approx 0.47$ and the datum at $x = 0.60$ is significantly positive. The new data clearly show the trend that A_1^n turns positive and continue to increase at large x.

Figure 6-11: A_1^n results compared with model predictions. Curves: predictions of A_1^n from pQCD based BBS parameterization [38], constituent quark model (yellow, or light shaded band) [36] and the SU(6) symmetry [22].
Data from Hermes [29] and SLAC [26][27][20] are published results without being re-analyzed for the improved nuclear corrections. However the effect due to nuclear corrections is small, as described in Section 5.7.5, and will not affect the final conclusion.

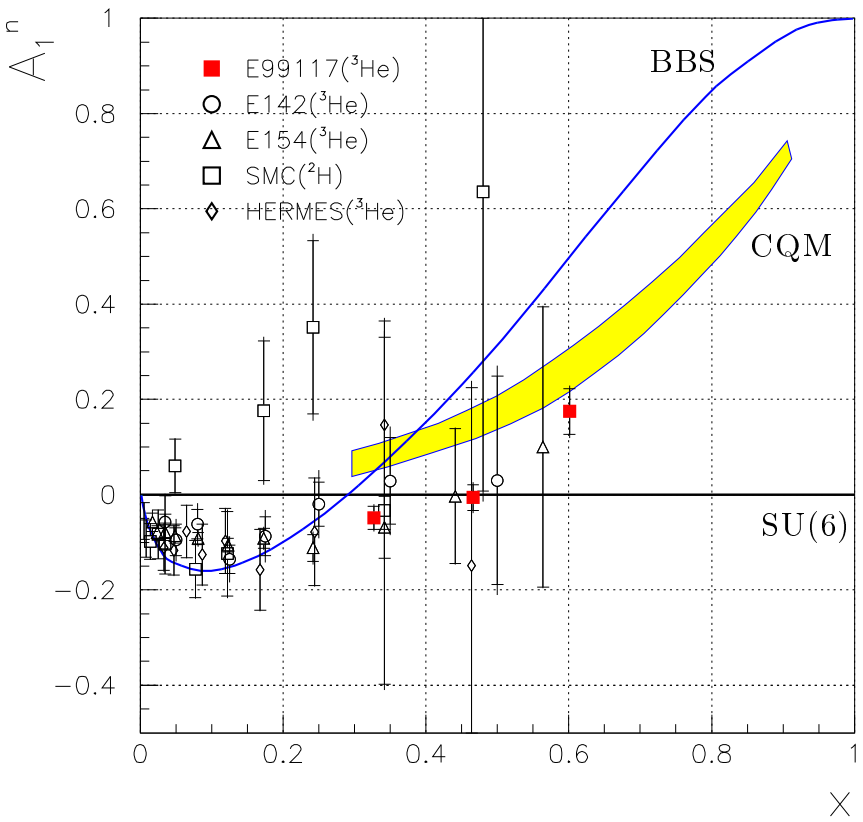

- The new data do not agree with the SU(6) prediction that A_1^n is a constant zero. This is within our expectation since SU(6) symmetry is known to be broken [32].
- Compared with the predictions from the BBS parameterization, which is based on the pQCD predicted hadron helicity conservation (HHC):
  - In the region of $0.4 < x < 1$, as shown in Figure 6-11, the prediction is in general higher than data. This disagreement may mean that there is problem with the theoretical basis of the pQCD calculation.
  - The pQCD calculation is based on the hadron helicity conservation (HHC). Its disagreement with the data might indicate that HHC cannot be applied to the quarks probed in our DIS region. Since HHC is derived from the assumption that the orbital angular momentum of the quarks is zero, the discrepancy between data and the prediction might further imply that the quarks' orbital angular momentum contributes significantly to the nucleon's spin at the limit of $x \to 1$ in the deep inelastic domain.
- Compared with the CQM predictions:
  - The CQM predictions are higher than the new data at all three x points. In the best case, the new datum at $x = 0.60$ is smaller than the CQM prediction by about one standard deviation (1σ);
  - However, only the CQM gives roughly the approximate trend of A_1^n data in the large x region, i.e., A_1^n is positive and continues to increase in the large x region.

  One may interpret the disagreement between the CQM prediction and the data as follows:
  - The main problem of CQM, besides the fact that the constituent quark concept does not have a clear origin in quantum chromodynamics (QCD), is that in the CQM there is no $q - \bar{q}$ sea and no gluon. As a result, it is unlikely that the CQM gives the correct prediction for A_1^n over all x;
  - The disagreement between the CQM predictions and the data might be explained by the polarization of the $q - \bar{q}$ sea quarks and the gluons. Also, this disagreement becomes larger in the low x region. This can be understood as the fact that there are more $q - \bar{q}$ sea quarks and gluons at low x, as can be seen from Figure 2-1.

6.5.2 A_1^n and Parton Distribution Parameterizations

In Figure 6-12 we compare the A_1^n results with predictions from the pQCD hadron helicity conservation (HHC) based LSS(BBS) parameterization [39] and the statistical model prediction [46]. The g_1^n/F_1^n predictions from the LSS parameterization [44], which is not constrained by the pQCD based HHC, are compared with the g_1^n/F_1^n results in Figure 6-13. We itemize the discussion as follows:

Figure 6-12: A_1^n results compared with A_1^n predictions from the pQCD based LSS(BBS) parameterization and from the statistical model at $Q^2 = 4$ (GeV/c)^2.

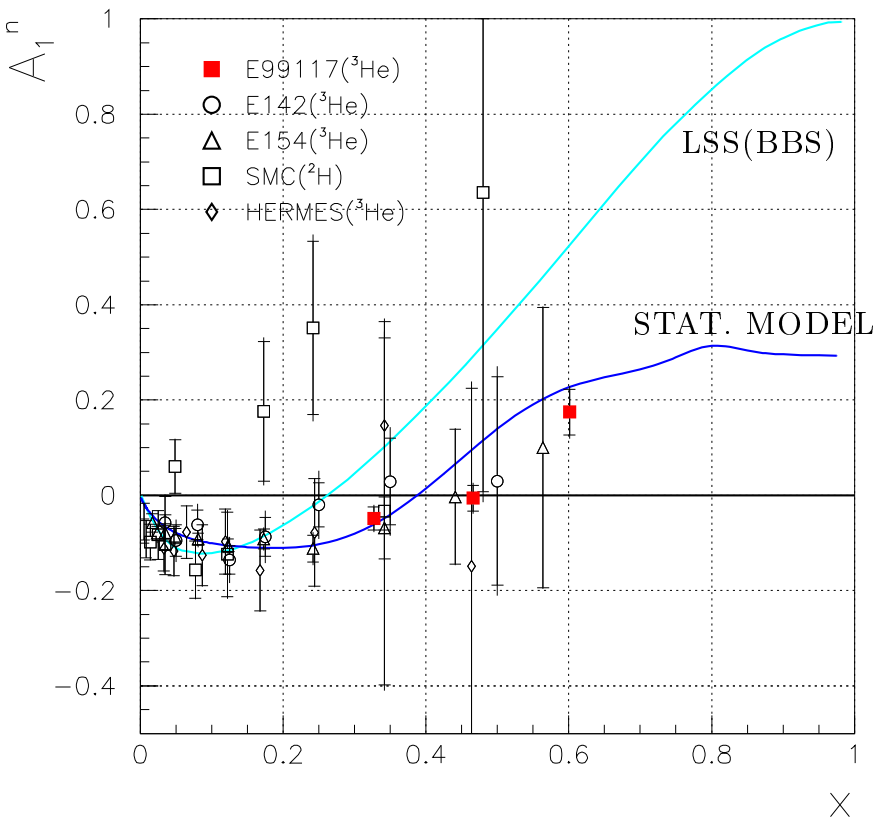

- In Figure 6-12, the new A_1^n results at all three x points and existing world data in the region $x > 0.2$ do not agree with the pQCD based calculation using LSS(BBS) parameterization;
  The results for the flavor decomposition of the polarized quark distribution $(\Delta d + \Delta\bar{d})/(d + \bar{d})$ presented in Section 6.3 also do not agree with the pQCD based predictions using LSS(BBS) parameterization and favor the CQM predictions. These two observations, following the previous data for $F_2^{p,el}(Q^2)/F_1^{p,el}(Q^2) \sim 1/Q$ [41][42], may again indicate that pQCD based hadron helicity conservation

Figure 6-13: g_1^n/F_1^n results compared with g_1^n/F_1^n predictions from the LSS parameterization at $Q^2 = 5$ (GeV/c)^2.

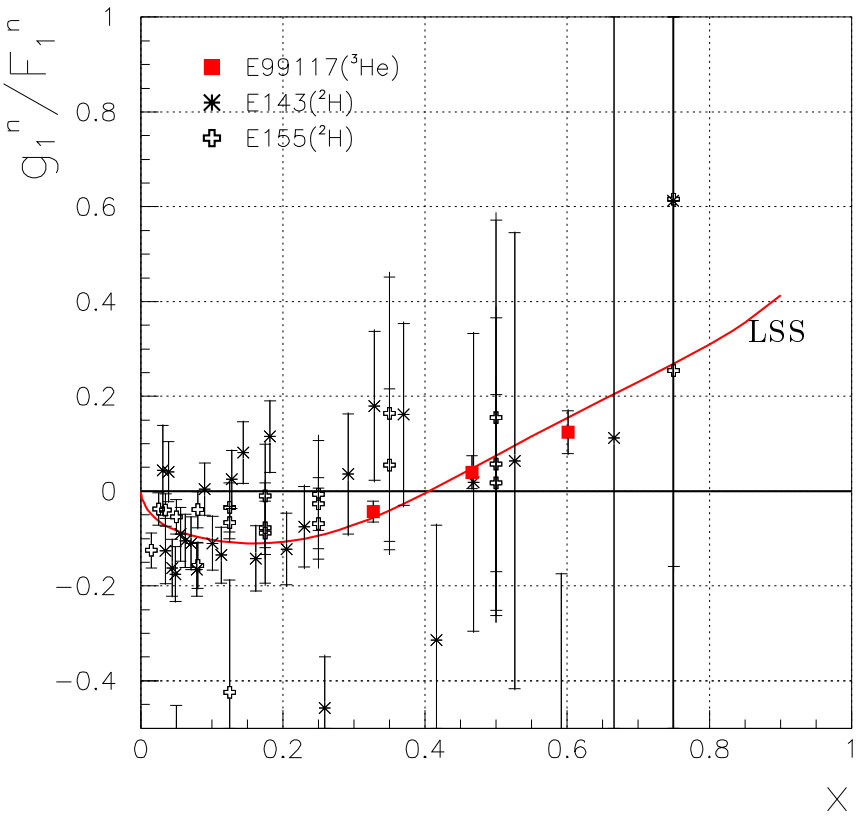

cannot be applied to the quarks probed in DIS. As was described in Section 2.5, the orbital angular momentum of the quarks may play an important role.

- In Figure 6-12, the new A_1^n datum at $x = 0.33$ agrees with the prediction of the statistical model. But the data at $x = 0.47$ and $x = 0.60$ are smaller than this prediction. Although this model can be refined if the new data are included in the fit, as has been explained in Section 2.6, the statistical model itself should not work well in the region $x > 0.6$.

- In Figure 6-13, the new g_1^n/F_1^n data at $x = 0.33$ and $x = 0.47$ agree well with the calculation based on the LSS parameterization. However the LSS parameterization is a pure fit to world data and does not have any physical interpretation in terms of an explicit model. This parameterization can be improved at the highest data point at $x = 0.60$.

6.5.3 Future of A_1^n Measurements

In this experiment we have measured A_1^n up to $x = 0.60$. We have observed a trend that A_1^n turns positive around $x = 0.47$ and continues to increase. However it is not clear whether the data will follow the prediction from CQM that A_1^n continues rising and approaches 1 for $x > 0.60$, or will stay around 0.2, which would agree more with the predictions from the statistical model. If A_1^n increases dramatically in the region $x > 0.7$ and exceeds A_1^p, then the ratio $\Delta d/d$ will turn positive at higher x and will favor the pQCD prediction that $\Delta d/d \to 1$ at $x \to 1$, instead of the CQM prediction that $\Delta d/d \to -1/3$ at $x \to 1$. On the other hand, if the CQM is validated by the new data at higher x, then one can obtain information about how the current quarks and gluons in QCD form constituent quarks in the non-perturbative regime. This will be of fundamental importance in the study of the nucleon structure.

Therefore an extension of the A_1^n measurement to larger x will reveal more about the spin structure of the neutron in the valence quark region. This has been planned at JLAB. A measurement of A_1^n in the resonance region and the testing of duality for the polarized structure functions will be carried out in Hall A in 2003 [176]. As one of the major physics programs of the JLAB 12 GeV upgrade [177], the measurement of A_1^n will be extended up to $x = 0.8$ and a larger Q^2 range of $2 < Q^2 < 10$ (GeV/c)^2.

6.6 Conclusions

To conclude, we have presented precise data on the ^{3}He and the neutron spin asymmetries and polarized structure functions A_1, g_1/F_1, and g_1 at three kinematics $x = 0.33$, 0.47 and 0.60, with $Q^2 = 2.7$, 3.6 and 4.9 (GeV/c)^2, respectively. The data in the region of $x > 0.4$ have improved the precision of the world data by one order of magnitude. The new data were compared with various theoretical predictions. The data do not agree with the predictions from the SU(6) symmetry and the pQCD based parameterizations. The prediction from the constituent quark models is in general considerably larger than the data, but it gives approximately the correct trend of data at the larger values of x. The new data may provide critical inputs to the polarized parton distribution parameterizations. The data presented in this dissertation can greatly help to elucidate the valence quark structure and the constituent quark concepts. Within the framework of models, the new data may also provide valuable information as to the importance of the sea quark and the gluon polarizations inside the nucleon.

Results for the transverse asymmetry and the polarized structure function A_2, g_2/F_1 and g_2 for ^{3}He and the neutron were presented. The uncertainties in the neutron results are comparable to the most recent data from SLAC experiment E155x [168]. Although the new data are not conclusive enough because of the relatively large error bars, they might provide information on higher twist effects in the polarized structure function g_2.

Results on asymmetries in pion photo-production were presented as a byproduct of the experiment. If the theories of pion asymmetries can be extended to the JLAB kinematic range, these data may provide information on the polarized quark distribution functions and the gluon polarization.

Finally, results on the polarized quark distribution $(\Delta u + \Delta\bar{u})/(u + \bar{u})$ and $(\Delta d + \Delta\bar{d})/(d+\bar{d})$ deduced from our data were presented. The new results for $(\Delta d+\Delta\bar{d})/(d+\bar{d})$ do not agree with the predictions from pQCD based hadron helicity conservation.

Appendix A

^{3}He Unpolarized Structure Functions from World Fits

The ^{3}He unpolarized structure functions $F_1^{^3\mathrm{He}}$ and $F_2^{^3\mathrm{He}}$ can be calculated from world fits of the proton and the deuteron F_2 structure functions [142], a world fit for the ratio $R = \sigma_L/\sigma_T$ [143], and the deuteron and ^{3}He EMC effects [144].

The latest world fit of the proton and the deuteron structure functions F_2^p and F_2^D in the deep inelastic region [142] was performed by the New Muon Collaboration (NMC). It is usually referred to as the "F2NMC95 fit". In Section 1.5 we have mentioned that there are two definitions of the F_2 structure function for a nuclear target. The deuteron F_2^D published in F2NMC95 fit is given in the *per nucleon* definition. To be consistent, in the following we still use the *not per nucleon* definition for F_2^D, which is two times the F2NMC95 fit.

To correct for the nuclear EMC effect [2] we define the EMC ratios for the deuteron and the ^{3}He as

$$\mathcal{R}^D \equiv \frac{F_2^D}{F_2^n + F_2^p} \; ; \tag{A.1}$$

$$\mathcal{R}^{^3\mathrm{He}} \equiv \frac{F_2^{^3\mathrm{He}}}{F_2^n + 2F_2^p} \; . \tag{A.2}$$

For the data analysis in this experiment we used the calculations of $\mathcal{R}$ by Melnitchouk [144], and construct the F_2 structure functions for the neutron and the ^{3}He as

$$F_2^n = \frac{F_2^D}{\mathcal{R}^D} - F_2^p \; ; \tag{A.3}$$

$$F_2^{^3\mathrm{He}} = \mathcal{R}^{^3\mathrm{He}}(F_2^n + 2F_2^p) \; . \tag{A.4}$$

The ^{3}He structure function $F_1^{^3\mathrm{He}}$ is calculated using Eq. (1.18)

$$F_1(x,Q^2) \;=\; \frac{F_2(x,Q^2)(1+\gamma^2)}{2x\Big(1+R(x,Q^2)\Big)}\;,$$

where the ratio $R = \sigma_L/\sigma_T$ is from the latest world fit [143]. It was performed by the E143 collaboration at SLAC and is usually referred to as the "R1998 fit". In this fit, the ratio R is assumed to be nuclear independent, i. e., $R^n = R^p = R^{^3\mathrm{He}}$.

Appendix B

Radiation Length of Materials for Hall A Polarized ^{3}He Target

In this appendix we summarize the thickness and the radiation length for material traversed by the incident and the scattered electrons during the A_1^n experiment. The information listed here was used in the single arm Monte-Carlo (SAMC) simulation for evaluating radiation effects caused by internal and external bremsstrahlung, and energy loss due to ionizations.

Figure B-1 shows the material traversed by the incident and the scattered electrons.

- Material traversed by the incident electrons includes:
  (1) Exit window of beam pipe, 16 mils [a] Be;
  (2) 5cm air [b];
  (3) Aluminum enclosure of the target scattering chamber, 15 mils Al;
  (4) Target cell upstream window, 132 μm glass for "Gore" and 144 μm glass for "Tilghman";
  (5) ^{3}He gas inside the target chamber of the polarized cell under running conditions, 1/2 of target cell length. For the A_1^n experiment it is 12.5 cm.

- Material traversed by the scattered electrons includes:
  (6) ^{3}He gas inside the target chamber of the polarized cell under running conditions, $(r - x_{tg})/\sin\theta$, where r$\sim$1cm is the target cell radius, x_{tg} is the x position of scattering point in hall coordinates, θ is scattering angle;
  (7) Target cell wall, 1.3$\sim$1.7 mm glass;
  (8) ^{4}He inside target enclosure, 45.7 cm;
  (9) Aluminum enclosure of the target scattering chamber, 15 mils Al [c];
  (10) Air gap between target enclosure and HRS, 65.1 cm for left arm and 64.2 cm for right arm;
  (11) Spectrometer entrance window, 14 mils Kapton;
  (12) Spectrometer exit window, 4 mils Ti.

Figure B-1: Radiation length of materials for Hall A Polarized ^{3}He Target

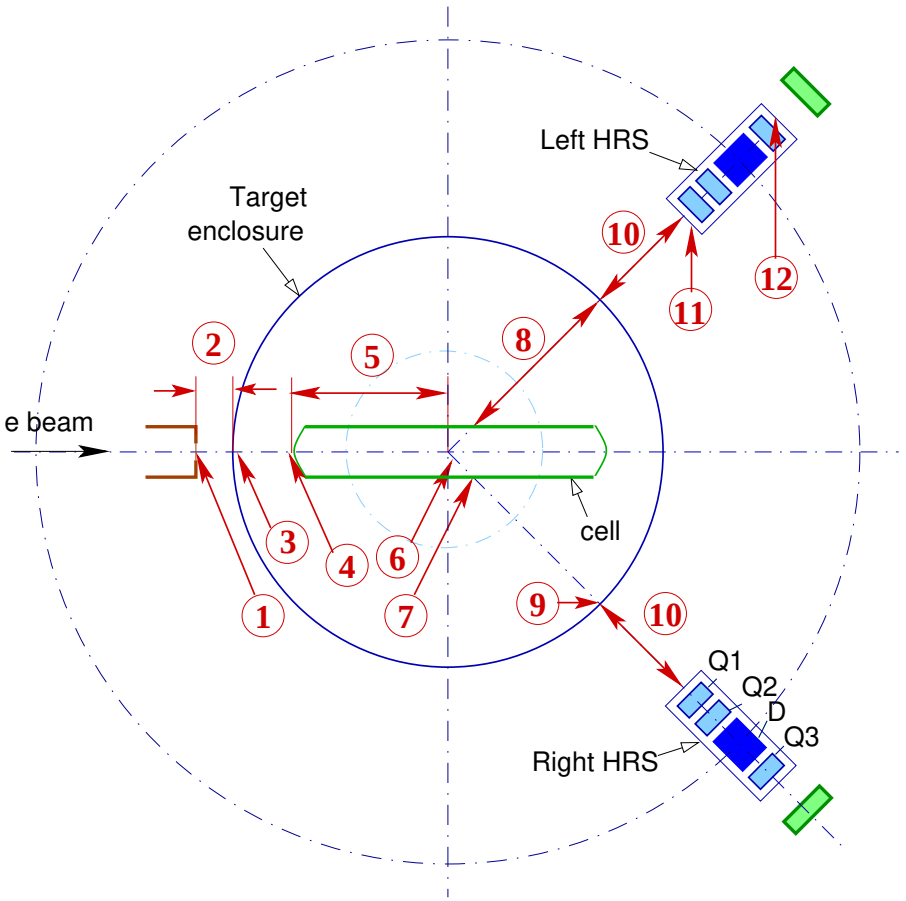

The radiation length for each material is listed in Table B.1.

a. 1 mil=2.54×10^{-3}cm
b. density for gases are evaluated at 20° C, 1 atm
c. for E94010 it was 10 mil

Table B.1: Radiation length X_0 and density for material traversed by the electrons during the A_1^n experiment.

material	X_0 (g/cm^2)	(cm)	density
air	36.66	30420	1.205 g/l [c]
^{4}He	94.32	755164	0.1249 g/l
^{3}He	67.42	-	
Be	65.19	35.28	1.848 g/cm^3
Al	24.01	8.9	2.70 g/cm^3
Kapton	40.56	28.6	1.42 g/cm^3
Ti	16.17	3.56	4.54 g/cm^3
Glass	19.5	7.04	GE180, 2.77 g/cm^3

Appendix C

Cell Wall Thickness Data

The thickness of the target cell glass wall and its upstream window are important inputs for external radiative correction, as described in Section 5.4.3. In this appendix we list the cell wall and window thickness data for the cells used during the A_1^n experiment.

The measurements of the cell windows were performed at the Univ. of Virginia (UVa) [119] and the results are given in Table C.1 for cell "Gore", "Tilghman" and the 25 cm reference cell.

Table C.1: Cell window thickness data. For each cell, the two windows are labeled either by numbers or by letters.

cell	upstream (μm)	downstream (μm)
Gore	(B) 132	(A) 126
Tilghman	(A) 144	(B) 152
Reference Cell	(#17) 135	(#16) 138

For the cell walls, since the wall thickness varies along the beam direction, one needs to take the average value within the spectrometer acceptance as the input for the external radiative correction. The acceptance is determined by the spectrometer central angles θ and the software z_{tg} cuts used in the data analysis. This information is given in Table C.2 for each kinematics of the A_1^n experiment. The measurements of the cell glass wall were done at both UVa [119] and at JLAB Target Lab [120]. For each cell, the measurements were performed at a few points on each side of the target chamber. The locations of the measurements are labeled alphabetically and the data for these measured points are given in Table C.3, C.4 and C.5, for cell "Gore", "Tilghman" and the 25 cm reference cell, respectively. The location of each point on the target chamber is shown in Figure C-1, C-2 and C-3, for the three cells, respectively. The paths of the scattered electrons at the upstream and downstream

Table C.2: Data taking kinematics and the three cells used for the A_1^n experiment.

kinematics	θ	z_{tg} cut	cell
elastic	20°	±6 cm	Gore, Reference Cell
$x = 0.61$	20°	±6 cm	Gore, Reference Cell
$x = 0.48$	35°	$\sim$ ±10 cm	Tilghman, Reference Cell
$x = 0.33$	35°	$\sim$ ±10 cm	Tilghman, Reference Cell

extremes of the acceptance are shown in the Figures. For the radiative corrections at each kinematics, only the data points between the two extreme paths should be averaged.

Table C.3: "Gore" wall thickness data from UVa and JLAB.

source	A	B	C	D	E	F	G	H	I	J
UVa	1.32	1.34	1.54	1.51	1.31	-	-	-	-	-
JLab	1.54	1.56	1.33	1.33	1.29	1.35	1.49	1.50	1.30	1.27

Table C.4: "Tilghman" wall thickness data from UVa and JLAB.

source	A	B	C	D	E	F	G	H	I	J
UVa	1.31	1.35	1.33	1.33	1.43	1.44	1.43	1.48	-	-

Figure C-1: "Gore" wall thickness data from UVa (cyan labels) and JLAB (purple labels); The arrows show the upstream and downstream extremes of the acceptance for $x = 0.61$ (blue) and elastic (green) kinematics.

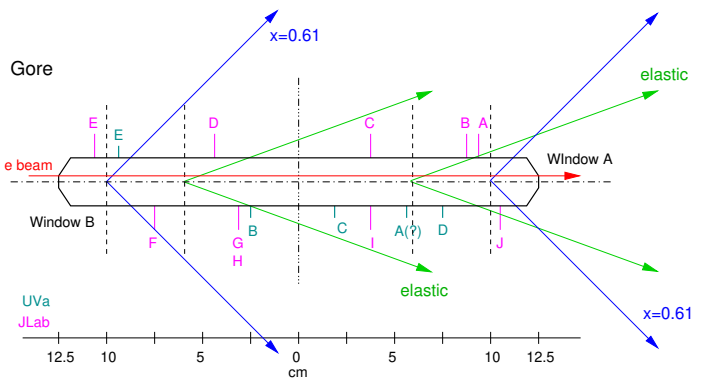

Figure C-2: "Tilghman" wall thickness data from UVa (cyan labels) and JLAB (purple labels); The arrows show the upstream and downstream extremes of the acceptance for $x = 0.33$ and 0.48 kinematics.

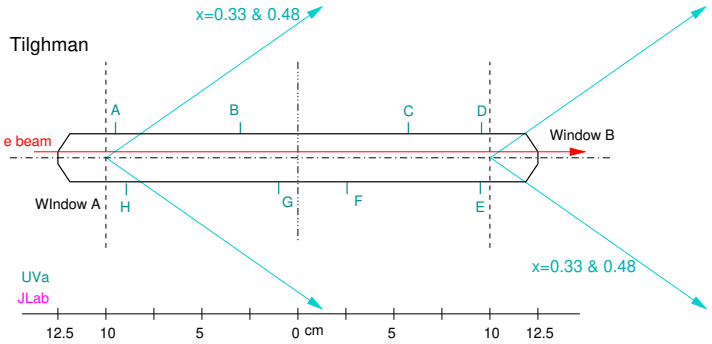

Table C.5: 25 cm reference cell wall thickness data from UVa and JLAB.

source	A	B	C	D	E	F	G	H	I	J
UVa	1.41	1.39	1.40	1.38	1.41	1.38	1.46	1.45	1.45	1.48
JLab	-	1.44	1.44	14.6	1.38	1.43	1.39	-	1.38	1.33

Figure C-3: 25 cm reference cell wall thickness data from UVa (cyan labels) and JLAB (purple labels); The arrows show the upstream and downstream extremes of the acceptance for $x = 0.33$ and 0.48 (cyan), $x = 0.61$ (blue), and elastic (green) kinematics.

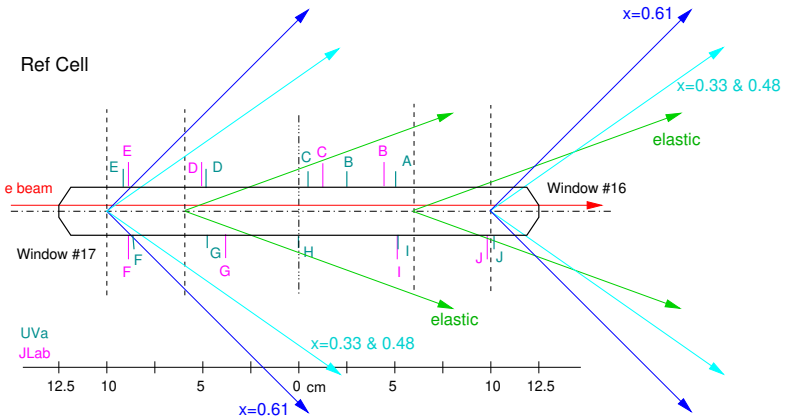

Appendix D

Structure Functions for Radiative Corrections

For radiative corrections, one needs polarized and unpolarized structure functions within a large kinematic range. In this section we give a list of world fits for the structure functions which we used for the internal and the external radiative corrections in the A_1^n experiment.

D.1 Internal Radiative Correction

The structure functions' kinematic coverage required by POLRAD 2.0 [145] to do the internal radiative correction at each x point of the A_1^n experiment is shown in Figure D-1. For $x = 0.33$ and $x = 0.48$, the required coverage extends from the deep inelastic to the resonance region ($W^2 < 4$ GeV^2). For $x = 0.61$, only coverage of the resonance region is required. However, the structure functions in the original POLRAD 2.0 do not cover the resonance region and the ones in the deep inelastic region are not up-to-date. Also the nuclear EMC effects are not included. We have added to POLRAD 2.0 the latest world fits for the unpolarized and the polarized structure functions in both the deep inelastic and the resonance region, corrections for the nuclear EMC effects, and the latest world fit for the ratio $R = \sigma_L/\sigma_T$. We list them as follows:

- Proton and deuteron unpolarized structure functions $F_2^p(x, Q^2)$, $F_2^D(x, Q^2)$ in the deep inelastic region:
  - f2nmc95 [142]: This is a fit performed by the NMC collaboration. It is valid for $0.006 < x < 0.9$ and $0.5 < Q^2 < 75$ (GeV/c)^2.
- Proton unpolarized structure function $F_2^p(x, Q^2)$ in the resonance region:

Figure D-1: Kinematic range needed by POLRAD 2.0 for internal radiative corrections.

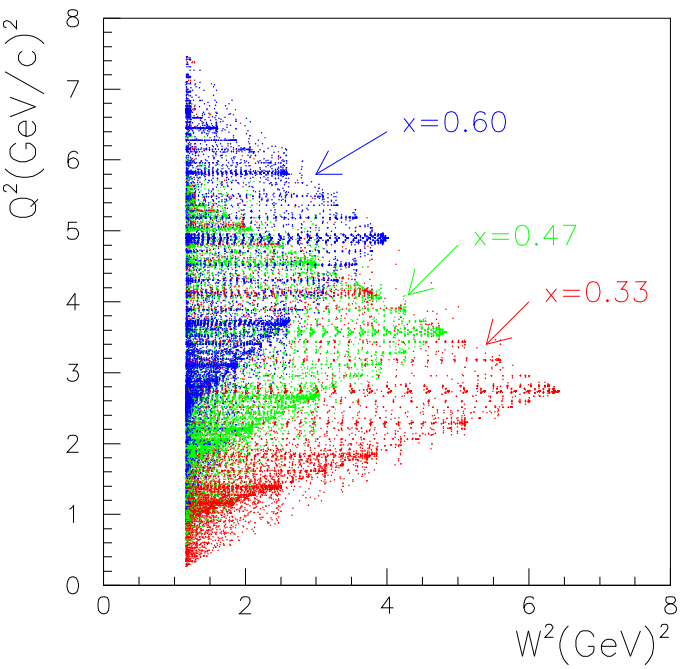

- slac94 [156]: This is a fit including all the inclusive SLAC data in the range $1.1 < W^2 < 5$ GeV^2. It has three background terms and three resonances. Each of these terms is multiplied by a polynomial in Q^2;
- hallc02 [157]: This fit includes the latest JLAB Hall C data in the resonance region of $1.15 < W^2 < 3.9$ GeV^2, $0.16 < Q^2 < 6.0$ (GeV/c)^2.

- EMC effects of the deuteron and ^{3}He [144]:
  The nuclear EMC ratios for the deuteron and the ^{3}He are defined as $\mathcal{R}^{^2\mathrm{D}}(x) \equiv F_2^{^2\mathrm{D}}(x)/[F_2^p(x) + F_2^n(x)]$ and $\mathcal{R}^{^3\mathrm{He}}(x) \equiv F_2^{^3\mathrm{He}}(x)/[2F_2^p(x) + F_2^n(x)]$. These two EMC ratios are used to obtain the neutron and the ^{3}He structure function F_2's from the fits of the proton and the deuteron F_2^p and F_2^D;

- The ratio $R = \sigma_L/\sigma_T$:
  We use the latest world fit "R1998" [143] for the ratio R. In this fit R is assumed to be independent of the nuclear target, i. e., $R^p = R^n = R^A$. "R1998" is valid for $0.005 \leqslant x \leqslant 0.86$ and $0.5 \leqslant Q^2 \leqslant 130$ GeV^2.

- Proton and neutron polarized structure functions $g_1^p(x, Q^2)$, $g_1^n(x, Q^2)$ in the deep inelastic region:
  - The polarized structure function g_1 is obtained by $g_1 = F_1(\frac{g_1}{F_1})$;
  - The unpolarized structure function F_1 is calculated from Eq. (1.18) using the F_2 and R fits listed above;
  - The proton structure function ratio g_1^p/F_1^p is obtained from a fit to all world data using a functional form $x^\alpha(a + bx)$, see Appendix F;
  - The neutron structure function ratio g_1^n/F_1^n is obtained from a fit to all world data from polarized ^{3}He target experiments using a second order polynomial fit $a + bx + cx^2$, see Appendix F.

D.2 External Radiative Correction

The single arm Monte-Carlo (SAMC) program does not include the helicity dependent internal radiation effects. So we used SAMC only for the external corrections, and the internal ones were performed by POLRAD 2.0, as described in Section 5.6.6,.

In order to do external radiative corrections, the internally radiated polarized structure functions g_1^{ir} and g_2^{ir} are needed by SAMC. Their kinematic coverages required by SAMC are shown in Figure D-2. A grid of (x, y, Q^2, W^2) covering these ranges was created and we ran POLRAD 2.0 for each kinematics on this grid. The g_1^{ir} and g_2^{ir} generated by POLRAD 2.0 on the grid were then read by SAMC which simulates the external radiation effects and gives the full radiative corrections.

Figure D-2: Kinematic range for external radiative corrections

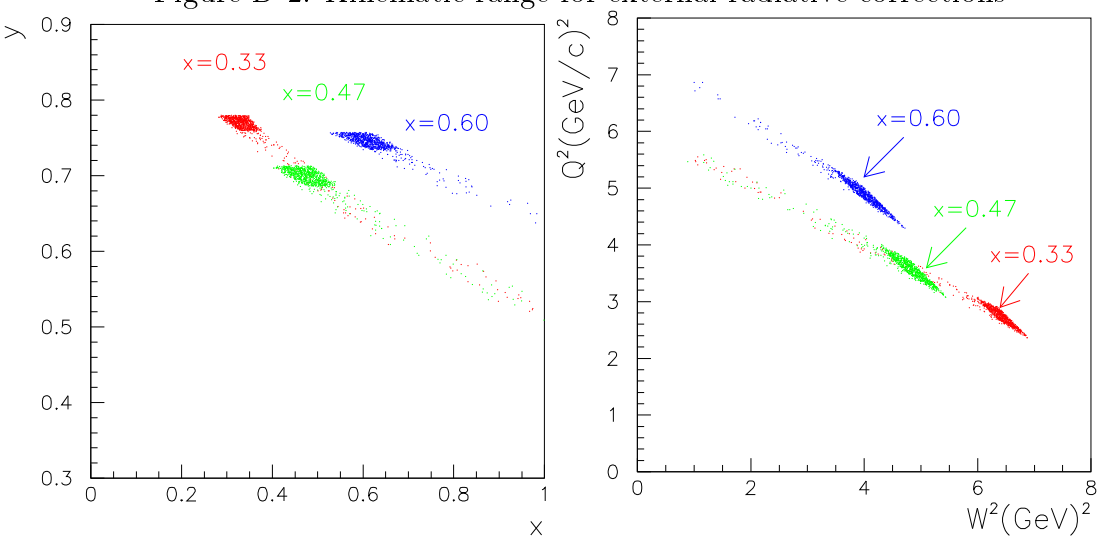

Appendix E

Polarized Structure Functions from the E155 Fit

The latest world fits of the proton and the neutron structure function ratios g_1^p/F_1^p and g_1^n/F_1^n were performed by the E155 collaboration at SLAC [20]. They are usually referred to as the "E155 fit". In this section we describe how to obtain the proton and the neutron polarized structure functions g_1, g_2 and the asymmetries A_1, A_2 from the E155 fit. The neutron structure functions and asymmetries calculated from the E155 fit are used to compare with the new data form this experiment in Chapter 6.

The E155 fit gives

$$\left(\frac{g_1^p}{F_1^p}\right)^{\text{E155 fit}} = x^{0.700}(0.817 + 1.014x - 1.489x^2)(1 - \frac{0.04}{Q^2}) \; ; \tag{E.1}$$

$$\left(\frac{g_1^n}{F_1^n}\right)^{\text{E155 fit}} = x^{-0.335}(-0.013 - 0.33x + 0.761x^2)(1 + \frac{0.13}{Q^2}) \; , \tag{E.2}$$

where Q^2 is the four momentum transfer in $(\text{GeV/c})^2$. To calculate the asymmetries A_1 and A_2, we assume the higher twist effects are small and use $g_2 = g_2^{WW}$, where g_2^{WW} is the twist-two term given by Eq. (1.37). In the following we denote $g_2^{p,WW}(g_2 n, WW)$ the twist-two term of the proton g_2^p (neutron g_2^n). The assumption $g_2 = g_2^{WW}$ is reasonable since at least for the proton, the g_2^p data from the E155x experiment [168] at SLAC show good agreement with the twist-two term $g_2^{p,WW}$. We then perform the following procedure at a constant Q^2:

- For the proton structure function F_2^p, we use the latest world fit "F2NMC95" [142] directly;

- For the neutron structure function F_2^n, we use proton and deuteron unpolarized structure functions F_2^p and F_2^D from F2NMC95 fit [142], with the deuteron

EMC effect included, as

$$F_2^n = \frac{F_2^D}{\mathcal{R}^D} - F_2^p \ ,$$

where $\mathcal{R}^D$ is the deuteron EMC ratio [144].

- We calculate F_1^p (F_1^n) using Eq. (1.18) and the calculated F_2^p (F_2^n). For the ratio $R = \sigma_L/\sigma_T$ we used R1998 fit [143]. In R1998 fit, the ratio R is assumed to be independent of the nuclear target, i. e., $R^n = R^p = R^A$;

- We multiply the ratio g_1/F_1 from the E155 fit by the F_1 calculated above, obtain g_1;

- We calculate g_2^{WW} using Eq. (1.37) and the g_1 constructed above;

- Taking the ratio of g_2^{WW} and the calculated F_1, we obtain g_2^{WW}/F_1;

- Using Eq. (1.41) and (1.42) and the F_1, g_1 and g_2^{WW} calculated above, we obtain A_1 and A_2. Since the assumption $g_2 = g_2^{WW}$ was used and g_2 is the dominant term of the transverse asymmetry A_2 in Eq. (1.42), the A_2 obtained from the above procedure is often called A_2^{WW}.

Appendix F

Fit for Proton and Neutron g_1/F_1

Fits for world data g_1/F_1 were used for the ^{3}He nuclear correction and radiative corrections. The fits were performed using GNUPLOT version 3.7 [182]. In this section we first describe the fitting algorithm used by GNUPLOT. Then the results of the proton and neutron g_1/F_1 fits will be presented.

The program GNUPLOT [182] implements the NonLinear Least-Squares (NLLS) Marquardt-Levenberg algorithm to minimize the chi-square χ^2, between the central values of the fit $f(x_i)$ and the data f_i:

$$\chi^2 = \sum_{i=1}^{N} \left[\frac{[f_i - f(x_i)]^2}{\sigma_i^2} \right] . \tag{F.1}$$

The reduced chi-square χ^2_v is defined as the chi-square per degree of freedom, where v is the number of degrees of freedom.

$$\chi^2_v = \frac{\chi^2}{v} ; \tag{F.2}$$

$$v = N - n - 1 , \tag{F.3}$$

where N is the number of data points used and n is the number of parameters of the fitting function. Each data point used in the fitting procedure is weighted by the statistical error σ_i as

$$w_i = \frac{1}{\sigma_i^2} . \tag{F.4}$$

The error of the fitted function can be calculated by standard deviation of each fitted parameter σ_{a_i} and the error matrix $\epsilon = \{\epsilon_{ij}\}$.

$$(\delta f)^2 = (\frac{\partial f}{\partial a_i})^2 \epsilon_{ii} (\sigma_{a_i})^2 + 2 \sum_{i \neq j} (\frac{\partial f}{\partial a_i})(\frac{\partial f}{\partial a_j}) \epsilon_{ij} (\sigma_{a_i})(\sigma_{a_j}) ; \tag{F.5}$$

ϵ is also called covariance matrix because its elements are the variances and covariance of the fitted parameters a_i and a_j, hence it must be a symmetric matrix with unit diagonal elements, i.e., $\sigma_{ij} = \sigma_{ji}$ and $\sigma_{ii} = 1$.

Assuming that in reality the distribution of the fitted data set is described by a parent function, then if the fitting function is a good approximation to the parent function, the reduced chi-square should be approximately unity, $\chi^2_v = 1$. A large χ^2_v may be caused by poor data quality or a bad fitting function. A too small χ^2_v may indicate an error in the assignment of the uncertainties in the measured variables. For most purposes, the reduced chi-square χ^2_v is an adequate measure of the fitting quality directly. For a good fit it should be close to 1, and less than 1.5.

The latest fits for the proton and neutron g_1/F_1 were done by the E155 collaboration [20] using function $x^\alpha(a + bx + cx^2)(1 + \beta/Q^2)$. A factor of x^α in the fitting function takes into account the feature of the gluon distribution at small x. However, we found that The E155 fits are not ideal for the purpose of data analysis for the A_1^n experiment. Since the fits are used for nuclear and radiation correction for data points up to $x = 0.61$, the behavior of the fits in the high x region is very important. Figure F-1 and F-2 show the E155 fit for proton and neutron (black curves). The proton fit starts to drop above x=0.6 and finally reach 0.4 at x=1.0. The neutron fit is not in good agreement with data from this experiment.

To choose a reasonable good fit for g_1^p/F_1^p and g_1^n/F_1^n, five different fitting functions have been tested and a comparison has been made in the reduced chi-square, as well as the error in the fitted function. The error in the fitted function is calculated using Eq. (F.5), then is further fitted by a 3^{rd} order polynomial $\delta f = e_0 + e_1 x + e_2 x^2 + e_3 x^3$.

The results of χ^2_v for each fitting function are listed in Table F.1. The first three functions have a factor of x^α for the gluon distribution at small x. However for neutron, because there is a large amount of data in the small x region which puts a strong constraint on the fitting result, it turns out that none of these three is in a good agreement with high x data from this experiment, especially the $x = 0.61$ point. For the neutron two polynomial fits have also been tested and are listed in Table F.1. The reduced chi-square of all five fits for neutron are above 1.5, which is again caused by the large amount of data in the low x region, while some of them do not have good statistics.

The world data set for the proton g_1^p/F_1^p includes those from HERMES [30], E143 [23] and E155 [20]. The neutron data g_1^n/F_1^n are from E143 (^{2}H target) [23], E155 (^{2}H target) [20] and this experiment E99-117 (^{3}He target).

Fits of the form $g_1^p/F_1^p = x^\alpha(a+bx)(1+\beta/Q^2)$ and $g_1^n/F_1^n = (a+bx+cx^2)(1+\beta/Q^2)$ have been chosen for the analysis of this experiment. The proton fit is shown in Figure F-1. The fitted parameters, their errors and the error matrix are given in Table F.2. Compared with the E155 fit, the new fit result is increasing in the large x region, which is expected from the theoretical predictions given in Chapter 2.

Table F.1: Reduced chi-square of five fitting function for g_1^p/F_1^p and g_1^n/F_1^n

$f(x,Q^2)$	g_1^p/F_1^p	g_1^n/F_1^n
$x^\alpha(a+bx)(1+\beta/Q^2)$	0.7843	1.3426
$x^\alpha(a+bx+cx^2)(1+\beta/Q^2)$	0.7811	1.3776
$x^\alpha(a+bx+cx^2+dx^3)(1+\beta/Q^2)$	0.7740	1.3520
$(a+bx+cx^2)(1+\beta/Q^2)$	0.7844	1.3271
$(a+bx+cx^2+dx^3)(1+\beta/Q^2)$	0.7942	1.3539

Table F.2: Result of the fit $g_1^p/F_1^p = x^\alpha(a+bx)(1+\beta/Q^2)$.

α = 0.8126 ± 0.0488
a = 1.2307 ± 0.1224
b = -0.4128 ± 0.2162
β = 0.0303 ± 0.1235

$$\epsilon = \begin{bmatrix} 1.0000 & 0.9080 & -0.8510 & 0.7230 \\ 0.9080 & 1.0000 & -0.9670 & 0.4010 \\ -0.8510 & -0.9670 & 1.0000 & -0.3690 \\ 0.7230 & 0.4010 & -0.3690 & 1.0000 \end{bmatrix}$$

The neutron fit is shown in Figure F-2 and the fitted parameters are given in Table F.3. Compared with the E155 fit, the new fit agrees more with the three new data points from this experiment.

Table F.3: Result of the fit $g_1^n/F_1^n = (a+bx+cx^2)(1+\beta/Q^2)$.

a = -0.0490 ± 0.0518
b = -0.1618 ± 0.2173
c = 0.6979 ± 0.3445
β = 0.7510 ± 2.1740

$$\epsilon = \begin{bmatrix} 1.0000 & -0.7370 & 0.1480 & 0.9600 \\ -0.7370 & 1.0000 & -0.7520 & -0.5810 \\ 0.1480 & -0.7520 & 1.0000 & -0.0390 \\ 0.9600 & -0.5810 & -0.0390 & 1.0000 \end{bmatrix}$$

Figure F-1: Results of the fit $g_1^p/F_1^p = x^\alpha(a+bx)(1+\beta/Q^2)$. The three curves show the new fit from this analysis (red), the error in the new fit (green), and the E155 fit [20] (black).

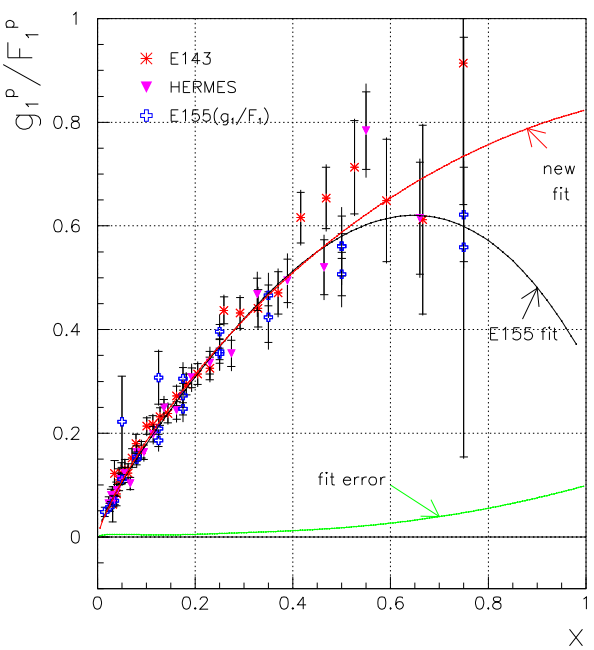

Figure F-2: Results of the fit $g_1^n/F_1^n = (a + bx + cx^2)(1 + \beta/Q^2)$. The three curves show the new fit from this analysis (red), the error in the new fit (green), and the E155 fit [20] (black).

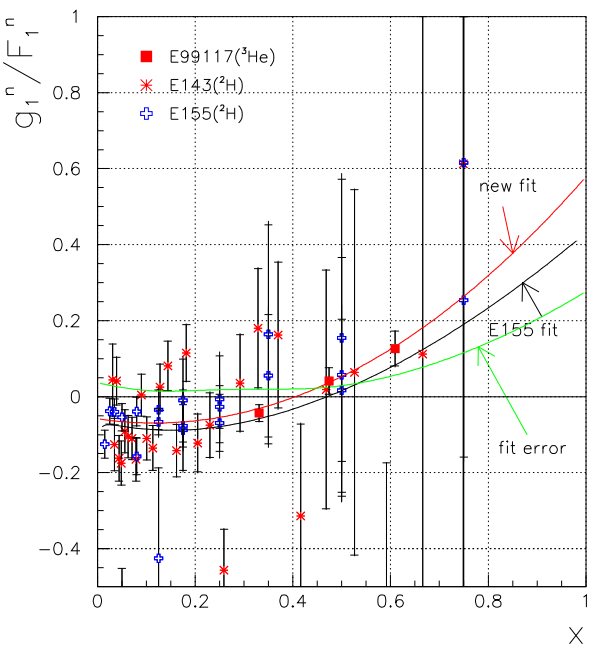

Bibliography

[1] SLAC E-080, M.J. Alguard *et al.*, *Phys. Rev. Lett.* **41**, 70 (1978); SLAC E-130, G. Baum *et al.*, *Phys. Rev. Lett.* **51**, 1135 (1983).

[2] EMC, J. Ashman *et al.*, *Phys. Lett.* **B206**, 364 (1988); EMC, J. Ashman *et al.*, *Nucl. Phys.* **B328**, 1 (1989).

[3] N. N. Bogoliubov, *Ann. Inst. Henri Poincaré* **8**, 163 (1968); F. E. Close, *Nucl. Phys.* **B80**, 269 (1974); A. LeYaouanc *et al.*, *Phys. Rev.* D9, 2636 (1974); **D15**, 844 (1977); A. Chodos, R. L. Jaffe, K. Johnson, and C. B. Thorn, *ibid.* **10**, 2599 (1974); M. J. Ruiz, *ibid.* **12**, 2922 (1975); C. Hayne and N. Isgur, *Phys. Rev.* D25, 1944 (1982).

[4] B. W. Filippone and X. Ji, e-Print: hep-ph/0101224.

[5] X. Ji, *Phys. Rev. Lett.* **78**, 610 (1997); e-Print: hep-ph/9603249.

[6] A. W. Thomas, W. Weise, *The Structure of the Nucleon*, Wiley-Vch, Berlin, Germany, 2001.

[7] A. deShalit, H. Feshbach, *Theoretical Nuclear Physics Volume I: Nuclear Structure*, Chapter 2, Wiley Classics Library Edition, 1990.

[8] M. Anselmino, A. Efremov, E. Leader, *Phys. Rept.* **261**, 1 (1995); Erratum-ibid. **281** 399 (1997); e-Print: hep-ph/9501369v2.

[9] J. D. Bjorken and E. A. Paschos, *Phys. Rev.* **185**, 1975 (1969).

[10] H. W. Kendall, *Nobel Lecture, Rev. Mod. Phys.* **63**, 597 (1991).

[11] R. P. Feynman, *Phys. Rev. Lett.* **23**, 1415 (1969).

[12] R. G. Roberts, *The Structure of the Proton*, Cambridge University Press, New York, 1990.

[13] M. Arneodo *et al.*, *Nucl. Phys.* **B483**, 3 (1997); e-Print: hep-ph/9610231

[14] R. G. Roberts, *Plenary talk at 5th International Workshop on Deep Inelastic Scattering and QCD (DIS '97)*, Chicago, April 1997; e-Print: hep-ph/9706269

[15] Y. Dokshitzer, *Sov. Phys. JETP* **46**, 1649 (1977); V. N. Gribov and L. N. Lipatov, *Sov. Nucl. Phys.* **15**, 438 and 675 (1972); G. Altarelli, G. Parisi, *Nucl. Phys.* **B126**, 298 (1977).

[16] K. Wilson, *Phys. Rev.*, **179**, 1499 (1969).

[17] M. Anselmino, A. Efremov and E. Leader, *Phys. Reports*, **261**, 1 (1995).

[18] D. Drechsel, S. S. Kamalov, L. Tiator, *Phys. Rev.*, **D63**, 114010 (2001); e-Print: hep-ph/0008306.

[19] J. Soffer, and O. V. Teryaev, *Phys. Lett.* **B490**, 106 (2000); e-Print: hep-ph/0005132.

[20] P. L. Anthony *et al.*, *Phys. Lett.* **B493**, 19 (2000); e-Print: hep-ph/0007248.

[21] Global fit from the Coordinated Theoretical-Experimental Project on QCD (CTEQ). J. Pumplin, D. R. Stump, J. Huston *et al.*, *J. High Energy Phys.* **07**, 012 (2002); e-Print: hep-ph/0201195. Program downloaded from: http://www.pa.msu.edu/hep/cteq/cteq6/ (updated 02/02/2002).

[22] F. Close, *Phys. Lett.* **B43**, 422 (1973); *Nucl. Phys.* **B80**, 269 (1974); *An introduction to Quarks and Partons*, p. 197, Academic Press, New York (1979).

[23] K. Abe *et al.*, SLAC-PUB-7753 (Feb 1998), submitted to *Phys. Rev. D.*. This final data report supersedes those given in previous papers: *Phys. Rev. Lett.* **74**, 346 (1995); *Phys. Lett.* **B364**, 61 (1995); *Phys. Rev. Lett.* **75**, 25 (1995); *Phys. Rev. Lett.* **76**, 587 (1996) and *Phys. Rev. Lett.* **78**, 815 (1997).

[24] J. Ashman *et al.*, *Phys. Lett.* **B206**, 364 (1988); *Nucl. Phys.* **B328**, 1 (1989).

[25] B. Adeva *et al.*, *Phys. Rev.* **D60**, 072004 (1999).

[26] P. L. Anthony *et al.*, *Phys. Rev.* **D54**, 6620 (1996).

[27] K. Abe *et al.*, *Phys. Rev. Lett.* **79**, 26 (1997); *Phys. Lett.* **B405**, 180 (1997).

[28] D. Adams *et al.*, *Phys. Lett.* **B357**, 248 (1995).

[29] K. Ackerstaff *et al.*, *Phys. Lett.* **B404**, 383 (1997).

[30] A. Airapetian *et al.*, *Phys. Lett.* **B442**, 484 (1998).

[31] A. Bodek *et al.*, *Phys. Rev. Lett.* **30**, 1087 (1973); E. M. Riordan *et al.*, *Phys. Rev. Lett.* **33**, 561 (1974); J. S. Poucher *et al.*, *Phys. Rev. Lett.* **32**, 118 (1974).

[32] R. Carlitz, *Phys. Lett.* **B58**, 345 (1975).

[33] R. P. Feynman, *Photon Hadron Interactions*, Benjamin, Reading, Massachusetts (1972).

[34] The origin of the constituent quark model has a long history. The idea of elementary constituents with fractional charges can be found in: G. Zweig, CERN Reports 8182/TH.401, 8419/TH.412 (1964); M. Gell-Mann, Phys. Lett. 8, 214 (1964);
The two papers that were first cited as a non-relativistic quark model are: G. Morpurgo, *Physics* **2**, 95 (1965); R. H. Dalitz, in *High Energy Physics; Lectures Delivered During the 1965 Session of the Summer School of Theoretical Physics, University of Grenoble*, edited by C. De Witt and M. Jocab (Gordon and Breach Publishers, Inc., New York, 1965); and in *Proceedings of the Oxford International Conference on Elementary Particles, Oxford, England, 1965* (Rutherford High Energy Laboratory, Chilton, Berkshire, England, 1966), p. 157.

[35] N. Isgur and G. Karl, *Phys. Rev.* **D18**, 4187 (1978);
N. Isgur and G. Karl, *Phys. Rev.* **D19**, 2653 (1979).

[36] N. Isgur, *Phys. Rev.* **D59**, 034013 (1999); e-Print: hep-ph/9809255

[37] G. R. Farrar, D. R. Jackson, *Phys. Rev. Lett.* **35**, 1416 (1975).

[38] S. J. Brodsky, M. Burkardt, I. Schmidt, *Nucl. Phys.* **B441**, 197-214 (1995); e-Print: hep-ph/9401328v2

[39] E. Leader, A. V. Sidorov, D. B. Stamenov, *Int. J. Mod. Phys.* **A13**, 5573 (1998); e-Print: hep-ph/9708335

[40] J. P. Ralson, P. Jain and R. V. Buniy, *AIP Conf. Proc.* **549**, 302 (2000); e-Print: hep-ph/0206074v1.

[41] M. K. Jones *et al.*, *Phys. Rev. Lett.* **84**, 1398 (2000); e-Print: nucl-ex/9910005.

[42] O. Gayou *et al.*, *Phys. Rev. Lett.*, **88**, 092301 (2002); e-Print: nucl-ex/0111010.

[43] S. J. Brodsky and G. P. Lepage, *Phys. Rev.* **D22**, 2157 (1981).

[44] E. Leader, A. V. Sidorov, D. B. Stamenov, *Eur. Phys. J.* **C23**, 479 (2002); e-Print: hep-ph/0111267.

[45] E. Leader, D. B. Stamenov, *priv. comm.*

[46] C. Bourrely, J. Soffer, F. Buccella, *Eur. Phys. J.* **C23**, 487 (2002); e-Print: hep-ph/0109160v1.

[47] C. Bourrely, J. Soffer, *priv. comm.*

[48] E. D. Bloom and F. J. Gilman, *Phys. Rev. Lett.* **16**, 1140 (1970); *Phys. Rev.* **D4**, 2901 (1971).

[49] S. D. Drell and T. -M. Yan, *Phys. Rev. Lett.* **22**, 2157 (1980).

[50] G. B. West, *Phys. Rev. Lett.* **24**, 181 (1970); *Phys. Rev.* **D14**, 732 (1976).

[51] A. de Rújula, H. Georgi and H. D. Politzer, *Ann. Phys.* **103**, 315 (1975).

[52] W. Melnitchouk, *Phys. Rev. Lett.* **86**, 35 (2001); e-Print: hep-ph/0106073.

[53] P. Mergell, U. G. Meißner and D. Drechsel, *Nucl. Phys.* **A 596**, 367 (1996).

[54] W. Melnitchouk, *priv. comm.*

[55] D. Diakonov, *Lectures at Advanced Summer School on Non-Perturbative Field Theory*, Peniscola, Spain, June (1997), To be published by World Scientific in School proceedings; e-Print: hep-ph/9802298.

[56] D. Diakonov, in: *Selected Topics in Non-perturbative QCD*, A. Di Giacomo and D. Diakonov, eds., Bologna, 397 (1996); e-Print: hep-ph/9602375.

[57] D. Diakonov, V. Petrov, *Nucleons as chiral solitons*; e-Print: hep-ph/0009006.

[58] E. Witten, *Nucl. Phys.* **B160**, 57, (1979).

[59] R. Dashen and A. V. Manohar, *Phys. Lett.* **B 315**, 425, (1993); *Phys. Lett.* **B 315**, 438 (1993).

[60] Y. Nambu and G. Jona-Lasinio, *Phys. Rev.* **122**, 345 (1961); *Phys. Rev.* **124**, 246, (1961).

[61] R. Alkofer, H. Reinhardt, H. Weigel, *Phys. Rept.* **265**, 139 (1996); e-Print: hep-ph/9501213.

[62] H. Weigel, L. Gamberg and H. Reinhardt, *Phys. Lett.* **B399**, 287 (1997); *Phys. Rev.* **D55**, 6910 (1997). O. Schröder, H. Reinhardt and H. Weigel; e-Print: hep-ph/9902322

[63] L. Gamberg, H. Weigel, *pri. comm.*

[64] N. I. Kochelev, talk presented at the Workshop "Deep Inelastic Scattering off Polarized Targets: Theory Meets Experiment", Sept. 1997, DESY-Zeuthen; e-Print: hep-ph/9711226v1.

[65] N. I. Kochelev, Z. -E. Meziani, *pri. comm.*

[66] D. Dolgov, R. Brower, J. W. Negele and A. Pochinsky; e-Print: hep-lat/9809132v1.

[67] JLAB E99-117, J. P. Chen, Z. -E. Meziani, P. Souder *et al.*, http://hallaweb.jlab.org/physics/experiments/he3/A1n/

[68] A. Alley *et al.*, *Nucl. Inst. and Meth. in Phys. Res.* **A365**, 1 (1995).

[69] R. Prepost and T. Maruyama, *Ann. Rev. of Nucl. and Part. Sci.* **45**, 41 (1995).

[70] J. Berthot and P. Vemin, *Nucl. Phys. News* **9**, 12 (1990).

[71] D. Marchand, *Ph. D. thesis*, Université Blaise Pascal, Clermont-Ferrand, France (1997).

[72] A. Deur, *priv. comm.*.

[73] O. Ravel, *Ph. D. thesis*, Université Blaise Pascal, Clermont-Ferrand, France (1997).

[74] D. W. Higinbotham, *priv. comm.*

[75] JLAB Hall A Absolute Beam Energy Measurements, http://www.jlab.org/∼brittin/beam_energy_table.html

[76] A. V. Glamazdin, D. S. Dale, E. Chudakov, A. Gasparian *et al.*, *Operational Safety Procedure for the Hall A Møller Polarimeter*, (1999); *Møller Polarimeter in Hall A of Jefferson Lab*, http://www.jlab.org/ moller/index.html

[77] B. D. Anderson *et al.*, http://hallaweb.jlab.org/equipment/NIM.ps

[78] *The Operations Manual for Compton Polarimeter*, http://hallaweb.jlab.org/compton/OSP/index.php

[79] S. Binet, *Monitoring the polarization for the A_1^n and g_2^n experiments with the Compton polarimeter of the Jefferson Laboratory*, April (2002); http://hallaweb.jlab.org/physics/experiments/he3/A1n/doc/final-compton.pdf

[80] E. Burtin, D. Lhuillier, *priv. comm.*

[81] JLAB Hall A electronic logbook, entries # 62294, #62654, #63051, #63722, #65949, #68178, http://www.jlab.org/∼adaq/halog/html/logdir.html

[82] TJNAF OPERATIONS Logbook, entries #147845, #149301, http://opweb.acc.jlab.org/internal/ops/daily_activity_log/html/

[83] *Hall A Operations Manual*, 2000; *Hall A Operations Manual* Archive.

[84] National Instruments - GPIB Interface.

[85] A. Saha, *BCM calibration on Jan. 12th, 2001*, *priv. comm.*

[86] Manual for Experiment Scanning Program for hall A Collaboration Experiments (ESPACE); http://hallaweb.jlab.org/espace/manual.ps.gz

[87] G. D. Cates et al., *Polarization induced transport asymmetries of light pulses: The pita effect,* unpublished, Optics Communications (1991).

[88] B. Humensky, *General exam advanced project*, Princeton University (1999).

[89] A. Vacheret, *priv. comm.*

[90] W. Bertozzi *et al.*, *Nucl. Instrum. and Meth.*, **191**, 957 (1977).

[91] N. Liyanage, *Ph. D. thesis*, Massachusetts Institute of Technology, Cambridge, Massachusetts (1999).

[92] C. Grupen, *Particle Detectors*, Cambridge University Press, p. 193 (1996).

[93] P. A. Čerenkov, *Phys. Rev.* **52**, 378 (1937);
P. A. Čerenkov, I. M. Frank, and I. E. Tamm, *Nobel Lectures in Physics 1942-1962*, Elsevier Publ. Comp., NewYork, 426, 1964.

[94] E. Fermi, *Phys. Rev.* **57**, 485 (1940); I. M. Frank and I. E. Tamm, *Compt. Rend. Acad. Sci. U.R.C.S.* **14**, 109 (1937).

[95] DuPont (TM) Tedlar(R) PVF Film, E.I. du Pont de Nemours and Company, http://www.dupont.com/tedlar/

[96] A. Deur, TJNAF E94-010 Technical Note E94010-TN-03
http://www.jlab.org/e94010/tech_note_03.ps.gz

[97] X. Zheng, *JLAB Hall A detector PID efficiency analysis using high electron rate data*, report to E99-117/E97-103 collaboration,
http://hallaweb.jlab.org/physics/experiments/he3/A1n/pid/memo11_left/
http://hallaweb.jlab.org/physics/experiments/he3/A1n/pid/memo11_right/

[98] EPICS, http://www.jlab.org/accel/documents/epics_doc.html

[99] *Status Report on Activities in Hall A - 2001*, Edited by A. J. Sarty, C. de Jager;
http://hallaweb.jlab.org/publications/Talks/StatusReport/StatusReport2001.pdf

[100] F. D. Colegrove, L. D. Shearer, and G. K. Walters, *Phys. Rev.* **132**, 2561 (1963).

[101] T. E. Chupp *et al.*, *Phys. Rev.* **C 36**, 2244 (1987).

[102] M. V. Romalis, *Ph. D. thesis*, Princeton University, Princeton, New Jersey (1998).

[103] JLAB E94-010, G. D. Cates, Z. -E. Meziani *et al.*, http://www.jlab.org/e94010/

[104] JLAB E97-103, T. Averett, W. Korsch *et al.*,
http://www.jlab.org/exp_prog/CEBAF_EXP/E97103.html

[105] M. E. Wagshul and T. E. Chupp, *Phys. Rev.* **A 49**, 3854 (1994).

[106] W. Happer, *Rev. Mod. Phys.* **44**, 169 (1972).

[107] S. Appelt *et al.*, *Phys. Rev.* **A 58**, 1412 (1998).

[108] T. J. Killian, *Phys. Rev.* **27**, 578 (1926).

[109] *CRC Handbook of Chemistry and Physics*, 74th ed. (CRC Press, Cleveland, 1993) pp. 4-124.

[110] A. Ben-Amar Baranga *et al.*, *Phys. Rev.* **A48**, 4411 (1993).

[111] B. Larson, *et al.*, *Phys. Rev.* **A44**, 3108 (1991).

[112] K .P. Coulter, *et al.*, *Nucl. Instr. Meth. in Phys. Res.* **A40**, 4959 (1989).

[113] K. Kramer, *priv. comm.*; *JLAB Hall A Polarized* ^{3}*He Target Lab Logbook*, 2001.

[114] G. D. Cates, *priv. comm.*

[115] N. R. Newbury *et al.*, *Phys. Rev.* **A48**, 4411 (1993).

[116] H. L. Middleton, *Ph. D. thesis*, p. 445, Princeton University, Princeton, New Jersey (1994).

[117] G. D. Cates, S. R. Schaefer and W. Happer, *Phys. Rev.* **A37**, 2877 (1988); G. D. Cates, D. J. White, T. R. Chien, S. R. Schaefer and W. Happer, *Phys. Rev.* **A38**, 5092 (1988).

[118] JLAB E95-001, H. Gao *et al.*, http://www.jlab.org/∼ddutta/e95001/

[119] J. Singh, *Cell Data Table*, Univ. of Virginia, http://galileo.phys.virginia.edu/research/groups/spinphysics/celldata.htm

[120] K. Kramer, E99117/E97103 technical note #1, http://www.jlab.org/∼kramerk/tnote_t1.ps; V. Sulkosky, *Cell Wall Thickness Measurements*, http://www.jlab.org/∼vasulk/cell_thickness.html

[121] KEPCO power supply BOP 36-12D, *Product Catalog*, KEPCO INC., Flushing, New York (1996); http://www.kepcopower.com/bopmod.htm

[122] A. Abragam, *Principles of Nuclear Magnetism*, (Oxford University Press 1961).

[123] H. Goldstein, *Classical Mechanics*, Addison-Wesley, Reading, Massachusetts, (1980).

[124] S. Meiboom, Z. Luz, D. Gill, *J. Chem. Phys.* **27**, 1411 (1957); S. Meiboom, *J. Chem. Phys.* **34**, 375 (1961); R. E. Glick, K. C. Tewari, *J. Chem. Phys.* **44**, 546 (1966).

[125] K. Kramer, *Ph. D. thesis*, College of William and Mary, Williamsburg, Virginia (2003).

[126] PIN 10D photodiode, *Product Catalog*, UDT sensors INC., Hawthorne, California (2000); http://www.udt.com

[127] Laser Line Bandpass Filters, Model 10LF10-780, *Product Catalog*, Newport Corporation, Irvine, CA (2000).

[128] HP3324A Synthesized Function/Sweep Generator, *Operationg and Programming Manual*, Hewlett Packard Inc., Boeblingen, Germany (1990); DS345 Synthesized Function Generator, *User's Manual*, Stanford Research System Inc., Sunnyvale, CA (1997); SR844 RF Lock-in Amplifier, *User's Manual*, Stanford

Research System Inc., Sunnyvale, CA (1997); Models 80/81 50MHz Function and Pulse Function Generator, *Operation and Maintenance Manual*, Waveteck Instruments Division, San Diego, CA (1996).

[129] N. F. Ramsey, *Molecular Beams*, Oxford Science Publications (1990).

[130] K. Kramer, *priv. comm.*

[131] K. Kramer, *Field Calibration For The Polarized ^{3}He Target During E99117/E97103*, E99117/E97103 technical note #2, http://www.jlab.org/∼kramerk/tnote_t2.ps

[132] W. Korsch, TJNAF E94-010 Technical Note E94010-TN-11 http://www.jlab.org/e94010/tech_note_11.ps.gz

[133] M. V. Romalis, G. D. Cates, *Phys. Rev.* **A58**, 3004 (1998).

[134] J. Kestin *et al.*, *J. Phys. Chem. Ref. Data* **13**, 229 (1984).

[135] M. Rvachev, TJNAF Hall A Technical Note Jlab-TN-01-055 http://tnweb.jlab.org/tn/2001/01-055.pdf

[136] X. Zheng, *Hall A detector PID efficiency analysis using DIS high pion rate data from E99-117*, report to E99-117/E97-103 collaboration, http://hallaweb.jlab.org/physics/experiments/he3/A1n/pid/memo15_pideff_e99117/

[137] T. W. Donnelly and A. S. Raskin, *Annals of Phys.* **169**, 247 (1986).

[138] M. Iodice, E. Cisbani *et al.*, *The CO_2 Gas Cherenkov Detectors for the Jefferson Lab Hall-A Spectrometers*, http://hallaweb/jlab.org/publications/Talks/1998/Publications/Iodice-instruments-98.ps

[139] A. Amroun *et al.*, *Nuc. Phys.* **A579**, 596 (1994).

[140] A. Deur, TJNAF E94-010 Technical Notes E94010-TN-33 http://www.jlab.org/e94010/tech_note_33.ps.gz

[141] J. J. Lerose, *Transfer Functions for the Hall A Spectrometers*, http://hallaweb.jlab.org/news/minutes/tranferfuncs.html

[142] M. Arneodo *et al.*, *Phys. Lett.* **B364**, 107 (1995); e-Print: hep-ph/9509406.

[143] K. Abe *et al.*, *Phys. Lett.* **B452**, 194 (1999); e-Print: hep-ex/9808028.

[144] W. Melnitchouk and A. W. Thomas, *Acta Phys. Polon.* **B27**, 1407 (1996); e-Print: nucl-th/9603021; W. Melnitchouk, *pri. comm.*

[145] I. Akushevich *et al.*, *Comp. Phys. Comm.* **104**, 201 (1997); e-Print: hep-ph/9706516.

[146] J. Singh, *priv. comm.*

[147] N. Liyanage, *Spectrometer constant determination for the Hall-A High Resolution Spectrometer Pair*, Jefferson Lab Hall A technote, JLAB-TN-01-049.

[148] JLAB Hall A Survey Reports, May 30, (2001); http://hallaweb.jlab.org/news/minutes/Survey_Reports/Survey_Reports.html

[149] H. Ibrahim, P. Ulmer, N. Liyanage, JLAB Hall A Technical Notes JLAB-TN-02-032, (2002).

[150] A. Deur, *Ph. D. thesis*, Université Blaise Pascal, Clermont-Ferrand, France (2000).

[151] Seonho Choi, *priv. comm.*

[152] X. Zheng, *E99-117 Runplan*, June 9th (2001), report to E99-117/E97-103 collaboration; http://hallaweb.jlab.org/physics/experiments/he3/A1n/runplan/index.html

[153] P. R. Bevington, D. K. Robinson, *Data Reduction and Error Analysis for the Physical Siences*, 2^{nd} edition, WCD/McGraw-Hill Press (1992).

[154] L. Mo, Y. S. Tsai, *Rev. Mod. Phys.* **41**, 205 (1969).

[155] P. Amaudruz *et al.*, *Nucl. Phys* **B371**, 3 (1992).

[156] C. Keppel, *Ph. D. thesis*, American University, Washington, DC (1994).

[157] Y. Liang, *pri. comm.*

[158] Y. S. Tsai, in *Proceedings of the International Conference on Nuclear Structure*, Stanford Univ. Press, Stanford, California (1964), p. 221.

[159] S. Stein *et al.*, *Phys. Rev.* **D12**, 1884 (1975).

[160] S. I. Bilenkaya, Y. M. Kazarinov and L. I. Lapidus, *Pisma ZhETF*, **61**, 2225 (1971); *Sov. Phys. JETP* **34** 1192 (1972); *Pisma ZhETF*, **19**, 613 (1974).

[161] R. Arnold *et al.*, *Phys. Rev. Lett.* **57**, 174 (1986).

[162] S. Galster *et al.*, *Nucl. Phys.* **B32**, 221 (1971).

[163] P. Amaudruz *et al.*, *Nucl. Phys.* **B441**, 3 (1995); M. Arneodo *et al.*, *Nucl. Phys.* B441, 12 (1995).

[164] R. L. Jaffe, in *Relativistic Dynamics and Quark-Nuclear Physics*, M. B. Johnson and A. Picklesiner (Eds.), Wiley, New York, 1986.

[165] F. Bissey *et al.*, *Phys.Rev.* **C65**, 064317 (2002); e-Print: hep-ph/0109069.

[166] C. Ciofi degli Atti *et al.*, *Phys. Rev.* **C48**, R968 (1993).

[167] F. Bissey *et al.*, *Phys. Rev.* **C64**, 024004 (2001).

[168] P. L. Anthony *et al.*, SLAC-PUB-8813 (2002), submitted to *Phys. Rev. Lett.*; e-Print: hep-ex/0204028.

[169] A. Nogga, *Ph. D. thesis*, Ruhr-Universität Bochum, Bochum, Germany (2001).

[170] A. Afanasev, C. E. Carlson and C. Wahlquist, *Phys. Rev.* **D58**, 054007 (1998); e-Print: hep-ph/9706522.

[171] A. Afanasev, C. E. Carlson and C. Wahlquist, e-Print: hep-ph/9706522.

[172] J. Wendland, Preliminary results on *quark polarisations from a five parameter fit assuming a symmetric strange sea polarisation*, (2002) http://hermes.desy.de/notes/pub/TRANS/Deltaq.5p.ps.gz

[173] W. Melnitchouk, A. W. Thomas, *Phys. Lett.* **B377**, 11 (1996); e-Print: nucl-th/9602038.

[174] G. G. Petratos, I. R. Afnan, F. Bissey *et al.*; e-Print: nucl-ex/0010011.

[175] H. Abramowicz *et al.*, *Z. Phys.* **C25**, 29 (1983).

[176] J. P. Chen, Seonho Choi, N. Liyanage *et al.*, http://www.jlab.org/exp_prog/CEBAF_EXP/E01012.html

[177] Jefferson Lab, *The Science Driving the 12 GeV Upgrade of CEBAF*, (2001); http://www.jlab.org/div_dept/physics_division/GeV/WhitePaper_V11.ps

[178] F. W. Brasse *et al.*, *Nucl.Phys.* **B110**, 413 (1976).

[179] P. Amaudruz *et al.*, *Phys. Lett.* **B295**, 159 (1992).

[180] A. Schaefer, *Phys. Lett.* **B208**, 175 (1988).

[181] M. Gluck, E. Reya, M. Stratmann and W. Vogelsang, *Phys. Rev.* **D53**, 4775 (1996).

[182] H. -B. Broeker *et al.*, *GNUPLOT, An Interactive Plotting Program, Version 3.7*, Thomas Williams, Colin Kelley (1998); http://www.gnuplot.info/